

A Thesis Submitted for the Degree of PhD at the University of Warwick

Permanent WRAP URL:

<http://wrap.warwick.ac.uk/135207>

Copyright and reuse:

This thesis is made available online and is protected by original copyright.

Please scroll down to view the document itself.

Please refer to the repository record for this item for information to help you to cite it.

Our policy information is available from the repository home page.

For more information, please contact the WRAP Team at: wrap@warwick.ac.uk

Ab Initio Temperature Dependence of EXAFS:
Multiple Scattering and Configurational Averaging
for a Biologically Significant Model Compound
(Zinc Tetraimidazole Complex)

by Paul William Loeffen

B.Sc. (honours) Physics

submitted for the degree of Ph.D. to:

Warwick University

Coventry CV4 7AL

United Kingdom

research position held at:

European Molecular Biology Laboratory

c/o DESY Notkestraße 85

D-22603 Hamburg

Germany

submitted: December 1993

Contents

Acknowledgements	vi
Declaration	vii
Abstract	viii
1 Introduction	1
1.1 Layout of this Thesis	6
2 TLS Analysis	9
2.1 Introduction	9
2.2 Standard Theory of TLS Analysis	12
2.2.1 Rigid-Body Motion	13
2.3 Crystallography of Zinc (II) Tetraimidazole Tetrafluoroborate	15
2.4 Methodology for TLS Analysis	18
2.4.1 Rigid Body Test	18
2.4.2 Choice of Rigid-Body - Separation of Internal Displacements	20
2.5 Results	22
2.5.1 Mean-Squared Displacements of Overall Disorder	22
2.5.2 Mean-Squared Displacements of Internal Motion	23
2.6 Discussion of TLS Analysis	25
2.6.1 Summary	30
3 Inelastic Neutron Scattering	31

3.1	Introduction	31
3.2	Essential Elements of INS Theory	34
3.2.1	Partial Differential Cross Section	34
3.2.2	Coherence and Incoherence - Scattering from Protons	37
3.2.3	Correlation and Response Functions	39
3.2.4	Response Function for Isolated Harmonic Oscillator	41
3.2.5	Fundamentals, Overtones and Combinations - Spectral Intensity	42
3.2.6	Phonon Wings	45
3.3	Molecular Vibrations and Normal Mode Analysis	47
3.3.1	Classical Description of Small Vibrations	48
3.3.2	Normal Coordinates and Zero Frequencies	50
3.3.3	Quantum-Mechanical Considerations	51
3.3.4	Temperature and the Mean-Squared-Amplitude Matrix	53
3.3.5	Internal coordinates	54
3.3.6	The Wilson GF method	55
3.3.7	Inclusion of Symmetry - Group Theory	58
3.3.8	Internal Symmetry Coordinates	60
3.4	Inelastic Neutron Scattering Experiment	62
3.4.1	The TFXA spectrometer	63
3.4.2	Samples for INS experiment	67
3.4.2.1	Preparation of $Zn(imid)_4(ClO_4)_2$	68
3.4.2.2	Preparation of $Zn(imid)_4(^{11}BF_4)_2$	69
3.4.2.3	Preparation of $Zn(imid-d_{(1)})_4(ClO_4)_2$	69
3.4.2.4	Preparation of $Zn(imid-3d_{(2,4,5)})_4(ClO_4)_2$	69
3.4.3	Analytical Software - CLIMAX	70
3.5	INS Study of Imidazole	73
3.5.1	Physical Characteristics of Imidazole	73
3.5.2	Experimental Results	76
3.5.3	Normal Mode Analysis - Input Parameters	81

3.5.3.1	reference geometry	82
3.5.3.2	target eigenvalues and INS intensities	82
3.5.3.3	molecular model	83
3.5.3.4	starting estimate for force field	83
3.5.4	Normal Mode Analysis - Methodology of Refinement	87
3.5.5	Results and Discussion	90
3.5.6	Summary of INS Study of Imidazole	99
3.6	INS Study of Zinc Tetraimidazole Complex	100
3.6.1	Physical Characteristics of Zinc Tetraimidazole Complex	100
3.6.2	Experimental Results	102
3.6.3	Low Frequency Regime ($< 500\text{cm}^{-1}$) - Strategy for Normal Mode Analysis	106
3.6.3.1	5-atom model: T_d symmetry	109
3.6.3.2	9-atom model: T_d symmetry	111
3.6.3.3	13-atom model: S_4 symmetry	112
3.6.3.4	21-atom model: S_4 symmetry	112
3.6.3.5	37-atom final model: C_2 symmetry	114
3.6.4	Low Frequency Regime ($< 500\text{cm}^{-1}$) - Force Field and Eigenvectors .	116
3.6.5	Imidazole Regime ($> 500\text{cm}^{-1}$) - Mode Assignment	121
3.6.6	Imidazole Regime ($> 500\text{cm}^{-1}$) - Force Field and Eigenvectors	125
3.6.7	Self-Consistency of Force Field - Deuteration	129
3.6.8	Summary of INS study of Zinc (II) tetraimidazole	134
4	Temperature Dependence of EXAFS	137
4.1	Introduction	137
4.2	Theory	139
4.2.1	Calculation of EXAFS signal - MSXAS software	140
4.2.1.1	Multiple scattering theory	140
4.2.1.2	One-electron approximation	142
4.2.1.3	Exchange-correlation potential	144

4.2.1.4	Many-body effects	144
4.2.1.5	Muffin-tin approximation	145
4.2.1.6	MSXAS software	145
4.2.2	Configurational Averaging Approximation	146
4.3	Experimental Procedure	150
4.3.1	Sample Preparation and Experimental Apparatus	150
4.3.2	Data Collection	151
4.3.3	Preliminary Analysis of Experimental Fine Structures	154
4.4	Configurational-Averaging Computation	159
4.4.1	EXAFS Signal without Damping	159
4.4.2	Test of Configurational-Averaging Algorithm	165
4.5	Results	167
4.5.1	Individual Multiple Scattering Paths	167
4.5.2	Temperature Dependence of Total EXAFS Spectrum	170
5	Discussion	174
5.1	Confidence in the Vibrational Correlation Function (VCF)	175
5.1.1	Consistency of Atomic Displacements from INS and TLS Studies	176
5.1.2	Check of Zn-N Pair Correlation Function	179
5.1.3	Anharmonicity	180
5.2	Discussion of Configurational Averaging Results	182
5.3	Implications for EXAFS Analysis	185
5.3.1	Various Approaches to EXAFS Data Evaluation	185
5.3.2	Significance of Results for Structure Determination	187
5.4	Conclusions	189
A	Extension to Standard TLS Theory	192
B	Mean-Squared-Deviation of Harmonic Oscillator	194
C	Symmetry Species of Normal Modes	196

D Projection of Symmetry Coordinates	199
E Character Tables	201
F Imidazole Force Field: Non Minimum Basis	202
G Low Frequency Skeletal Modes of Zinc Tetraimidazole Complex	203
H Temperature Dependence of Individual Multiple Scattering Paths	206
References	217

Acknowledgements

I would like to acknowledge the assistance of the following people (in alphabetical order):

Dr. N. Alcock, (University of Warwick, Coventry) for allowing me to use the X-ray crystallography data of zinc (II) tetraimidazole tetrafluoroborate, Dr. Z. Dauter, (EMBL, Hamburg) for his helpful discussions, Gwyndaf Evans, (EMBL and University of Warwick) for his friendship and encouragement, Dr. F. Fillaux, (CNRS, Thiais) for permitting me to analyse the INS data of imidazole, Dr. A. Filipponi, (Università dell'Aquila, L'Aquila), for his helpful comments at the 1992 Camerino workshop, Dr. Mariane Hegemann, (Universität, Münster) for her help in preparing deuterated samples, Dr. C. Hermes and Dr. H. F. Nolting (EMBL, Hamburg) for their help collecting EXAFS data, Dr. G. J. Kearley, (Institut Laue Langevin, Grenoble) for his advice and help using the INS analysis software CLIMAX, Dr. M. Majoube, (CEA Saclay) for his information about the deuteration of imidazole, Dr. E. Maverick, (UCLA, Los Angeles) for her helpful comments at the 1991 Erice workshop, Prof. C. R. Natoli, (INFN, Frascati) for helpful discussion and the use of the MSXAS package, Dr. J. Tomkinson, (Rutherford Appleton Laboratory, Oxon) for his assistance and advice in measuring and analysing INS spectra, Prof. K. Trueblood, (UCLA, Los Angeles) for helpful discussion at the 1991 Erice workshop, Prof. J. W. White (Australian National University, Canberra) for his comments and encouragement at the 1991 Erice workshop, Dr. K. Wilson, (EMBL, Hamburg) for his support, and Dr. J. D. Woollins, (Imperial College, London) for his help in taking Raman spectra

I would also like to express my gratitude to the *European Molecular Biology Laboratory* for its financial support for the period of study.

Finally, I would like to give a special thanks to Dr. Robert Pettifer (University of Warwick, Coventry) for his supervision and guidance.

Declaration

I hereby declare that the work contained in this thesis is my own, or a product of joint research, except where specifically cited or referenced otherwise.

The joint research involved contributions from the following people (in the order presented in this thesis):

In chapter 2 the X-ray diffraction data of zinc (II) tetraimidazole tetrafluoroborate was measured by Dr. N. Alcock of the University of Warwick, Coventry, and crystallographic structure refinement was performed by him.

In chapter 3 the inelastic neutron scattering data was collected at Rutherford Appleton Laboratory, Oxon, in collaboration with Dr. J. Tomkinson and Mark Adams. The inelastic neutron scattering data of imidazole was collected by Dr. F. Fillaux and was analysed with his consent.

In chapter 4 the EXAFS data of zinc (II) tetraimidazole was collected with the assistance of Dr. H. F. Nolting.

The entire project was in collaboration with, and under the supervision of, Dr. Robert Pettifer of the University of Warwick, Coventry.

Abstract

An ab initio calculation of the temperature dependence of the EXAFS spectrum of the zinc (II) tetraimidazole complex has been made and compared to low noise, energy calibrated EXAFS spectra at seven temperatures. The ab initio calculation was based on the MSXAS package, (122), and was adapted to incorporate a full configurational average to account for the temperature dependent damping of the EXAFS spectra due to thermal atomic disorder and it did not involve the fitting of free parameters. The information about the atomic disorder was obtained from two sources: (i) a TLS analysis of x-ray crystallography data which yielded estimates of total atomic displacements and (ii) a full normal mode analysis based on the refinement of a model force field which reproduces the hydrogen-weighted vibrational density of states measured via inelastic neutron scattering. In the latter, a vibrational force field for solid state imidazole was determined which is shown to be a significant improvement over existing force fields, mainly obtained via ab initio methods, since it more accurately reproduces both the eigenvalues and the eigenvectors of the force field (the eigenvectors correspond to the atomic displacements in the normal vibrations and are frequently not checked for consistency with experiment). The imidazole force field was subsequently incorporated into the much larger force field for zinc (II) tetraimidazole. This latter force field was shown to be consistent with inelastic neutron scattering measurements of zinc (II) tetraimidazole borofluorate (boron-11 enriched), zinc (II) tetraimidazole perchlorate and two deuterated states of the perchlorate compound; this demonstrates the validity of the isolated molecule approach used to model the force field for this case. The mean discrepancy in the rms atomic displacements derived from the normal mode analysis and the TLS analysis is shown to be $\pm 50\%$. The 105 normal modes of the zinc (II) tetraimidazole complex are interpreted in terms of their effect on the damping of the individual multiple scattering paths in the EXAFS spectrum. The Zn-N pair correlation function is found to be dominant in causing damping of the most significant partial signals from both single and multiple scattering paths but it is shown that the cumulative damping effect of other intramolecular motions cannot be neglected. The total configurationally averaged theoretical EXAFS spectra exhibit an underestimate of the amplitude compared to experiment. The magnitude of this underestimate is not uniform through the spectrum and it is shown that the Muffin-Tin energy discontinuity in the modelling of the emitter optical potential causes a significant oscillatory modulation of the theoretical amplitude up to $\pm 25\%$ which persists strongly in the high wavevector regime. The implications of the underestimate and oscillatory modulation of the theoretical amplitude for the EXAFS method as an analytical tool are an impairment of the structural determination beyond the first coordination shell and in particular an underestimate of the values determined for atomic disorder.

Chapter 1

Introduction

EXAFS (extended x-ray absorption fine structure) spectroscopy is an analytical technique which is used to determine short-range static and dynamic atomic structure in materials. The quantity of interest in an EXAFS experiment is the oscillatory component of the x-ray absorption coefficient observed above the characteristic absorption edge for a particular type of atom in the sample; the form of the oscillatory structure is determined by the local environment of this type of atom up to a radius of a few Angstroms. The oscillatory component may be isolated, to give the EXAFS spectrum, and then, in principle, interpreted to yield quantitative information concerning interatomic distances and angles, coordination numbers and atomic disorder. The method compliments other spectroscopic techniques such as infrared, Raman and nuclear magnetic resonance which mostly generate qualitative information. The probe of the local structure is a photoelectron, emitted from the x-ray absorbing atom, with wavelengths typically in the range $0.5 \rightarrow 0.05 \text{ \AA}$; consequently structure determination via EXAFS is potentially of very high accuracy (i.e. $\pm 0.001 \text{ \AA}$ for nearest-atom distances). In contrast to x-ray crystallography, the EXAFS technique may also be applied to non-crystalline samples such as gases, liquids or amorphous solids such as glasses and is important in the study of surface interactions and catalysis; see the review articles, (37), (75), (112), (126), (137), (138). In the biological field, EXAFS spectroscopy is an important method for examining the environment of metal centres in large protein molecules, such as enzymes, with an order of magnitude better precision than x-ray crystallography; in enzymes, the metal centres are often believed to be located at the active site and characterising the local structure is an important step to understanding the function of the enzyme. The strength of the technique in

CHAPTER 1. INTRODUCTION

this case is its selectivity since the EXAFS signal may be extracted from a single metal atom embedded in a protein molecule composed of many thousand less massive atoms. In addition, the protein may be studied under conditions which emulate its working environment *in vivo*, typically in aqueous solutions in the presence of a substrate or inhibitor, and consequently EXAFS is applicable to many proteins which do not yield to crystallography techniques. Numerous studies of metal centres in proteins have been reviewed in the articles (20), (21), (22), (52), (53), (111), (132).

The conventional method for EXAFS data analysis was described in 1971 by Sayers et al., (127), who proposed Fourier transforming an EXAFS signal to obtain a radial distribution function of the atomic environment about the photon-absorbing atom. The method is based on an approximation of the photoelectron scattering by a propagating plane-wave that undergoes back-scattering from nearby atoms. Unless a correction is applied, the distances inferred from the Fourier transform are shorter than the true radii of successive coordination spheres because the phase-shifts experienced by the back-scattered photoelectron are not taken into account. Sayers et al. showed that it is possible to extract these phase-shifts by comparison with a similar compound with known structure so that an accurate value for the distances may be determined. This approach is generally successful in extracting information within the first coordination sphere but is not appropriate at greater radii since the radial distribution function also contains features due to multiple scattering of the photoelectron. The general importance of multiple scattering in the interpretation of EXAFS spectra was first emphasised for the case of metal-bonded imidazole complexes, (108), (141), which mimic the histidine ligation of metals centres found in a number of common metalloenzymes such as carbonic anhydrase, (157), amine oxidase, (71) and superoxide dismutase, (7). The presence of multiple scattering components prevents a simple treatment of EXAFS spectra but implies that information may be extracted beyond the pair correlation function, potentially revealing such quantities as equilibrium bond angles and correlations in many body disorder. For example, in the case of histidine ligation in metalloenzymes, information could be obtained as to the angle of the imidazole rings with respect to the metal atom which could be important in determining the energetics of the active site. The determination of atomic disorder is of

CHAPTER 1. INTRODUCTION

great interest and has been recently been stressed by Pendry, (102), as an important direction in the development of the EXAFS technique since it holds the key to such processes as diffusion and surface reactions of catalysts. In order to yield such information, an *ab initio* approach has to be adopted in the EXAFS data analysis which embodies multiple scattering. However, for this method to have any success in extracting such information, which is usually characterised by the weakest features in the spectrum, it is essential that the *ab initio* theory is correct.

The neglect of the curvature of the wavefront in the plane-wave description of photoelectron scattering, which causes the theory to fail at low energies, was corrected by Schaich, (128), for single scattering and by Lee and Pendry, (76), and Ashley and Doniach, (1), for multiple scattering. These descriptions were based on the assumption that the multiple scattering is sufficiently weak, even at low energies, so that an expansion in the order of the multiple scattering is possible. Durham et al., (35), proposed a similar theory embodying a full solution including all orders of multiple scattering. These *curved-wave* theories are exact but are presently too slow to be incorporated in effective data analysis. The exact theory has since been simplified by Rehr et al., (117), Pettifer et al., (108) and Gurman et al., (47), (48) permitting fast and accurate computations of EXAFS signals. The latter two authors used a small atom approach which retained the least serious approximations of the plane-wave theory for systems involving light atoms such as carbons and nitrogens.

The above multiple scattering, curved-wave schemes for computing *ab initio* EXAFS spectra are currently incorporated in three independent computer packages for EXAFS data analysis: EXCURVE, (48), (140), from Daresbury Laboratory, FEFF, (94), (116), by Rehr and coworkers and GNXAS, (40), (which is based on MSXAS, (122)), by Natoli and coworkers. In each case a proposed atom cluster is modelled by effective one-electron optical potentials that are constructed within the Muffin-Tin approximation. The intrinsic and extrinsic energy loss mechanisms of the photoelectron, which result in an attenuation of the signal, are modelled either by an imaginary self-energy of the photoelectron or by a complex scattering potential. The data analysis is effected by fitting the generated EXAFS signal to the experimental spectrum by varying a parameterised model for the static and dynamic structure of

CHAPTER 1. INTRODUCTION

the atom cluster. However, shortcomings of the theory may be concealed by adjustments of free parameters that affect the spectrum in a similar way to the deficiencies in the theory. In other words, an excellent fit to experiment is not sufficient evidence to conclude that the theory is correct. The only rigorous way of determining the accuracy of the theory is therefore to eliminate the structure refinement by calculating the EXAFS signal from a system whose structural parameters are known; any discrepancies between theory and experiment can then be assessed on the basis of non-structural parameters. In this way, the validity of specific elements of the theory can be quantitatively evaluated, such as the Muffin-Tin approximation and the model for photoelectron inelastic loss.

In this thesis, an attempt is made to establish all the structural parameters of an interesting system and thereby predict the EXAFS spectrum entirely *ab initio* at a range of temperatures. The system selected is the zinc (II) tetraimidazole complex which is of relevance in the biological field as a model compound for the metal centre in carbonic anhydrase and is of special interest as a system which produces strong multiple scattering components in the EXAFS spectrum. It therefore constitutes an excellent test case for multiple scattering theory in a typical situation where the EXAFS technique is employed.

The static structure of the molecule has been determined from x-ray crystallography with two different counterions, (2), (79), and consists of four planar imidazole rings coordinated to a central zinc ion in an approximately tetrahedral configuration. Multiple scattering occurs as the photoelectron propagates through the imidazole rings.

Determining the dynamic structure of the subject molecule presents a greater challenge and a considerable part of this thesis is devoted to this problem. The dynamic structure in this context is defined as the probability distribution function of each scattering atom about its equilibrium position, described by the static structure, with respect to the primary absorber, which is the zinc atom. In general the dynamic structure is composed of both static and thermal disorder, both of which result in an attenuation of the EXAFS spectral amplitude. The attenuation arises since the disorder in the atom positions introduces an incoherence in the contributions to the total EXAFS which are then averaged over time and over all absorption sites in the sample; the resultant EXAFS signal is thus smeared out and

CHAPTER 1. INTRODUCTION

the amplitude is damped. Static disorder is significant in amorphous materials or crystals of very large molecules but is not expected to greatly affect the relative position of atoms within a small molecule such as the zinc (II) tetraimidazole complex; it is therefore assumed in this study that static disorder is negligible in the context of EXAFS damping. Thermal disorder is due to thermal vibrations of the molecule and only those vibrations, which cause displacements of the scattering atoms with respect to the zinc atom, are considered. The assumption is made that lattice vibrations do not effect the internal structure of the molecule and, therefore, this study is only concerned with internal vibrations of the molecule; this is known as the *isolated molecule* approach.

The frequencies of intramolecular vibrations can be routinely obtained via infrared and Raman spectroscopy but determining experimental values for the associated probability distribution functions of the atom positions is more difficult. In this thesis, two methods are employed:

1. TLS analysis of x-ray crystallography data. This involves a deeper consideration of the refined thermal parameters. The individual atomic anisotropic displacement parameters are reparameterised to take account of large scale correlated motions of the molecule. Within a simple model, this allows the internal displacement distributions of the atoms to be separated from the overall displacement distribution which includes all contributions, such as those from lattice vibrations. The result is a probability distribution function for each atom that describes the total displacements of the atom due to all types of internal molecular motion.
2. A full normal mode analysis of the internal thermal vibrations of the molecule based on data from inelastic neutron scattering, infrared and Raman studies. A dynamic model, based on a harmonic force field, is constructed for the isolated molecule which generates all the orthogonal normal modes of vibration. The elements of the force field are then best-fitted to reproduce the experimental hydrogen-weighted vibrational density of states of the molecule as measured by inelastic neutron scattering. The eigenvalues of the secular equation of motion map the vibrational frequencies of the

CHAPTER 1. INTRODUCTION

molecule and the eigenvectors describe the displacement distributions of the atoms corresponding to each of those frequencies.

The latter method provides the most detailed information since it effectively reproduces the many-body vibrational correlation function (VCF) of the molecule which fully describes the internal vibrational motion. By knowing the VCF of the molecule it is possible to rigorously model the damping effect of thermal vibrations on the theoretical EXAFS spectrum, even to the extent where the partial damping contribution of each normal mode of vibration is described. This is achieved by calculating a *configurational average* of the EXAFS signal over all the correlated displacements of the scattering atoms based on a linear expansion of the partial signals from each multiple scattering path, (3); this algorithm will be justified in the thesis. Within the harmonic approximation, the configurational average may then be extended to model the damping at any temperature.

The product of this study is a detailed vibrational analysis of the zinc (II) tetraimidazole complex which enables the first quantitative test of the current state of multiple scattering EXAFS theory. It is hoped that this will act as a benchmark for future studies by indicating the strengths and weaknesses of the EXAFS method as an analytical tool for structural determination.

1.1 Layout of this Thesis

The following three chapters of this thesis are self-contained studies each treating a different aspect of the problem; the following two chapters concern methods of obtaining the dynamic structure of the zinc (II) tetraimidazole complex, the results of which are inserted into the configurationally averaged EXAFS calculations in the subsequent chapter. All the results are brought together in the final discussion in chapter 5 where they are put into the context of the overall study. This general layout is depicted schematically in figure 1.1.

In chapter 2, estimates for the total mean-squared displacements of the atoms due to all modes of internal motion are obtained via a TLS analysis of x-ray crystallography data of zinc (II) tetraimidazole tetraborofluorate. Standard TLS analysis is explained and a methodology

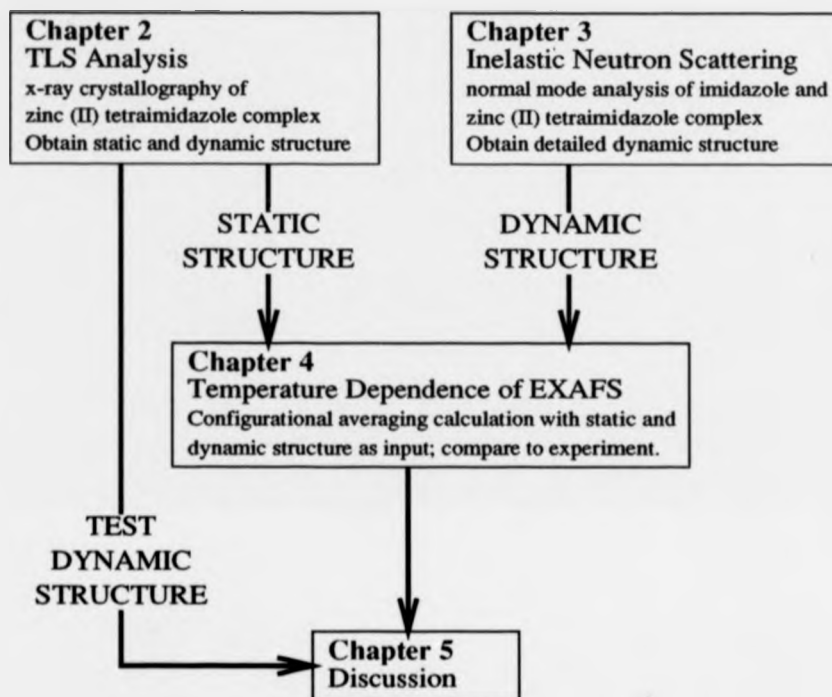


Figure 1.1: Schematic diagram showing the layout of this thesis.

for implementing the technique is described that permits the displacement distributions due to intramolecular motion to be separated from the total distribution function. The latter includes all contributions due to lattice motion and any static disorder, if it is present. The atomic displacements due to internal motion are subsequently interpreted in terms of correlated motion of the whole imidazole ring.

In chapter 3, a normal mode analysis is applied, first to the imidazole molecule, and subsequently to the zinc (II) tetraimidazole complex and detailed information about the correlated many-body motion of the molecules is obtained. The experimental information is obtained principally via inelastic neutron scattering and a brief overview is given of the relevant theory necessary to interpret the data. The physics and methodology of normal mode analysis are also explained. A dynamic force field for imidazole is developed and tested

CHAPTER 1. INTRODUCTION

for consistency with both neutron and optical experiments and a comparison is made with published force fields for imidazole. The force field for imidazole is then incorporated in a much larger force field describing the normal mode vibrations of the zinc (II) tetraimidazole complex. A methodology is described for modelling the elusive low frequency skeletal modes of the complex. The force field is finally tested for consistency with deuteration studies.

In chapter 4, the ab initio temperature dependence of the EXAFS spectrum of the zinc (II) tetraimidazole complex is calculated based on the static structure from the crystallography in chapter 2 and the dynamic structure from the normal mode analysis in chapter 3. A brief description is given of the theory used to calculate the EXAFS signal and of the algorithm used to include the dynamic information via a configurational average. New, high quality EXAFS data of zinc (II) tetraimidazole tetraborofluorate ^{are} presented and discussed. The input of the complete dynamic structure permits a novel breakdown of the effect of the individual normal modes on the EXAFS spectrum. Finally, a comparison is made between the experimental temperature dependent EXAFS and the ab initio calculations permitting a quantitative assessment of the theory.

Chapter 2

TLS Analysis

2.1 Introduction

In this chapter a deeper analysis of x-ray crystallography data of the zinc (II) tetraimidazole complex is described which yields estimates of the magnitudes of the total internal thermal motion of the molecule.

Generally in x-ray crystallography the static structure of a primitive cell in a crystal is established via a least squares refinement that minimises the difference between the calculated and observed integrated peak intensities of the x-ray diffraction image. The calculated integrated peak intensities are determined from the square of the *structure factor*, F , which is the function that dictates the amplitude of coherently diffracted x-rays in directions that satisfy the Bragg condition. The structure factor equation may be written as, (63);

$$F(h_j) = \sum_{r=1}^n f^{(r)}(h_j) \exp(2\pi i x_j^{(r)} h_j - \frac{1}{2\pi} U_{jk}^{(r)} h_j h_k) \quad (2.1)$$

in which Einstein's summation convention is assumed for $j, k = 1, 2, 3$. The structure factor is defined with respect to the reciprocal lattice Miller indices, h_1 , h_2 and h_3 and takes account of the various types of atom, r , present in the lattice via the atomic form factors, $f^{(r)}$, and the situation, $x_j^{(r)}$, of the atoms in the unit cell via the phase-like term in the exponent. The second term in the exponent simulates the damping of the diffracted amplitude due to the distributions of displacements of the atoms about their static equilibrium positions; the damping occurs because the distribution in the static structure introduces an incoherence to the reflected x-rays that reduces the integrity of the Bragg interference. The probability density functions (pdf) describing the displacement distributions are assumed to be trivariate

CHAPTER 2. TLS ANALYSIS

Gaussians and are completely characterised by the six quantities U_{11} , U_{22} , U_{33} , U_{12} , U_{13} and U_{23} known as the *anisotropic displacement parameters* (ADP). The ADP's of a given atom form the symmetric second rank tensor U and describe the second moments of the Gaussian pdf along three oriented orthogonal axes; it is the physical information that the ADP's contain that is of interest in this study.

The assumption that the atomic pdf's may be modelled by Gaussians merits some discussion. Atoms in a crystal are displaced from their equilibrium positions for several reasons: Of great significance are the displacements caused by thermal vibrations of both the molecule and the crystal lattice; the resultant pdf's represent the time- and lattice-averaged motion of the atoms. If the vibrations are assumed to be harmonic and rectilinear the approximation of the atomic pdf's by a multivariate Gaussian is appropriate. However the approximation breaks down for anharmonic vibrations or vibrations in curvilinear space both of which become increasingly poorly modelled with increasing temperature. In the case of large amplitude anharmonic motion it would be desirable to express the pdf with additional higher cumulants. However large amplitude motion causes a rapid decrease in the diffracted amplitude from atoms at high scattering angle so the determination of additional parameters becomes especially difficult experimentally. Another source of atomic displacements is that of static disorder throughout the lattice. This is always present to varying degrees and is difficult to predict or model without doing extensive temperature dependent studies; therefore for static disorder, the contributions to the atomic pdf's are only arbitrarily modelled by a trivariate Gaussian. A further concern about the modelling of the atomic pdf's via Gaussians is that the description does not take into account the correlations in the displacements between different atoms. Highly correlated atomic displacements can result in different x-ray Bragg intensities than those predicted using the Gaussian model since the correlations affect the damping of the Bragg reflection. This can in turn lead to systematic errors in the refined ADP's. However, in spite of these reservations, the Gaussian approximation to the pdf is virtually universally made and is therefore adopted here.

The ADP's obtained experimentally from x-ray crystallography can be further inspected via TLS analysis. In this technique, additional information is obtained from the atomic ADP's

CHAPTER 2. TLS ANALYSIS

by making some assumptions about the large-scale correlated displacements of the molecule. By inspection, parts of the molecule are designated as rigid, to within a specified deviation, which implies that all the atoms within the rigid-body are coupled and can only displace *en masse*. The displacement distributions of these so-called *rigid-bodies* may then be described by a translation tensor, **T**, and a libration tensor, **L**, plus a coupling screw tensor, **S**, for the general case when the libration axes do not intersect at the rigid-body centre of mass. The **T** tensors for those atoms within the rigid-body may all be individually determined from its **T**, **L** and **S** tensors. This constitutes a re-parameterisation of the system such that the coupled motions of the atoms in the rigid-bodies are implicit in the ADP's and, in most cases, implies fewer refinable parameters. Consequently, TLS analysis is used as an extra constraint to facilitate difficult crystallographic refinements, but it is also widely employed as an analytical tool in its own right for obtaining information about static and dynamic disorder.

Apart from providing estimates of correlated displacements, TLS analysis is also widely used to correct interatomic distances from crystallography that suffer Bastiansen-Morino shrinkage¹. It has also been used to derive approximate force constants, (146), identify low energy paths for molecular isomerisations, (8), (30), (158), and the onset of phase changes, (43), (158), and with the advent of improved experimental resolution from synchrotrons is beginning to be applied to macromolecules such as the small protein rubredoxin, (151). A comprehensive background is contained in the review articles, (31), (32), (63).

In this study, the experimentally determined ADP's, at two temperatures, of zinc (II) tetraimidazole tetrafluoroborate are inspected via TLS analysis. The aim is to obtain information about the atomic displacements caused by intramolecular vibrations. This requires that the experimental ADP's for each atom are separated into a part assumed to result solely from internal motion and a part representing the displacements due to all other causes; i.e. lattice vibrations and static disorder (henceforward referred to as overall disorder). To do this requires an adapted implementation of the standard theory so that the **T**, **L** and **S** tensors are determined for a rigid-body whose displacements are predominantly due to overall

¹The apparent foreshortening of interatomic distances due to the centroids of Gaussian atomic pdf's not accurately reflecting the equilibrium positions of atoms that experience vibrations with curved trajectories, (see (26), chapter 14). Corrections were first suggested by Cruickshank, (23), (25).

disorder. The rigid-body chosen for this purpose is the Zn-4N tetrahedral core of the zinc (II) tetraimidazole complex since its participation in internal motion is assumed to be small compared to other parts of the molecule; i.e. the imidazole branches are expected to show larger amplitude motion due to internal vibrations. Based on this assumption, the T, L and S tensors for the core of the molecule may be used to determine the ADP's, attributed solely to overall disorder. It is hoped that these generated ADP's are smaller than the experimental ones, which embody all types of disorder, and thus, via subtraction of the calculated ADP's from the experimental ADP's, a residual set of atomic pdf's may be established that are associated only with internal thermal motion. The residual pdf's are subsequently interpreted in terms of more intuitive displacements of the imidazole rings such as stretches and wags.

TLS analysis provides estimates of quantities that are difficult to obtain via other methods but it has inherent limitations that can be severe. The analysis that is described here is taxing TLS to its limit and the result is a large margin of error; this is in part difficult to estimate quantitatively since it depends on the quality of the model used; errors are discussed further in the last section of this chapter. Also considered in the final discussion is a recent development to TLS theory (see appendix A) that attempts to automatically separate one degree of internal motion from the overall disorder; it is described why this was not applicable in this case.

2.2 Standard Theory of TLS Analysis

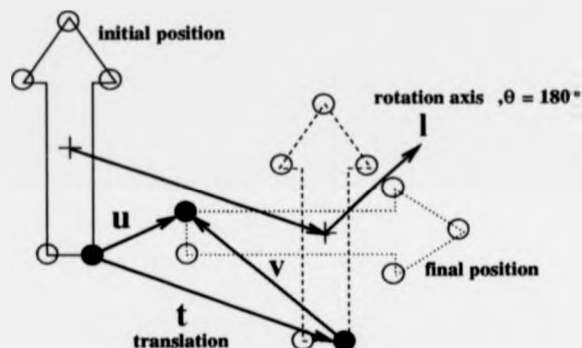
TLS analysis is essentially a re-parameterisation of the ADP's obtained via x-ray crystallography based on the designation of portions of the molecule as being rigid. (The exact definition of what constitutes a rigid-body in this context is addressed in section 2.4.1.) The distribution of displacements of a rigid body about its equilibrium position may be described by a T, L and S tensor which, within the Gaussian approximation, define the second moments of the partial pdf's of translation, libration and their coupling respectively. In the next subsection the T, L and S tensors for a rigid-body are derived illustrating how they relate to the individual U tensors for each constituent atom.

2.2.1 Rigid-Body Motion

The most general type of displacement for a rigid-body is a screw; i.e. a translation of the body along a vector \mathbf{t} followed by a rotation of magnitude θ about the unit vector \mathbf{l} . An atom in the rigid-body with the equilibrium position \mathbf{r} experiences the displacement \mathbf{u} such that

$$\mathbf{u} = \mathbf{t} + \mathbf{v} \quad (2.2)$$

where \mathbf{v} is the linear displacement of the atom due to the rotation alone, as illustrated below:



\mathbf{v} may be expanded in terms of the axial vector $\lambda \equiv \theta \mathbf{l}$ i.e.

$$\mathbf{v} = \lambda \times \mathbf{r} + \frac{1}{2} \lambda \times (\lambda \times \mathbf{r}) + \frac{1}{6} \lambda \times [\lambda \times (\lambda \times \mathbf{r})] + \dots \quad (2.3)$$

in which the elements of λ are infinitesimal so that the rotations are commutative about the components of \mathbf{l} . To first order Eq. (2.2) becomes

$$\mathbf{u} = \mathbf{t} + \lambda \times \mathbf{r} = \mathbf{t} + \mathbf{A} \lambda \quad (2.4)$$

where

$$\mathbf{A} \equiv \begin{bmatrix} 0 & r_3 & -r_2 \\ -r_3 & 0 & r_1 \\ r_2 & -r_1 & 0 \end{bmatrix} \quad (2.5)$$

Eq. (2.4) relates a single arbitrary displacement of the rigid body, involving a translation, \mathbf{t} , and a rotation, λ , into the corresponding linear displacement, \mathbf{u} , of a constituent atom at \mathbf{r} ; this may now be generalised to express the pdf of an atom in three dimensions in terms of the translational and librational distributions of the rigid-body.

If the displacements u of the atom in the rigid-body obey a trivariate Gaussian distribution when averaged over time and throughout the lattice then the pdf of the atom may be characterised by its second moments with respect to three orthogonal principal axes. This is equivalent to generating the variance-covariance matrix, $U = \langle u * u \rangle$, for the displacement u ; note that $*$ denotes the direct product such that the elements of $\langle u * u \rangle$ are $\langle u_i u_j \rangle$. Applying the same treatment to both sides of Eq. (2.4) yields

$$\begin{aligned} \langle u * u \rangle &= \langle t * t \rangle + \langle A \lambda * A \lambda \rangle + \langle A \lambda * t \rangle + \langle t * A \lambda \rangle \\ U &= \langle t * t \rangle + A \langle \lambda * \lambda \rangle A^\dagger + A \langle \lambda * t \rangle + \langle t * \lambda \rangle A^\dagger \end{aligned} \quad (2.6)$$

where \dagger denotes matrix transpose. The matrices $\langle t * t \rangle$ and $\langle \lambda * \lambda \rangle$ are the second moment matrices of the partial pdf's of the translational and librational displacements of the rigid-body and, similarly to U , are symmetric second rank tensors denoted by T and L containing the elements $\langle t_i t_j \rangle$ and $\langle \lambda_i \lambda_j \rangle$ respectively. The matrix $\langle \lambda * t \rangle \equiv \langle t * \lambda \rangle^\dagger$ is identified as the coupling between T and L and is denoted as S ; it is also a second rank tensor composed of the elements $\langle \lambda_i t_j \rangle$ and is not generally symmetric. Eq. (2.6) may be rewritten in matrix form as

$$\begin{aligned} U &= T + A L A^\dagger + A S + S^\dagger A^\dagger \\ &= \begin{bmatrix} I & A \end{bmatrix} \begin{bmatrix} T & S^\dagger \\ S & L \end{bmatrix} \begin{bmatrix} I \\ A^\dagger \end{bmatrix} \end{aligned} \quad (2.7)$$

in which I is the identity matrix. Eq. (2.7) gives the desired result of the derivation in which the individual atomic ADP's contained in the U matrix are related to the second moment matrices of the rigid-body translational and librational pdf's.

Note that the original formalism, (24), did not include a coupling matrix S ; this was subsequently incorporated, (131), to account for molecules that do not exhibit inversion site symmetry or, put another way, for the case where the axes of libration do not intersect at the rigid-body centre of mass. If the S matrix is generated from observed ADP's, only the differences of the diagonal elements, $S_{ii} - S_{jj}$, may be determined and not the actual values; this stems from the loss of coupling information through expressing the atomic displacement distributions in terms of ADP's. The sum of the diagonal in S is normally arbitrarily set to

zero and consequently an experimentally determined S matrix is expressed by 8 parameters. Together with the 6 parameters for each of the symmetric T and L matrices, the rigid-body displacement pdf is characterised by 20 independent parameters. In view of the six ADP's required to express individual atomic pdf's, this formalism implies a reduction of parameters for rigid-bodies with more than three constituent atoms; for less than three atoms the TLS tensors can not be determined uniquely.

The T , L and S tensors may be refined concurrently or after the static structure refinement. In the former case this implies an improvement of the ratio of free parameters to observed Bragg intensities which can expedite a refinement. In the work presented here, the TLS study was done for analytical purposes after the static structure and atomic ADP's had been established.

2.3 Crystallography of Zinc (II) Tetraimidazole Tetrafluoroborate

The TLS analysis was made on the ADP's obtained from the x-ray crystallography of zinc (II) tetraimidazole tetrafluoroborate, $(Zn(imid)_4(BF_4)_2)$. Measurements and analysis were done at two temperatures, 100K and 150K, in collaboration with N. Alcock, (79).

The crystals were prepared from hydrated zinc (II) tetrafluoroborate, $(Zn(BF_4)_2 \cdot 6H_2O)$, and pure imidazole, $(C_3N_2H_4)$, after the method of Reedijk for the analogous perchlorate substance, (115); see also page 68. Crystals of the compound are colourless prisms.

The space group is monoclinic, $C2/c$, with unit cell dimensions $a = 18.035\text{\AA}$, $b = 6.761\text{\AA}$, $c = 19.077\text{\AA}$ and $\beta = 115.628^\circ$ at 100K and $a = 17.994\text{\AA}$, $b = 6.818\text{\AA}$, $c = 19.139\text{\AA}$ and $\beta = 115.632^\circ$ at 150K. Data were collected with a Phillips PW1100 four circle diffractometer using x-rays of wavelength 0.71069\AA (Mo, K_α).

Reflections were processed to give 5624 unique reflections; 1608 were considered observed ($\frac{I}{\sigma(I)} \geq 2.0$) and used in refinement; they were corrected for Lorentz polarisation and absorption effects, the latter by the Gaussian method. Maximum and minimum transmission factors were 0.86 and 0.74. The structure was solved by standard Patterson and Fourier

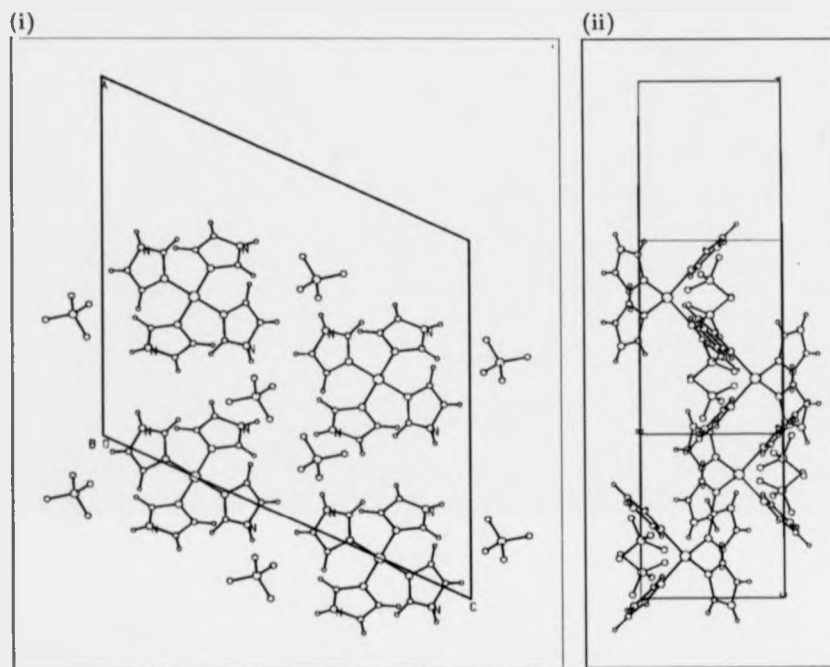


Figure 2.1: Unit cell of crystalline zinc(II) tetraimidazole tetrafluoroborate. The two projections are (i) parallel to the *b* axis and (ii) parallel to *c*. Projection (i) is equivalent to viewing the molecules along their two-fold axes.

methods and subjected to full-matrix least squares refinement. A weighting scheme of the form $W = 1/[\sigma^2(F) + 0.011F^2]$ was adopted for the object function being optimised; the final R-factor was 0.039 at 100K and 0.041 at 150K. The software used was SHELXTL PLUS, (133).

The unit cell is depicted in figure 2.1; it contains four cations and eight anions. The zinc atoms lie on special positions on the two-fold axis and are coordinated to the nitrogen atoms of four imidazole molecules in an approximately tetrahedral configuration (i.e. the N-Zn-N angles are all to within 3.1° of the tetrahedral angle, 109.4°). Due to the C_2 point group symmetry there are only two crystallographically independent imidazole branches in the asymmetric group; henceforth they are referred to as imidazole 1 and imidazole 2. The Zn-N bond lengths in the asymmetric group are both $1.983(2)\text{\AA}$ at 100K and $1.987(2)\text{\AA}$ and

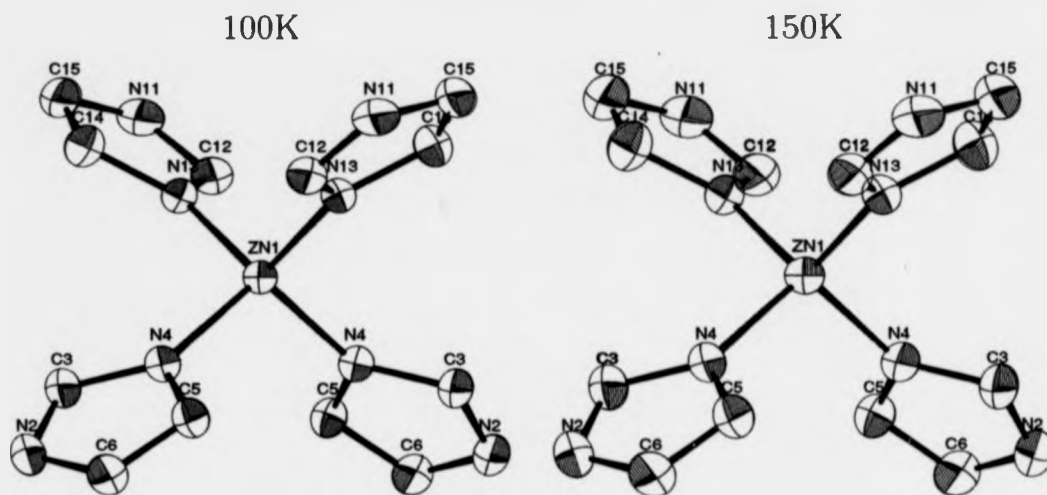


Figure 2.2: Diagrams showing the refined structure at two temperatures of the cation of crystalline zinc (II) tetraimidazole tetrafluoroborate including displacement probability ellipsoids. The ellipsoids represent the surfaces that enclose 50% of the probability of the atomic pdf's described by the refined anisotropic displacement parameters, U_{ij} . The atomic labelling is duplicate for the two asymmetric groups per molecule. The molecules are projected so that the two-fold axis is vertical and in the plane of the page; hydrogen atoms are not shown since their isotropic displacement parameters were not used in the TLS analysis. The diagrams were generated by the programme ORTEP, (62). Note that the ellipsoids in the two plots appear very similar but are not the same; the amplitudes of the ellipsoids in the 150K plot are greater which reflects the increase in amplitude of the thermal vibrations.

1.981(2)Å at 150K; this compares with 1.997(7)Å and 2.001(7)Å for the Zn-N bonds in the published structure of zinc (II) tetraimidazole perchlorate at room temperature, (2). The imidazole rings are planar to within the errors of the experiment and are inclined towards the C_2 axis such that the angles made between the imidazole planes and the Zn-N bonds are 4.9° and 1.9° at 100K and 5.3° and 1.9° at 150K where the estimated standard deviation in these angles is 0.1°.

Figure 2.2 depicts the final refined structure of the cation at the two temperatures including atomic displacement probability ellipsoids. The ellipsoids are generated by

$$\mathbf{x} \mathbf{U}^{-1} \mathbf{x} = \text{constant} \quad (2.8)$$

and are surfaces enclosing a specified probability, in this case 50%. As such, the ellipsoids permit the refined ADP's, upon which the TLS analysis was done, to be visualised. Hydrogen

atoms are not included in the TLS analysis since the ADP's are refined isotropically; i.e. the pdf is described by just one parameter. This is a consequence of the weak x-ray scattering by hydrogen atoms which dictates extreme economy in the description of their pdf's. It is encouraging that the plots are so similar at the two temperatures with the 150K plot exhibiting clear increases in the atomic ADP's compared to the lower temperature. The magnitudes of the ADP's increase towards the extremities of the molecules but otherwise it is not easy to draw conclusions, from inspection alone, as to the nature of the intramolecular thermal motion.

The ADP's of the perchlorate salt were not presented with the published crystal structure, (2), but an ORTEP plot similar to those in figure 2.2 was given for 50% probability. In that plot, the ellipsoids show a marked elongation out of the imidazole planes; the measurements in that case were made at room temperature.

2.4 Methodology for TLS Analysis

In this section, a standard test is described that sets the criterion for a group of atoms to be designated as a rigid-body suitable for TLS analysis. Subsequently, the rigid body used in this study is described with the aim of separating the atomic displacements due to intramolecular vibrations from all other kinds of displacements that the atoms undergo.

2.4.1 Rigid Body Test

A quantity Δ_{AB} may be deduced for any pair of atoms, A and B , in the molecule such that

$$\Delta_{AB} = \langle u_A^2 \rangle - \langle u_B^2 \rangle = \mathbf{n}^T \mathbf{U}_A \mathbf{n} - \mathbf{n}^T \mathbf{U}_B \mathbf{n} \quad (2.9)$$

where \mathbf{n} is the unit vector in the direction AB . This quantity describes the difference in the mean-squared displacements of the two atoms along their connecting vector. For two atoms in an ideally rigid body this difference would be zero by definition; (note that the converse is not necessarily true, i.e. $\Delta_{AB} = 0$ does not automatically imply a rigid body). Hirschfeld, (59), proposed an experimental tolerance of $\Delta_{AB} = 10 \text{ pm}^2$ (i.e. 10^{-3} \AA^2) for atoms of about the mass of carbon that are bonded together. This limit takes account of the typical differences

	N2	C3	N4	C5	C6	N11	C12	N13	C14	C15
Zn1	9	23	(8)	33	40	26	21	(6)	58	16
C15	-18	16	24	42	43	(-37)	13	0	(6)	
C14	-8	3	5	38	53	-25	26	(-3)		
N13	2	20	24	51	61	11	(10)	imidazole 2; rms $\Delta_{AB} = 19 \text{ pm}^2$		
C12	-58	-40	-6	42	26	(27)				
N11	-108	-72	-29	16	-14					
C6	(-17)	2	-22	(13)						
C5	-31	18	(22)							
N4	-9	(-8)	imidazole 1; rms $\Delta_{AB} = 17 \text{ pm}^2$							
C3	(6)									
N2										

Table 2.1: Matrix of Δ_{AB} values (pm^2) for all atoms in the sinc (II) tetraimidazole cation. The values are calculated using the experimental ADP's from the crystallography of sinc (II) tetraimidazole tetraborofluorate at 100K. The values correspond to $\mathbf{n}^i \mathbf{U}_{A\mathbf{n}} - \mathbf{n}^j \mathbf{U}_{B\mathbf{n}}$ where A are the atoms along the top of the matrix, B are the atoms on the left and \mathbf{n} is the unit vector between A and B . The labelling of the atoms is that shown in figure 2.2. The encircled values denote Δ_{AB} between two bonded atoms. The estimated standard deviation (esd) of the Δ_{AB} 's is $\sim 8 \text{ pm}^2$.

due to interatomic stretching vibrations and holds well for organic compounds, (32), thus serving as a useful quantitative test of the quality of the experimental ADP's. Inspection of Δ_{AB} values also indicates which subgroups of the molecule might qualify as rigid-bodies and thus yield to a TLS analysis. Regions in which the Δ_{AB} values are significantly greater than 10 pm^2 indicate large relative displacements of the atoms and a lack of rigidity.

Table 2.1 gives the Δ_{AB} values for all atoms in the asymmetric group of the zinc (II) tetraimidazole cation from the crystallography of the tetrafluoroborate compound at 100K. Negative values indicate that the mean-squared displacement of the atom on the left of the table is greater than that on the top along their connecting vector. The matrix is divided into blocks that collect the atoms of each imidazole together and by inspection it is clear that the values in the off-diagonal block coupling imidazole 1 to imidazole 2 are generally much larger than the values in the diagonal blocks relating the two imidazoles to themselves; i.e the rms Δ_{AB} values of the off-diagonal block is 41 pm^2 compared to 17 and 19 pm^2 for the

diagonal blocks. This indicates a high degree of relative displacements of the two imidazoles with respect to one another and greater level of rigidity of the atoms within each imidazole group. The estimated standard deviation (esd) of the Δ_{AB} values is $\sim 8\text{pm}^2$; the encircled Δ_{AB} values for bonded atom pairs have an rms Δ_{AB} of 17pm^2 which lies just within the esd margin of the Hirschfeld tolerance indicating that the data are probably of reliable quality.

2.4.2 Choice of Rigid-Body - Separation of Internal Displacements

In order to separate the ADP's into contributions from internal vibrations and other types of displacements (overall disorder) it was necessary to make some broad assumptions about the system under study:

1. All averaged motions and disorders are describable by Gaussian pdf's of the atoms.
2. Intramolecular and intermolecular motions are effectively decoupled each producing atomic mean-squared displacements that are wholly attributable to one type of motion; i.e. intermolecular motion and static disorder in the lattice cause displacements of the whole molecule as a rigid unit and do not involve relative displacements of the atoms within a molecule.
3. Librational displacements of the whole molecule due to intermolecular motion and static disorder are assumed to take place about the zinc atom.
4. The zinc atom, being massive compared to the other atoms, only experiences small displacements due to internal modes of motion. Consequently the zinc atom pdf approximates the translational displacements undergone by the whole molecule due to intermolecular motion and any static disorder.

On the basis of assumption 4, the zinc atom pdf determines a T tensor for the whole molecule that characterises intermolecular motion and static disorder. However the L tensor cannot be determined by one atom alone; more atoms must be included and so the TLS rigid-body was assigned as the zinc atom plus its four nearest neighbours, the nitrogen atoms from the four imidazole groups. The assumption implicit in making this assignment is that the five atoms of

	N4	N13	N22	N31
Zn1	8	6	8	6
N31	23	0	24	
N22	0	23		
N13	24			
N4	rms $\Delta_{AB} = 15 \text{ pm}^2$			

Table 2.2: Matrix of Δ_{AB} values (pm^2) for the five atoms in the rigid-body chosen for the TLS analysis. The encircled values denote pairs of atoms which are bonded. Note that atoms N22 and N31 are symmetry generated from N4 and N13 respectively and conform to the atom labelling that is adhered to throughout this thesis.

the Zn-N rigid-body, which constitute the tetrahedral core of the molecule, do not participate significantly in internal molecular vibrations. This is a rather crude assumption and is not entirely satisfactory; the core of the molecule certainly is involved in intramolecular motion but it is intuitively expected that the amplitudes of the displacements are much smaller than those caused by the relatively free librations of the imidazole rings towards the periphery of the molecule. A further implicit assumption is that the librations of the imidazole rings all have their libration axes passing through the zinc-bonded nitrogens. These assumptions are discussed further in the final section of this chapter.

The displacements of the Zn-4N rigid-body therefore define a T, L and S tensor for the molecule which represent all kinds of displacements *except* those due to internal motion. The ADP's generated from the T, L, S tensors are contained in the tensors U_{TLS} for each atom and may be subtracted from the observed ADP's, U_{obs} , to produce residual tensors, U_{res} , that are assumed to represent the atomic pdf's resulting from internal motion alone; i.e. for each atom:

$$U_{\text{res}} = U_{\text{obs}} - U_{\text{TLS}} \quad (2.10)$$

The rigid-body test should be applied to the selected Zn-4N group of atoms. Table 2.1 is recast in table 2.2 including only those atoms of the Zn-4N rigid group, where the symmetry generated nitrogens labelled N22 and N31 are equivalent to N4 and N13 respectively. The root-mean-squared Δ_{AB} value for this sub-group is 15pm^2 which is less than that for either of the two asymmetric imidazole groups indicating a relatively high degree of rigidity; the

Zn-4N sub-group thus appears to be well suited to rigid-body analysis.

2.5 Results

2.5.1 Mean-Squared Displacements of Overall Disorder

The TLS analysis of the Zn-4N rigid body was done using the software CRYSTALS, (152), the product of which are the T, L and S matrices. As discussed in the last section, these are assumed to model the translational and librational pdf's for the whole molecule due to interatomic vibrations and static disorder.

The calculated T, L and S matrices for the Zn-4N rigid-body at the two experimental temperatures are:

$$\begin{aligned}
 \mathbf{T}_{100K} &= \begin{bmatrix} 0.015 & 0 & 0 \\ 0 & 0.020 & 0 \\ 0 & 0 & 0.026 \end{bmatrix} & \mathbf{T}_{150K} &= \begin{bmatrix} 0.019 & 0 & 0 \\ 0 & 0.025 & 0 \\ 0 & 0 & 0.032 \end{bmatrix} \\
 \mathbf{L}_{100K} &= \begin{bmatrix} 0.600 & 0 & 0 \\ 0 & 1.100 & 0 \\ 0 & 0 & 7.200 \end{bmatrix} & \mathbf{L}_{150K} &= \begin{bmatrix} 0.200 & 0 & 0 \\ 0 & 1.400 & 0 \\ 0 & 0 & 9.000 \end{bmatrix} \\
 \mathbf{S}_{100K} &= \begin{bmatrix} -0.06 & 0 & 0 \\ 0 & 0 & 0 \\ 0 & 0 & 0.06 \end{bmatrix} & \mathbf{S}_{150K} &= \begin{bmatrix} -0.08 & 0 & 0 \\ 0 & -0.02 & 0 \\ 0 & 0 & 0.10 \end{bmatrix}
 \end{aligned}$$

where the matrices are given in diagonalised form for clarity. Note the units are \AA^2 , $(^\circ)^2$ and (\AA°) for the T, L and S matrices respectively.

The librational pdf's for overall disorder show a pronounced anisotropy; the translational pdf's are nearly isotropic; i.e. the rms displacements along the principal axes of the translational pdf are between 0.12 and 0.16 \AA at 100K and 0.14 and 0.18 \AA at 150K.

The orientations of the T and L tensors with respect to the molecule are shown in figure 2.3 and listed in table 2.3 as direction cosines with respect to a defined set of orthogonal axes;

		100K			150K		
		a*	b	c	a*	b	c
T principal axes	1.	-0.276	0.000	0.961	-0.268	0.000	0.964
	2.	0.000	1.000	0.000	0.000	1.000	0.000
	3.	0.961	0.000	0.276	0.964	0.000	0.268
L principal axes	1.	0.000	1.000	0.000	0.000	1.000	0.000
	2.	0.797	0.000	-0.604	0.716	0.000	-0.698
	3.	-0.604	0.000	-0.797	-0.698	0.000	-0.716

Table 2.3: Direction cosines of principal axes of refined T and L tensors. The orientations are with respect to the orthogonal axes a^* , b and c where $a^* = c \times b$. The principal axes are denoted from 1. to 3. in order of increasing magnitude.

both tensors maintain the same orientations at the two temperatures. The orientation of the T tensor, i.e. translational pdf, is not of great interest since it is approximately isotropic. The orientation of the L tensor indicates that the largest librational displacements of the rigid-body occur about an axis perpendicular to the two-fold axis that bisects the N-Zn-N angle of the asymmetric group. The smallest librational displacements occur about the two-fold axis. (It is a consequence of symmetry that one of the principal axes in each case lies along the two-fold axis but the magnitude of that axis is not dictated).

2.5.2 Mean-Squared Displacements of Internal Motion

The method described in section 2.4.2 was used to obtain a set of residual ADP's for each atom, U_{res} , that were assumed to characterise the atomic pdf's due only to the total averaged internal motion of the molecule.

In order to interpret the U_{res} , the internal motion of the molecule is greatly simplified such that it is assumed to be composed of four rigid imidazole rings each with four degrees of freedom. The four degrees of freedom are depicted in figure 2.4 and are: an in-plane stretching displacement, an in-plane wagging displacement about the zinc-bonded nitrogen, a torsional displacement about the Zn-N bond and an out-of-plane bending displacement.

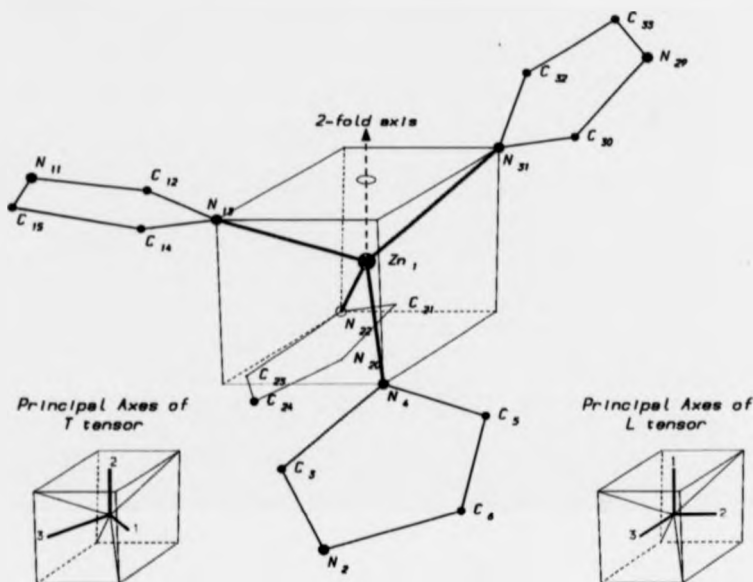


Figure 2.3: Diagram showing the orientation of the principal axes of the T and L tensors with respect to the sinc (II) tetraimidazole cation. The sinc is approximately tetrahedrally coordinated and is viewed here at the centre of a cube; the cube permits a reference frame with respect to which the principal axes are drawn. Axis 1 in each case has the smallest associated second moment and axis 3 the greatest. Note that the T and L tensors have the same orientations at both of the experimental temperatures, 100K and 150K.

Note that the torsional and bending modes both produce atomic displacements out of the ring plane; they are therefore indistinguishable since no correlation information is retained in the experimental ADP's. Having made this assumption about the motion, estimates for the stretching, wagging and torsion/bending displacements can be obtained by evaluating respectively the magnitudes of the residual U_{res} tensors (i) parallel to the Zn-N bond, (ii) in the imidazole ring plane but perpendicular to the Zn-N bond and (iii) perpendicular to the imidazole ring plane.

The components of the second moment tensors in the three directions mentioned above are tabulated in table 2.4. Notice that in the torsion/bending direction most of the components are negative and therefore cannot be meaningfully interpreted; this is discussed in the next section. In the stretching and wagging directions the values are positive and show the expected

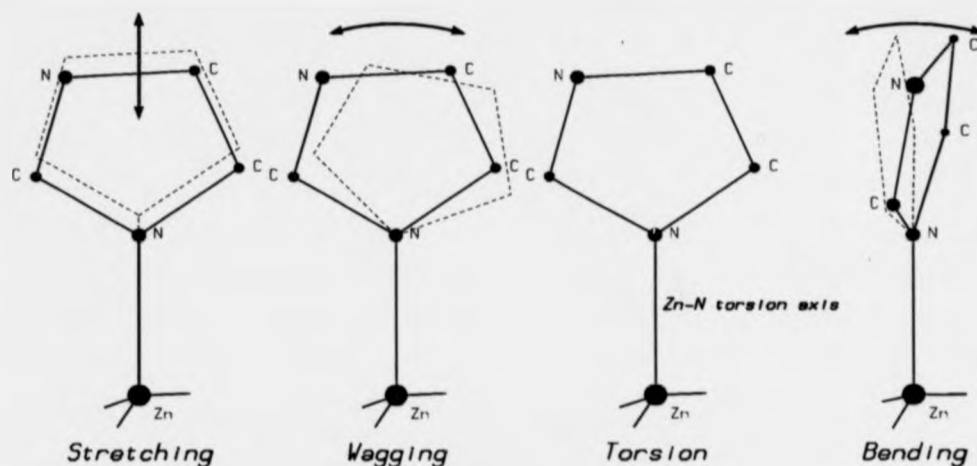


Figure 2.4: The assumed four degrees of freedom of each imidazole branch in the internal motion of the zinc (II) tetraimidazole cation. The assumption is necessary to aid the intuitive interpretation of the residual atomic ADP's from the TLS analysis.

increases with temperature and are translated into root-mean-squared displacements (in Å and degrees) for each whole imidazole ring in table 2.5. These values are averages of the individual displacements for each atom and should only be viewed as estimates; this is especially true for the wagging motion where the angular displacements are based on libration about an axis passing through the zinc-bonded nitrogen; this was an arbitrary choice of libration axis which was an inherent assumption in the definition of the Zn-N4 group as the TLS rigid-body. Notice that the average rms displacements in both stretching and wagging are consistently greater for imidazole 2.

2.6 Discussion of TLS Analysis

The mean-squared displacements quoted in the last section have an associated calculated error margin of the order 10^{-3}\AA^2 . This is a result of the estimated standard deviations of the measured ADP's and the goodness of fit of the TLS tensors to the data. However, the crystallographic experimental errors may in fact be much larger, as has been argued, (32), due to inadequate correction for absorption, thermal diffuse scattering etc., in which case

		Component of residual atomic U_{res} tensor, (10^{-3}\AA^2)					
		to Zn-N bond <i>stretching</i>		in ring plane & \perp to Zn-N bond <i>wagging</i>		out of ring plane <i>torsion/bending</i>	
		100K	150K	100K	150K	100K	150K
imidazole 1	N_4	2.2	2.2	2.1	2.0	0.3	0.4
	C_3	6.2	7.6	3.7	4.2	3.3	7.6
	N_2	2.9	2.9	6.9	13.8	-8.6	-4.1
	C_6	6.0	6.0	9.2	15.0	-18.1	-16.8
	C_5	7.5	6.9	1.1	4.8	-2.2	-1.1
imidazole 2	N_{13}	2.2	2.6	-0.3	0.4	1.3	0.8
	C_{12}	6.5	8.9	4.3	6.7	-4.8	-6.6
	N_{11}	5.2	4.8	17.8	23.9	-14.5	-21.6
	C_{18}	6.7	8.3	22.6	28.9	0.3	-1.1
	C_{14}	13.4	14.2	2.8	4.9	18.1	23.7

Table 2.4: Table showing components of the residual U_{res} tensors for each atom in the asymmetric group of sinc (II) tetraimidazole. The tensors are projected in the three directions in which the imidazole rings are assumed to displace in the simplified model for their internal motion; see figure 2.4. The error margin of these values is approximately 10^{-3}\AA^2 .

the additional systematic errors tend to be incorporated in the ADP's rather than in the static structure. Nevertheless, the calculated errors are small compared to the mean-squared displacements contained in the T and L tensors ($< 10\%$) and they therefore represent good estimates of the overall disorder. However, the mean-squared displacements amplitudes of the residual ADP's, assumed to represent intramolecular pdf's, are much smaller (as much as ten times smaller than the overall disorder) and consequently the calculated errors are much more significant ($10 \rightarrow 50\%$). This constitutes a weakness in the approach described in this study, where small residual ADP's are obtained by subtracting large ADP's (derived from the TLS analysis) from slightly larger observed ADP's. The actual error margin may in fact be even worse than the calculated one since some broad assumptions are made in separating the internal displacements from the overall disorder; the true error depends on the validity of these assumptions.

	average rms displacements of imidazole rings			
	<i>stretching</i>		<i>wagging</i>	
	100K	150K	100K	150K
imidazole 1	0.069Å	0.070Å	3.0°	4.1°
imidazole 2	0.079Å	0.085Å	4.1°	4.6°

Table 2.5: Root-mean-squared displacements of imidazole rings due to internal stretching motion and wagging motion as defined in figure 2.4. The values are the averages of all the atomic rms displacements. The wagging angular displacements are calculated from linear displacements with the zinc-bonded nitrogen atom lying on the librational axis.

The central assumption was that the ADP's of the rigid-body, assigned to be the Zn-4N tetrahedral core of the molecule, completely define the overall disorder of the molecule, which is modelled by the fitted TLS tensors. For this to be true, the intramolecular disorder and overall disorder must be effectively decoupled which can only be discussed in the light of spectroscopic information and is left to the discussion in chapter 5.

Another assumption is that the axis of the internal librations of the imidazole rings pass through the zinc-bonded nitrogens which therefore do not displace in the wag and bend projections; this is required by the main assumption above because the nitrogen displacements are used to define the *L* tensor. This is certainly not completely true, as is evidenced by the Δ_{AB} values for the rigid-body in table 2.2 which show that the zinc-bonded nitrogens do exhibit relative displacements and therefore do participate in internal motion of the molecule; the *L* tensor must therefore be an overestimate about at least one of its principal axes. The consequence of this is that the residual mean-squared displacements in the wag and bend projections are underestimates since the *L* tensor is effectively stealing a proportion of their value. In the case of the out-of-plane bend displacements, the underestimate is so great that many of the residual mean-squared displacements are negative, which prevents interpretation. Consequently, the principal axis of the *L* tensor parallel to the libration axis of the imidazole

bend vibration is certainly overestimated; this corresponds to the principal axis of the fitted L tensor with the greatest magnitude, i.e. about the bisector of the N-Zn-N bond in the asymmetric group. Thus, no information can be gained about the intramolecular out-of-plane bend displacements of the imidazole rings via TLS analysis.

In the case of the in-plane wag modes, the residual mean-squared displacements are all positive. This implies that the zinc-bonded nitrogens participate less in wag motion than they do in bend motion and the assumption, that the libration axis passes through the nitrogen, is more appropriate. This conclusion is further supported by the fact that the magnitudes of the displacements in the wag projection increase towards the periphery of the molecule, which suggests a wag libration axis of the imidazole rings towards the core of the molecule; (i.e. the most out-lying atoms, N_2 , C_6 , N_{11} and C_{15} have the largest wagging displacements). Consequently, for this molecule, TLS analysis yields quantities for the intramolecular in-plane wag displacements of the imidazole rings, although these may be underestimates. It is important to note that the axes of libration for the wag and bend vibrations of the imidazole are nearly orthogonal; this means that the overestimate in the L tensor in one projection, which results in the underestimate of the bend displacements, is uncoupled from the other two projections and therefore does not affect the wag displacements.

The axes of libration of the in-plane wag vibrations of the imidazole rings are approximately parallel to the two-fold symmetry axis; the mean-squared libration displacement about this axis, due to overall disorder, is given by the L tensor as $1.1(^{\circ})^2$ and $1.4(^{\circ})^2$ at 100K and 150K respectively. This corresponds to a linear mean-squared displacement of $10 \times 10^{-3} \text{\AA}^2$ of the atoms at the periphery of the molecule, which is of the same order of magnitude as the internal wag libration. It is difficult to draw conclusions about the relative amplitudes of libration in the bend projection because no result was obtained for the internal librations; however the overall librations of $7.2(^{\circ})^2$ and $9.0(^{\circ})^2$, at 100K and 150K respectively, correspond to linear mean-squared displacements of $\sim 50 \times 10^{-3} \text{\AA}^2$ at the periphery of the molecule. This is ~ 5 times greater than mean-squared displacements of the internal wag motion.

The most confidence can be placed in the results for the mean-squared displacements in the stretch projection. They are essentially determined by the deduction of the T tensor

from the observed ADP's, and the T tensor is predominantly determined by the pdf of the zinc atom. Thus, the stretch displacements are based on the assumptions, firstly, that the zinc atom pdf reproduces the displacements due to overall translational disorder, and secondly, that the whole molecule librates about the zinc atom. Both are probably good approximations; the former because the zinc atom is massive compared to the other atoms and will not displace significantly in intramolecular vibrations, and the latter because the molecule is almost tetrahedrally symmetric and the centre of mass is close to the equilibrium zinc position. Internal translational mean-squared displacements are of the order $5 \times 10^{-3} \text{Å}^2$, which is a factor of five smaller than the overall translational motion.

Finally, an extension to the standard TLS theory is considered which is specifically aimed at automatically separating one degree of internal freedom from the overall disorder; it is known as the segmented rigid-body model, (11), (33), (64), and is outlined in appendix A. In this model, an attached-rigid-group (ARG) is defined within the molecule to which an extra degree of internal freedom can be assigned, for example an internal libration about one specified axis. The method is not applicable to the zinc (II) tetraimidazole molecule for the following reasons:

- The internal libration of the ARG is only distinguishable from the overall librations about the parallel axis if the latter is small in comparison. It was shown in this study that the overall librations and the internal librations can produce mean-squared displacements of similar magnitude.
- The ARG's have to be attached to a main rigid-body from which the overall TLS tensors are established. The only useful candidates for the ARG's would be the imidazole rings, but this only leaves the zinc atom as the main rigid-body, which is not sufficient to determine an L tensor.
- The model would not permit estimates of internal displacements in the stretching projection parallel to the Zn-N bond.

2.6.1 Summary

A TLS analysis of the zinc (II) tetraimidazole molecule has been made based on x-ray crystallography ADP's at 100K and 150K. Separate estimates were obtained for mean-squared displacements of atoms due to intramolecular vibrations and overall disorder (i.e. disorder due to lattice vibrations and static disorder).

Overall disorder was described in terms of translational and librational pdf's of the whole molecule. The translation pdf was found to be isotropic with a second moment of the order $25 \times 10^{-3} \text{\AA}^2$. The molecule has a preferred axis of librational displacement parallel to the bisector of the N-Zn-N bond in the asymmetric group; mean-squared librational displacements are in the range $1 \rightarrow 9(^{\circ})^2$ about the zinc atom which corresponds to a linear mean-squared displacement of the order $10 \rightarrow 50 \times 10^{-3} \text{\AA}^2$ at the periphery of the molecule.

The intramolecular motion was categorised as mean-squared displacements in three projections relative to the imidazole rings: (i) In the stretch projection (parallel to Zn-N bond) mean-squared displacements were of the order $5 \times 10^{-3} \text{\AA}^2$ averaged over the ring. This is a factor of 5 smaller than the mean-squared displacements due to overall translation disorder. (ii) In the wag projection (in-plane wags about Zn-bonded nitrogen) the librations were of the order $\sim 16(^{\circ})^2$ which implies mean-squared displacements at the periphery of the molecule of $10 \times 10^{-3} \text{\AA}^2$ which is in the range 1 \rightarrow 5 times smaller than the mean-squared displacements caused by overall librational disorder. (iii) In the bend projection (out-of-plane bends) no information could be obtained.

The results can only be regarded as estimates due to the large calculated error of $\pm 1 \times 10^{-3} \text{\AA}^2$ but mainly due to the broad assumptions necessary for this kind of analysis which incur errors that are difficult to assess.

Chapter 3

Inelastic Neutron Scattering

3.1 Introduction

In this chapter, a precise analysis of the dynamic structure of the zinc (II) tetraimidazole complex is described based on a fundamentally distinct experimental method from that of chapter 2. In contrast to the coherent elastic photon scattering of X-ray crystallography, the physical process employed here is *incoherent inelastic neutron scattering*, (denoted henceforth as INS).

In neutron scattering spectroscopy, a beam of thermal neutrons impinging on a molecular crystal containing hydrogen is scattered predominantly incoherently. The energy spectrum of the out-going neutrons may be analysed by time-of-flight techniques because the neutron is a massive particle whose velocity depends on energy; it is found that the neutrons scatter both elastically and inelastically. The elastic component is analogous to optical Rayleigh scattering whereas the inelastic part corresponds to the Stokes and anti-Stokes lines in the Raman effect. The inelastic scatter is a result of quantised energy transfer to and from the quantised motion present in the sample and, as for light scattering, the separation between the elastic and inelastic peaks permits determination of the energies of the modes responsible for the scattering. Unlike the scattering of light however, the entire vibrational-rotational spectrum is revealed since optical selection rules do not apply for this method of excitation and thus, poorly defined peaks in the optical spectrum may be well defined in the INS spectrum. A further, very important advantage of neutron scattering over optical scattering, from systems which give mostly incoherent scattering (i.e. hydrogenous), is that the intensity

CHAPTER 3. INELASTIC NEUTRON SCATTERING

of the inelastic peaks in the energy spectrum may be directly related to the partial amplitudes of motion of the nuclei in each vibrational mode. This differs from optical intensities where assumptions about electronic motion must be made to explain the peak intensities.

In this study, the INS spectra of imidazole and zinc (II) tetraimidazole molecular crystals and some deuterated analogues have been measured at very low temperature. At these temperatures, the anti-Stokes excitations are negligible since most, if not all, of the modes of motion are in their ground states and can not impart energy. We consider the Stokes spectrum in the energy range of 5 meV to 2 eV , which encompasses most lattice and molecular vibrational energies. A central assumption in this work is that the lattice modes are weakly coupled to the internal molecular vibrational modes in the samples chosen, i.e. the latter are non-dispersive; we are interested in the intramolecular modes and this assumption permits an *isolated molecule* approach to the problem which is essential for the treatment described here. The validity of the isolated molecule approach may be assessed directly from the experimental INS spectrum: if peaks are seen to be broader than the intrinsic resolution it suggests that the associated vibrational modes are dispersive through the lattice. Furthermore, neutron scattering yields information about the excitations throughout the Brillouin zone (BZ) whereas optical experiments, in contrast, determine excitation energies only at the BZ centre. Therefore, in neutron scattering, the excitations near the edge of the BZ dominate, due to the so-called volume effect, and consequently large energy discrepancies ($> \text{few cm}^{-1}$) in the INS peak positions with respect to the optical frequency spectra provide further evidence of dispersion in the vibrational modes.

Assignments of the INS spectra are aided by the peak intensities which reveal modes involving large hydrogen motion. Subsequently, based on the isolated molecule approach, force fields for the respective molecules are developed via normal mode analysis that model both the INS peak energies and intensities. This is equivalent to modelling the complete hydrogen-weighted vibrational density of states of the samples. In a series of articles, (81), (101), (118), (119), (120), (147), (153), White and coworkers concluded that INS intensities were a far more sensitive test of the accuracy of a force field in predicting the dynamic behaviour of a molecule than simply equating the eigenvalues to the vibrational energies of the modes. The

CHAPTER 3. INELASTIC NEUTRON SCATTERING

normal mode analysis yields both the energies and nature of the molecular vibrations, which is equivalent to specifying both the eigenvalues and eigenvectors of the secular equation of motion. This enables the complete vibrational correlation function (VCF) to be determined, which wholly defines the relative motion of atoms in the molecule.

The description of the dynamic behaviour of an isolated molecule by force fields presupposes the harmonic approximation. Anharmonicities in the vibrations cause broadening and splitting of peaks in the INS spectra. However, at low temperature, the anharmonicity effects are minimised, and according to White, (119), a quasi-harmonic model may be adopted if at low temperatures the peak widths correspond to the experimental resolution. This is found to hold in the INS spectra presented here.

The aim of the work was to obtain the VCF for the zinc (II) tetraimidazole complex so that it could be input to the EXAFS simulations described in chapter 4. In order to address such a large problem, it was first necessary to partially solve the dynamic structure by determining the VCF for the isolated imidazole molecule. The force field for imidazole was then incorporated into the larger and more complex force field for the zinc (II) complex.

The first two sections in this chapter provide an introduction to the theoretical background required to do an analysis of this kind; the nomenclature in these two sections is then referred to in the subsequent sections. The first section describes the partial differential cross section, which is the observed quantity in an INS experiment, and shows why it is dominated by incoherent scattering from hydrogen atoms and how it may be interpreted to yield information about the magnitude of molecular vibrations in the sample. The second section describes the physics of molecular vibrations in orthogonal normal modes and goes on to describe the formalism and manipulations required to do a normal mode analysis. An experimental section describes the spectrometer used to record the INS spectra and also discusses the sample preparation and analytical software employed; the latter is based on the theory described in the first two sections. Finally, the last two sections present the results of the INS studies on pure imidazole and the zinc (II) tetraimidazole complex and the methodology used in the normal mode analysis.

3.2 Essential Elements of INS Theory

The intensity of nuclear scattered neutrons measured experimentally is proportional to the mean-squared relative displacements of the target nuclei about their equilibrium positions and is dominated by the incoherent scattering contribution from the hydrogen atoms in the sample. Rigorous proof of this assertion is quite involved and may be found by reference to texts on Neutron Scattering Theory, (e.g. see (82)). However the essential elements of the theory directly related to this effect are summarised here. The subsections 3.2.1, 3.2.2, 3.2.3 and 3.2.4 are compiled mainly from reference to (82) and (143). At the end of this section, some effects observed in experimental spectra, such as combination bands and phonon wings, are described.

3.2.1 Partial Differential Cross Section

In a nuclear scattering event the variables of interest are the change in neutron energy, equivalent to the quantum $\hbar\omega$, and the momentum transfer, $\hbar\mathbf{Q}$, such that

$$\hbar\omega = E - E' \quad (3.1)$$

$$\mathbf{Q} = \mathbf{k} - \mathbf{k}' \quad (3.2)$$

in which E and E' are the neutron energy and \mathbf{k} and \mathbf{k}' the neutron wave vector before and after scattering respectively. In both the initial and final states, the wave function, ψ , of the neutron is described as a plane wave; for the out-going wave this is equivalent to the asymptotic form of the wave function in the limit that the wave is detected far from the point of scatter, i.e.

$$\begin{aligned} \psi_{\mathbf{k}} &= C e^{i\mathbf{k} \cdot \mathbf{r}} \\ \psi_{\mathbf{k}'} &= C e^{i\mathbf{k}' \cdot \mathbf{r}} \end{aligned} \quad (3.3)$$

in which C is a normalisation constant. From perturbation theory the probability governing the transition from the initial to the final state of the neutron is proportional to the square of the matrix element of the nucleon-nucleon interaction operator, V , between the two states

CHAPTER 3. INELASTIC NEUTRON SCATTERING

involved; this probability is stated in *Fermi's Golden Rule*:

$$W_{k \rightarrow k'} = \frac{2\pi}{\hbar} \left| \int d\mathbf{r} \psi_{\mathbf{k}}^* \hat{V} \psi_{\mathbf{k}'} \right|^2 \rho_{\mathbf{k}'}(E) \quad (3.4)$$

where $\rho_{\mathbf{k}'}(E)$ is the density of final scattering states per unit energy range. Normalisation is achieved by enclosing the entire system in a large box of volume L^3 ; this enables the neutron wave functions in Eq. (3.3) to be normalised via $C = L^{-3/2}$ and permits the density of final states per unit energy range to be written explicitly as:

$$\rho_{\mathbf{k}'}(E) = \left(\frac{L}{2\pi} \right)^3 \frac{d\mathbf{k}'}{dE} \quad (3.5)$$

If the total cross section for nuclear scattering from a given nucleus is denoted by σ , and the incident flux of neutrons by $\hbar k/mL^3$, it may thus be seen that, (82),

$$\begin{aligned} d\sigma &= W_{k \rightarrow k'} / \text{incident flux} \\ &= \left(\frac{m}{2\pi\hbar^2} \right)^2 \left| \int d\mathbf{r} e^{-i\mathbf{k}' \cdot \mathbf{r}} \hat{V} e^{i\mathbf{k} \cdot \mathbf{r}} \right|^2 d\Omega \\ &= |\langle \mathbf{k}' | \hat{V} | \mathbf{k} \rangle|^2 d\Omega \end{aligned} \quad (3.6)$$

where $d\Omega$ is an element of the solid angle about the point of scatter; *Bra-Ket* notation has been introduced for convenience to denote the integration of the initial and final state wave functions over all space. The so-called *differential cross-section* for elastic nuclear scattering may thus be written as

$$\frac{d\sigma}{d\Omega} = |\langle \mathbf{k}' | \hat{V} | \mathbf{k} \rangle|^2 \quad (3.7)$$

and is an experimental observable. It describes the angular dependence of the strength of elastic neutron scattering about the nucleus and is determined by the form of the interaction potential, \hat{V} .

When *inelastic* scattering occurs the change of the target nucleus from its initial state λ to its final state λ' has to be considered. The state functions in the matrix element of Eq. (3.7) should therefore be rewritten as the product state functions describing the neutron and target, i.e. $\langle \lambda' \mathbf{k}' |$ and $|\lambda \mathbf{k} \rangle$. Conservation of energy, cf. Eq. (3.1), is incorporated via the delta function

$$\delta(\hbar\omega + E_{\lambda} - E_{\lambda'})$$

CHAPTER 3. INELASTIC NEUTRON SCATTERING

in which E_λ and $E_{\lambda'}$ are the initial and final state energies of the target nucleus. The integral of this delta function over all final state energies is, by definition, equal to unity, which implies

$$\frac{d}{dE'} = \delta(\hbar\omega + E_\lambda - E_{\lambda'}) \quad (3.8)$$

Premultiplying both sides of Eq. (3.7) by this relation, and denoting the probability of occupation of the initial state λ by the factor p_λ , an expression for the *partial differential cross section* may be expressed as a sum over all possible transitions, $\lambda \rightarrow \lambda'$, i.e.

$$\frac{d^2\sigma}{d\Omega dE'} = \frac{k'}{k} \sum_{\lambda\lambda'} p_\lambda |\langle \lambda' k' | \hat{V} | \lambda k \rangle|^2 \overline{\delta(\hbar\omega + E_\lambda - E_{\lambda'})} \quad (3.9)$$

It is this basic quantity that is measured in every inelastic neutron scattering experiment. Notice the factor (k'/k) , which was unity for elastic scattering in Eq. (3.7). The horizontal bar in Eq. (3.9) represents any further averaging necessary such as the distribution of isotopes, nuclear spin orientations or static disorder of nuclei positions.

Note that, when dealing with neutrons, it is not usually necessary to employ the full *partial wave description* from formal scattering theory to express scattering events. In other words, the state functions, $|\lambda k\rangle$, and interaction operator, \hat{V} , need not be expressed as a sum of terms over all angular momentum components but rather by a single term. The justification for this stems from both the very short range of the nucleon-nucleon interaction, ($\sim 1.5 \times 10^{-3} \text{ \AA}$), therefore limiting the length of the *impact parameter*¹ and the small size of the nuclear radius ($\sim 10^{-2} \text{ \AA}$), in comparison with the wavelength of thermal neutrons, ($\sim 1 \text{ \AA}$). Consequently only s-wave components ($l = 0$ angular momentum) are significant in the partial wave description and all other terms may be safely neglected; i.e. the nucleus behaves as a point scatterer. All of this means that the nuclear scattering of neutrons is isotropic and may be characterised by a single scalar quantity, b , known as the *scattering length*. b is equivalent to the scattering amplitude $f(\theta, \phi)$ (from formal scattering theory) for s-wave scattering alone and indicates the strength of scattering from a particular nucleus.

¹The *impact parameter*, I , is the distance of closest approach of the neutron trajectory to the nucleus. In the partial wave description, only those components whose angular momentum quantum number, l , satisfies $l \leq 2\pi I/\lambda$ produce appreciable contributions to the scattering. With thermal neutrons ($\lambda \sim 1 \text{ \AA}$) scattering via the nucleon-nucleon interaction limits $I \leq 1.5 \times 10^{-3} \text{ \AA}$ and only the $l = 0$ component is significant.

CHAPTER 3. INELASTIC NEUTRON SCATTERING

3.2.2 Coherence and Incoherence - Scattering from Protons

Scattering, both elastic and inelastic, may be subdivided into a coherent and an incoherent part. Essentially the distinction arises due to the variation in the scattering potentials throughout the target, or more precisely, the distribution of the nuclear scattering lengths, b . This may be demonstrated by considering the form of Eq. (3.9) for an idealised, rigid array of N bound nuclei. The so-called *Fermi pseudo potential* is employed to generate isotropic scattering centred on the j^{th} nuclei at position \mathbf{R}_j , i.e.

$$\hat{V}(\mathbf{r}) = \frac{2\pi\hbar^2}{m} \sum_j b_j \delta(\mathbf{r} - \mathbf{R}_j) \quad (3.10)$$

Note that each nucleus is characterised by a separate scattering length, b_j . The prefactor, $\frac{2\pi\hbar^2}{m}$, is a normalisation constant; it is the reciprocal of the prefactor to the scattering matrix element, cf. Eq. (3.6), and thus disappears when the Fermi pseudo potential is substituted into Eq. (3.9); i.e.

$$\begin{aligned} \frac{d^2\sigma}{d\Omega dE'} &= \frac{k'}{k} \sum_{\lambda\lambda'} p_\lambda \left| \langle \lambda' | \sum_j b_j \int d\mathbf{r} e^{-i\mathbf{k}'\cdot\mathbf{r}} \delta(\mathbf{r} - \mathbf{R}_j) e^{i\mathbf{k}\cdot\mathbf{r}} | \lambda \rangle \right|^2 \delta(\hbar\omega + E_\lambda - E_{\lambda'}) \\ &= \frac{k'}{k} \sum_{\lambda\lambda'} p_\lambda \left| \langle \lambda' | \sum_j b_j e^{i\mathbf{Q}\cdot\mathbf{R}_j} | \lambda \rangle \right|^2 \delta(\hbar\omega + E_\lambda - E_{\lambda'}) \end{aligned} \quad (3.11)$$

Note that the right-hand side of Eq.(3.10), and therefore also the function in the matrix element of Eq. (3.11), are not operators. Consequently, the state function $|\lambda\rangle$ is not acted upon and the matrix element obeys

$$\langle \lambda' | A | \lambda \rangle = A \langle \lambda' | \lambda \rangle = A \delta_{\lambda'\lambda}$$

where A is a constant. This implies that the matrix element vanishes unless $\lambda' = \lambda$ from which it follows that $E_{\lambda'} = E_\lambda$, i.e. scattering from a totally rigid array of nuclei is elastic².

Eq. (3.11) may thus be rewritten in the form:

$$\begin{aligned} \frac{d\sigma}{d\Omega} &= \sum_{jj'} e^{i\mathbf{Q}\cdot(\mathbf{R}_j - \mathbf{R}_{j'})} \overline{b_{j'}} b_j \\ &= \sum_{jj'} e^{i\mathbf{Q}\cdot(\mathbf{R}_j - \mathbf{R}_{j'})} \left[|\overline{b}|^2 + \delta_{j'j} (|\overline{b}|^2 - |\overline{b}|^2) \right] \end{aligned} \quad (3.12)$$

²This is an idealised case. Real nuclei are not totally rigid and succumb to lattice and molecular vibrations and are capable of recoil so that momentum transfer occurs to varying degree.

CHAPTER 3. INELASTIC NEUTRON SCATTERING

It may be seen that Eq. (3.12) has been reduced to the sum of two parts, which may be identified as coherent and incoherent scattering.

In coherent scattering, there is strong interference between the scattered neutron waves such that Bragg scattering results; in this case only the mean scattering length for the whole target, \bar{b} , satisfies this condition; coherent scattering is thus proportional to $|\bar{b}|^2$. The *deviations* from the mean scattering length however are randomly distributed, producing a random distribution of scattering from the nuclei which cannot interfere. This is known as the incoherent scattering and is proportional to the mean-squared deviation of b : $|\bar{b} - \bar{b}|^2 = (\overline{|b|^2} - |\bar{b}|^2)$.

The variation in the scattering length is generally due to the presence of isotopes and the interaction of the neutron (a spin $\frac{1}{2}$ particle) with a nucleus of spin i . In the latter, the interaction can take place in states of total spin corresponding to $i + \frac{1}{2}$ and $i - \frac{1}{2}$, which have associated scattering lengths of $b^{(+)}$ and $b^{(-)}$. These scattering lengths are then weighted according to the multiplicity of states with the respective total spins.

An important example is that of the scattering of neutrons by protons. The proton is also a spin $\frac{1}{2}$ particle and hence there are three states with total spin 1 and one state with total spin zero. The scattering lengths are found to be:

$$b^{(+)} = 1.04 \times 10^{-12} \text{cm}^2 \quad (\text{triplet})$$

$$b^{(-)} = -4.74 \times 10^{-12} \text{cm}^2 \quad (\text{singlet})$$

(where a negative scattering length describes a phase difference of π compared to positive values). Hence

$$\bar{b} = \frac{3}{4}b^{(+)} + \frac{1}{4}b^{(-)} = -0.38 \times 10^{-12} \text{cm}^2$$

and

$$\overline{|b|^2} = \frac{3}{4}|b^{(+)}|^2 + \frac{1}{4}|b^{(-)}|^2 = 6.49 \text{ bn } (10^{-24} \text{cm}^2)$$

which results in

$$\sigma_{\text{total}} = 81.7 \text{bn}$$

$$\sigma_{\text{coher}} = 1.8 \text{bn}$$

$$\sigma_{\text{incoh}} = 79.8 \text{bn}$$

CHAPTER 3. INELASTIC NEUTRON SCATTERING

Clearly, the scattering from ^1H Hydrogen nuclei is dominated by the incoherent component, σ_{incoh} , (this is also the case for naturally occurring Hydrogen due to the low abundance of other isotopes). Additionally, it is found that the total scattering cross section, σ_{total} , is very much larger than for most nuclei (generally $\sim 5 \text{ bn}$). Consequently, most inelastic neutron scattering experiments, including that described in this study, are essentially probes of the incoherent scattering from hydrogen nuclei in the target.

3.2.3 Correlation and Response Functions

It is possible to recast Eq. (3.11) so that the partial differential cross section is factorised into a term derived from the interaction of neutrons with matter and a response function that reflects the physical properties of the particular sample under inspection.

For this purpose, the delta function in Eq. (3.11) is written as

$$\delta(\hbar\omega + E_{\lambda} - E_{\lambda'}) = \frac{1}{2\pi\hbar} \int_{-\infty}^{\infty} dt e^{-\frac{it}{\hbar}(\hbar\omega + E_{\lambda} - E_{\lambda'})} \quad (3.13)$$

where the integral is over time, t . Inserting Eq. (3.13) into Eq. (3.11) gives

$$\frac{d^2\sigma}{d\Omega dE'} = \frac{k'}{k} \frac{1}{2\pi\hbar} \int_{-\infty}^{\infty} dt \sum_{\lambda\lambda'} p_{\lambda} \left| \langle \lambda' | \sum_j b_j e^{i\mathbf{Q}\cdot\mathbf{R}_j} | \lambda \rangle \right|^2 e^{-\frac{it}{\hbar}(\hbar\omega + E_{\lambda} - E_{\lambda'})} \quad (3.14)$$

The energy terms in the exponent may be incorporated in the scattering matrix element and reexpressed in terms of the hamiltonian of the target system. Then, assuming that the coupling between target states and the interaction potentials is insignificant, (i.e. that b_j is independent of λ and λ' and may be written outside of the scattering matrix element), Eq. (3.14) becomes

$$\frac{d^2\sigma}{d\Omega dE'} = \frac{k'}{k} \frac{1}{2\pi\hbar} \int_{-\infty}^{\infty} dt e^{-i\omega t} \sum_{jj'} \overline{b_j^* b_{j'}} Y_{jj'}(\mathbf{Q}, t) \quad (3.15)$$

where the modified scattering matrix element, summed over all possible transitions $\lambda \rightarrow \lambda'$, is represented by the so-called *correlation function*, $Y_{jj'}(\mathbf{Q}, t)$. The derivation of the correlation function involves making some subtle manipulations of the scattering matrix element that are beyond the scope of this thesis (refer to (82), (83)); the result is therefore simply stated as

$$Y_{jj'}(\mathbf{Q}, t) = \langle e^{-i\mathbf{Q}\cdot\mathbf{R}_j} e^{i\mathbf{Q}\cdot\mathbf{R}_{j'}(t)} \rangle \quad (3.16)$$

CHAPTER 3. INELASTIC NEUTRON SCATTERING

in which $\bar{R}_j(t)$ is a time-dependent operator, incorporating the hamiltonian of the target system, which acts on the initial and final stationary states of the system. The angled-brackets in Eq. (3.16) denote the statistical average over all initial states, which is equivalent to replacing p_λ , the probability of occupation of the state λ , by the normalised thermodynamic factor $\exp(-E_\lambda/k_B T)/\sum_\lambda \exp(-E_\lambda/k_B T)$. The correlation function is therefore a thermal average of a combination of operators belonging to the target and has implicit in it the 3-dimensional static and dynamic structure of the particular sample.

The response of the target system to the scattering of neutrons with a given \mathbf{Q} and ω is given by the Fourier transform of the correlation function with respect to time, i.e.

$$S(\mathbf{Q}, \omega) = \frac{1}{2\pi\hbar N} \int_{-\infty}^{\infty} dt e^{-i\omega t} \sum_{jj'} Y_{jj'}(\mathbf{Q}, t) \quad (3.17)$$

This result, $S(\mathbf{Q}, \omega)$, is known as the *response function*, (148), of the system and projects a surface in (\mathbf{Q}, ω) space. It is analogous to the structure factor in x-ray diffraction, the Fourier transform of which is a 3-dimensional map of the electron density of the target; in the case of the response function, the Fourier transform is the correlation function which characterises the 3-dimensional interaction of neutrons with the nuclei of a specific sample. For a given momentum transfer \mathbf{Q}_0 , $S(\mathbf{Q}_0, \omega)$ describes the frequency composition of the many-body motion of the target system.

Consequently, the observed quantity, $d^2\sigma/d\Omega dE'$, may be expressed as the product of two independent terms, i.e.

$$\frac{d^2\sigma}{d\Omega dE'} = \left[N \frac{k'}{k} \overline{b_j^* b_{j'}} \right] \cdot S(\mathbf{Q}, \omega) \quad (3.18)$$

The first term governs the strength of the neutron interaction with the target sample based on the scattering lengths of the operators b_j^* and $b_{j'}$; it depends only on the type and relative proportions of the nuclei present in the sample (it is this term for example that determines the coherent and incoherent character of the scattering). The second term, the response function $S(\mathbf{Q}, \omega)$, is determined wholly by the physical and chemical nature of the target system and its behaviour in time. It is the evaluation of the response function that is sought after in inelastic neutron scattering experiments.

3.2.4 Response Function for Isolated Harmonic Oscillator

For a vibrating molecule it is appropriate to express \mathbf{R} , the position of a given nucleus, as a sum of \mathbf{l} , the position of the centre of mass of the molecule, and \mathbf{d} the position of the nucleus relative to \mathbf{l} . Thus

$$\mathbf{R} = \mathbf{l} + \mathbf{d} \quad (3.19)$$

The important assumption is now made that the motion of the centre of mass of the molecule and the relative motion of the nuclei are mutually independent, in which case, the correlation function in Eq. (3.16) factorises into a term with respect to \mathbf{l} and a term with respect to \mathbf{d} . We consider the latter term and, according to a proof given in (82), chapters 3.5, 3.6.2 and 3.8, involving Bloch's identity, may write the correlation function, in the frame of the molecule, as

$$\langle e^{-i\mathbf{Q}\cdot\mathbf{d}} e^{i\mathbf{Q}\cdot\mathbf{d}(t)} \rangle = e^{-\langle(\mathbf{Q}\cdot\mathbf{d})^2\rangle} e^{\langle(\mathbf{Q}\cdot\mathbf{d})(\mathbf{Q}\cdot\mathbf{d}(t))\rangle} \quad (3.20)$$

where $\mathbf{d}(t)$ is a time-dependent operator, analogous to $\mathbf{R}(t)$ in Eq. (3.16), which incorporates the target interaction operators and the hamiltonian, \mathcal{H} , describing the stationary states of the molecule. (Note that the notation convention has been maintained whereby the angled brackets denote the statistical average over all initial stationary states). For a nucleus of mass M , in an isotropic, harmonic potential the hamiltonian may be written as

$$\mathcal{H} = \frac{1}{2M} \hat{\mathbf{p}}^2 + \frac{M\omega_0^2}{2} \hat{\mathbf{d}}^2 \quad (3.21)$$

where $\hat{\mathbf{p}}$ is the momentum operator and ω_0 is the associated frequency of vibration of the nucleus about its equilibrium position. By assuming a harmonic potential, whose energy level structure is well understood, the statistical average (canonical average) over initial energy states in Eq. (3.20) may be expressed analytically; consequently the two exponential terms on the right-hand side of Eq. (3.20) may be written explicitly.

The first term of Eq. (3.20) may be written as

$$e^{-\langle(\mathbf{Q}\cdot\mathbf{d})^2\rangle} = e^{-Q^2\langle\mathbf{d}^2\rangle} = \exp \left[-Q^2 \frac{\hbar}{2M\omega_0} \coth \left(\frac{\hbar\omega_0}{2k_B T} \right) \right] \equiv e^{-Q^2 U^2} \quad (3.22)$$

in which the coth term in the exponent is identified as the mean-squared-displacement of the nucleus (see appendix B, Eq. (B.11)) and is denoted by the conventional symbol U . The

CHAPTER 3. INELASTIC NEUTRON SCATTERING

first term of the correlation function has a damping effect and is known as the Debye-Waller factor.

Similarly, by substitution of the harmonic form of the operators and by taking the canonical average, the second term of Eq. (3.20) can be written as:

$$e^{i(\mathbf{Q} \cdot \mathbf{d})(\mathbf{Q} \cdot \mathbf{d}(t))} = \exp \left[\frac{\hbar Q^2 \cosh \left(i\omega_0 t + \frac{\hbar\omega_0}{2k_B T} \right)}{2M\omega_0 \sinh \left(\frac{\hbar\omega_0}{2k_B T} \right)} \right] \equiv \exp\{y \cosh(x)\} \quad (3.23)$$

in which

$$y = \frac{\hbar Q^2}{2M\omega_0 \sinh \left(\frac{\hbar\omega_0}{2k_B T} \right)} \quad \text{and} \quad x = i\omega_0 t + \frac{\hbar\omega_0}{2k_B T}$$

Thus, using the identity

$$\exp\{y \cosh(x)\} = \sum_{n=-\infty}^{\infty} \exp(nz) I_n(y) \quad (3.24)$$

the second term in the correlation function may be described by modified Bessel functions³, $I_n(y) = I_{-n}(y)$, of integer order n .

With both terms in the correlation function, Eq. (3.20), expressed explicitly for the harmonic potential, the response function for the harmonic oscillator may be evaluated using Eq. (3.17) to give

$$S(\mathbf{Q}, \omega) = e^{-Q^2 U^2} \sum_{n=-\infty}^{\infty} I_n(y) e^{\frac{n\hbar\omega_0}{2k_B T}} \delta(\hbar\omega - n\hbar\omega_0) \quad (3.25)$$

3.2.5 Fundamentals, Overtones and Combinations - Spectral Intensity

It is evident from the formula for the harmonic response function, Eq. (3.25), that the integer n measures the amount of energy, $n\hbar\omega_0$, lost ($n > 0$) or gained ($n < 0$) by the neutron. However since experiments are generally carried out at low temperature, i.e. $T \sim 20K$, when the target is mostly in its ground state and cannot impart energy to the neutron, it is usually only necessary to consider the case when $n \geq 0$. On this basis, it is possible to identify the case $n = 0$ as the elastic interaction, $n = 1$ as the fundamental excitation, $n = 2$ as the first overtone and so on. The response function for each of these events and hence the spectral intensity is thus easily obtained using Eq. (3.25). The elastic line intensity accounts for most

³ Modified Bessel functions are Bessel functions of imaginary argument; $I_n(y) = J_n(iy)/i^n$

CHAPTER 3. INELASTIC NEUTRON SCATTERING

of the scattered neutrons and is exactly analogous to the Rayleigh line in Raman scattering; it does not however yield much information and is normally suppressed from inelastic scattering spectra in the study of molecular vibrations. In keeping with the analogy to Raman spectra, the ($n > 0$) excitations in inelastic neutron scattering may be thought of in terms of the *Stokes* lines. The ($n < 0$) components therefore form the *Anti-Stokes* lines but are quenched at low temperature.

It is possible to simplify the form of the harmonic response function given by Eq. (3.25) in the regime where $\hbar\omega_0 \gg 2k_B T$ so that $y \rightarrow 0$. Consequently, for $n > 0$, the modified Bessel function may be written as

$$\lim_{y \rightarrow 0} I_n(y) = \frac{1}{n!} (y/2)^n$$

and the response function, for a single nucleus undergoing harmonic motion, becomes

$$\lim_{\hbar\omega_0 \gg 2k_B T} S(Q, \omega)_n = \frac{1}{n!} (Q^2 U^2)^n e^{-Q^2 U^2} \quad (3.26)$$

Eq. (3.26) demonstrates clearly the very simple relation that the spectral intensity of a fundamental, or overtone excitation, is determined by the mean-squared-displacement, U^2 , and attenuated by the Debye-Waller factor, $e^{-Q^2 U^2}$. At typical experimental temperatures of 20K, $\hbar\omega_0 > 2k_B T$ for neutron energy transfer greater than $\sim 3.5 \text{ meV}$ ($\equiv 28 \text{ cm}^{-1}$), hence Eq. (3.26) is valid for most studies involving optical modes.

Eq. (3.25) and Eq. (3.26) are only strictly true for one-dimensional isolated harmonic oscillators. In the case of molecules, the damping of the scattering intensity in a particular mode due to the statistical distribution of the nucleus about its equilibrium position, (represented by the Debye-Waller factor, $e^{-Q^2 U^2}$), should include the mean-squared-displacement of the nucleus in *all* its modes of vibration. In order to achieve this, tensor notation is required, and the one-dimensional mean-squared displacement, U^2 , is replaced by a symmetric second-rank tensor, U_ν , whose elements describe the second moments of the 3-dimensional probability distribution function of the nucleus in the ν^{th} intramolecular vibrational mode. The exponent in the Debye-Waller factor is then written in terms of a new symmetric second-order tensor \mathbf{U} where $\mathbf{U} = \sum_\nu \mathbf{U}_\nu$. Thus, the spectral intensity for fundamentals and overtones in

CHAPTER 3. INELASTIC NEUTRON SCATTERING

the ν^{th} mode for an atom vibrating in a molecule is represented by (145)

$$S(\mathbf{Q}, \omega)_n^\nu \propto I_n(\mathbf{Q}\mathbf{Q} : \mathbf{U}_\nu) e^{-(\mathbf{Q}\mathbf{Q}:\mathbf{U})} \quad (3.27)$$

where the vector $\mathbf{Q}\mathbf{Q}$ is the direct product of the momentum transfer vector \mathbf{Q} . In this notation, the scalar arguments $(\mathbf{Q}\mathbf{Q} : \mathbf{U}_\nu)$ and $(\mathbf{Q}\mathbf{Q} : \mathbf{U})$ represent the projection of the \mathbf{U}_ν or \mathbf{U} tensors respectively in the direction of the vector $\mathbf{Q}\mathbf{Q}$ multiplied by the magnitude of $\mathbf{Q}\mathbf{Q}$.

Multiphonon scattering is also possible and may be categorised into three types:

- single excitation of more than one mode. This is known as a *combination* excitation.
- multiple excitation of one mode. Strictly speaking this is also a combination mode although within the harmonic approximation it effectively produces an overtone line; its intensity however is distinct from the overtone intensity caused by a single excitation.
- excitation of external vibrational modes (lattice modes) as well as the internal mode.

This produces so-called *phonon wings* and is dealt with in the following subsection.

The intensities in the first two categories above are described to a good approximation by the response function for double-excitation combinations (69)

$$S(\mathbf{Q}, \omega)_{n,n'}^{\nu,\nu'} \propto I_n(\mathbf{Q}\mathbf{Q} : \mathbf{U}_\nu) \cdot I_{n'}(\mathbf{Q}\mathbf{Q} : \mathbf{U}_{\nu'}) e^{-(\mathbf{Q}\mathbf{Q}:\mathbf{U})} \quad (3.28)$$

where the multiple excitation of the ν and ν' modes produces a line at $\omega = n\omega_0^\nu + n'\omega_0^{\nu'}$.

In general, the \mathbf{U}_ν and \mathbf{U} tensors are anisotropic; consequently the intensity of scattered neutrons depends on the orientation of the momentum transfer vector \mathbf{Q} as well as the magnitude. This can be interesting for single crystal experiments but for powder samples the calculated intensities should be averaged over all orientations; a so-called *powder average*. Analytical techniques for achieving powder averages in neutron scattering experiments have been applied, (142), (145), (150) and found to be accurate when the geometry of the \mathbf{U} tensor for each atom is known. For the case where the \mathbf{U}_ν tensors are best-fitted and the form of the \mathbf{U} tensor is not known, numerical powder averages are found to be more appropriate, (17).

3.2.6 Phonon Wings

There is a finite probability that a neutron will scatter inelastically exciting an optical molecular mode and an acoustic lattice mode; this produces additional structure in the spectrum above the optical excitation energy that mimics the low frequency acoustic regime of the spectrum. The acoustic regime is composed of broad peaks as a function of energy due to the highly dispersive nature of lattice modes (i.e. lattice modes may be excited by a range of neutron energy transfer, albeit with the corresponding phonon wave vector determined by the pertinent dispersion relation); hence the additional structure above the optical excitation line (often referred to as the zero-phonon line) appears as a broad featureless wing or *phonon wing*.

It is also possible for more than one acoustic phonon to be excited as well as the optical phonon. This results in additional wings above the zero-phonon line distinct from the single-phonon wing; their form may be understood as the convolution of those broad peaks associated with the acoustic modes in question. Consequently, the many-phonon wings extend higher in energy from the zero-phonon line than does the single-phonon wing. The concept of phonon wings is illustrated in figure 3.1 for the ideal case of a one-dimensional diatomic lattice.

The spectral intensity of the zero-phonon line, described by Eq. (3.27), is distributed between the zero-phonon line and its phonon wings; the fraction in the phonon wings is given by (144)

$$1.0 - e^{-Q^2 u^2} \quad (3.29)$$

where the exponential is the Debye-Waller factor for the external modes and u is the mean-squared-displacement amplitude of the lattice vibrations. The assumption in this expression is that the molecular modes are completely uncoupled from the lattice modes so that the latter may be independently described by the parameter u . Also, the motion of the atoms due to the lattice modes is assumed to be isotropic so that u is just a scalar quantity and not a tensor. By expanding Eq. (3.29), the distribution of the intensity among the single and

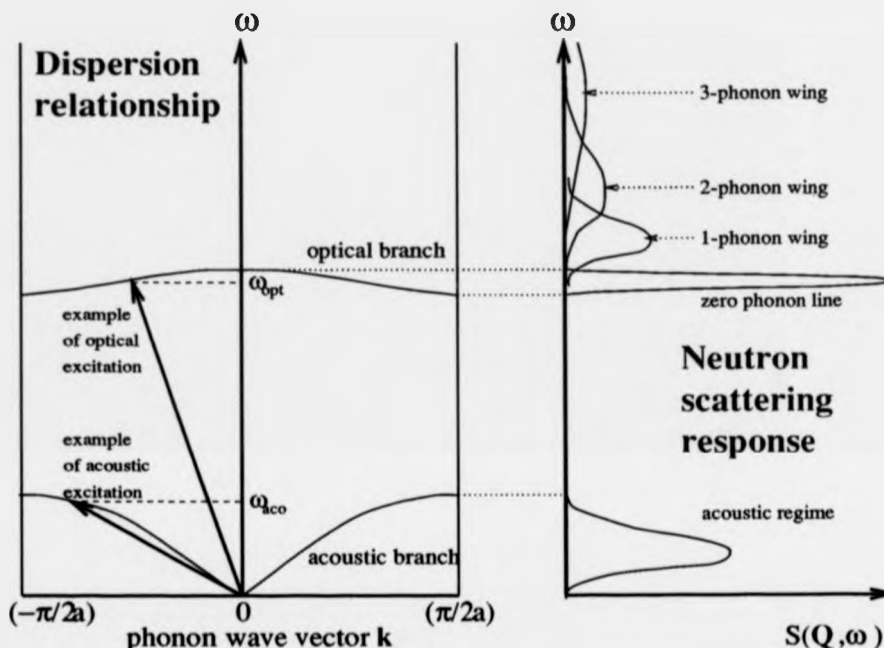


Figure 3.1: Illustration of the phonon wing phenomenon in the idealised case of a perfect one-dimensional diatomic lattice. The diagram on the left shows the dispersion relationship of longitudinal waves within the first Brillouin zone and for this case exhibits one optical and one acoustic branch. Neutrons impinging on the lattice may scatter inelastically, transferring energy and momentum by exciting a vibrational phonon whose frequency and wave vector satisfy the dispersion relationship; two possible phonon excitations are denoted by the arrows corresponding to an energy transfer of $\hbar\omega_{opt}$ and $\hbar\omega_{aco}$ respectively. The graph on the right is the corresponding response function for this idealised case and represents therefore the partial differential cross section of a neutron scattering experiment. It corresponds to a weighted density of states spectrum for the system and as such the two branches from the dispersion diagram appear as peaks; effectively the branches are collapsed onto the ω axis and consequently produce a narrow optical peak (zero-phonon line) but a broad band in the acoustic region. For the case where a neutron excites both an optical and acoustic phonon the energy transfer corresponds to $\hbar\omega_{opt} + \hbar\omega_{aco}$ and the associated feature in the response function occurs above the zero-phonon line as the 1-phonon wing reproducing the form of the peak in the acoustic region. For multiphonon excitation the energy transfer corresponds to $\hbar\omega_{opt} + \hbar\omega_{aco_1} + \hbar\omega_{aco_2} + \dots$ and produces wings extending further above the zero-phonon line. The form of the n^{th} phonon wing is the n^{th} convolution of the acoustic peak, in this case with itself.

CHAPTER 3. INELASTIC NEUTRON SCATTERING

multi-phonon wings may be expressed as

$$\begin{array}{ccccccc} e^{-Q^2 u^2} Q^2 u^2 & + & e^{-Q^2 u^2} \frac{(Q^2 u^2)^2}{2!} & + & e^{-Q^2 u^2} \frac{(Q^2 u^2)^3}{3!} & + & \dots \\ \text{1-phonon} & & \text{2-phonon} & & \text{3-phonon} & & \text{etc.} \end{array} \quad (3.30)$$

It may be deduced from Eq. (3.30) that the multi-phonon wings are more significant for experiments in which there is a large momentum transfer and for samples which exhibit large scale motion due to lattice modes. For light molecular species in particular, high-order phonon wings may even dominate the spectrum; for all samples, phonon wings become more significant and more extended as the temperature rises.

To summarise this section, the most important points are noted. The measured quantity in an inelastic neutron scattering experiment is the partial differential cross section; the expression for which may be shown to be separable into two terms, one due to the type of nuclei present and the other one dependent on a response function for the sample. The former term dictates that incoherent scatter from hydrogen atoms present in the sample dominate any experimental spectra. The latter term reflects the physical make-up of the sample, such as the vibrational motion undergone by the constituent nuclei, and it is this response function that determines the spectral form. The response function is written down for the specific case of harmonic motion of nuclei and is decomposed into contributions from fundamentals, overtones, and combinations. It is found that the spectral intensity is shared among the various molecular modes according to the displacement of the atom in each mode and attenuated by the displacements of the atom in all other modes. In the general case, the anisotropy of the motion requires that powder averages be done. The situation is complicated by external lattice modes of the sample which produce phonon-wings in the spectra.

3.3 Molecular Vibrations and Normal Mode Analysis

The method of determining the frequency and nature of small molecular vibrations from a proposed or observed local potential energy function assumed to be harmonic is known as *normal mode analysis*. Classical treatment is mostly adequate due to the property that the motion can be resolved into combinations of uncoupled simple harmonic oscillations whose

CHAPTER 3. INELASTIC NEUTRON SCATTERING

frequencies may then be established. Quantum mechanical considerations applying to the nature of the motion may be introduced subsequently. All internal vibrations may be treated approximately independently of translations and rotations of the molecule provided the correct coordinate system is adopted⁴. Wider and more rigorous discussion of the topic may be found in the standard texts, (26) and (156).

3.3.1 Classical Description of Small Vibrations

The Newtonian equations of motion for a vibrating molecule composed of N atoms may be expressed in Lagrangian form⁵ as

$$\frac{d}{dt} \left(\frac{\partial L}{\partial \dot{q}_j} \right) - \frac{\partial L}{\partial q_j} = 0 \quad j = 1, 2, \dots, n \quad (3.31)$$

The *Lagrangian* $L = T - V$ is a function of the kinetic energy, T , and the potential energy, V , defined with respect to the set of n generalised coordinates, q_j . It is convenient to choose q_j to be the $3N$ cartesian *displacement* coordinates of each of the N atoms about their equilibrium positions and to weight each coordinate by the square root mass of the respective atom. The q_j 's in this case are referred to as *mass weighted* cartesian displacement coordinates. The kinetic energy of the vibrating system may thus be expressed as

$$T = \frac{1}{2} \sum_{i=1}^{3N} \dot{q}_i^2 \quad (3.32)$$

We consider conservative systems in which the potential energy is a function of position only and we assume all displacements to be small. The potential energy may therefore be expanded in a Taylor series about equilibrium, retaining only the lowest order terms, as

$$V(q_1, \dots, q_n) = V(q_{01}, \dots, q_{0n}) + \sum_{i=1}^{3N} \left(\frac{\partial V}{\partial q_i} \right)_0 q_i + \frac{1}{2} \sum_{i,j=1}^{3N} \left(\frac{\partial^2 V}{\partial q_i \partial q_j} \right)_0 q_i q_j + \dots \quad (3.33)$$

Linear terms in q_i vanish automatically since by definition at equilibrium the generalised forces acting on the system are zero which requires

$$\left(\frac{\partial V}{\partial q_i} \right)_0 = 0 \quad i = 1, 2, \dots, 3N \quad (3.34)$$

⁴ See (156), chapter 11, for rigorous treatment of the separation of rotation and vibration of a molecule

⁵ General treatment may be found in (44).

CHAPTER 3. INELASTIC NEUTRON SCATTERING

The first term in Eq. (3.33) is also made to vanish by shifting the arbitrary zero of potential to coincide with the equilibrium potential to leave just the quadratic terms as the first approximation to V , so that

$$V = \frac{1}{2} \sum_{i,j=1}^{3N} f_{ij} q_i q_j \quad (3.35)$$

where the f_{ij} 's are symmetric coefficients, i.e. $f_{ij} = f_{ji}$, given by

$$f_{ij} = \left(\frac{\partial^2 V}{\partial q_i \partial q_j} \right)_0 \quad (3.36)$$

The Lagrangian, L , may be re-expressed in terms of Eq. (3.32) and Eq. (3.35) as

$$L = \frac{1}{2} \sum_{i=1}^{3N} \dot{q}_i^2 - \frac{1}{2} \sum_{i,j=1}^{3N} f_{ij} q_i q_j \quad (3.37)$$

and substituted into Eq. (3.31) to yield the set of $3N$ equations of motion

$$\ddot{q}_j + \sum_{i=1}^{3N} f_{ij} q_i = 0 \quad j = 1, 2, \dots, 3N \quad (3.38)$$

These are second order differential equations which are satisfied by an oscillatory solution of the form

$$q_i = R A_i e^{-i\lambda \frac{1}{2} t + \epsilon} \quad (3.39)$$

where A_i gives the amplitude of oscillation for each coordinate, q_i , λ is introduced as a constant related to the frequency of oscillation and ϵ is an additional phase. Substitution of Eq. (3.39) into Eqs. (3.38) leads to the following $3N$ homogenous linear algebraic equations in the unknown amplitudes A_i ,

$$\sum_{i=1}^{3N} (f_{ij} - \delta_{ij} \lambda) A_i = 0 \quad j = 1, 2, \dots, 3N \quad (3.40)$$

in which δ_{ij} is the Kronecker delta symbol. For these equations to have a non trivial solution the determinant of the coefficients must vanish, i.e.,

$$\begin{vmatrix} f_{11} - \lambda & f_{12} & \dots & f_{1,3N} \\ f_{21} & f_{22} - \lambda & \dots & f_{2,3N} \\ \dots & \dots & \dots & \dots \\ f_{3N,1} & f_{3N,2} & \dots & f_{3N,3N} - \lambda \end{vmatrix} = 0 \quad (3.41)$$

CHAPTER 3. INELASTIC NEUTRON SCATTERING

Eq. (3.41) is known as the *secular equation*⁶ and gives a $(3N)^{th}$ order polynomial in λ whose $3N$ roots are the *eigenvalues* λ_k . For a given λ_k Eq. (3.40) may be solved to give a non unique set of amplitudes A'_{ik} . A unique set, l_{ik} , may be found by imposing the normalisation condition

$$l_{ik} = \frac{A'_{ik}}{[\sum_i (A'_{ik})^2]^{\frac{1}{2}}} \quad (3.42)$$

The physical amplitudes of oscillation, A_{ik} , are proportional to the l_{ik} 's via a set of constants, K_k , ($A_{ik} = K_k l_{ik}$), that are dependent on the total energy of the system. Assuming knowledge of the coefficients, f_{ij} , which in this particular coordinate system correspond to mass weighted harmonic force constants, the vibrations of the molecule may be fully described by

$$q_i = \Re \sum_{k=1}^{3N} l_{ik} K_k e^{-i\lambda_k^{\frac{1}{2}} t + \epsilon_k} \equiv \sum_{k=1}^{3N} l_{ik} K_k \cos(\lambda_k^{\frac{1}{2}} t + \epsilon_k) \quad (3.43)$$

The constants K_k and ϵ_k depend on the initial conditions, i.e. the starting values of q_i and \dot{q}_i .

3.3.2 Normal Coordinates and Zero Frequencies

The general solution, Eq. (3.43), to the equations of motion set up in section 3.3.1 describes $3N$ modes of simple harmonic oscillation of the atoms each with a characteristic frequency $\lambda_k^{\frac{1}{2}}/2\pi$. However since our definition of the potential energy, Eq. (3.35), depends only on the internal configuration of the molecule it can be shown (see (156), chapter 2.6) that six of the roots, λ_k , of the secular equation, see Eq. (3.41), must be identically zero. These so called *zero frequencies* correspond to the three translational and three rotational modes of the entire molecule. The remaining $(3N - 6)$ roots correspond to the $(3N - 6)$ free vibrational modes of the molecule known as the *normal modes*.

From the above description it is clear that the generalised coordinates, q_i , employed in section 3.3.1 do not compose a minimum basis set. There always exists a set of $(3N-6)$ independent generalised coordinates, Q_k , which express the *normal modes* such that one finite root of the secular equation, λ_k is entirely associated with just one coordinate. The

⁶Justification of this technique may be found in standard mathematics books dealing with eigenvalue problems, e. g. see (89) chapter 6.

CHAPTER 3. INELASTIC NEUTRON SCATTERING

minimum set of Q_k is known as the *normal coordinates* and is defined such that

$$Q_k = \Re K_k e^{-i\lambda_k^{\frac{1}{2}} t + \epsilon_k} \equiv K_k \cos(\lambda_k^{\frac{1}{2}} t + \epsilon_k) \quad k = 1, 2, \dots, (3N - 6) \quad (3.44)$$

By comparison with Eq. (3.43) it is apparent that coefficients l_{ik} determine the linear combination of the normal coordinates, Q_k , which constitute the mass weighted generalised coordinates, q_i . Eq. (3.43) may therefore be rewritten as

$$q_i = \sum_{k=1}^{(3N-6)} l_{ik} Q_k \quad i = 1, 2, \dots, 3N \quad (3.45)$$

Since by definition the normal coordinates are orthogonal the transformation represented by the l_{ik} 's is also orthogonal and due to the condition in Eq. (3.42) normalised. This means the inverse transformation $(l^{-1})_{ki}$ is simply obtained by

$$(l^{-1})_{ki} = l_{ik} \quad (3.46)$$

Normal coordinates may thus be expressed in terms of the mass weighted cartesian displacement coordinates by

$$Q_k = \sum_{i=1}^{3N} l_{ki} q_i \quad k = 1, 2, \dots, (3N - 6) \quad (3.47)$$

3.3.3 Quantum-Mechanical Considerations

The motion of atoms in a molecule may be described by inserting the appropriate total wave equation, ψ , into Schrödinger's equation and solving for the wave function, i.e.

$$\mathcal{H}\psi = E\psi \quad (3.48)$$

It may be shown (see (156), chapter 11) that the total wave function, ψ , can be approximately treated as the product of three separate equations, one for vibration, translation and rotation.

$$\psi \cong \psi_V \psi_T \psi_R \quad (3.49)$$

The vibrational part, ψ_V , is a function of the displacement coordinates which are chosen for convenience to be the normal coordinates as described in section 3.3.2. By substituting

CHAPTER 3. INELASTIC NEUTRON SCATTERING

Eq. (3.45) into Eq. (3.35) the potential energy may be expressed in terms of normal coordinates

$$\begin{aligned} V &= \frac{1}{2} \sum_{k=1}^{(3N-6)} \left(\sum_{i,j=1}^{3N} l_{ik} l_{jk} f_{ij} \right) Q_k^2 \\ &= \frac{1}{2} \sum_{k=1}^{(3N-6)} \lambda_k Q_k^2 \end{aligned} \quad (3.50)$$

The kinetic energy is of the same form as Eq. (3.32)

$$T = \frac{1}{2} \sum_{i=1}^{3N} \dot{q}_i^2 = \frac{1}{2} \sum_{k=1}^{(3N-6)} \dot{Q}_k^2 \quad (3.51)$$

Notice that neither expression contains cross terms in Q_k which is the property of normal coordinates. The time independent *Hamiltonian* operator of Eq. (3.48) may thus be written as a differential operator for each individual normal coordinate, Q_k , as

$$\mathcal{H} = -\frac{1}{2} \sum_{k=1}^{(3N-6)} \left(\frac{h^2}{4\pi^2} \frac{\partial^2}{\partial Q_k^2} - \lambda_k Q_k^2 \right) \quad (3.52)$$

whose stationary states are those of the simple harmonic oscillator

$$E = \sum_{k=1}^{(3N-6)} E_k = \frac{h}{4\pi} \sum_{k=1}^{(3N-6)} \lambda_k^{\frac{1}{2}} \left(n + \frac{1}{2} \right) \quad n = 0, 1, 2, \dots, \quad (3.53)$$

in which $\lambda_k^{\frac{1}{2}}$ is related to the wave number, ν_k , of the k^{th} normal mode via

$$\lambda_k = 4\pi^2 c^2 \nu_k^2 \quad (3.54)$$

The corresponding solutions to the wave function are given by

$$\psi_k(\xi_k) = (2^n n! \pi^{\frac{1}{2}})^{-\frac{1}{2}} e^{-\frac{1}{2} \xi_k^2} H_n(\xi_k), \quad \xi_k = \sqrt{\frac{4\pi^2 c \nu_k}{h}} Q_k \quad (3.55)$$

where H_n are the Hermite polynomials. There is one independent solution, ψ_k , per normal coordinate, Q_k , hence the vibrational wave function, ψ , has effectively been separated into the product

$$\psi_V = \psi_1(Q_1), \psi_2(Q_2), \dots, \psi_{3N-6}(Q_{3N-6}) \quad (3.56)$$

The advantage of using normal coordinates is now apparent since Schrödinger's equation for molecular vibrations separates into $(3N - 6)$ independent wave equations of the form

$$-\frac{1}{2} \left[\frac{h^2}{4\pi^2} \frac{\partial^2}{\partial Q_k^2} - \lambda_k Q_k^2 - h c \nu_k \left(n + \frac{1}{2} \right) \right] \psi_k(Q_k) = 0 \quad n = 1, 2, \dots, \quad (3.57)$$

CHAPTER 3. INELASTIC NEUTRON SCATTERING

It has been demonstrated via quantum mechanical arguments that, by using normal coordinates, the vibrations of a molecule may be resolved into $(3N - 6)$ *uncoupled* one-dimensional simple harmonic oscillators. In this context, *uncoupled* means that if a system is set oscillating in a particular normal mode no other modes will be excited. This is a central assumption in normal mode analysis.

3.3.4 Temperature and the Mean-Squared-Amplitude Matrix

The effect of temperature in the classical picture is to alter the amplitude of the molecular vibrations. This translates to changing the initial conditions via the constants K_k in Eq. (3.43) and Eq. (3.44). In the quantum mechanical sense the temperature dictates the probability distribution over all energy states of an ensemble of equivalent harmonic oscillators representing a particular normal mode. It, therefore, influences the ensemble expectation values of observables.

We consider the expectation values of the squared displacements of the normal coordinates, $\langle Q_k^2 \rangle$. As was demonstrated in section 3.3.3, oscillation about a normal coordinate may be treated as simple harmonic and entirely independent of all other oscillations. $\langle Q_k^2 \rangle$ may thus be obtained from the *canonical*⁷ average over all energy states of the simple harmonic oscillator and is expressed as

$$\langle Q_k^2 \rangle = \frac{h}{8\pi^2 c \nu_k} \coth \left(\frac{h c \nu_k}{2 k_B T} \right) \quad (3.58)$$

(The derivation of this equation is given in appendix B)⁸.

These expectation values may be considered to be the diagonal elements of the diagonal matrix, δ , such that

$$\delta_{kk} = \langle Q_k^2 \rangle \quad ; \quad \delta_{kl} = \langle Q_k Q_l \rangle = 0 \quad (3.59)$$

Considering the transformation of Eq. (3.47) we see that

$$\delta_{kk} = \sum_{i,j=1}^{3N} l_{ik} l_{jk} \langle q_i q_j \rangle \quad (3.60)$$

⁷Weakly interacting systems in equilibrium with a large reservoir at temperature, T , are said to be in their canonical state.

⁸Note that the reduced mass term, μ , in appendix B is here implicit in the definition of the normal coordinates, Q_k , which are mass weighted. Also note that ν_k in Eq. (3.58) is the wave number with dimensions $[L^{-1}]$ but ω_0 in appendix B represents angular frequency.

CHAPTER 3. INELASTIC NEUTRON SCATTERING

Adopting the notation $M_{ij} = \langle q_i q_j \rangle$ and using the transformation of Eq. (3.45) the inverse relation is obtained

$$\begin{aligned} M_{ij} &= \sum_{k=1}^{(3N-6)} l_{ik} l_{jk} \langle Q_k Q_k \rangle \\ &= \sum_{k=1}^{(3N-6)} l_{ik} l_{jk} \delta_{kk} \end{aligned} \quad (3.61)$$

The symmetric matrix, M , is known as the mean-squared-amplitude matrix or *vibrational correlation function*. It is extremely useful since it fully describes all many-body correlations in the vibrating system at a given temperature, T , and may be expressed in a chosen generalised coordinate system which, for example, may be simple cartesian displacements.

3.3.5 Internal coordinates

A specific subset of the generalised coordinates, q_i , are the internal coordinates, S_t . They do not necessarily present a minimum set as do the normal coordinates but are physically the easiest to interpret since they correspond to internal structure distortions of the molecule. As such they are unaffected by translations and rotations of the molecule as a whole and provide a coordinate basis that does not mix with the basis describing overall motion. (That is not the case for example with cartesian displacement coordinates). The four principle types of internal coordinate are depicted in figure 3.2. The arrows in figure 3.2 denote displacement vectors for each atom in the directions which cause the greatest increase in the respective S_t . The magnitudes of these vectors are equal to the increase in S_t produced per unit displacement of the atom in this most effective direction. (Calculation of these vectors depends on the geometry of the molecule and is trivial; see (156), pp.55-61). The n internal coordinates may always be written as linear combinations of the $3N$ cartesian displacement coordinates, ξ_i , such that

$$S_t = \sum_{i=1}^{3N} B_{ti} \xi_i \quad t = 1, 2, \dots, n \quad (3.62)$$

in which the coefficients B_{ti} define the above-mentioned displacement vectors in cartesian coordinates.

An important advantage of casting the vibrational problem in internal coordinates is that the expression for the potential energy

$$V = \frac{1}{2} \sum_{t,t'} F_{tt'} S_t S_{t'} \quad t, t' = 1, 2, \dots, n \quad (3.63)$$

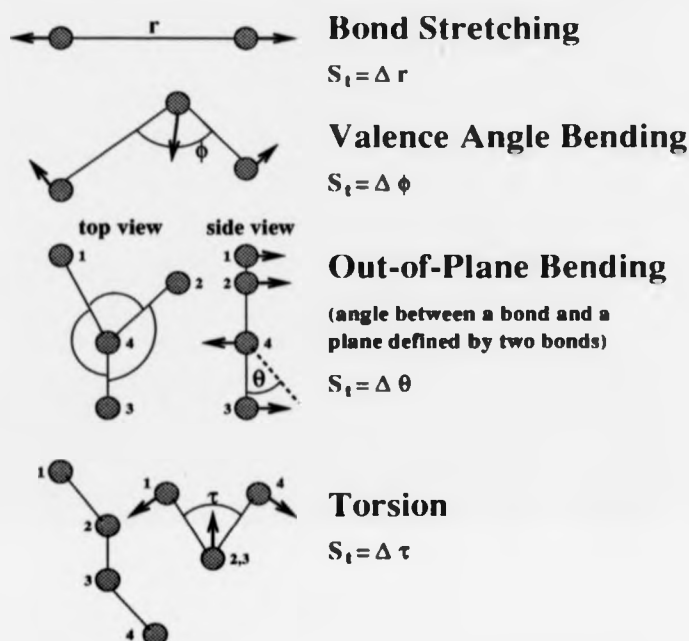


Figure 3.2: The four principle types of *internal coordinate*. For the out-of-plane bending the dashed line represents the position the 3-4 bond would occupy if the distorted molecule were rotated and translated to return atoms 1, 2 and 4 to their original positions.

yields coefficients, $F_{ii'}$, that are chemically significant: the harmonic force constants of bond stretches, angle bends etc.. This makes intuitive estimates possible where the $F_{ii'}$ are not known.

3.3.6 The Wilson GF method

A concise formalism for expressing the vibrational problem was developed in 1939 by Wilson, (155), and has been widely adopted since. A set of quantities, $G_{ii'}$, are defined by

$$G_{ii'} = \sum_{s=1}^{3N} \frac{1}{m_s} B_{si} B_{s i'} \quad i, i' = 1, 2, \dots, n \quad (3.64)$$

in which m_s is the mass of the s^{th} atom and B_{si} are the coefficients introduced in Eq. (3.62) relating the internal coordinates, S_i , to the cartesian displacement coordinates, ξ_s . The

CHAPTER 3. INELASTIC NEUTRON SCATTERING

physical significance of $G_{tt'}$ is evident from the expression for the kinetic energy in terms of internal coordinates in which G assumes the role of an inverse mass matrix

$$T = \frac{1}{2} \sum_{tt'} (G^{-1})_{tt'} \dot{S}_t \dot{S}_{t'} \quad t, t' = 1, 2, \dots, n \quad (3.65)$$

in which the quantities $(G^{-1})_{tt'}$ are related to the $G_{tt'}$ via the equations

$$\sum_{t'} (G^{-1})_{tt'} G_{t't''} = \delta_{tt''} \quad ; \quad \sum_{t'} G_{tt'} (G^{-1})_{t't''} = \delta_{tt''} \quad (3.66)$$

where $\delta_{tt''}$, the Kronecker delta, is unity if $t = t''$ and zero otherwise.

Matrix and vector notation is now adopted for convenience. The quantities $G_{tt'}$ and $F_{tt'}$ (see Eq. (3.63)) are defined as the elements of the matrices G and F respectively. S and \dot{S} are column matrices composed of the internal coordinates, S_t , and their time derivatives, \dot{S}_t . The Lagrangian is written as

$$L = \frac{1}{2} (\dot{S}^\dagger G^{-1} \dot{S} - S^\dagger F S) \quad (3.67)$$

in which the superscript \dagger denotes matrix transpose. Substitution of this expression into Eq. (3.31) and then premultiplying by G yields the equations of motion in the form

$$\ddot{S} + GFS = 0 \quad (3.68)$$

where 0 is the zero matrix. As in section 3.3.1, a trial periodic solution for S analogous to Eq. (3.39) produces n homogenous linear equations in the unknown amplitudes A_{tk} ; i.e.,

$$(GF - E\lambda_k)A_k = 0 \quad (3.69)$$

in which A_k is the k^{th} column of the matrix $A = ||A_{tk}||$. This yields the secular equation

$$|GF - E\lambda_k| = 0 \quad (3.70)$$

(where E is the unit matrix) which may be solved for the n eigenvalues λ_k . As remarked in section 3.3.2 the normal mode frequencies may be identified as $\lambda_k^{1/2}/2\pi$.

In order to describe the normal coordinates, Q_k , (denoted by the column matrix Q), in terms of the internal coordinates S the transformations L and K are required such that

$$S = LQ \quad ; \quad Q = KS \quad (3.71)$$

CHAPTER 3. INELASTIC NEUTRON SCATTERING

Note that $\mathbf{K} = \mathbf{L}^{-1}$. The k^{th} column of \mathbf{L} , \mathbf{L}_k , is related to the amplitudes \mathbf{A}_k by a simple coefficient which means that the \mathbf{L}_k 's must also satisfy Eq. (3.69), i.e.

$$(\mathbf{GF} - \mathbf{E}\lambda_k)\mathbf{L}_k = 0 \quad (3.72)$$

but subject to the normalisation condition

$$\lambda = \mathbf{L}^\dagger \mathbf{F} \mathbf{L} \quad (3.73)$$

in which λ is the diagonal matrix

$$\lambda = \text{diag}(\lambda_1, \lambda_2, \dots, \lambda_n) \quad (3.74)$$

This condition is obtained by requiring that the potential energy, V , is equivalent whether expressed with respect to internal coordinates, \mathbf{S} , as in Eq. (3.63), or normal coordinates. The inverse transformation \mathbf{K} may be found directly by solving the linear equations analogous to Eq. (3.69) and Eq. (3.72)

$$(\mathbf{FG} - \mathbf{E}\lambda_k)\mathbf{K}_k = 0 \quad (3.75)$$

subject to the normalisation condition

$$\mathbf{F} = \mathbf{K}^\dagger \lambda \mathbf{K} \quad (3.76)$$

Note that the transformations \mathbf{L} and \mathbf{K} are *not* composed of the dimensionless elements l_{ik} of Eq. (3.42) and are *not* orthonormal (thus $\mathbf{K} = \mathbf{L}^\dagger$ does not hold in this case). Section 3.43 dealt with the particular case of mass-weighted generalised coordinates, q_i , transforming to the mass-weighted normal coordinates, (both having dimensions $[M^{\frac{1}{2}}L]$). In the present case the internal coordinates, \mathbf{S} , have dimensions of length only and consequently \mathbf{L} and \mathbf{K} have dimensions, in mass, of $[M^{-\frac{1}{2}}]$ and $[M^{\frac{1}{2}}]$ respectively.

Knowledge of the transformation, \mathbf{L} , from normal to internal coordinates, allows the *vibrational correlation function*, (VCF, see section 3.3.4), to be expressed in the internal coordinate system

$$\mathbf{M}_{int} = \mathbf{L} \delta \mathbf{L}^\dagger \quad (3.77)$$

in which δ is the diagonal matrix defined in Eq. (3.59) whose elements are the mean-squared-displacements of the normal coordinates. Perhaps more useful however is the VCF expressed

CHAPTER 3. INELASTIC NEUTRON SCATTERING

in the cartesian coordinate basis. From the relationship given in Eq. (3.62), and denoting the quantities B_{ti} by the matrix B , it is easy to derive

$$M_{\text{cart}} = B^{-1} L \delta (B^{-1} L)^{\dagger} = B^{-1} L \delta L^{\dagger} (B^{-1})^{\dagger} \quad (3.78)$$

It has been shown here how the Wilson GF method simplifies the expression of the vibrational problem when the coordinate basis used is that of internal coordinates. All of the vibrational motion of the molecule may then be conveniently expressed by the many-body VCF in terms of *non-mass-weighted* cartesian coordinates.

3.3.7 Inclusion of Symmetry - Group Theory

In many systems the inherent symmetry of the molecule may be used to considerably simplify the analysis. The mathematical tool for implementing this is *group theory*. Group theory⁹ may be applied to determine:

- the number, symmetry species and degeneracy of the normal modes
- the symmetry restrictions on the form of the F matrix
- a *minimum* coordinate basis which partially factorises the secular determinant

The latter point is dealt with in the next subsection.

The symmetry type of a molecule is identified by its *point group*. These are specific symmetry groups which leave at least one point in space fixed under all of the group *operations*. (Here we are concerned with the 32 *crystallographic point groups* which are the possible point symmetries that can occur in a repeated structure). The group operations act on the molecule in such a way as to leave it in a position indistinguishable from its original position. They comprise the symmetry classes of reflection, rotation, inversion, identity and combinations of the above. A group may be classified by its character; which provides a method of determining all the *irreducible representations* present in the group; the irreducible representations are essentially the *symmetry species* of the normal modes and have an associated degeneracy of

⁹ A useful practical text of the application of group theory to molecular vibrations is (77). Some familiarity with the common terms used in group theory is assumed.

CHAPTER 3. INELASTIC NEUTRON SCATTERING

1, 2 or 3 fold. (Knowledge of the symmetry species is instrumental in determining infrared and Raman selection rules which are significant when characterising observed frequencies in unassigned spectra). Thus, before any normal mode analysis need take place, it is possible to predict, from knowledge of the structure and point group of a given molecule, how many normal modes exist, which symmetry species each one belongs to and what the pattern of degeneracy is. (For more detail on determination of symmetry species of normal modes refer to appendix C).

Perhaps the most significant advantage of the application of group theory is that the permitted qualitative form of the F matrix can be predefined. Consideration of the symmetry of the molecule determines relationships connecting different elements of F and in some cases which elements are identically zero. This is particularly advantageous when the elements of F are not known exactly, which is frequently the case, since it considerably reduces the number of independent quantities to be determined. This is true even for molecules with low symmetry point groups.

The symmetry restrictions stem from the definition of the potential energy given in Eq. (3.63). (We confine ourselves here to the internal coordinate basis set). Under consideration is the effect of symmetry operations on the atomic displacements as distinct from the atomic configuration. The internal coordinates are acted upon individually by the group operations to create a set of allowed permutations. For example, it may be found that under a given group operation the bond stretch, $S_e = 1$ (in arbitrary units), permutes to the bond stretch $S_v = 1$ and upon further operation to $S_s = 1$. Since under all permutations the potential energy must be the same we have, from Eq. (3.63), when all other displacement are zero

$$V = \frac{1}{2} F_{ee} S_e S_e = \frac{1}{2} F_{vv} S_v S_v = \frac{1}{2} F_{ss} S_s S_s \quad (3.79)$$

which yields the relationship

$$F_{ee} = F_{vv} = F_{ss} \quad (3.80)$$

Similarly it may be found that the internal coordinate displacements $S_x = 1$ and $S_y = 1$ permute to $S_y = 1$ and $S_x = 1$ (with all other displacements zero). The condition,

$$V = \frac{1}{2}(F_{xx}S_xS_x + F_{yy}S_yS_y + 2F_{xy}S_xS_y) = \frac{1}{2}(F_{yy}S_yS_y + F_{xx}S_xS_x + 2F_{yx}S_yS_x) \quad (3.81)$$

therefore, produces the relationship

$$F_{xy} = F_{yx} \quad (3.82)$$

The above example demonstrates how a correspondence between elements of F may be constructed; in this way the total number of parameters defining the matrix may be significantly reduced.

3.3.8 Internal Symmetry Coordinates

A further practical advantage of the application of group theory to the vibrational problem is in the determination of yet another coordinate basis which partially factorises the secular determinant. This has the following advantages:

- The F matrix becomes block diagonalised and is therefore described by significantly fewer parameters than the arbitrary full matrix. This is *not* the same as restricting the form of the F matrix via symmetry as described in section 3.3.7.
- A minimum coordinate basis may be established. Minimum, in this context, means there are as many coordinates as normal modes. Thus, as well as being block diagonalised, the F matrix may, in some cases, be made smaller.
- The secular equation is easier to solve.

The new coordinates are conveniently described as a linear combination of the internal coordinates, S_i , discussed in section 3.3.5, (which are written in column matrix form as S); they are known as *internal symmetry coordinates* and are denoted by S' . The relation between the two sets of coordinates is expressed by the transform¹⁰ W such that

$$S' = WS \quad (3.83)$$

¹⁰Note that the transform W is denoted as U by Wilson *et al.* (156). It is changed here to avoid confusion with the mean-squared-displacement tensor, U , in other chapters.

CHAPTER 3. INELASTIC NEUTRON SCATTERING

Since S and S' have the same dimensions, W is dimensionless; it is also unitary so that

$$WW^\dagger = E \quad (3.84)$$

The effect of the transform W is to decompose the internal coordinate basis into its irreducible representations; that is to find linear combinations of the S_i that form non-mixing blocks under the point group operations. Each block is identified as belonging to one of the symmetry species, μ , ($\mu = \{A, B, E, T\}$), discussed in appendix C. The technique for determining the W matrix involves the use of projection operators and is discussed in appendix D.

The F and G matrices are changed to their *symmetrised* forms by the unitary transformations

$$\begin{aligned} F' &= WFW^\dagger \\ G' &= WGW^\dagger \end{aligned} \quad (3.85)$$

Hence

$$(GF)' = WGFW^\dagger \quad (3.86)$$

The secular equation is thus

$$|(GF)' - \lambda E| = 0 \quad (3.87)$$

$(GF)'$ is defined with respect to the irreducible representation of the internal coordinate basis and is consequently block diagonalised such that each block has an associated symmetry species, μ . The secular equation may therefore be more specifically written as

$$\begin{vmatrix} (GF)^{(\mu_1)} - E\lambda & 0 & 0 & 0 \\ 0 & (GF)^{(\mu_2)} - E\lambda & 0 & 0 \\ 0 & 0 & (GF)^{(\mu_3)} - E\lambda & 0 \\ 0 & 0 & 0 & etc. \end{vmatrix} = 0 \quad (3.88)$$

in which $(GF)^{(\mu)}$ represent the irreducible representations of GF . This block-diagonalisation results in the secular determinant being partially factorised.

One of the advantages, mentioned above, of using symmetry coordinates is that a minimum coordinate basis may be determined. If the internal coordinate basis, S , is over-defined, that

CHAPTER 3. INELASTIC NEUTRON SCATTERING

is, there are more than $(3N - 6)$ internal coordinates, the concept of *redundant* coordinates in the S' basis arises. This is frequently the case because complete internal coordinate sets are usually desired that include all the valence bond stretches, bends, torsions etc. present in a molecule. The symmetry species of the redundancies can be deduced by comparing the reduction of the internal coordinate basis (i.e., the symmetry species contained in that representation) with the reduction of the cartesian basis; the latter contains the symmetry species of the normal modes once the pure rotations and translations have been taken out. The redundant coordinates, S_{red} , may then usually be identified by inspection leaving the remaining $(3N - 6)$ coordinates forming a minimum set of internal symmetry coordinates, S_{min} , i.e.,

$$S' = \begin{pmatrix} S_{min} \\ S_{red} \end{pmatrix} \quad (3.89)$$

The rows and columns of the symmetrised G' matrix corresponding to the S_{red} should automatically vanish¹¹ after the transformation by W such that

$$G' = \begin{pmatrix} G_{min} & 0 \\ 0 & 0 \end{pmatrix} \quad (3.90)$$

where G_{min} is the $(3N - 6) \times (3N - 6)$ matrix acting on the minimum set of S_{min} . The same rows and columns of the F' matrix should be set to zero to obtain a minimum, block-diagonalised force constant matrix.

3.4 Inelastic Neutron Scattering Experiment

The INS experiments were performed using the UK pulsed neutron facility ISIS at the Rutherford Appleton Laboratory. Neutrons are produced on ISIS when $0.4\mu s$ proton pulses at $50 Hz$ from an $800 MeV$ proton synchrotron (design current $200\mu A$) are incident on a spallation target. The target, of either uranium-238 or tungsten, produces about 25 neutrons per incident proton with energies in the MeV range. These *epithermal* neutrons are slowed in four fluid moderators at three different temperatures (ambient H_2O , $100 K$ CH_4 and $20 K$ H_2)

¹¹ This is proved in (156), chapter 5.8.

CHAPTER 3. INELASTIC NEUTRON SCATTERING

and, after passing through beam-choppers (to prevent pulse overlap), are delivered to various neutron scattering instruments.

3.4.1 The TFXA spectrometer

The measurements reported here were taken using the *time-focused crystal analyser spectrometer*, TFXA, (103); see figure 3.3. TFXA is an inverted geometry spectrometer and therefore determines the incident neutron energy via time-of-flight over a known distance. A water-moderated white pulse of thermal neutrons is incident on the sample 12m from the source; back-scattered neutrons are then Bragg-diffracted from two pyrolytic graphite crystal analysers so that $\sim 4\text{meV}$ neutrons are selected from the white backscattered beam; beryllium filters serve to remove higher harmonics from the Bragg reflection. The $\sim 4\text{meV}$ neutrons are subsequently detected by two arrays of 16 high pressure ^3He filled detectors.

Energy resolution is effected since the very short time-span for generation of neutrons at the target produces a well defined spatial distribution of neutron energies within the incident pulse by the time it reaches the sample. The energy of the incident neutrons is therefore a function of the time of impact on the sample within each 50Hz cycle. A particular geometry is chosen for the spectrometer such that the time of flight between the sample and detector banks for a neutron of any energy is constant; this permits a broader band of neutron energies around 4meV to be admitted (thus enhancing the detected intensity) without adversely affecting the energy resolution. In this geometry, the sample is positioned in the same plane as the two detector arrays. The time taken, t_a , for neutrons to traverse the distance from the sample to a specific point on the crystal analyser and back to the plane of the detector is thus independent of the neutron energy and may be shown to be, (143),

$$t_a = \frac{4sdm}{h} \quad (3.91)$$

where s is the separation of the analyser plane from the sample-detector plane (as shown in figure 3.3), d is the separation of the Bragg planes in the graphite crystal, m is the neutron mass and h is Plancks constant. The response , $S(\mathbf{Q},\omega)$, of the sample as a function of the energy transfer at the sample (i.e. $E - E' = E_{\text{incident}} - 4\text{meV}$) may thus be obtained from

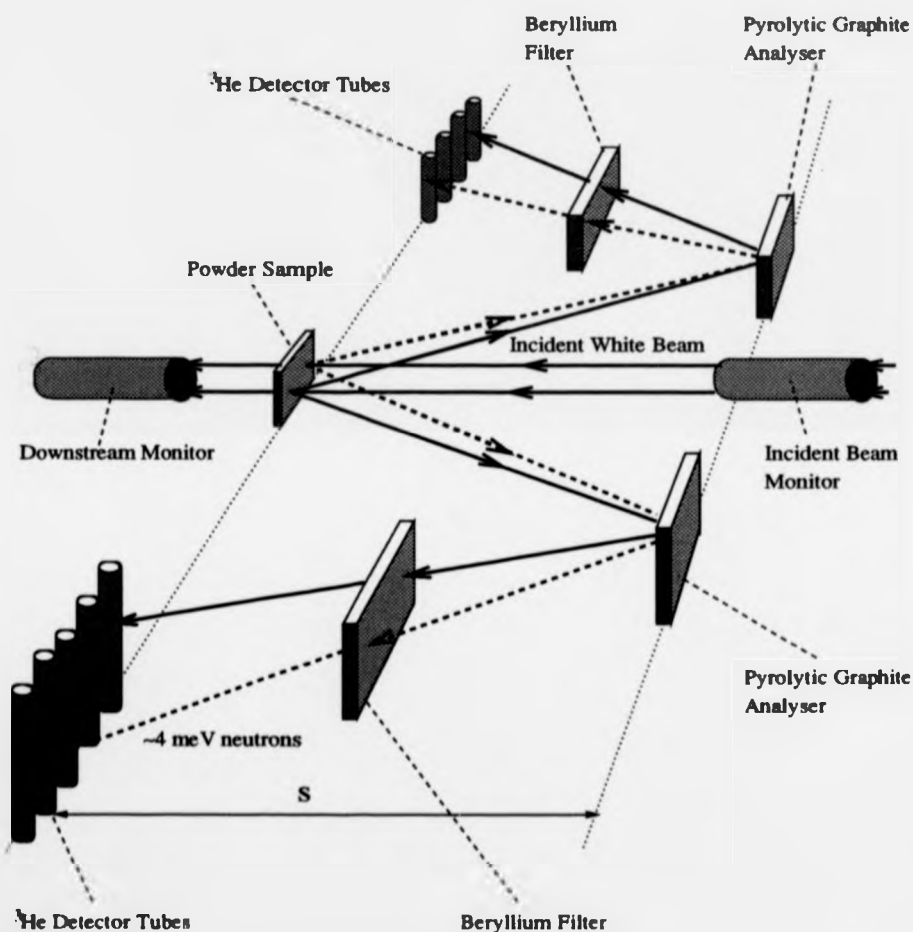


Figure 3.3: Schematic diagram of the TFXA spectrometer at the ISIS pulsed neutron facility, Rutherford Appleton Laboratory, U.K.. The spectrometer makes use of a particular inverted geometry in which the time of flight of neutrons of all energies (chosen to constitute a band about 4 meV) is constant for neutron trajectories from the sample to the detectors, via one point on the crystal analyser; this condition is essential for energy resolution.

CHAPTER 3. INELASTIC NEUTRON SCATTERING

the detected intensity versus the time of impact on the detector array. A complete spectrum is thus collected in every 50Hz cycle and cumulated with the detector counts from previous cycles to reduce noise.

The intrinsic energy resolution is dictated by the crystal analyser and is consequently the differential of Bragg's law, ($\lambda = 2d \sin \theta_B$):

$$\frac{\Delta E}{E} = 2 \frac{\Delta \lambda}{\lambda} = 2 \left\{ [\cot \theta_B \Delta \theta_B]^2 + \left[\frac{\Delta d}{d} \right]^2 \right\}^{\frac{1}{2}} \quad (3.92)$$

where θ_B is the Bragg angle. For $\theta_B \rightarrow 90^\circ$ the resolution tends to zero. The TFXA spectrometer is set up such that $2\theta_B = 135^\circ$, which gives an energy transfer resolution equal to $\sim 1.5\%$ over an energy range from 5meV to 2eV which adequately covers most lattice and molecular vibrational energies. The calibration is quoted as being $\pm 4\text{cm}^{-1}$ at energy transfers of 150meV ($\cong 1200\text{cm}^{-1}$).

The low final neutron energy of $\sim 4\text{meV}$ utilised on the TFXA spectrometer is selected so that the detected intensity of the measured response function, $S(\mathbf{Q}, \omega)$, is optimised. This may be understood by reference to figure 3.4 in which the ideal two-dimensional response function of a simple harmonic oscillator is depicted. In the limit $\hbar\omega \gg 2k_B T$ (which holds at low temperature for optical molecular vibrations and many lattice vibrations, see section 3.2.5) the response function may be described by Eq. (3.26). For each inelastic excitation, (i.e. $n \geq 1$), the $S(\mathbf{Q}, \omega)$ curves for constant ω (i.e. $\omega = n\omega_0$) as a function of \mathbf{Q} exhibit common maxima occurring at \mathbf{Q}_{opt} . Via differentiation of Eq. (3.26) it may be seen that $Q_{opt}^2 U^2 = 1$ which, for oscillators of proton mass, translates to very low final neutron energies; hence the selected final energy of $\sim 4\text{meV}$ for the TFXA spectrometer. A drawback of intensity optimisation is that strong phonon wings are usually present in experimental spectra because of the need for the relatively large momentum transfer, \mathbf{Q}_{opt} ; the strength of phonon wings increases as \mathbf{Q} is increased or as the temperature is raised, see section 3.2.6.

The expression for the overtone sequence of an isotropic harmonic oscillator on an intensity optimised spectrometer is (45)

$$S(\mathbf{Q}, \omega)_n = \frac{n^n}{n!} \left\{ \frac{1}{\mu} \exp \left(\frac{1}{\mu} \right) \right\}^n \quad (3.93)$$

where μ is the oscillator mass. Eq. (3.93) is instructive because it indicates that the overtone

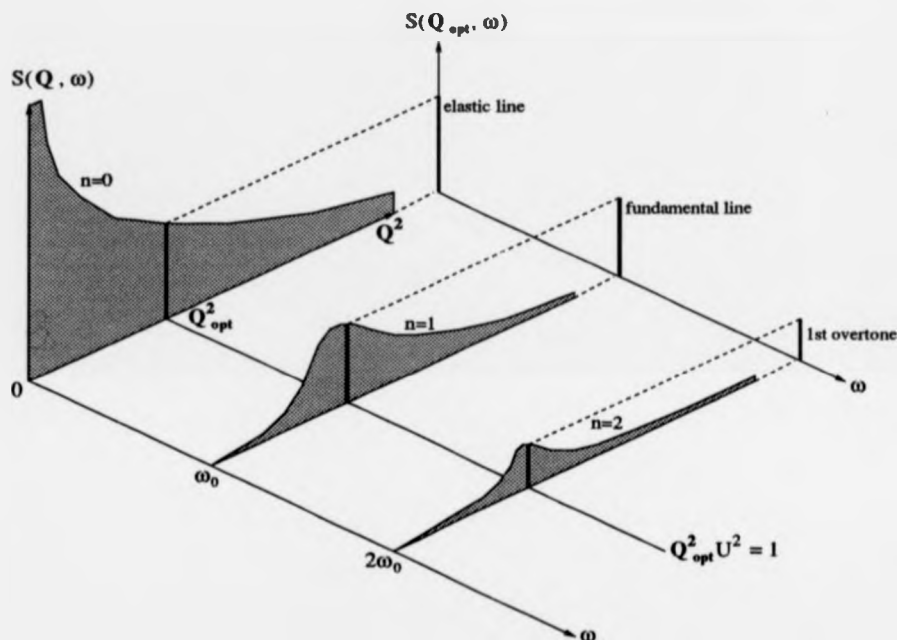


Figure 3.4: The ideal two-dimensional response function, $S(\mathbf{Q}, \omega)$, of a simple harmonic oscillator vibrating at angular frequency ω_0 and the projection on to the ω axis for intensity-optimised momentum transfer, Q_{opt} . The curves may be generated from the approximate description for the response function in the limit when $\hbar\omega \gg 2k_B T$, see Eq. (3.26) and interpreted such that $n = 0$ is the elastic response, $n = 1$ the fundamental excitation and $n \geq 2$ the consecutive overtone excitations. From Eq. (3.26) it may be seen that the maxima of these excitation curves occur such that $Q_{opt}^2 U^2 = 1$; for an oscillator mass equivalent to that of a single proton this corresponds to low final neutron energies for inverted geometry spectrometers (i.e. $\sim 4\text{meV}$ on TFXA). The function projected on to the ω axis is the idealised spectrum as measured on a perfect, intensity optimised spectrometer. (To determine the experimental spectrum, the instrument function for the given spectrometer should be convoluted with the delta functions from the ideal spectrum.)

CHAPTER 3. INELASTIC NEUTRON SCATTERING

sequence for $\mu = 1$, the proton mass, is extensive. However, for $\mu > 1$, the overtone sequence diminishes rapidly with increasing μ ; this is significant since it implies that low frequency oscillations, whose reduced mass of oscillation is usually greater than unity, (i.e. skeletal modes etc.), do not have strong overtones that complicate the spectrum at higher frequencies.

3.4.2 Samples for INS experiment

Inelastic neutron scattering measurements were performed on the following four samples:

1. Zinc (II) tetraimidazole perchlorate, ($Zn(imid)_4(ClO_4)_2$), at 20K.

The perchlorate anion is believed to be well decoupled dynamically from the zinc tetraimidazole cation and has a low absorption cross section.

2. Boron-11 enriched zinc (II) tetraimidazole borofluorate, ($Zn(imid)_4(^{11}BF_4)_2$), at 20K.

This sample was chosen to determine the effect on the vibrational spectrum of changing the anion from perchlorate to borofluorate. This is a test of the sensitivity of the intermolecular modes to changes in the crystal field; small changes would support the assertion that the anion is well decoupled from the cation. Naturally occurring boron could not be used since the isotope boron-10 (20% abundant) has an immense absorption cross section for thermal neutrons of 3800 barns; this would screen any scattering signal. The borofluorate anion was therefore boron-11 enriched to 99% isotopic purity; (the absorption cross section of boron-11 is 0.006 barns).

3. Zinc (II) tetraimidazole- d_1 perchlorate, ($Zn(imid-d_{(1)})_4(ClO_4)_2$), at 20K.

The cation is deuterated at the nitrogen position on each of the four imidazole branches. Shifts in the vibrational frequencies and relative changes in the intensity of vibrational peaks in the spectrum compared to the undeuterated sample should aid with assignment of peaks and help with the development of a model force field. Due to the relatively small change in mass from deuteration the frequency shifts would probably only be detectable for internal imidazole modes. The scattering cross section of deuterons (7.6 barns) is an order of magnitude smaller than that of protons (81.7 barns) and so a weaker signal was anticipated; measurements were recorded over correspondingly longer time

CHAPTER 3. INELASTIC NEUTRON SCATTERING

periods.

4. Zinc (II) tetraimidazole-3 $d_{(2,4,5)}$ perchlorate, ($Zn(imid-3d_{(2,4,5)})_4(ClO_4)_2$) at 20K.

The cation is deuterated at the three carbon positions on each of the four imidazole branches; the nitrogen position is protonated. In this case more significant shifts might be expected in the vibrational spectrum, including small shifts in the low frequency skeletal modes of the molecule. Again, the shifts and relative intensity changes in the vibrational peaks should help to develop and corroborate a model dynamical force field for the undeuterated cation. The measurement time period was again increased due to the further reduction in the proportion of protons in the sample.

All samples were in powder form and mounted in the neutron beam in approximately 5cm \times 1cm \times 1cm folded aluminium foil sachets. The mass of sample required per measurement was of the order of a few grams. Exposure time ranged from 24 hours for samples 1 and 2, to 48 hours for sample 4.

The following paragraphs detail the chemical preparation of the samples.

3.4.2.1 Preparation of $Zn(imid)_4(ClO_4)_2$

Firstly, hydrated zinc (II) perchlorate, ($Zn(ClO_4)_2 \cdot 6H_2O$) was prepared:

- 0.6 moles of 11.6M perchloric acid, $HClO_4$, (Merck), was added to 40ml of distilled water.
- Zinc oxide, ZnO , (Merck), was added to slight excess i.e. approximately 0.3 moles.
- The solution was filtered to yield white crystals.

Zinc (II) tetraimidazole perchlorate was then prepared according to the prescription of Reedijk, (115)

- 0.16 moles of hydrated zinc (II) perchlorate was dissolved in 160ml of ethanol.
- 1.13 moles of 99%+ pure imidazole (Sigma) was dissolved in 160ml of ethanol with 48ml of triethyl orthoformate as a dehydrating agent.

CHAPTER 3. INELASTIC NEUTRON SCATTERING

- The two solutions were mixed together and 370ml of dry diethyl ether added. The molar ratio of zinc to imidazole was 1:7 which is in excess of the 1:4 ratio required for the product via stoichiometry. After standing for 1 day in refrigeration, white monoclinic crystals appeared. The crystals were filtered, washed 3 times in dry diethyl ether and then thoroughly dried *in vacuo*.

The crystal yield was 42%. The product was checked via mass spectroscopy and infrared and Raman spectroscopy.

3.4.2.2 Preparation of $Zn(imid)_4(^{11}BF_4)_2$

Boron-11 enriched hydrated zinc (II) borofluorate, ($Zn(^{11}BF_4)_2 \cdot 6H_2O$), was specially prepared and obtained from CENTRONICS Plc. with an isotopic purity of 99%.

Boron-11 enriched zinc (II) tetraimidazole borofluorate was then prepared using this compound with the same prescription as for the perchlorate sample. The crystal yield after filtering and drying was 60%.

3.4.2.3 Preparation of $Zn(imid-d_{(1)})_4(ClO_4)_2$

Crystals of Zinc (II) imidazole perchlorate were washed three times in cold D_2O and dried *in vacuo* and sealed under nitrogen.

3.4.2.4 Preparation of $Zn(imid-3d_{(2,4,5)})_4(ClO_4)_2$

Firstly, imidazole- $3d_{(2,4,5)}$ was prepared¹² according to the prescription of Majoube, (85)

- D_2O was condensed on to imidazole crystals in a glass ampule under vacuum. The molar ratio of D_2O to imidazole was 20:1 which gives a deuteron to proton ratio of 10:1.
- The ampule was sealed with a nitrogen counter pressure of 20 bar and heated at $210 \pm 30^\circ C$ for 3 hours. At this stage the imidazole was anticipated to be $\sim 90\%$ deuterated at all positions.

¹² The author would like to acknowledge the kind assistance of Dr. Marianne Hegemann and Prof. J. Grobe at the Universität Münster, Germany.

CHAPTER 3. INELASTIC NEUTRON SCATTERING

- The D_2O/H_2O solution was condensed off to leave white imidazole-4d crystals. These were checked for deuteration via infrared spectroscopy and nuclear magnetic resonance.
- The crystals were washed three times in pure water to effect protonation at the nitrogen-1 position of imidazole and sealed under nitrogen. The washing should be done quickly to avoid additional exchange at the carbon-2 position. The product, imidazole-3d_(2,4,5), was confirmed by infrared spectroscopy.

Finally, zinc (II) tetraimidazole-3d_(2,4,5) perchlorate was prepared using the 3d-deuterated imidazole with the same prescription as for the undeuterated case and stored under nitrogen. For this preparation, the zinc (II) perchlorate used was obtained commercially (Alfa, Ventron).

3.4.3 Analytical Software - CLIMAX

The experimental INS spectra were analysed using the CLIMAX software package from G. J. Kearley et al., (67), (68). The object of the analysis was to obtain the cartesian mean-squared-displacement vectors of every atom in every normal mode of the zinc tetraimidazole complex. In other words, the output of CLIMAX is assumed to define the *vibrational correlation function* (VCF) of the complex, see section 3.3.4, and thus entirely describe the vibrational motion of the molecule.

The analysis centres on the least squares refinement of a harmonic force field for a proposed model that is supposed to reflect the dynamic behaviour of the subject molecule. (This is discussed in section 3.3.5). From a proposed force field, the tentative VCF of the model may be extracted via normal mode analysis, which is made tractable by using the Wilson GF method, (see section 3.3.6), and the inclusion of symmetry considerations, (sections 3.3.7 and 3.3.8). The VCF and eigenvalues from the normal mode analysis are subsequently used to generate a calculated INS profile in the following way: A spectrum of delta functions is created based on the calculated fundamental, overtone and combination energies; the delta functions are then weighted by the INS integrated intensities. These intensities are calculated according to the theory described in section 3.2.5 from a knowledge of the mean-squared-

CHAPTER 3. INELASTIC NEUTRON SCATTERING

displacement amplitude of each atom in each mode and are subsequently powder averaged to account for anisotropies in the thermal motion. The weighted delta functions are then given a spectral profile by assuming a gaussian natural width¹³. At this point the phonon wings (see section 3.2.6) are calculated and the integrated intensity from each gaussian peak is distributed between the main peak and the phonons wings. After convoluting this spectrum with the instrument function of the TFXA spectrometer the final calculated spectrum may be compared quantitatively with the experimental spectrum to produce an object function upon which the least squares refinement may take place. The force field is then modified and the process is repeated until the object function is minimised. A flow chart representing the refinement process in CLIMAX is given in figure 3.5.

The necessity for powder averaging may be appreciated by recalling Eq. (3.27). It is apparent that the spectral intensity contribution of a particular atom in a given mode is attenuated by a term involving the projection of the momentum transfer vector, Q , in the second rank tensor, U , which describes the total thermal motion of that atom in *all* modes; i.e. the term is $\exp - (QQ : U)$. For a powder sample containing all orientations of U , the product $(QQ : U)$ has to be isotropically averaged for the general case in which U is anisotropic. The method chosen is that of Conroy, (17), and is implemented in CLIMAX as described in reference (69). The error in the powder average as compared with analytical methods is ca. 5%. CLIMAX also offers a fast powder average in which the magnitudes of the principal axes of U are summed and divided by three to produce a pseudo-isotropic tensor. The full powder averaging is particularly important in the case of highly asymmetric molecules; it was therefore very desirable in the case of isolated imidazole but was found not to be so important for the zinc tetraimidazole complex. For a wider background to the subject of powder averages in neutron spectroscopy reference may be made to (142), (145) and (150).

In order to calculate ab initio phonon wings, it is first necessary to have a full description

¹³The natural width is actually an anachronism stemming from the early days of INS when resolution was poor and all features were modelled by gaussians. The expression for natural width, W , is: $W = QT/M_{eff}$ where M_{eff} is the so-called effective mass. However, the natural width used in CLIMAX is the intrinsic resolution of the TFXA spectrometer, which is 1.5% of the energy transfer.

CHAPTER 3. INELASTIC NEUTRON SCATTERING

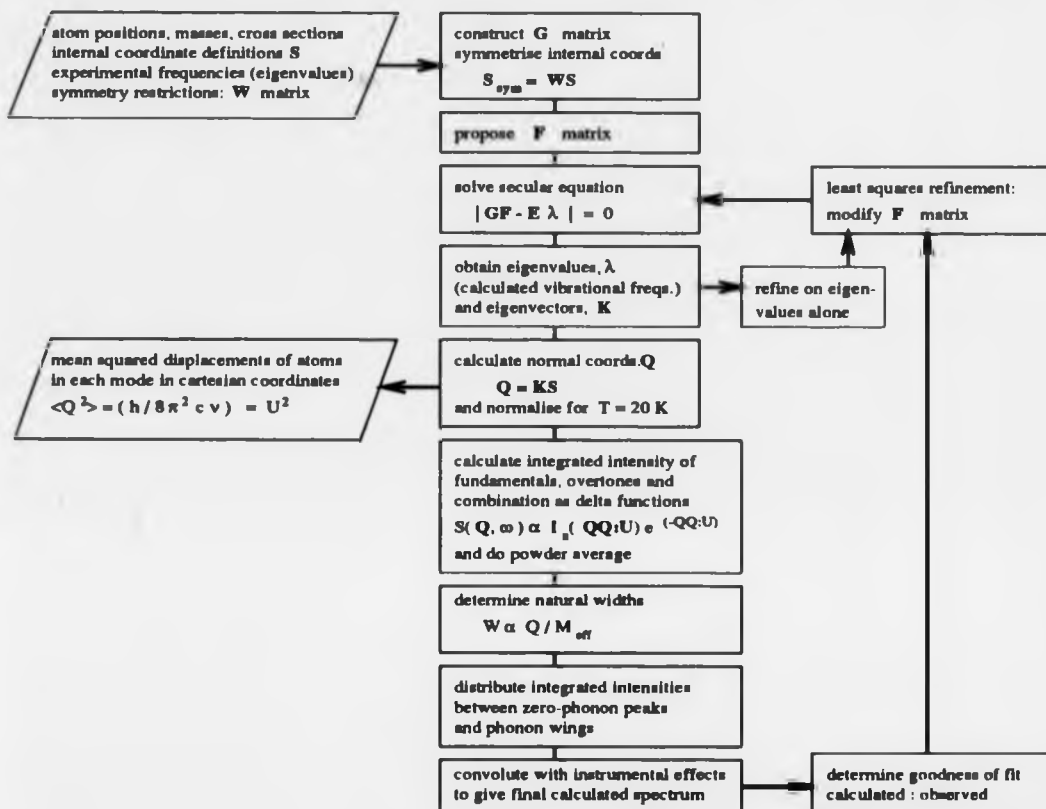


Figure 3.5: Flow chart outlining the main steps in the INS profile refinement package CLIMAX.

of the lattice mode density of states. As this is normally impracticable, an approximation is adopted in which a portion of the experimental INS spectrum is assumed as being wholly due to lattice vibrations. This segment of the spectrum is exported and convoluted repeatedly with the calculated zero-phonon lines (the calculated gaussian peaks) to generate the successive terms in the phonon wing expansion (see Eq.(3.30)) up to a maximum of 8 terms. It has been shown, (144), that even for light molecules, which experience significant recoil¹⁴, that

¹⁴Recoil is said to occur when the initial state molecular momentum is much less than the momentum transfer, Q . The final state wave function of the molecule then resembles the *free state* wavefunction.

CHAPTER 3. INELASTIC NEUTRON SCATTERING

this approximation is adequate. An effective mean-squared-displacement amplitude for the lattice modes is required, i.e. denoted by u in Eq. (3.29), and is treated in CLIMAX as an adjustable parameter.

There is an option in CLIMAX to refine the force field purely against the observed vibrational frequencies. This uses only the eigenvalues from the normal mode analysis and can be done equivalently with experimental infrared or Raman data in addition to, or instead of, the INS peak positions. This option is generally used in the beginning stages of a refinement but was also extensively used in this case to simultaneously refine a force field against the vibrational frequencies from the subject molecule in various states of deuteration. By alternately employing this option and the spectral profile refinement, it was possible to refine a force field which is consistent with experimental INS intensities and produces the correct frequency shifts upon deuteration.

There are several examples of practical applications of CLIMAX appearing in the literature, e.g. (15), (19), (41), (69).

3.5 INS Study of Imidazole

3.5.1 Physical Characteristics of Imidazole

It is assumed throughout that the imidazole molecule, $C_3N_2H_4$, as shown in table 3.1, is planar, the asymmetric shape of the molecule being stabilised by the formation of an aromatic π -system similar to benzene, (78). The molecule belongs to the C_s point group¹⁸ and vibrates in 21 normal modes. Of these 21 normal modes, there are 15 A' in-plane singlet modes and 6 A'' out-of-plane singlet modes corresponding to the two one-dimensional irreducible representations of the C_s symmetry group. (Refer to appendix E for the character table of the C_s point group).

The crystal structure has been determined by X-ray diffraction, (154): the crystal is centered monoclinic, space group $P2_1/c$, and the unit cell contains 4 molecules, see figure 3.6. Within the unit cell, it is found that the imidazole molecules are situated in identical pairs

¹⁸Schönflies notation will be used throughout to denote symmetry point groups.

CHAPTER 3. INELASTIC NEUTRON SCATTERING

$R(1,2) = 1.363 \text{ \AA}$	$\angle (5,1,2) = 106.9^\circ$
$R(2,3) = 1.312 \text{ \AA}$	$\angle (1,2,3) = 112.0^\circ$
$R(3,4) = 1.381 \text{ \AA}$	$\angle (2,3,4) = 104.9^\circ$
$R(4,5) = 1.362 \text{ \AA}$	$\angle (3,4,5) = 110.7^\circ$
$R(5,1) = 1.376 \text{ \AA}$	$\angle (4,5,1) = 105.5^\circ$
$R(1,6) = 0.991 \text{ \AA}$	$\angle (5,1,6) = 126.9^\circ$
$R(2,7) = 1.077 \text{ \AA}$	$\angle (1,2,7) = 122.5^\circ$
$R(4,8) = 1.070 \text{ \AA}$	$\angle (5,4,8) = 127.9^\circ$
$R(5,9) = 1.071 \text{ \AA}$	$\angle (1,5,9) = 121.9^\circ$

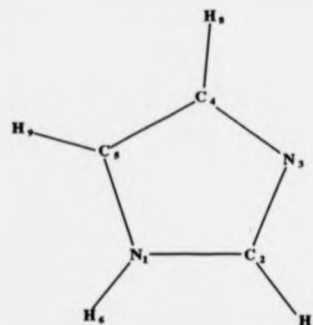
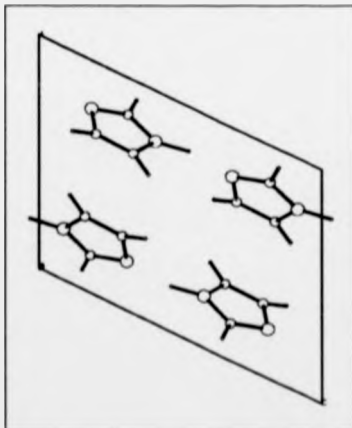


Table 3.1: Reference geometry and labelling of imidazole as used in the present study; the molecule is assumed to be perfectly planar. The geometry is that used by Fan et al., (38), to calculate their published *ab initio* force field, (refer to tables 3.6 and 3.7 for the eigenvalues of this force field.). The geometry is based upon a microwave spectroscopic study by Christen et al., (13).

(i) projection \perp to **b**-axis



(ii) projection \perp to **c**-axis

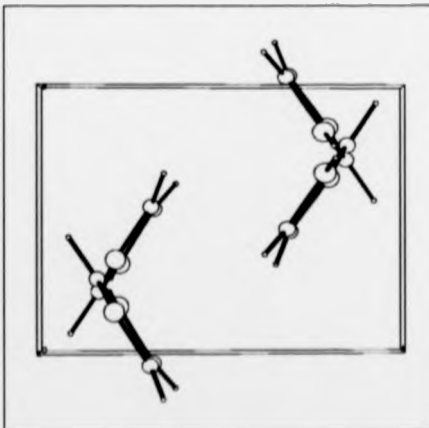


Figure 3.6: Crystal structure of imidazole according to Will, (154), (retrieved from Berlin database). The figure shows the unit cell projected (i) in the *ac* plane, perpendicular to the **b**-axis and (ii) in the *ab* plane perpendicular to the **c**-axis. The crystal may be considered as being composed of infinite H-bonded chains extending parallel to the **c**-axis with an imidazole dimer basis. The C_{2h} dimer is most apparent in projection (ii) in which the two dimers of the unit cell are viewed along the chain axes.

CHAPTER 3. INELASTIC NEUTRON SCATTERING

	symmetry species of modes	number of normal modes	description of modes	optical activity
Free molecule monomer point group C_s	A' A''	15 6	in-plane out-of-plane	ir,Raman ir,Raman
Unit cell 2 dimers (4 molecules) space group $P2_1/c$ factor group C_{2h}	A_g B_g A_u B_u	21 21 21 21	in-phase anti-phase in-phase anti-phase	Raman Raman ir[$\vec{M}(b)$] ir[$\vec{M}(ac)$]

Table 3.2: Symmetry representations and optical selection rules for free imidazole molecule and crystal. In the case of the infrared activity of the unit cell modes, the direction of the electric dipole transition moment, \vec{M} , is indicated with respect to the unit cell axes.

whose collective point group is C_{2h} . In fact, the imidazole crystal may be considered as being composed of infinite, non-interacting parallel chains, (66), (46), (99), (154), whose basis is the C_{2h} dimer; the link in the chain is the 2.83\AA $N_1-N'_3$ hydrogen bond. The symmetry representations of the modes of the unit cell are thus A_g , B_g , A_u and B_u ¹⁶, each being composed of 21 singlet modes. This symmetry information plus optical selection rules are summarised in table 3.2. Notice that only two of the four symmetry species of the unit cell are either infrared or Raman active; consequently each vibration of the isolated molecule gives rise to two bands in both the infrared and Raman spectra of powdered imidazole. These correspond to in-phase and anti-phase vibrations of neighbouring molecules in each dimer. The infrared active modes of the unit cell can be further classified in terms of the direction of the electric dipole transition moment, \vec{M} , since the A_u modes have a transition moment parallel to the unit cell b-axis and the B_u modes have a transition moment parallel to the plane defined by the a- and c-axes. Within each of these species, the transition moment of the monomer *out-of-plane* modes is always perpendicular to the c-axis whereas the transition moment of the *in-plane* modes is, in the A_u case, perpendicular, but in the B_u case parallel,

¹⁶The subscripts *g* and *u* from the German *gerade* and *ungerade* denote even and odd parity. This specifies whether the eigenfunctions of the hamiltonian of a spherically symmetric system (i.e. one whose point group contains only proper rotations) are invariant or change sign under inversion.

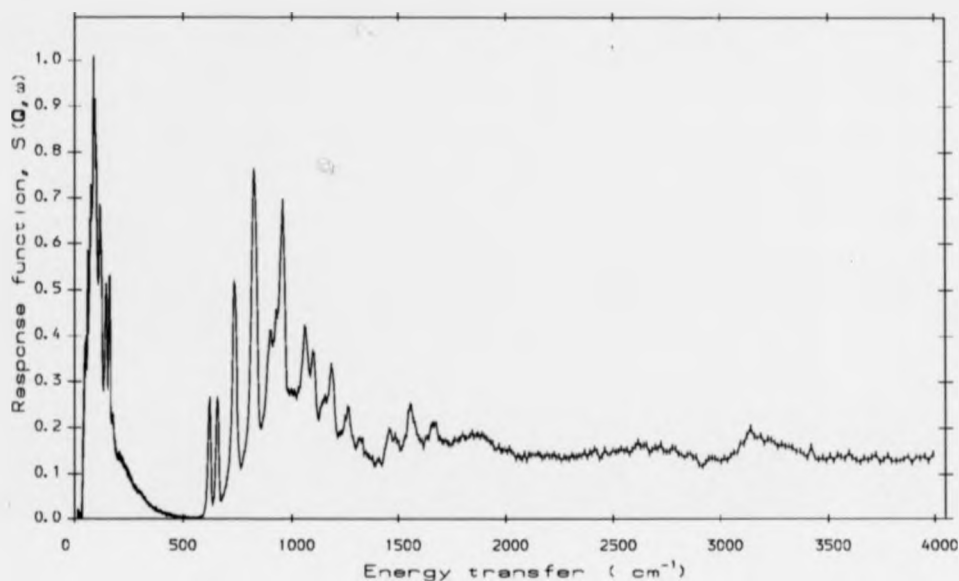


Figure 3.7: The full experimental inelastic neutron scattering spectrum of a powder sample of crystalline imidazole at 20K recorded on the TFXA spectrometer, Rutherford Appleton Laboratory, U.K., by F.Fillaux, (80). Error bars are shown and the spectrum of background neutron scatter from the cryostat and cadmium sample holder has been subtracted.

to the c-axis. The in-plane modes therefore exhibit a dichroism which may be exploited by polarisation studies of oriented single crystals which effectively distinguish A' modes from A'' modes of the monomer. This has been done by Perchard et al., (104), and the results are discussed in the next subsection and compared to oriented single crystal INS studies of imidazole.

3.5.2 Experimental Results

The experimental INS spectrum of powdered imidazole was recorded, in a collaboration, by F.Fillaux, (80), and it is shown in figure 3.7. The raw data ^{were} ~~was~~ recorded at 20K on the TFXA spectrometer (section 3.4.1) and is presented here after the spectrum of background neutron scatter from the cryostat and cadmium sample holder was subtracted.

The spectrum in figure 3.7 depicts the response function, $S(Q, \omega)$, (refer to section 3.2.3

CHAPTER 3. INELASTIC NEUTRON SCATTERING

and 3.2.5), or hydrogen-weighted vibrational density of states, of crystalline imidazole sampled over the whole of the Brillouin zone; it clearly separates into two regions above and below 500cm^{-1} .

The region below 500cm^{-1} describes the acoustic phonon density of states or lattice mode spectrum. There is a large body of literature concerned with acoustic lattice vibrations of crystalline imidazole, (16), (78), (87), (105), (160); acoustic modes generally have very dispersive phonon branches within the Brillouin zone and consequently tend to produce a broad featureless hump as is visible in the INS spectrum below 500cm^{-1} (this effect was illustrated in figure 3.1). Some sharp peaks are visible in the acoustic region at around 150cm^{-1} suggesting the presence of non-dispersive modes with large scale hydrogen motion; it is believed, (16), (78), that these peaks correspond to in-phase and anti-phase hydrogen-bond stretching modes. However, due to the low energy of these modes it is assumed, (16), that they do not influence the optical modes in the higher frequency regime of the spectrum and we therefore confine ourselves to considering the spectrum above 500cm^{-1} in which the internal modes of imidazole occur.

The internal modes of imidazole are optical modes and are assumed to be completely non-dispersive. The peaks in the INS spectrum corresponding to these modes are narrow; they have a full width at half maximum (FWHM) corresponding to the intrinsic resolution of the TFXA spectrometer convoluted with its instrument function (see section 3.4.1). Most of the discernible modes occur in the region $500 - 1800\text{cm}^{-1}$. The integrated intensity of each peak indicates the magnitude of the hydrogen motion of the mode(s) associated with that peak, (see section 3.2.5); for example it may be deduced from inspection of figure 3.7 that the imidazole modes vibrating in the range $500 - 1000\text{cm}^{-1}$ involve comparatively large scale hydrogen atom motion. As well as the sharp peaks a broad background intensity may be observed above 500cm^{-1} ; this is due partly to the superposition of very many combination bands of comparatively low intensity but principally due to the effect of phonon wings. Phonon wings are always present in intensity optimised spectrometers such as TFXA but are minimised at low temperature.

Oriented single crystal experiments on imidazole were also performed, the results of which

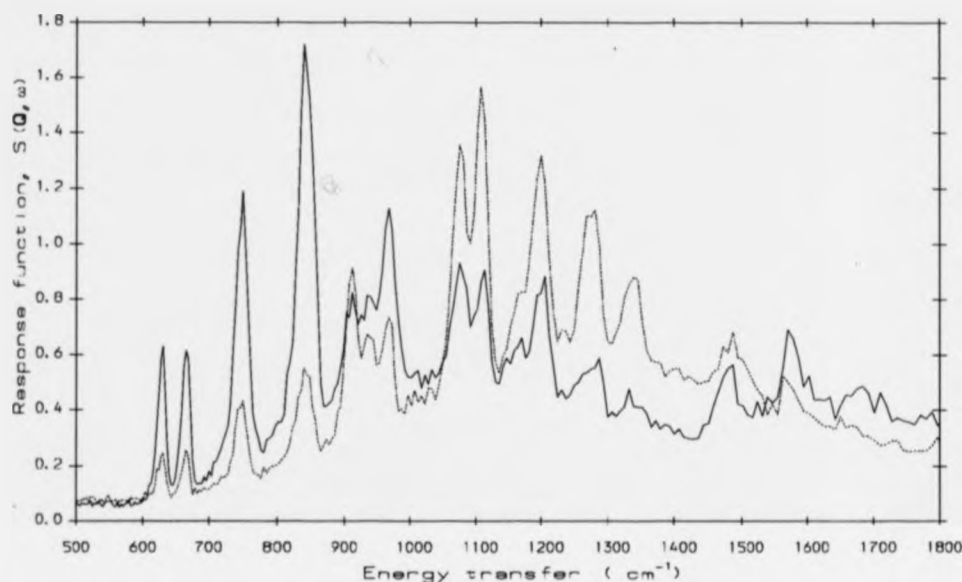


Figure 3.8: INS spectra of an oriented single crystal of imidazole recorded by F. Fillaux, (80), on the TFXA spectrometer at Rutherford Appleton Laboratory, U.K.. Two curves are shown corresponding to two orientations of the crystal. The full line is the spectrum taken with the momentum transfer vector of the scattered neutrons parallel to the b-axis of the unit cell and the dashed line with the momentum transfer vector parallel to the c-axis. The spectra are shown over the range $500 - 1800\text{cm}^{-1}$ thereby encompassing all the clearly defined peaks in the imidazole INS powder spectrum. The spectra were treated by first subtracting the spectrum of background scatter from the crystal and then by scaling with respect to one another; scaling was effected by equating the integrated intensity of each spectrum over the range $2000 - 4000\text{cm}^{-1}$ which includes no strong optical peaks.

are shown in the region of interest, $500 - 1800\text{cm}^{-1}$, in figure 3.8. The experiment was carried out such that the momentum transfer vector, \mathbf{Q} , of the scattered neutrons was, in the one case parallel to the b-axis of the unit cell (full line in figure 3.8), and in the other case parallel to the c-axis. By recalling figure 3.6, it may be seen that this corresponds to the momentum transfer vector lying perpendicular and parallel respectively to the plane of the imidazole molecules. Correspondingly there is a preferred excitation of A'' out-of-plane modes when \mathbf{Q} is parallel to the b-axis, whereas A' in-plane mode excitations become more significant when \mathbf{Q} is parallel to the c-axis. When comparing the INS spectra at the two orientations, this preferred excitation of A' or A'' modes manifests itself as an apparent enhancement

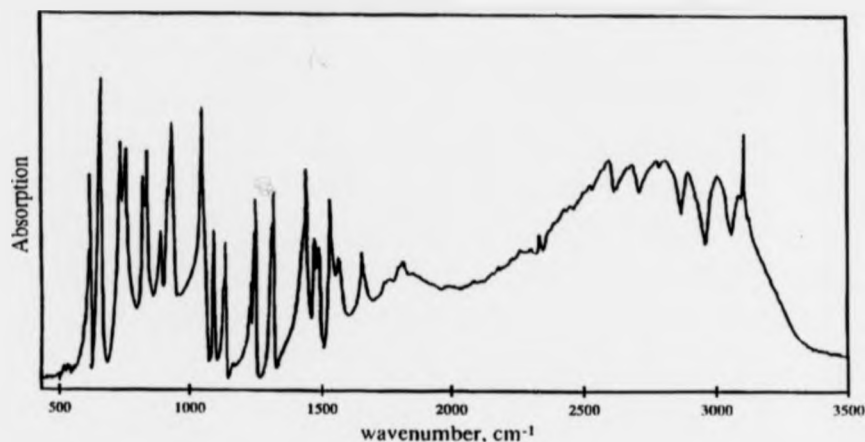


Figure 3.9: Infrared spectrum of powdered imidazole in potassium bromide matrix at room temperature. The spectrum was measured on a Bruker FT-IR ISS Lucke 48 spectrometer at the Universität Münster, Germany.

or attenuation of peak intensities. This permits an unambiguous symmetry assignment of the peaks in the INS imidazole spectrum: in figure 3.8, A' peaks are identifiable as being enhanced in the dashed line spectrum whereas A'' peaks are diminished when compared to the full-line spectrum. The experiment therefore represents the INS analogue of the optical dichroism experiments performed by Perchard et al. (104). Note that the two spectra were scaled with respect to one another by equating the intensity integral in a part of the spectra without strong optical peaks ($2000 - 4000\text{cm}^{-1}$); this scaling also produced equal integrated intensities in the acoustic regime (i.e. $< 500\text{cm}^{-1}$).

The quantitative interpretation of the oriented single crystal INS experiment is given in table 3.3 and compared with the published optical dichroism experiments of Perchard et al.. In the latter, the only modes unambiguously classified were those bands which were more intense when the electric field vector lay parallel to the c -axis, i.e. the π -bands, which could only be of A' symmetry. The other bands, identified as σ bands, could be of either symmetry species since the transition moment of the A'' modes also lies in the allowed plane of the transition moment of the A' modes. Note that, as discussed earlier, each monomer mode gives rise to

CHAPTER 3. INELASTIC NEUTRON SCATTERING

INS spectra of imidazole vibrational frequencies in cm ⁻¹			i.r. spectra of imidazole vibrational frequencies in cm ⁻¹		
powder sample at 20K	single crystal at 25K with Q parallel to the b axis c axis	symmetry species	powder sample at r.t.	single crystal at r.t.	polarisation & symmetry species
1675			1669		
1561	1577 1571		{1576 1542}	{1577 1543 1540}	π } A'
1498	1483 < 1489	A'	{1497 1479 1448}	{1498 1480 1448}	π } A'
1445				π }	
1326	1340 < 1345	A'	1327	{1329 1322}	π, σ } A'
1265	1281 < 1278	A'	{1263 1244}	{1263 1244}	π } A'
1186	1204 < 1201	A'		1175	σ A'
1143	1172 < 1172	A'	{1147 1138}	{1146 1138}	π } A'
1098	1113 < 1111	A'	{1102 1098}	{1100 1098 1068 1060 1050}	π } A'
1061	1081 < 1079	A'	1055		π }
961	972 > 969	A''			
935	943 > 940	A''	937	938 936 921	π } A' σ } A''
908	914 < 914	A'	896	895	π A'
834	844 > 842	A''	{842 828}	837 830	σ } A''
743	754 > 751	A''	{759 737 670}	760 738	σ } A''
661	669 > 669	A''	659	659	σ A''
623	631 > 631	A''	620	622	σ A''

Table 3.3: The results of INS and infrared oriented single crystal experiments on imidazole to determine the symmetry species of the vibrational modes. The INS experiment determines the symmetry from the relative peak intensities of modes in the two crystal orientations. The frequencies of the peaks are taken from the INS powder spectrum (figure 3.7) and the two oriented single crystal spectra (figure 3.8); the symbols > and < denote which of the two orientations gives the greater intensity for each peak. The symmetry species implied by the relative intensities is shown. The infrared experiment determines the symmetry species by virtue of the optical dichroism of the A' and A'' modes. The control infrared powder spectrum is given in figure 3.9 but the dichroism results are those published by Perchard et al. (104). The bands are labelled π or σ depending on whether the bands become more or less intense when the electric field vector of plane polarised infrared radiation is projected parallel or perpendicular to the c-axis of the crystal. A π -band is then positively identified as an A' mode. A σ -band is ambiguous since the A'' transition moment vector lies in the allowed plane of the A' transition moment. The symmetry assignments made by Perchard et al. based on this experiment are shown. There is good agreement between the two methods.

CHAPTER 3. INELASTIC NEUTRON SCATTERING

two bands in the infrared spectrum. A symmetry assignment was made by Perchard et al., and the agreement with the INS study is excellent.

The INS oriented single crystal study is mostly unambiguous. By recalling figure 3.8 it may be seen that all the peaks between 500 and 1500cm^{-1} are clearly either enhanced or attenuated when comparing the two spectra. The one peak which could be regarded as ambiguous is at 935cm^{-1} ; lying closely between the two peaks at 908cm^{-1} and 961cm^{-1} it is not obvious how much of its intensity is influenced by overlap with its neighbours and the change in the phonon wing background. It is therefore difficult to state unequivocally that it is an A'' mode; it is in fact later assigned to be due to one A' and one A'' mode that are almost degenerate, as is suggested from the dichroism studies. An advantage of the INS study is that it clearly defines the peak at 961cm^{-1} as being due to an A'' mode. This was not possible in the infrared study since the 961cm^{-1} peak was masked by the broad 937cm^{-1} peak.

The result of the INS study is that it positively corroborates the symmetry assignment published by Perchard et al. and conclusively identifies the 961cm^{-1} peak as being of A'' symmetry. The six expected A'' out-of-plane modes are thus taken to be at 623, 661, 743, 834, 935 and 961cm^{-1} . Of the 15 expected A' in-plane modes, 11 are positively identified by the joint studies at 908, 938, 1061, 1098, 1143, 1186, 1265, 1326, 1445, 1498 and 1561cm^{-1} . Four A' modes corresponding to hydrogen stretches are expected to occur at much higher frequencies (around 3000cm^{-1}) which means all modes are accounted for.

The infrared spectrum of powder imidazole at room temperature is given in figure 3.9 for completeness. The qualitative frequency assignment discussed in this section is an essential precursor to the normal mode analysis that is described in the next subsection.

3.5.3 Normal Mode Analysis - Input Parameters

The normal mode analysis of the imidazole molecule was accomplished using the CLIMAX package (described in section 3.4.3) which required the following items of input

- reference geometry, masses and neutron scattering cross sections of atoms.
- target eigenvalues and target INS intensities

CHAPTER 3. INELASTIC NEUTRON SCATTERING

- molecular model - including description of internal symmetry coordinates
- starting estimate for force field

3.5.3.1 reference geometry

The reference geometry is based on a thorough microwave spectroscopic study, (13), but the exact coordinates are those used by Fan et al., (38), in their calculations of an ab initio force field for imidazole (this is discussed in more detail further on); the geometry used is given in table 3.1. Neutron scattering cross sections were obtained from a published compilation of neutron data, (72).

3.5.3.2 target eigenvalues and INS intensities

The target eigenvalues used for imidazole were the symmetry assigned peak positions from the INS powder spectrum listed in table 3.3. These are consistent with the the extensive infrared and Raman vibrational data that exists in the literature (see (16), (18), (38), (70), (84), (86), (104)) although small discrepancies can be observed between the various data sets ($< 10\text{cm}^{-1}$).

INS data for deuterated variants of imidazole were not obtained but Perchard et al., (104), published a detailed assignment of imidazole in three deuterated states; i.e. imidazole- $d_{(1)}$, imidazole- $3d_{(2,4,5)}$ and imidazole- $4d$ based on infrared and Raman spectra. Their results have been used in this study with minor changes to their assignment based on expected deuteration shifts from the undeuterated assignment. The changes are listed below:

1. For imidazole- $d_{(1)}$ (i.e. deuterated at the N_1 position) the 1495cm^{-1} band is reassigned to the 1572cm^{-1} band.
2. For imidazole- $3d_{(2,4,5)}$ (i.e. deuterated at the C_2 , C_4 and C_5 positions) the previously unassigned 600cm^{-1} band is assigned as an A' mode (which is a reassignment also made by Fan et al., (38), in their study) and the assignments for the 930 and 962cm^{-1} bands are swapped around to be A' and A'' respectively. The lowest frequency A' mode is reassigned to be enclosed in the 768cm^{-1} doublet from the expected shift of the

CHAPTER 3. INELASTIC NEUTRON SCATTERING

1060 cm^{-1} band in the undeuterated case. The previously unassigned 1510 cm^{-1} band is assigned as an A' mode.

3. For imidazole-4 d the changes correspond to those for imidazole-3 $d_{(2,4,5)}$.

All INS intensities were taken from the spectrum in figure 3.7.

3.5.3.3 molecular model

The molecular model for imidazole is defined by its geometry (as described above) and by the set of generalised coordinates that describe the displacements of the atoms within the assumed harmonic oscillator model. These generalised coordinates were discussed in detail in section 3.3.5 and are known as the internal coordinates, S . They are a basis set describing the dynamics of the molecule in terms of bond stretches, bends etc. and are listed for imidazole in table 3.4. The internal symmetry coordinates, S' , (which are discussed in section 3.3.8) and are also listed in table 3.4. Both the internal coordinates S and the matrix that transforms S to the internal symmetry coordinates S' (denoted as W in section 3.3.8) must be entered as input to CLIMAX.

3.5.3.4 starting estimate for force field

The starting point in multi-parameter least squares refinement is invariably critical. It determines how quickly the object function will minimise and quite often if at all. In the case of imidazole there have been many attempts at generating ab initio force fields that appear in the literature, (16), (86), (88), (124), (125), but, to the authors knowledge, the only paper in which the force field itself is given is that by Fan et al., (38). The study by Fan et al. involved generating a force field by the ab initio gradient method¹⁷ and scaling it with previ-

¹⁷The ab initio calculations were carried out within the MO-LCAO-SCF approximation using the Hartree-Fock gradient programme TEXAS, (113). In brief: the method involves minimising the total energy of a proposed model of the molecular orbitals (MO) for imidazole according to the quantum mechanical variation theory and determining the implied harmonic force field from the resultant potential distribution. The MO's are modelled using linear combinations of atomic orbitals (LCAO); it is the coefficients in the LCAO that are parameters in the minimisation of the total energy of the MO's. The atomic orbitals (AO) are themselves composed of linear combinations of Gaussian functions with fixed coefficients that model the solutions to the Hartree-Fock self consistent field (SCF) equations. The basis set of Gaussians used is discussed further on page 92.

CHAPTER 3. INELASTIC NEUTRON SCATTERING

internal coordinates, S	internal symmetry coords, S'	
non-minimum basis set of 31 coordinates	minimum basis set of 21 coordinates plus 10 redundant coordinates	notation
A' coordinates $S_1 = R(2,7)$ $S_2 = R(1,6)$ $S_3 = R(5,9)$ $S_4 = R(4,8)$ $S_5 = R(1,2)$ $S_6 = R(5,1)$ $S_7 = R(4,5)$ $S_8 = R(3,4)$ $S_9 = R(2,3)$ $S_{10} = \angle(7,2,3)$ $S_{11} = \angle(7,2,1)$ $S_{12} = \angle(6,1,2)$ $S_{13} = \angle(6,1,5)$ $S_{14} = \angle(9,5,1)$ $S_{15} = \angle(9,5,4)$ $S_{16} = \angle(8,4,5)$ $S_{17} = \angle(8,4,3)$ $S_{18} = \angle(1,2,3)$ $S_{19} = \angle(5,1,2)$ $S_{20} = \angle(4,5,1)$ $S_{21} = \angle(3,4,5)$ $S_{22} = \angle(2,3,4)$	A' coordinates: in-plane displacements $S'_1 = S_1$ $S'_2 = S_2$ $S'_3 = S_3$ $S'_4 = S_4$ $S'_5 = S_5$ $S'_6 = S_6$ $S'_7 = S_7$ $S'_8 = S_8$ $S'_9 = S_9$ $S'_{10} = S_{10} - S_{11}$ $S'_{11} = S_{12} - S_{13}$ $S'_{12} = S_{14} - S_{15}$ $S'_{13} = S_{16} - S_{17}$ $S'_{14} = 4S_{18} - 3S_{19} + S_{20} + S_{21} - 3S_{22}$ $S'_{15} = -S_{19} + 2S_{20} - 2S_{21} + S_{22}$ $S'_{red} = S_{10} + S_{11}$ $S'_{red} = S_{12} + S_{13}$ $S'_{red} = S_{14} + S_{15}$ $S'_{red} = S_{16} + S_{17}$ $S'_{red} = 4S_{18} + 3S_{19} + S_{20} + S_{21} + 3S_{22}$ $S'_{red} = S_{18} - 2S_{20} - 2S_{21}$ $S'_{red} = 2S_{19} + S_{20} - S_{21} - 2S_{22}$	 CH_7 NH_6 CH_9 CH_8 $N_1C_2 \equiv R_1$ $C_5N_1 \equiv R_2$ $C_4C_5 \equiv R_3$ $N_3C_4 \equiv R_4$ $C_2N_3 \equiv R_5$ δCH_7 δNH_6 δCH_9 δCH_8 R_6 R_7 <i>redundant</i> <i>redundant</i> <i>redundant</i> <i>redundant</i> <i>redundant</i> <i>redundant</i> <i>redundant</i>
A'' coordinates $S_{23} = O(7,2,3,1)$ $S_{24} = O(6,1,2,5)$ $S_{25} = O(9,5,1,4)$ $S_{26} = O(8,4,5,3)$ $S_{27} = \tau(3,2,1,5)$ $S_{28} = \tau(2,1,5,4)$ $S_{29} = \tau(1,5,4,3)$ $S_{30} = \tau(5,4,3,2)$ $S_{31} = \tau(4,3,2,1)$	A'' coordinates: out-of-plane displacements $S'_{16} = S_{23}$ $S'_{17} = S_{24}$ $S'_{18} = S_{25}$ $S'_{19} = S_{26}$ $S'_{20} = S_{27} - 3S_{28} + 4S_{29} - 3S_{30} + S_{31}$ $S'_{21} = -2S_{27} + S_{28} - S_{30} + 2S_{31}$ $S'_{red} = S_{27} + 3S_{28} + 4S_{29} + 3S_{30} + S_{31}$ $S'_{red} = -2S_{27} + S_{29} - 2S_{31}$ $S'_{red} = -S_{27} - 2S_{28} + 2S_{30} + S_{31}$	 γCH_7 γNH_6 γCH_9 γCH_8 R_8 R_9 <i>redundant</i> <i>redundant</i> <i>redundant</i>

Table 3.4: Basis set of generalised coordinates to which the force field for imidazole (see table 3.5) is referenced. The starting point are the internal coordinates, S, which fully describe the displacements of the molecule in terms of *bond stretches*, $R(a,b)$, *valence angle bends*, $\angle(a,b,c)$, *out-of-plane bends*, $O(a,b,c,d)$, and *torsions*, $\tau(a,b,c,d)$, (see figure 3.2). This description forms a non-minimum set which, via symmetry considerations (refer to section 3.3.8 and appendix D), may be transformed into a minimum set comprising linear combinations of the internal coordinates. The new basis contains the smaller set of internal symmetry coordinates, S', plus the remaining redundant coordinates. The force field corresponding to S' is said to be block-diagonalised in its irreducible representations; in this form it contains far fewer elements to be determined.

CHAPTER 3. INELASTIC NEUTRON SCATTERING

ously determined scale factors from a fitted vibrational spectrum of benzene. The force field predicted the vibrational frequencies of *gaseous* free imidazole relatively well and was tested for consistency against the solid state infrared/Raman vibrational spectra of imidazole in the 1d, 3d and 4d-deuterated states from Perchard et al..

The force field of Fan et al. is evidently a good starting point. It already predicts the vibrational frequencies reasonably well but has not been tested to see how accurately it reproduces the hydrogen-weighted vibrational density of states of imidazole. This is done in figure 3.10 in which the published force field of Fan et al. is directly entered into CLIMAX. (Care has been taken so that the conditions of the calculation are identical to those employed later to generate the final results; figure 3.10 may thus be directly compared with the results presented further on in figure 3.11). Despite the fact that the vibrational frequencies are relatively well predicted, the force field of Fan et al. only poorly models the experimental INS intensities for solid imidazole. This highlights the danger of assessing the reliability of a given force field on the basis of its eigenvalues (vibrational frequencies) alone. It nevertheless represents an adequate starting point from which to develop a fully consistent force field and was consequently used in this study.

It should be noted that the calculations of Fan et al. were for the *free* molecule, i.e. in the gaseous state. However, according to the assignments of Perchard et al. and others, the vibrational spectrum of free imidazole only differs significantly from that of solid imidazole in the frequency of the *NH* modes (this being a consequence of the hydrogen bonding in crystalline imidazole as described in section 3.5.1); the other internal modes do not appear to participate greatly in the H-bond modes and remain at approximately the same frequency in the free molecule as in the solid state. The principal difference between the vibrational spectrum of solid state and free imidazole is the solid state band at 961cm^{-1} which disappears in the gaseous and aqueous spectra and reappears at 514cm^{-1} . This is seen as the very intense peak at about 450cm^{-1} in the calculated spectrum in figure 3.10 and is due to the A'' out-of-plane *NH* mode.

In summary, the force field of Fan et al. is taken as the starting point in developing a force field that is more consistent with the experimental INS observations. The fact that the

CHAPTER 3. INELASTIC NEUTRON SCATTERING

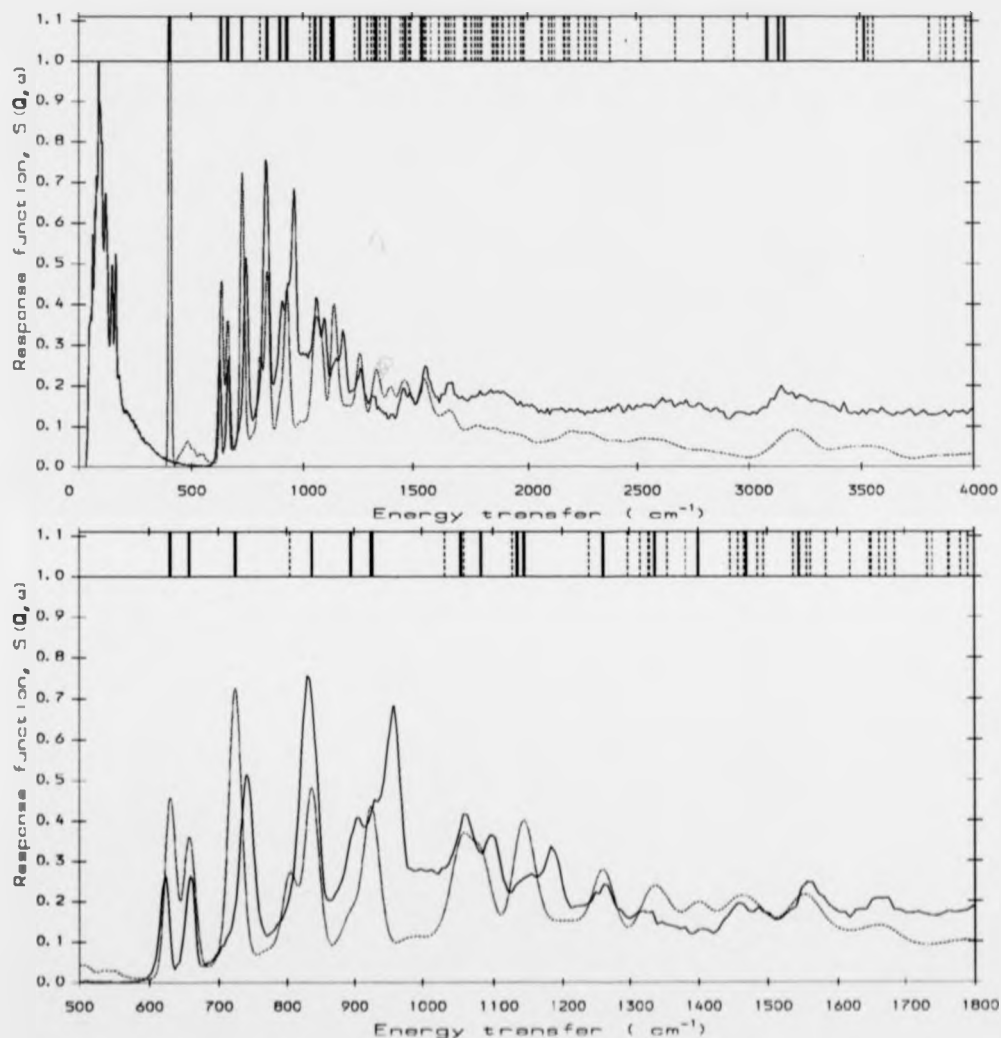


Figure 3.10: Calculated INS spectrum of imidasole (dashed curve) using the published force field of Fan et al. (38) superimposed on the experimental INS spectrum (solid curve). The upper plot shows the entire spectrum and the lower plot the same spectrum over the range of particular interest (i.e. 500–1800 cm^{-1}). The bands at the top of each spectrum indicate the frequencies of calculated fundamental vibrations (solid lines) and calculated overtone and combination vibrations (dotted lines). All other parameters in the calculation were the same as those for the force field developed by the author and the spectra may therefore be directly compared with the results presented further on in table 3.11.

CHAPTER 3. INELASTIC NEUTRON SCATTERING

force field of Fan et al. is actually for free imidazole is not regarded as a disadvantage since essentially only the A'' NH mode is significantly affected and it is seen to be virtually a pure mode (i.e. almost no interaction with other motion in the imidazole ring); in effect the NH mode can therefore be treated independently and the participation of NH modes in H-bond vibrations may effectively be modelled by simply modifying the diagonal element of the force field relating to the A'' NH wagging internal coordinate.

3.5.4 Normal Mode Analysis - Methodology of Refinement

The task of refining a multi-parameter force field so that it simultaneously models the vibrational spectra of four isotopic variants of imidazole while still rendering an acceptable fit to the experimental INS spectrum involves a great deal of patience and a degree of luck. The most important criterion is that the number of free parameters never exceeds the number of observations to which they are fitted. This invariably means that elements of the force field must be arbitrarily coupled together in order to reduce the number of free parameters whilst still allowing most regions of the force field to be altered. Table 3.5 presents the finished force field after completed refinement; the results which it generates are presented and discussed in the next subsection. In total the force field contains 141 independent elements: 120 in the upper block, belonging to A' modes, and 21 in the lower block, which describe the A'' modes. These two blocks have zero interaction elements which is a consequence of describing the force field in terms of internal symmetry coordinates; this reduces the number of independent elements to 141 from the 465 needed to describe the 31×31 force field based on the non-minimum set S (see table 3.4). The 31×31 force field is however more chemically informative since it is based on the more intuitive set of internal coordinates S (i.e. simple bond stretches etc.). It is easily generated via the back unitary transformation using the transform W and is given in appendix F.

The strategy for eliciting the force field in table 3.5 essentially involved refining the force field in four modes each with a different object function to be minimised. These modes were alternately run and are described below:

1. Refine the force field against the frequency spectrum of imidazole: this involves releasing

S' 1		5.311	
S' 2		0.014 4.248	
S' 3		0.000 0.014 5.254	
S' 4		0.000 0.000 0.014 5.277	
S' 5		0.052 0.019 -0.019 -0.026 7.268	
S' 6		-0.026 0.013 0.039 0.013 0.752 7.547	
S' 7		-0.026 -0.019 0.013 0.026 -0.029 0.715 8.169	
S' 8		-0.026 -0.026 -0.013 0.065 -0.665 0.000 0.403 6.003	
S' 9		0.078 -0.052 -0.052 -0.019 1.533 0.685 -0.295 1.288 8.045	
S' 10		-0.020 0.000 0.000 0.010 -0.234 0.124 0.000 0.000 0.151 0.499	
S' 11		0.010 0.000 0.000 0.000 0.134 -0.269 -0.249 0.061 0.003 0.000 0.469	
S' 12		0.000 0.000 0.010 -0.010 -0.163 0.228 -0.076 0.000 0.000 -0.020 0.020 0.422	
S' 13		-0.010 0.000 0.000 0.020 -0.027 0.000 0.366 -0.282 0.001 -0.020 -0.020 0.020 0.414	
S' 14		0.113 -0.102 0.023 0.034 1.182 -0.998 0.599 -0.632 -0.015 0.020 0.102 -0.143 0.123 2.484	
S' 15		-0.011 -0.068 0.124 -0.113 -0.047 1.158 -0.013 -0.314 1.529 0.102 -0.123 -0.020 0.000 0.082 2.441	
S' 16			0.314
S' 17			0.001 0.473
S' 18			0.043 0.000 0.424
S' 19			0.000 0.016 0.004 0.451
S' 20			0.000 0.170 -0.351 0.226 0.791
S' 21			0.243 -0.235 0.090 0.065 -0.079 0.643

Table 3.5: Final refined force field for solid state imidazole. The elements are in $\text{mdyne } \text{\AA}^{-1}$ and are defined with respect to the basis set of 21 internal symmetry coordinates defined in table 3.4. The block-diagonalisation is by virtue of the choice of coordinates and separates the force field into two non-interacting blocks representing the irreducible representations of the C_s point group inherent to the imidazole molecule; i.e. the upper block defines the force field of the A' modes whereas the lower block is associated only with the A'' modes. The dotted lines show how the off-diagonal interaction constants were grouped together in some of the refinement modes (refer to main body text). These groups arbitrarily collect elements of the force field together which belong to symmetry coordinates of similar types (e.g. ring deformations etc.) so that they may be refined with just one free parameter. This partitioning is necessary to bring the number of free parameters in a refinement below the number of observations.

CHAPTER 3. INELASTIC NEUTRON SCATTERING

- all or part of the leading diagonal of the force field and using the fundamental frequencies as targets. (target frequencies = $15[A'], 6[A'']$; free parameters = $15[A'], 6[A'']$)
2. Simultaneously refine the force field against the frequency spectra of two, three or four deuterated variants of imidazole: the larger number of target frequencies means that off-diagonal interaction constants can be included in the refinement. The most extensive scheme involves releasing all of the diagonal elements and then grouping the off-diagonal elements into the sub-blocks indicated by the dotted lines in table 3.5 with one free parameter per sub-block. These sub-blocks group internal symmetry coordinates of similar type. For the smaller A'' block the number of target frequencies exceeds the number of elements and thus every element in that block can be refined independently in this mode. (target frequencies (for all four deuterated variants) = $60[A'], 24[A'']$; free parameters = $25[A'], 21[A'']$).
 3. Refine the force field against the frequency spectrum and numerical INS intensities of imidazole: in this mode only the fundamental INS spectrum is calculated using fast powder average¹⁸ and the integrated intensities from the calculation are compared against the input intensities in the object function. No INS data file is required. The relative weights of frequency refinement and intensity refinement are critical in this mode. Independent refinable parameters were allocated in the same way as in mode 2 except for the A'' block which was grouped into three blocks, as shown by the dotted line in table 3.5, in the same fashion as the A' block. (target values, (frequency and intensity) = $30[A'], 12[A'']$; free parameters = $25[A'], 9[A'']$).
 4. Full refinement against experimental INS spectrum: this mode is only helpful when the fit is already quite good because it frequently finds false minima. The INS spectrum is calculated including fundamentals, overtones, combinations, phonon wings and using the full powder average and is directly compared to the input INS spectrum over ranges that may be input interactively. The overall Debye-Waller factor due to lattice modes

¹⁸This is a time saving approximation; the INS intensity is calculated along the cartesian x , y and z directions only and simply divided by three.

CHAPTER 3. INELASTIC NEUTRON SCATTERING

must also be input to determine the extent of the phonon wing spectrum and may subsequently be refined; it is discussed in the next subsection. The scale factor is also refined. This mode is very slow, one cycle takes about 2 minutes of CPU time on a SGI Crimson (UNIX) or 46 minutes on a VAX 3100 for this particular problem. The allocation of refinable parameters is the same as in mode 3. (i.e. free parameters = $25[A']$, $9[A'']$).

In all cases the refinement of the A' and A'' blocks were addressed separately and great flexibility was possible within each mode by adjusting weighting schemes and altering target frequencies in order to guide the refinement out of the frequently encountered local minima.

3.5.5 Results and Discussion

The INS spectrum for imidazole generated by the force field presented in table 3.5 is shown in figure 3.11. The calculation involves fundamental excitations plus first overtones and 178 of the most significant combination bands. A full numerical powder average is employed to ensure isotropic averaging. Phonon wings are also calculated up to the eighth phonon excitation (see section 3.2.6) based on the experimental INS density of states in the range $0 - 500\text{cm}^{-1}$ (refer to section 3.4.3 for method); this range encloses no internal modes and is thus a good approximation to the lattice mode spectrum. The overall Debye-Waller factor in the phonon wing expression was taken as 0.011\AA^2 ; this value was refined down from a starting estimate of 0.014\AA^2 which was obtained from a quick calculation, using Eq. (B.11), of the isotropic mean-squared-deviation of the whole molecule from the lattice mode frequencies published in reference (105).

The spectrum in figure 3.11 may be directly compared to that in figure 3.10 which is the INS spectrum calculated from the starting force field of Fan et al.; the parameters for both calculations are identical. There is a distinct improvement in the fit of the calculated curve to the observed spectrum using the new refined force field which is especially apparent in the range $500 - 1800\text{cm}^{-1}$ in which most of the fundamental vibrational frequencies occur. It should be recalled that the force field of Fan et al. was not intended to model the dynamics of imidazole in the solid state but rather of the free molecule in the gaseous state and so

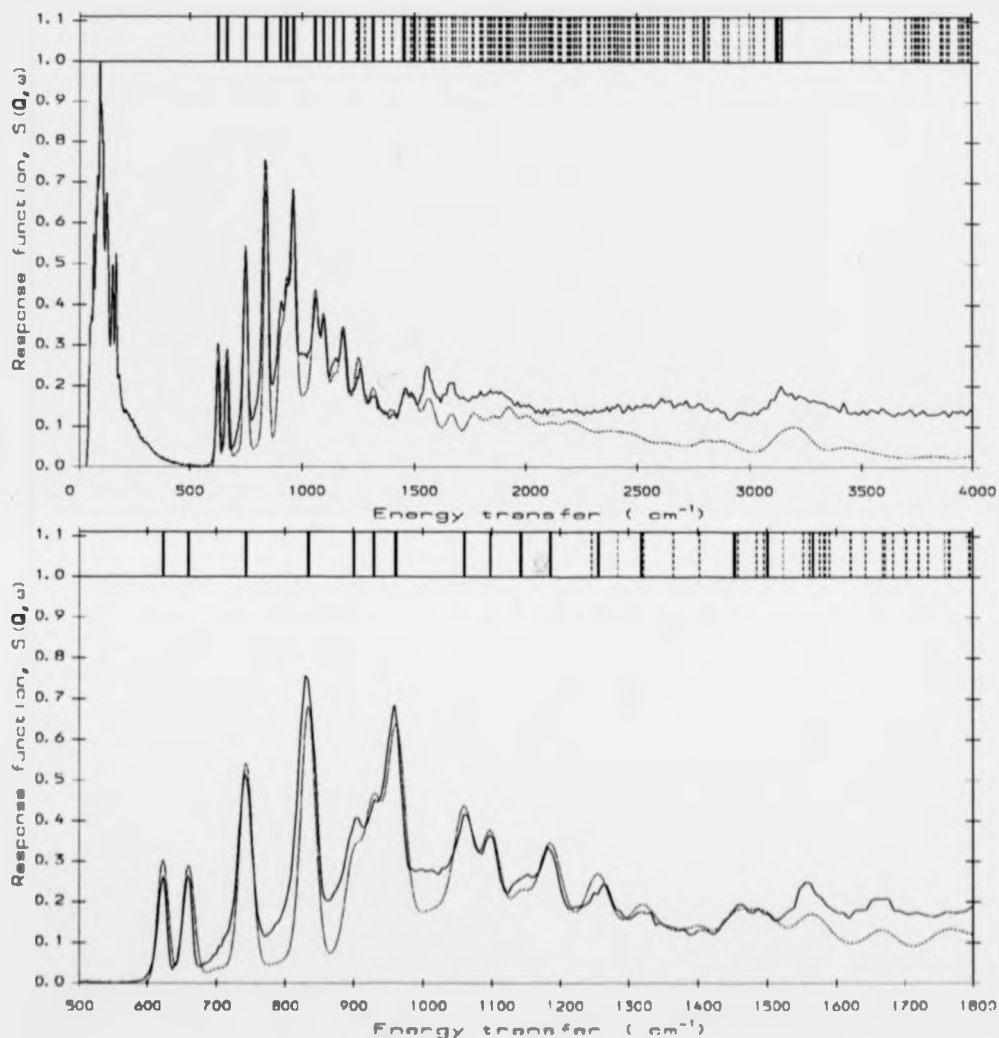


Figure 3.11: Calculated INS spectrum of solid state imidasole (dashed curve) using the force field developed in this study (presented in table 3.5) superimposed on the experimental INS spectrum (solid curve). The upper plot shows the entire spectrum and the lower plot shows the same spectrum over the range of particular interest (i.e. $500 - 1800\text{cm}^{-1}$). The calculation includes fundamental, overtone and combination excitations whose frequencies are indicated in the bands at the top of each plot, (i.e. solid lines are fundamentals and dotted lines are overtones or combinations). A full numerical powder average is employed and phonon wings are calculated up to 8 terms based on the experimental lattice phonon spectrum from $0 - 500\text{cm}^{-1}$ and an overall Debye-Waller factor of 0.011\AA^2 .

CHAPTER 3. INELASTIC NEUTRON SCATTERING

the comparison is not strictly justified. It is nevertheless instructive to make the comparison because the gaseous and aqueous vibrational spectra only differ significantly from the solid state in the frequency of one mode, the A'' NH wag. Since the NH wagging motion is effectively uncoupled from the motion in the rest of the molecule the calculated spectrum from the force field of Fan et al. does yield to comparison with figure 3.11 in all regions except around 961cm^{-1} , which is the frequency at which the NH wag occurs in the solid state. As may be seen from the frequency bands at the top of each plot in figures 3.11 and 3.10, the pattern of fundamental excitations generated by the two force fields is almost the same; the intensities of the corresponding peaks are however very different. This emphasizes the danger in judging the quality of a force field from its eigenvalues alone; the INS intensities are determined from the eigenvectors of a force field.

In table 3.6 the eigenvalues of force fields from a further five studies are listed and compared to the experimental assignment of the fundamental frequencies as used in this study. Of the published results in table 3.6 all but those of Colombo et al. are ab initio calculations similar to those of Fan et al. already discussed on page 83 for free imidazole. The difference between the ab initio calculations lies in the choice of the basis set of elementary functions¹⁹ used to model the solutions to the Hartree-Fock self consistent field (HF-SCF) equations, the molecular geometry employed, and subsequently the factors used to scale the results. Fan et al. use the standard 4-21G atomic basis set, (114), which is similar to the 4-31G basis (widely used in early MO-LCAO-SCF calculations) of Ditchfield et al., (29), but is less time consuming and supposedly of equal accuracy. The other ab initio calculations either similarly use the 4-21G basis or comparable bases using fewer (3-21G) or more (6-31G) Gaussian components in the linear combinations representing the atomic orbitals. Ab initio force fields are sensitive functions of the molecular geometry (due to the anharmonicity of molecular

¹⁹In all cases, the radial part of the atomic orbitals (AO) was emulated by fixed linear combinations of Gaussians with predetermined coefficients that model the HF-SCF orbitals. A widely used basis set is the 4-21G basis. This denotes linear combinations of 4,4,2 and 1 Gaussians to model the radial part of the $1s$, $2s$, $3s$, and $4s$, AO's respectively and 4,2 and 1 Gaussians to model the $2p$, $3p$, and $4p$, AO's (where i and o denote inner and outer orbitals). This grouping of simple functions in linear combinations with constant relative coefficients in order to model AO's is called contraction. Although the relative coefficients of the Gaussians in each AO is fixed, the coefficients of the AO's themselves in the linear combinations (LCAO) describing the molecular orbitals (MO) are not fixed and are optimised to produce a minimum total energy for the system in question.

CHAPTER 3. INELASTIC NEUTRON SCATTERING

Assignment used in present study cm^{-1}	Loeffen et al. (80):Results of present study cm^{-1}	Fan et al. (38):ab initio 4-21G basis cm^{-1}	Majoube et al. (86):ab initio 3-21G basis cm^{-1}	Majoube et al. (88):ab initio 4-21G basis cm^{-1}	Sadlej et al. (125):ab initio 4-21G basis cm^{-1}	Sadlej et al. (124):ab initio 6-31G basis cm^{-1}	Colombo et al. (16):fitted force field cm^{-1}
A' modes							
ν_1 3145	3146	3161	3160	3160	3495	3336	3140
ν_2 3126	3127	3133	3133	3133	3467	3312	3133
ν_3 3125	3120	3083	3132	3132	3464	3308	3119
ν_4 2800	2800	3518	3518	3517	3885	3674	2820
ν_5 1561	1567	1545	1541	1570	1689	1570	1573
ν_6 1498	1500	1474	1467	1486	1612	1537	1546
ν_7 1445	1452	1397	1395	1394	1529	1496	1545
ν_8 1326	1319	1334	1313	1336	1440	1402	1505
ν_9 1265	1255	1259	1267	1257	1395	1303	1451
ν_{10} 1186	1186	1145	1161	1151	1253	1202	1406
ν_{11} 1142	1143	1132	1118	1095	1164	1179	1349
ν_{12} 1098	1098	1083	1092	1083	1136	1129	1199
ν_{13} 1061	1060	1059	1073	1045	1113	1106	1171
ν_{14} 938	945	926	926	928	1040	946	1128
ν_{15} 908	901	896	894	893	996	906	1086
A'' modes							
ν_{16} 961	961	514	-	509	1065	526	932
ν_{17} 935	930	853	-	867	1004	819	887
ν_{18} 834	834	806	-	823	900	771	871
ν_{19} 743	742	729	-	712	740	693	760
ν_{20} 661	661	659	-	647	704	686	611
ν_{21} 623	623	635	-	632	695	641	526

Table 3.6: Comparison of the vibrational spectra (eigenvalues) of the force field of imidazole from various studies that exist in the literature. The results are compared both with the experimental assignment used in the present study and the eigenvalues from the force field developed by the author.

vibrations, especially stretches). The experimental geometry of Christen et al., (13), is used in all but two cases, (124), (125), in which the theoretically optimised geometry is preferred. Due to the deficiency of the HF-SCF approximation and the finite basis set, the calculated frequencies of the ab initio force fields are systematically too high. In the Fan et al. study 9 scale factors are exported from a fitted calculated spectrum of benzene; in the two studies by Majoube et al. 9 scale factors are calculated and shown to be similar to those of Fan et al.; the results in the studies by Sadlej et al. are unscaled. The study by Colombo et al. is an early normal mode analysis using estimates for the diagonal elements of the force field (based on previous works) that were partly adjusted for the best fit to experiment; it is the only other study which was intended to model the *solid state* imidazole modes.

The vibrational frequencies from the present study fit the experimental assignment with

CHAPTER 3. INELASTIC NEUTRON SCATTERING

a mean deviation of $\pm 3\text{cm}^{-1}$. Fan et al. quoted their results as having a mean deviation of $\pm 14\text{cm}^{-1}$ (i.e. $\pm 9\text{cm}^{-1}$ for A^{-1} modes and $\pm 27\text{cm}^{-1}$ for A'' modes); for the studies of Majoube the mean deviation was quoted as being between 9.7 and 13.5cm^{-1} . For the other studies the discrepancy between predicted and experimental frequencies was considerably greater. If the results of Fan et al. are compared with the solid state assignment used in this study then, ignoring the poorly modelled NH modes, (ν_4 and ν_{16}), the mean deviation is 18cm^{-1} . It is clear that the force field from the present study predicts the vibrational spectrum of solid state imidazole considerably better than any of the published works that the author is aware of.

A further test of the quality of the force field presented here is to compare the frequencies it predicts for imidazole, after isotopic substitution, with experimental values. This is shown in table 3.7 in which the experimental vibrational spectra from Perchard et al., (104), is taken for three deuterated variants; imidazole- $\text{d}_{(1)}$, imidazole- $3\text{d}_{(2,4,5)}$ and imidazole- 4d in the solid state. In each case the mean deviation between the predicted and experimental frequency is given which, for the results of Fan et al., do not include the frequencies belonging to the poorly modelled NH modes, ν_4 and ν_{16} . Even with this concession in calculating the mean deviation, it is evident that the force field presented here reproduces the vibrational frequencies in the deuterated states of imidazole more precisely than that of Fan et al. and also accurately predicts the ν_4 and ν_{16} frequencies.

The advantage of the INS studies is that there is scope to refine the eigenvectors of a force field while still retaining a good fit of the calculated eigenvalues to the experimental frequencies; this translates to refining the calculated peak intensities in the INS spectrum while maintaining the peak positions. It is therefore possible to confidently interpret the eigenvectors of the force field as the normal modes of the molecule. This is done pictorially in figure 3.12 in which the eigenvectors of the force field have been transformed into cartesian displacement coordinates and normalised so as to represent the standard deviation of the displacement probability density in the ground state, (refer to section 3.3.4). These displacements are represented as vectors attached to each atom which have been further mass-weighted and scaled by a factor of 10 for clarity.

CHAPTER 3. INELASTIC NEUTRON SCATTERING

mode	imidazole			imidazole-d ₍₁₎			imidazole-3d _(2,4,5)			imidazole-4d		
	Exp. assign. Loeffen et al. cm ⁻¹	Calc. freq. Loeffen et al. cm ⁻¹	Calc. freq. Fan et al. cm ⁻¹	Exp. assign. Perchard et al. cm ⁻¹	Calc. freq. Loeffen et al. cm ⁻¹	Calc. freq. Fan et al. cm ⁻¹	Exp. assign. Perchard et al. cm ⁻¹	Calc. freq. Loeffen et al. cm ⁻¹	Calc. freq. Fan et al. cm ⁻¹	Exp. assign. Perchard et al. cm ⁻¹	Calc. freq. Loeffen et al. cm ⁻¹	Calc. freq. Fan et al. cm ⁻¹
A'												
ν_1	3145	3146	3161	3140	3146	3161	2800	2800	3518	2376	2375	2366
ν_2	3125	3127	3133	3120	3127	3134	2376	2376	2366	2334	2348	2316
ν_3	3125	3120	3083	3120	3121	3083	2346	2346	2316	2334	2327	2292
ν_4	2800	2800	3518	2132	2117	2587	2329	2327	2293	2140	2110	2888
ν_5	1561	1567	1545	1542	1537	1524	1510	1495	1486	1453	1459	1462
ν_6	1498	1500	1474	1475	1487	1470	1458	1445	1400	1430	1435	1396
ν_7	1445	1452	1397	1355	1359	1332	1428	1431	1387	1338	1324	1309
ν_8	1326	1319	1334	1317	1312	1321	1257	1250	1271	1260	1258	1263
ν_9	1265	1255	1259	1241	1239	1255	1205	1209	1128	1114	1147	1104
ν_{10}	1186	1186	1145	1134	1148	1129	1122	1127	1104	1020	1022	984
ν_{11}	1142	1143	1132	1101	1109	1118	1020	994	947	955	983	937
ν_{12}	1098	1098	1083	1060	1056	1059	930	943	941	915	915	914
ν_{13}	1061	1060	1059	960	1005	921	882	874	881	850	831	821
ν_{14}	938	945	925	914	937	909	808	815	809	805	812	797
ν_{15}	908	901	896	875	834	838	768	728	771	764	716	767
A''												
ν_{16}	961	961	514	924	930	853	962	957	499	770	800	745
ν_{17}	935	930	853	836	851	806	770	780	745	725	731	731
ν_{18}	834	834	806	746	744	729	725	681	731	670	681	381
ν_{19}	743	742	729	672	705	383	600	627	582	598	612	582
ν_{20}	661	661	659	652	655	659	550	562	539	548	560	539
ν_{21}	623	623	635	615	623	632	525	513	521	525	512	505
mean discrep. between calc. and experim. cm ⁻¹		3.0	17.7	-	12.3	17.9	-	12.0	28.7	-	14.4	19.7

Table 3.7: Comparison of the predicted vibrational frequencies of imidazole and three of its deuterated variants using the force field developed by the author and that of Fan et al. (38) with the experimental values for solid state imidazole from Perchard et al. (104).

CHAPTER 3. INELASTIC NEUTRON SCATTERING

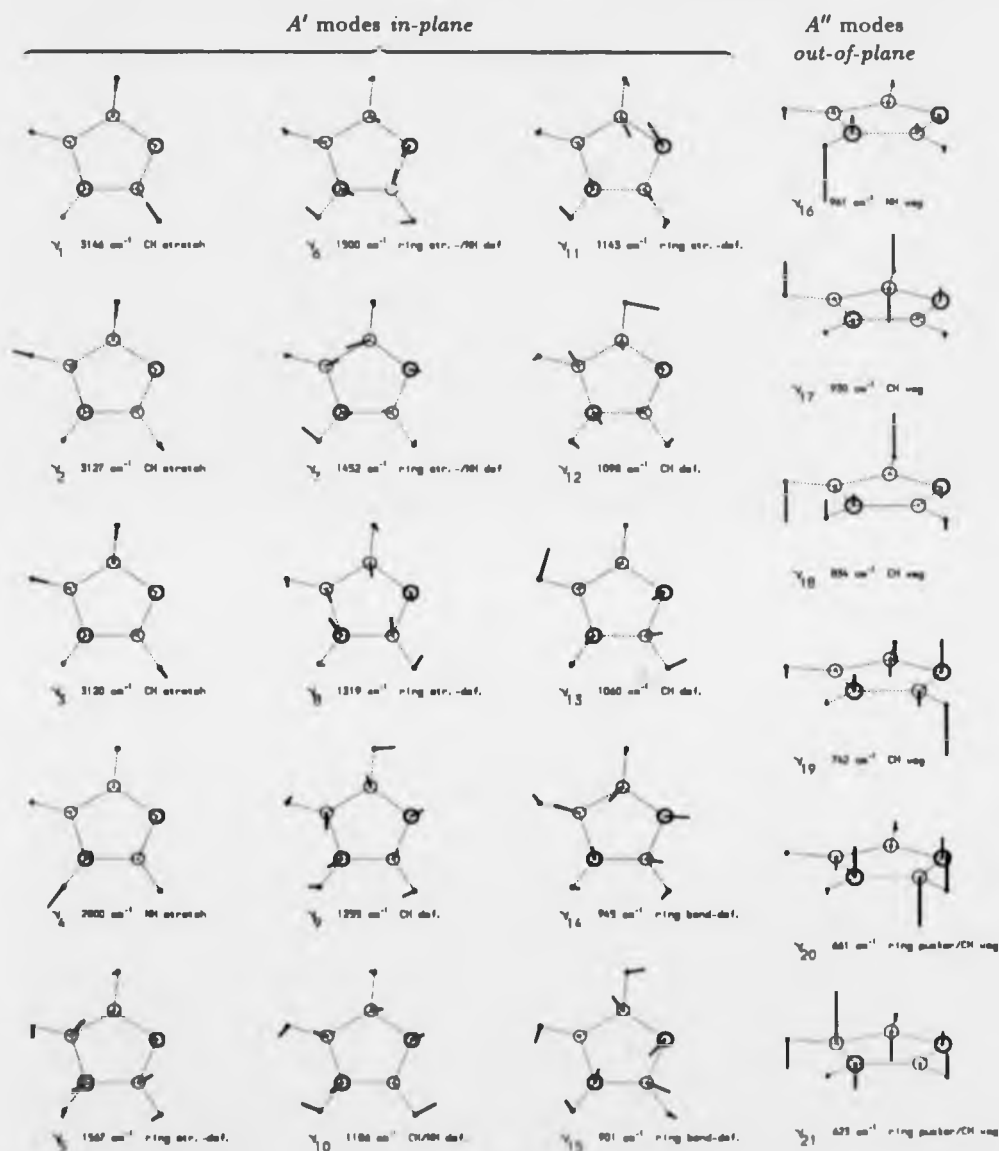


Figure 3.12: Ground state normal modes of solid state imidazole. The root-mean-squared atomic displacement vectors have been mass-weighted (to enhance the carbon and nitrogen atom motion) and are scaled by a factor of 10 for clarity. The nitrogen atoms are denoted by the heavy circles.

CHAPTER 3. INELASTIC NEUTRON SCATTERING

mode	calculated vibrational frequency cm ⁻¹	vibrational composition of normal mode based upon potential energy distribution among internal symmetry coordinates (8 most significant components above 5%)							approximate description of mode
A' : in-plane vibrations									
ν_1	3146	68% CH ₇	+	26% CH ₈				CH stretch	
ν_2	3127	51% CH ₉	+	39% CH ₈	+	7% CH ₇		CH stretch	
ν_3	3120	44% CH ₉	+	32% CH ₈	+	22% CH ₇		CH stretch	
ν_4	2800	97% NH ₆						NH stretch	
ν_5	1567	19% R ₃	+	17% R ₁	+	17% δ CH ₉	+	7% R ₂	
ν_6	1500	28% R ₃	+	21% δ NH ₆	+	11% δ CH ₇	-	10% δ CH ₈ /R ₁₋₅	
ν_7	1452	31% R ₃	+	17% δ NH ₆	-	12% R ₆ /R ₁₋₅	+	8% R ₄	
ν_8	1319	40% R ₂	+	23% R ₃	+	9% R ₆ /R ₁₋₅	+	8% δ CH ₈	
ν_9	1255	22% δ CH ₈	+	11% δ CH ₇	+	9% R ₁	+	7% R ₆	
ν_{10}	1186	22% δ CH ₇	+	16% δ NH ₆	+	13% R ₃	+	7% CH ₉	
ν_{11}	1143	34% R ₄	-	16% R ₆ /R ₁₋₅	+	13% R ₃	+	9% R ₂	
ν_{12}	1098	27% δ CH ₈	-	22% R ₂	-	14% R ₆ /R ₁₋₅	+	6% R ₁	
ν_{13}	1060	35% δ CH ₉	+	19% R ₁	+	13% R ₃	+	6% δ CH ₇	
ν_{14}	945	49% R ₇	+	11% R ₄	+	11% R ₁	+	6% δ CH ₇	
ν_{15}	901	27% R ₆	-	15% R ₆ /R ₁₋₅	+	6% R ₁		ring bend-def	
A'' : out-of-plane vibrations									
ν_{16}	961	85% γ NH ₆						NH wag	
ν_{17}	930	43% γ CH ₈	-	19% R ₆ / γ CH ₉	+	14% R ₃	+	11% R ₆ / γ CH ₉	
ν_{18}	834	34% γ CH ₈	+	27% γ CH ₉	+	13% R ₆ / γ CH ₉	+	9% R ₃ / γ CH ₈	
ν_{19}	742	33% R ₃	+	20% R ₆ / γ CH ₇	+	10% γ CH ₇	+	9% R ₂	
ν_{20}	661	26% R ₃	-	26% R ₆ / γ CH ₇	+	22% γ CH ₇	-	11% R ₄	
ν_{21}	623	27% R ₂	-	29% R ₆ / γ CH ₈	+	21% γ CH ₉	-	6% R ₆ / γ CH ₉	
							-	5% R ₆ / γ NH ₆	
								5% R ₆ / γ NH ₆	
								5% R ₆ / γ NH ₆	
								5% R ₆ / γ NH ₆	
								5% R ₆ / γ NH ₆	
								5% R ₆ / γ NH ₆	
								5% R ₆ / γ NH ₆	
								5% R ₆ / γ NH ₆	
								5% R ₆ / γ NH ₆	
								5% R ₆ / γ NH ₆	
								5% R ₆ / γ NH ₆	
								5% R ₆ / γ NH ₆	
								5% R ₆ / γ NH ₆	
								5% R ₆ / γ NH ₆	
								5% R ₆ / γ NH ₆	
								5% R ₆ / γ NH ₆	
								5% R ₆ / γ NH ₆	
								5% R ₆ / γ NH ₆	
								5% R ₆ / γ NH ₆	
								5% R ₆ / γ NH ₆	
								5% R ₆ / γ NH ₆	
								5% R ₆ / γ NH ₆	
								5% R ₆ / γ NH ₆	
								5% R ₆ / γ NH ₆	
								5% R ₆ / γ NH ₆	
								5% R ₆ / γ NH ₆	
								5% R ₆ / γ NH ₆	
								5% R ₆ / γ NH ₆	
								5% R ₆ / γ NH ₆	
								5% R ₆ / γ NH ₆	
								5% R ₆ / γ NH ₆	
								5% R ₆ / γ NH ₆	
								5% R ₆ / γ NH ₆	
								5% R ₆ / γ NH ₆	
								5% R ₆ / γ NH ₆	
								5% R ₆ / γ NH ₆	
								5% R ₆ / γ NH ₆	
								5% R ₆ / γ NH ₆	
								5% R ₆ / γ NH ₆	
								5% R ₆ / γ NH ₆	
								5% R ₆ / γ NH ₆	
								5% R ₆ / γ NH ₆	
								5% R ₆ / γ NH ₆	
								5% R ₆ / γ NH ₆	
								5% R ₆ / γ NH ₆	
								5% R ₆ / γ NH ₆	
								5% R ₆ / γ NH ₆	
								5% R ₆ / γ NH ₆	
								5% R ₆ / γ NH ₆	
								5% R ₆ / γ NH ₆	
								5% R ₆ / γ NH ₆	
								5% R ₆ / γ NH ₆	
								5% R ₆ / γ NH ₆	
								5% R ₆ / γ NH ₆	
								5% R ₆ / γ NH ₆	
								5% R ₆ / γ NH ₆	
								5% R ₆ / γ NH ₆	
								5% R ₆ / γ NH ₆	
								5% R ₆ / γ NH ₆	
								5% R ₆ / γ NH ₆	
								5% R ₆ / γ NH ₆	
								5% R ₆ / γ NH ₆	
								5% R ₆ / γ NH ₆	
								5% R ₆ / γ NH ₆	
								5% R ₆ / γ NH ₆	
								5% R ₆ / γ NH ₆	
								5% R ₆ / γ NH ₆	
								5% R ₆ / γ NH _{6</}	

Table 3.8: Vibrational composition of normal modes of solid state imidazole derived from the force field presented in table 3.5. The values represent the potential energy distribution (PED), in percent, among the intuitive non-minimum basis set of internal coordinates, S , given in table 3.4. Only the five largest components in the PED are listed for each mode and only if their contributions are greater than 5%. Coupling constants (i.e. off diagonal elements in the force field) which contribute to the PED are denoted by the row/column internal coordinates. An approximate description is offered for each mode.

Figure 3.12 should be interpreted in conjunction with the potential energy distribution (PED) in each normal mode as given in table 3.8. This provides a quantitative measure of the vibrational composition, or character, of each normal mode in terms of the non minimum basis set of internal coordinates. Based on the eigenvectors and the PED the following broad description of the imidazole vibrational spectrum is proposed:

- $\nu_1 \rightarrow \nu_4$ are high frequency in-plane stretch modes. Notice the purity of the NH stretch (97%) which is a vibration almost uniquely in the NH_6 internal coordinate.
- $\nu_5 \rightarrow \nu_8$ and ν_{11} are in-plane stretching deformations of the imidazole ring with very little associated hydrogen motion.

CHAPTER 3. INELASTIC NEUTRON SCATTERING

- $\nu_9, \nu_{10}, \nu_{12}$ and ν_{13} are essentially in-plane hydrogen wagging modes with some associated motion of the ring. ν_{10} resembles a ring breathing motion.
- ν_{14} and ν_{15} are large in-plane bending deformations of the ring; the effect is an oscillatory elongation of the ring.
- $\nu_{16} \rightarrow \nu_{18}$ are strong out-of-plane hydrogen wags but not including the C_2 hydrogen situated between the two nitrogen atoms. Again notice the purity of the NH wag which is almost entirely described (85%) by the γNH_6 internal coordinate.
- $\nu_{19} \rightarrow \nu_{21}$ are out-of-plane torsional puckers of the ring involving large scale hydrogen motion; this particularly involves wagging of the C_2 hydrogen.

Note that the NH in-plane wagging motion is distributed between the modes ν_8, ν_7 and ν_{10} (i.e. $1500, 1452$ and 1186cm^{-1}) with no one mode showing a dominant NH wagging character.

The assignment broadly corresponds to that of Perchard et al. and Fan et al.. Discrepancies arise for the 1245cm^{-1} band, represented here by ν_9 at 1255cm^{-1} , which Perchard et al. assigned as the NH in-plane wag whereas table 3.8 indicates it to have no NH wagging character. Also the 1160cm^{-1} band is unassigned whereas it is clearly seen in this study as an in-plane CH/NH deformation mode at 1186cm^{-1} . For the out-of-plane modes Perchard et al. assign the 740cm^{-1} band, represented here by ν_{19} at 742cm^{-1} , to be a CH wag whereas it is predominantly seen to be a torsional ring pucker in table 3.8.

Some controversy exists in the literature, amongst those articles which publish PED's, as to which of the in-plane normal modes have NH wagging character. Majoube et al., (88), calculate the NH wagging to be present in modes ν_8, ν_7 and ν_{10} using a 4-21G basis set but in a later article, (86), using a 3-21G basis set give the modes as ν_8, ν_7 and ν_{12} . In the fitted normal mode analysis by Colombo et al. the calculated bands at 1545cm^{-1} and 1451cm^{-1} , equivalent to ν_8 and ν_8 here, both contain about 25% NH wagging character. Sadlej et al., (124), assign the ν_8, ν_8 and ν_7 modes as having NH wagging character when they used the 6-31G basis set but obtained a different answer, (125), when they used the 4-21G basis; i.e. ν_8, ν_7 and ν_{10} . This latter article is the only case which corroborates the assignment here

CHAPTER 3. INELASTIC NEUTRON SCATTERING

in which the modes ν_6 , ν_7 and ν_{10} are found to have 21, 17 and 16% in-plane NH wagging character respectively.

There is also considerable difference between the PED of the out-of-plane A'' modes presented here and the results in the literature. In the studies of Majoube et al., (86), (88), the mode at 724cm^{-1} is predominantly due to out-of-plane CH wagging, whereas in the present study this mode, represented by ν_{19} at 742cm^{-1} , is predominantly a torsional ring pucker; this change is again corroborated by the ab initio calculations of Sadlej et al., (124), (125). In the normal mode analysis of Colombo et al. the torsional motion and CH or NH wagging motion is fairly distributed throughout all of the out-of-plane modes which is not corroborated anywhere else in the literature.

In short, there are several discrepancies in the wealth of assignments that exist for imidazole in the literature. Most of the PED assignments were based on ab initio calculations involving a variety of basis sets and molecular geometries. In the study by Majoube et al. (88), the PED assignment was calculated for imidazole based on three different geometries (involving the experimental microwave structure and the theoretical structure) and the vibrational compositions were found to vary significantly. In the same article it is quoted that great care has to be taken when the calculated frequencies are scaled as this appreciably changes the vibrational composition of the modes; the results of the present study are best corroborated by the ab initio PED's of Sadlej et al. whose calculations are left unscaled.

3.5.6 Summary of INS Study of Imidazole

A harmonic force field for solid state imidazole is presented. It was produced by refining a published force field for free imidazole which generates the correct eigenvalues (for all but the NH wagging mode) but does not reproduce the hydrogen-weighted vibrational density of states of imidazole (measured by INS); this is known to be a more sensitive test of a force field since it checks both the eigenvalues and eigenvectors of the secular equation of motion.

The new force field more accurately predicts the frequency spectrum of imidazole and three of its deuterated counterparts than previously published studies. It also models the hydrogen-weighted vibrational density of states significantly better than the starting force

CHAPTER 3. INELASTIC NEUTRON SCATTERING

field permitting the form of the 21 normal modes to be interpreted with confidence.

The assumptions made in the study were that the molecule may be treated as effectively decoupled from the crystal lattice thus generating only non-dispersive optical peaks in the INS spectrum above 500cm^{-1} and therefore yielding to the isolated molecule analysis. Further the known H-bonding was assumed to only affect the NH modes in the optical spectrum and was accounted for by increasing the NH mode force constants; this assumption is justified by the negligible shifts observed for all bands except the NH vibrations on comparing gaseous, aqueous and solid state data. The entire study was within the framework of the harmonic approximation.

The study issues a warning about the dangers of assessing the quality of molecular force fields on the basis of the frequency spectrum alone. It reaffirms the view that the scaling of *ab initio* force fields by several parameters, whilst yielding a better fit to the frequency vibrational spectrum, can seriously alter the vibrational composition of the various modes.

The result of this study is a reliable force field for imidazole that, in the following section, is incorporated into a much larger force field for the zinc (II) tetraimidazole molecule.

3.6 INS Study of Zinc Tetraimidazole Complex

3.6.1 Physical Characteristics of Zinc Tetraimidazole Complex

We consider the compounds containing the anions perchlorate and tetrafluoroborate. The crystal structure of the perchlorate compound exists in the literature at room temperature, (2), and that of the tetrafluoroborate has been done for this study at 100K and 150K, (79), and is discussed in section 2.3. The crystals of both compounds are white and monoclinic with melting points of 189 and 195°C respectively. The unit cells are $C2/c$ space group symmetry containing four molecules and have the same dimensions for each compound to within 6%. In the cation the zinc atom is approximately tetrahedrally coordinated to four imidazole rings at the N_3 position (e.g. in the perchlorate compound the N-Zn-N angles are all to within 4.1° of the exact tetrahedral angle). This slight deviation lifts the T_d symmetry of the coordination. The point group of the entire cation is C_2 as the zinc lies on a 2-fold axis.

CHAPTER 3. INELASTIC NEUTRON SCATTERING

Cartesian atomic coordinates of asymmetric unit (Å)							
atom	x	y	z	atom	x	y	z
Zn ₁	-2.0628	2.0847	4.3001	N ₁₁	-4.5128	4.2611	6.7620
N ₂	0.4697	-0.3252	6.4783	C ₁₂	-4.2480	3.4558	5.7330
C ₃	-0.5040	0.5823	6.3568	N ₁₃	-2.9527	3.1878	5.6873
N ₄	-0.6627	0.9190	5.0845	C ₁₄	-2.3804	3.8627	6.7453
C ₅	0.2663	0.1772	4.3762	C ₁₅	-3.3452	4.5290	7.4131
C ₆	0.9694	-0.5936	5.2302	H ₁₆	-5.2803	4.5522	6.9687
H ₇	0.7068	-0.6564	7.2396	H ₁₇	-4.9216	3.1178	5.1080
H ₈	-1.0325	0.9549	7.0874	H ₁₈	-1.4576	3.8216	6.9161
H ₉	0.3452	0.2471	3.4337	H ₁₉	-3.3282	5.0827	8.1696
H ₁₀	1.6775	-1.2193	5.0906				

Table 3.9: The cartesian coordinates of the asymmetric unit of the sinc (II) tetraimidazole complex as used in the normal mode analysis. The coordinates were taken from the x-ray crystallography of the tetrafluoroborate compound at 100K and modified such that the imidazole ring atoms lie exactly on the plane of best fit through the experimental coordinates. The crystallographic structure is depicted in figure 2.2 with consistent atomic labelling.

The independent Zn-N distances are 1.997(7) and 2.001(7)Å for the perchlorate compound and both 1.983(2)Å for the tetrafluoroborate compound. The imidazole molecules are planar within the errors of the crystallography but are forced to be exactly planar in this study as this is required for the normal mode analysis; the atom positions have therefore been projected onto the plane of best fit through the crystallographic positions. The imidazole rings are also inclined with respect to the Zn-N bonds such that the ring plane leans towards the 2-fold axis; for the perchlorate compound this inclination is 0.6 and 6.1° for the two imidazoles in the asymmetric group; for the tetrafluoroborate compound it is 4.9 and 1.9° at 100K. The inclinations are significant within the errors of the experiment and were observed to be important in causing certain degenerate vibrations to split in the normal mode analysis. The coordinate set adopted for the normal mode analysis was that given in table 3.9; the coordinates chosen were the tetrafluoroborate compound crystallographic coordinates at 100K; modified such that the imidazole rings are exactly planar.

The cation is engaged in hydrogen bonding with the anion via the outlying nitrogen atoms

CHAPTER 3. INELASTIC NEUTRON SCATTERING

of the imidazole ring. In the perchlorate compound the N-H...O distances are 2.95 and 3.06 Å for the two asymmetric branches respectively; in the tetrafluoroborate compound the N-H...F distances are 2.95 and 2.75 Å. Consequently the H-bonding is different in the two compounds and some small differences in the INS spectra might be expected in the vibrations of N-H and possibly in the acoustic modes.

A concern was the possible effect of the apparent bond shortening seen in x-ray crystallography due to the Bastiansen-Morino shrinkage effect (see (26), chapter 14) affecting, in particular, the NH and CH modes. Since INS is sensitive to hydrogen motion it was feared that an N-H or C-H bond length that was too short would not be able to correctly model the frequency and intensity of the peaks in the INS spectrum. This was tested by noting the effect on the calculated INS spectrum of increasing all the NH and CH bond lengths by 10%. There was no significant change and it is therefore assumed in this study that the Bastiansen-Morino effect is not significant with respect to the normal mode analysis of zinc tetraimidazole complexes.

3.6.2 Experimental Results

INS spectra of the four samples described in section 3.4.2 were recorded at 20K on the TFXA spectrometer, see section 3.4.1. The experimental results are compared after the spectrum of background neutron scatter from the cryostat and cadmium sample holder was subtracted.

Figure 3.13 presents the INS spectra of zinc (II) tetraimidazole compound with the perchlorate and tetrafluoroborate anion. The spectra are superimposed and expanded in the low frequency range, in which the skeletal modes of the zinc tetraimidazole cation are expected, and in the range $500 - 1800\text{cm}^{-1}$, in which most of the imidazole fundamental vibrations occur. The spectra are virtually identical throughout the entire frequency range except below 150cm^{-1} and the two peaks at 719 and 820cm^{-1} in the perchlorate spectrum which shift in the tetrafluoroborate spectrum. Since the crystal structures of the two compounds are known to be nearly identical, but differ in the hydrogen bonding, it is assumed that the differences in the INS spectra involve modes including H-bond vibrations. It is therefore probable that the two peaks at 719 and 820cm^{-1} in the perchlorate spectrum have significant NH vibrational

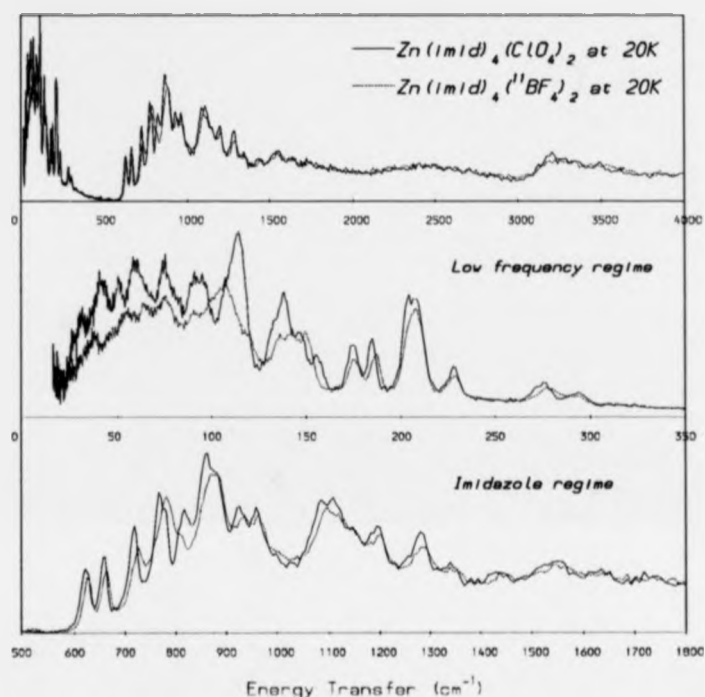


Figure 3.13: Inelastic neutron scattering spectra of powder samples of crystalline zinc (II) tetraimidazole perchlorate and tetrafluoroborate respectively at 20K recorded on the TFXA spectrometer, Rutherford Appleton Laboratory, U.K.. Boron-11 enriched tetrafluoroborate was used to prevent the very large neutron absorption cross section of boron-10 from masking the signal.

character. In the low frequency regime the shifts below 150cm^{-1} indicate that the cation is not completely independent of the anion; it may also be surmised that the different crystal field causes more restricted skeletal motion of the cation in the tetrafluoroborate compound since the INS intensities are less than in the perchlorate case. However it is significant that the peaks between 160 and 300cm^{-1} are much less affected than those lower in frequency; this will help in the assignment of these modes since it suggests skeletal modes involving vibrations of the core of the molecule which are less sensitive to changes in the crystal field. In general however the differences between the two spectra are small indicating that the isolated molecule assumption necessary for normal mode analysis is a reasonable one for this case.

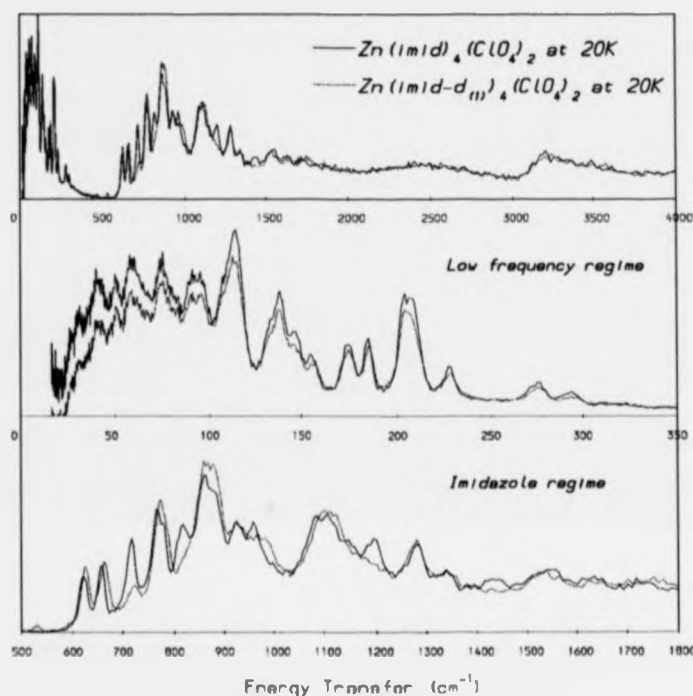


Figure 3.14: Inelastic neutron scattering spectra of powder samples of crystalline zinc (II) tetraimidazole perchlorate and its d_1 -deuterated analogue at 20 K recorded on the TFXA spectrometer, Rutherford Appleton Laboratory, U.K.. The imidazole rings of the cation were isotopically substituted at the NH positions.

Figure 3.14 depicts the same perchlorate spectrum as in figure 3.13 but superimposed on the INS spectrum of its d_1 -deuterated analogue. In this case the imidazole rings in the cation have been isotopically substituted at the nitrogen position as described in section 3.4.2. The spectra are almost identical at all frequencies except for some peaks which have disappeared in the deuterated case and in the low frequency regime where there is an increasing attenuation of the peak intensities. The peaks which disappear are at 719 , 820 and 1198cm^{-1} and a slight decrease at 1433cm^{-1} ; this confirms the supposition that the 719 and 820cm^{-1} peaks have strong NH vibrational character. A small peak appears at 533cm^{-1} which would correspond to the ND vibrations shifted from the above frequencies in the undeuterated spectrum. In

CHAPTER 3. INELASTIC NEUTRON SCATTERING

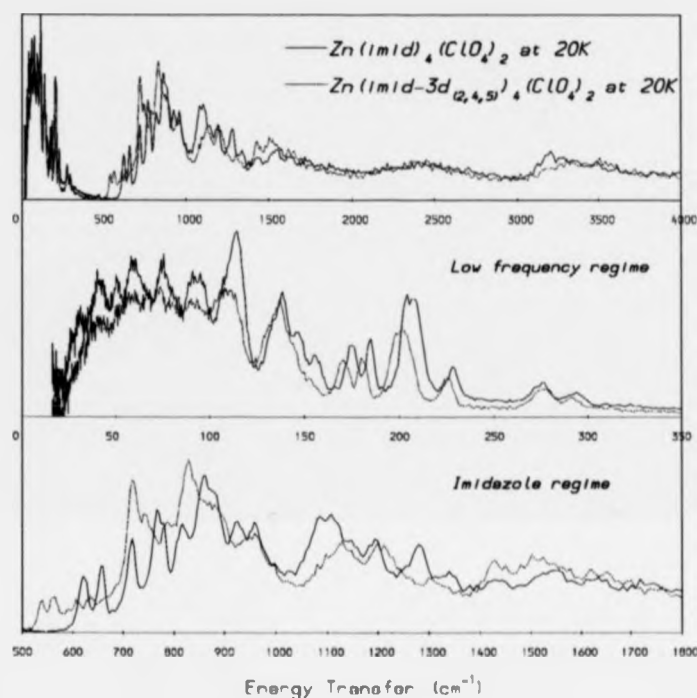


Figure 3.15: Inelastic neutron scattering spectra of powder samples of crystalline zinc (II) tetraimidazole perchlorate and its d_3 -deuterated analogue at 20K recorded on the TFXA spectrometer, Rutherford Appleton Laboratory, U.K.. The imidazole rings of the cation were isotopically substituted at all three carbon positions.

the low frequency regime an attenuation of all the modes is expected since the substituted hydrogen participates in all the skeletal modes whereas in the imidazole regime this is not true; in the imidazole regime the NH modes are very pure (see section 3.5) and deuteration only causes specific peaks to disappear while the rest of the spectrum is unaffected. However the increasing attenuation, especially below 100cm^{-1} , indicates an increasing contribution of the substituted hydrogen to each vibration and suggests lattice modes which are conveyed via the intermolecular H-bonds.

Figure 3.15 depicts the effect on the INS spectrum of deuteration the perchlorate compound at all three carbon positions of the imidazole branches. In this case the difference

CHAPTER 3. INELASTIC NEUTRON SCATTERING

between the two spectra is very great and they have been artificially scaled in order to compare features. Most of the imidazole regime exhibits large shifts in frequency and intensity upon deuteration, as would be expected. The peaks which remain unshifted and intense are those at 719 , 820 and 1198cm^{-1} which again indicates that they are pure NH modes. In the low frequency regime significant frequency shifts are evident. One source of concern with this data regards the quality of deuteration of the imidazole rings. Even if the yield was as high as 90% of deuterated sample, the 10% undeuterated material would contribute disproportionately to the overall INS signal due to the much larger neutron scattering cross section of protons compared to deuterons and the hydrogen-intensity-optimised nature of the spectrometer. This was not detected in the infrared product purity assay.

In the next sections the normal mode analysis of the zinc (II) tetraimidazole complex is described. For clarity the description of the analysis is split into two parts, one dealing with the low frequency regime of the INS spectrum i.e. the skeletal vibrations of the cation below 500cm^{-1} , and one dealing with the internal modes of the imidazole branches above

3.6.3 Low Frequency Regime ($< 500\text{cm}^{-1}$) - Strategy for Normal Mode Analysis

These low frequency modes may be broadly described as the skeletal vibrations of the molecule composed of large scale motion of the imidazole branches, which to a first approximation may be considered rigid at these low frequencies. The motions of the branches may be roughly categorised into Zn-N stretches, in-plane *wags* of the imidazole rings, out-of-plane *bends* and *torsions* of the imidazole rings about the Zn-N bond. (see figure 2.4.)

The initial problem in doing a normal mode analysis of zinc (II) tetraimidazole is the lack of information that already exists in the literature for this or similar compounds at low frequencies. To the authors knowledge, the only publications dealing with the vibrational spectrum of zinc (II) tetraimidazole compounds are those by Hodgson et al., (60), and Reedijk, (115), which involve infrared spectroscopy but do not extend below 185cm^{-1} . There is also some work dealing with the analogous compounds tetraphenylmethane and tetraphenylsilane, (39), (129), (130), (136), (159) but these vibrational spectra do show sig-

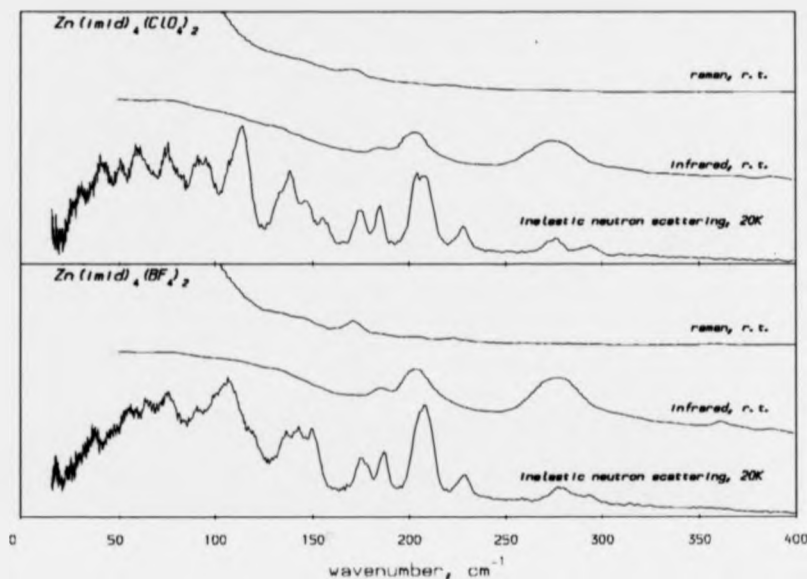


Figure 3.16: Superposition of experimental infrared, Raman and INS spectra below 500cm^{-1} of zinc (II) tetraimidazole perchlorate and tetrafluoroborate. Infrared spectra were recorded on a Bruker IFS 113V FT-IR spectrometer using compressed sample pellets of sample:polyethene in the ratio 1:10 with the assistance of Dr. M. Hegemann at the Universität Münster. Raman spectra were recorded using an argon ion laser with a 200mW excitation at 20498cm^{-1} , a double monochromator and Spex spectrometer with the assistance of Dr. J.D. Woollins at Imperial College, London.

nificant differences to that of zinc tetraimidazole although some general conclusions may be drawn.

In figure 3.16, the experimental infrared and Raman spectra of zinc (II) tetraimidazole perchlorate and tetrafluoroborate are compared with the experimental INS spectra of these compounds already presented; the significant peak positions are tabulated in table 3.10 and compared with existing information in the literature. There is a very clear one-to-one correspondence of vibrational frequencies between all methods despite the difference in experimental temperatures. However it is evident that the infrared and Raman spectra do not extend very low in frequency although they do represent a clear improvement over the published vibrational spectra.

CHAPTER 3. INELASTIC NEUTRON SCATTERING

Experimental Results, (cm^{-1})							Published Results, (cm^{-1})	
INS		infrared		Raman		symmetry assignment assuming T_d symmetry	Hodgson et al. ref. (60)	Reedijk ref. (118)
ClO_4	BF_4	ClO_4	BF_4	ClO_4	BF_4			
294	294					T_2	271 $\nu\text{Zn-N str.}$	272s $\nu\text{Zn-N str.}$
275	279	274s	277s	275w				
228	230			223s	223s			
202-208	202-208	203s	203s	203w	208w 205w 201w	T_2	199 $\delta\text{Zn-N-C def.}$	201m
185	187	184m	184m		187w			
175	176			171s	171s			
156	150			145w	156w	T_2	185 $\delta\text{Zn-N-C def.}$	
147	143				144m			
139	137		138w		133w			
132								
114	118				121w			
106	108							
97								
91	91							
76	75							
60	63							
51	55							
42	46							
30	37							

Table 3.10: Comparison of experimental and published results for the vibrational spectra of zinc (II) tetraimidazole perchlorate and tetrafluoroborate below 500cm^{-1} via the methods of infrared, Raman and INS. Note that in the case of infrared and Raman the intensity of the experimental peaks are denoted by w:weak, m:medium and s:strong. Also presented is a symmetry assignment of some of the modes assuming a T_d symmetry tetrahedral coordination of the zinc atom based on the infrared and Raman selection rules.

These data only yield limited information but it is possible to obtain an important indication as to a physical assignment of some of the modes; this forms the basis for the development of the normal mode analysis. To do this, the coordination of the zinc atom must first be assumed to be perfectly tetrahedral thus exhibiting a local T_d symmetry including the zinc and the four nearest nitrogen atoms. In this case, by consideration of optical selection rules²⁰, it is possible to identify the modes at 274, 203, 184 and 138cm^{-1} as belonging to the T_2 representation. These peaks are relatively intense in the infrared, which indicates a significant oscillation of the electric dipole of the molecule; a fact which would further indicate a strong involvement of the polar Zn-N bonds. As a consequence, these peaks are attributed

²⁰ For T_d symmetry only T_2 modes are infrared active whereas A_1 , E and T_2 modes are Raman active. Optical spectroscopy therefore positively identifies T_2 modes.

CHAPTER 3. INELASTIC NEUTRON SCATTERING

to the skeletal tetrahedral modes at the core of the molecule. This is in agreement with the observation made earlier (see page 103) for the peaks above 150cm^{-1} which were seen to be the least sensitive to changes in the crystal field incurred by exchanging the anion hence also indicating modes at the core of the cation. The assignment is further corroborated by the published studies, (60), (115), which also assign the modes 271, 199 and 185cm^{-1} to skeletal modes of the Zn-N core. As such, the low frequency regime has effectively been further subdivided into the region above 150cm^{-1} , which is associated with the skeletal tetrahedral modes about the coordination centre, and the region below 150cm^{-1} , which is thus composed of all the outer branch vibrations of the four rigid imidazole rings. This conclusion was also reached by Zelei, (159), in his study of the vibrational spectra of tetraphenylmethane in which he concludes that all benzene ring librations are expected to appear below 150cm^{-1} and the T_d skeletal modes occur above 200cm^{-1} .

The assumption of perfect tetrahedral coordination symmetry of the zinc atom is not exact since, as described in section 3.6.1, there are small deviations that lift the T_d symmetry to give C_2 . This is seen to split the triply degenerate T_2 modes into 2 B and 1 A singlets. However the deviations are slight implying that the assumption is a reasonable one for interpreting the sparse infrared and Raman spectra. The assumption of T_d coordination symmetry is the starting point in the development of a force field for the real molecule: this high T_d symmetry may be gradually lifted and replaced by symmetry of lower order, thereby making the molecular model more complicated until a final model evolves that reproduces the entire molecular vibrations of the zinc (II) tetraimidazole complex. The intermediate evolution of the model for the low frequency regime is displayed in figure 3.17 and each of the four stages are explained in the following subsections.

3.6.3.1 5-atom model: T_d symmetry

The model has perfect T_d symmetry and is composed of a central zinc atom and four extra-neous atoms whose bond distance to the zinc is the same as the Zn-N distance but whose mass and cross section are the same as an entire imidazole unit. The 5-atom tetrahedron has nine modes whose reduction is $A_1 + E + 2T_2$ (refer to appendix E for group table),

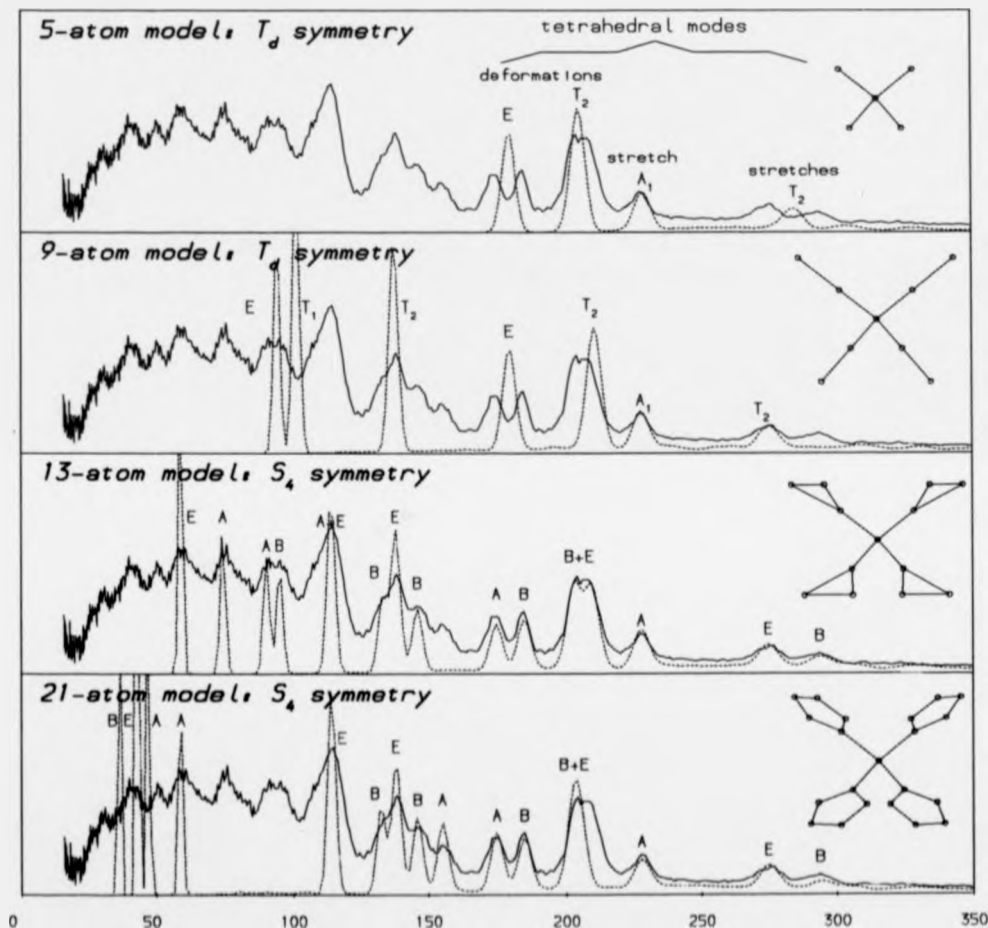


Figure 3.17: Diagram following the intermediate evolution of the molecular model for the sinc (II) tetraimidazole complex as used in the normal mode analysis. Each stage in the process is described by the size of the molecular model and the inherent symmetry; the model itself is depicted in the right-hand corner of each plot. The graphs show the theoretical INS spectra after refinement for each model (dashed lines) superimposed on the experimental INS spectrum of sinc (II) tetraimidazole perchlorate at 20K in the low frequency regime. The associated symmetry representations of each of the calculated peaks are also included.

CHAPTER 3. INELASTIC NEUTRON SCATTERING

four stretch modes ($A_1 + T_2$) and five deformation modes ($E + T_2$). The T_2 modes were targeted at the first two assigned frequencies from the infrared study i.e. 275 and 200cm^{-1} (the 275cm^{-1} mode is generally accepted as belonging to the Zn-N stretch, (60), (115)), the A_1 mode²¹ at the small peak at 228cm^{-1} and the E mode between the two peaks at 185 and 175cm^{-1} in the belief that the doublet E mode would later split when the symmetry was lifted. The model is described by 10 internal coordinates giving one redundancy in the internal symmetry coordinate set. The force field of 55 elements is completely described by 7 independent parameters due to the high symmetry but only 4 non-zero parameters were actually needed since the model refined quickly to produce the result in figure 3.17.

3.6.3.2 9-atom model: T_d symmetry

The imidazole mass and cross section in each branch is shared equally between two pseudo atoms and each branch is collinear with the zinc atom thereby retaining the T_d symmetry. The bond between the two pseudo atoms in each branch is made stiff by assigning a stretch constant of $500\text{mdyne}\text{\AA}^{-1}$ between them. The new model introduces eight new low frequency modes of symmetry ($E + T_1 + T_2$) which are associated with the indistinguishable rocking vibrations of the pseudo imidazoles to give a total of 17 low frequency modes. 22 internal coordinates are required with one redundancy in the internal symmetry coordinate set. The other 4 modes are high frequency vibrations of the stiff link between the pseudo atoms in each branch. The new T_2 mode was associated with the last assigned frequency from the optical study at 138cm^{-1} and the other two new modes were located at the positions of the next two peaks down in frequency. The force field has 253 elements but is completely described by 27 independent parameters due to the symmetry. Only nine non-zero parameters were needed since the model refined rapidly.

²¹This mode is predicted as being the A_1 symmetric breathing mode based on the similar assignment of the 236cm^{-1} band in the analogous tetraphenylmethane by Smith, (136) and Zelei, (189).

CHAPTER 3. INELASTIC NEUTRON SCATTERING

3.6.3.3 13-atom model: S_4 symmetry

The pseudo imidazoles are modelled as equilateral triangles with equal distribution of the imidazole mass and cross section. This lifts the T_d symmetry to give S_4 and means that the rocking vibrations of the branches are no longer indistinguishable but form distinct in-plane *wag* modes, out-of-plane *bend* modes and four new torsion modes ($A + B + E$). This produces the full complement of 21 low frequency internal modes. The lower symmetry (refer to appendix E for group table of S_4) permits many of the former degeneracies to split (e.g. all T_2 triplets split into an E doublet and a B singlet) although not all the lifted degeneracies actually separate until the pseudo imidazoles are inclined by 5° towards the S_4 axis to emulate the inclinations observed in the x-ray crystallography. In particular this is necessary in order to separate the A and B singlets generated from the former E mode between the two peaks at 185 and 175cm^{-1} . A schematic representation of the symmetry splittings through the development of the model up to the final model is given in figure 3.18. 34 internal coordinates are used including one redundancy; the remaining 12 modes ($3A + 3B + 3E$) are high frequency internal modes of the equilateral triangles. The internal force constants of the triangles are set at $99\text{mdyne}\text{\AA}^{-1}$ to avoid coupling with the low frequency modes. The force field of 595 elements is described by 30 independent parameters. This is rather a lot for the number of observations but was necessary in order to force some of the wags and bends etc. to appear higher than $5 \rightarrow 50\text{cm}^{-1}$ which was considered to be too low and to prevent their INS intensities from being too large. In retrospect it became obvious that this tendency was implicit in the model and in fact the model was wrong. This is discussed further in the next subsection.

3.6.3.4 21-atom model: S_4 symmetry

The equilateral triangles are expanded to be imidazole shaped pentagons with each apex of the pentagon constituting the mass and cross section of the respective carbon or nitrogen plus a hydrogen. The internal force constants of the pentagon are relaxed from the very stiff values used in the equilateral triangles in the previous model to approach more realistic values. No more low frequency modes appear although there are an extra 36 modes at high frequency

CHAPTER 3. INELASTIC NEUTRON SCATTERING

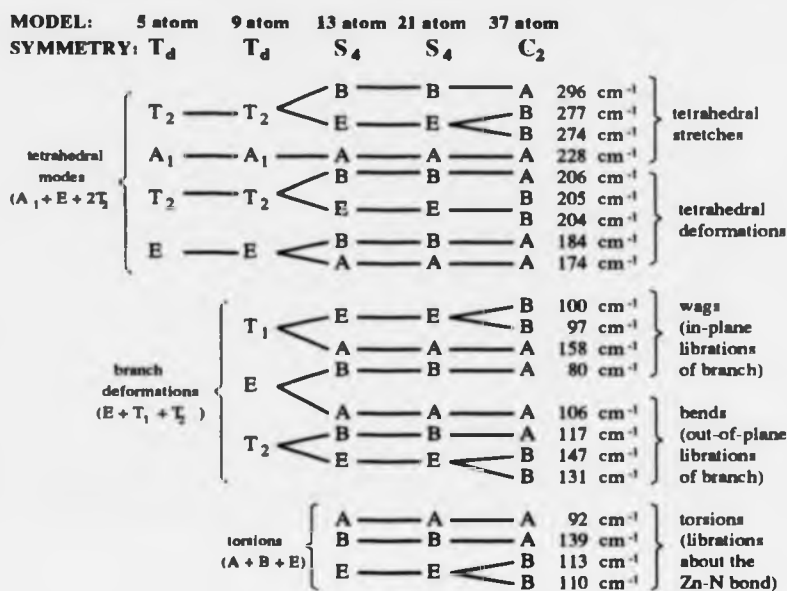


Figure 3.16: Flow diagram charting the evolution of symmetry of the normal modes of models developed to represent the low frequency vibrations of sinc (II) tetraimidazole. The chart marks the appearance of new modes as more complex models are introduced and how the inherent degeneracies are lifted as the group symmetry of the various models is lowered from 24-fold T_d to 2-fold C_2 which reflects the true symmetry of the molecule. The final refined eigenvalues of the normal mode analysis are also presented and broadly described in terms of physical vibrations of the molecule.

($9A + 9B + 9E$). The model is approximately complete at low frequency but in this form cannot properly model the INS intensities of the internal imidazole ring modes due to the lack of CH and NH bonds. As with the previous model four of the branch modes appear unexpectedly low in frequency except when many more force constants are introduced. This is considered to be a basic defect of the model because the pseudo imidazoles are held too loosely in position and therefore vibrate at very low frequencies with large INS amplitudes. For the fit shown in figure 3.17 the model has only 21 free parameters defining the force field (equivalent to the number of observations).

The fact that the 13-atom and 21-atom S_4 models tend to exhibit branch librations at very low frequencies is probably due to the inability of the two models to allow for the restraining

CHAPTER 3. INELASTIC NEUTRON SCATTERING

effects of inter-imidazole stearic interactions and intermolecular H-bonding. The former effect was concluded by Schlotter et al., (129), (130), to be very important for the analogous case of tetraphenylmethane. To model H-bonding is very difficult since in reality the entire crystal lattice should be taken into account. A first approximation was attempted by suspending the molecule in a *cage* of four massive atoms positioned at the extremities of the H-bonds and to which the molecule was hung. The results were confusing since the *cage* modes tended to mix strongly with the internal modes and the assigned modes (e.g. the tetrahedral skeletal modes) shifted significantly both in frequency and intensity. More importantly the *cage* model failed to significantly affect the very low frequency bending, wagging and torsional modes. A more appealing alternative was to try to model the stearic interaction between the imidazole branches via a network of connecting stretching force constants. This was favoured because it retained the isolated molecule model and impeded the free motion of the imidazole branches without having to emulate the complex effect of the crystal lattice.

3.6.3.5 37-atom final model: C_2 symmetry

The final model adopted for the normal mode analysis is represented in figure 3.19. All 37 atoms of the molecule are included at their crystallographic positions (as described in table 3.9) inferring a further lowering of the symmetry to C_2 . Stearic interaction between imidazole branches is modelled by a network of stretching force constants between the individual atoms. This coupling is described by just two force constants depending on whether the inter-imidazole link circumscribes the C_2 axis or crosses it. Their values were refined to be 0.064 and 0.056 mdyne \AA^{-1} respectively. The modelling of the stearic interaction in this way meant that far fewer independent parameters had to be included in the force field than was otherwise necessary to bring the calculated wag, bend and torsion modes to higher frequencies with appropriate INS intensities. The stearic interaction model does not significantly interfere with the internal imidazole modes which are also simultaneously generated by this model and are discussed in more detail further on. The refined force field for the low frequency regime based on this final model is discussed in the next section.

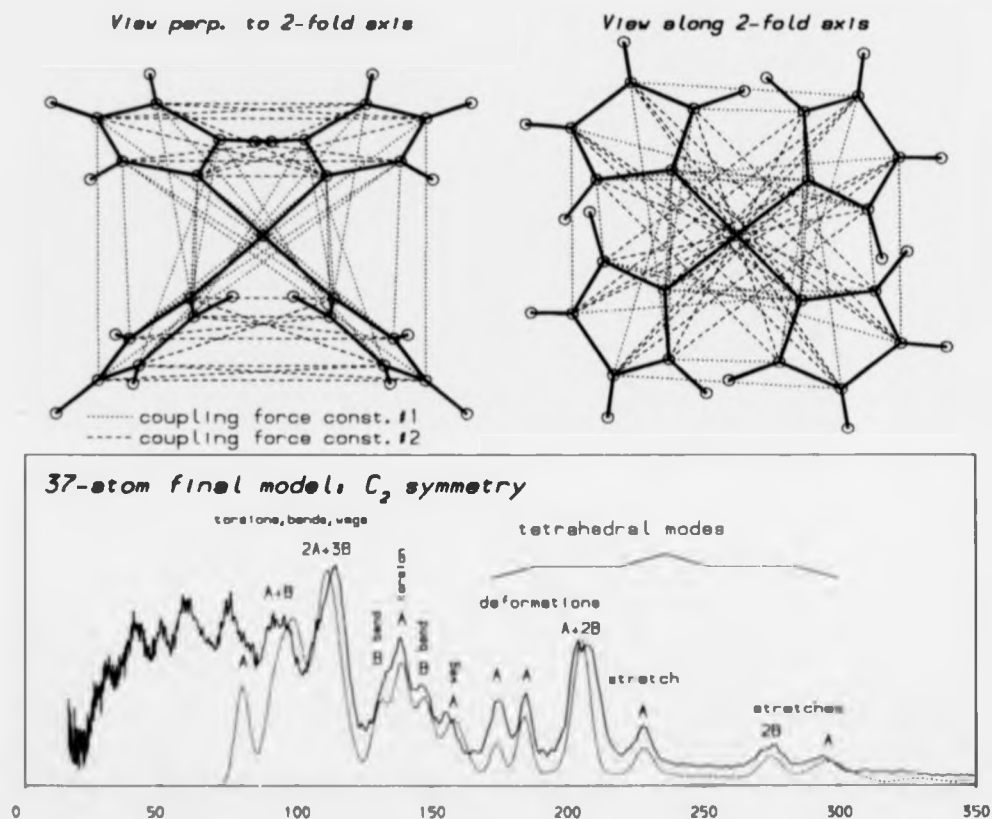


Figure 3.10: Diagram representing the final model employed in the normal mode analysis of the sinc (II) tetraimidazole complex. The schematic diagrams at the top show the model in two projections. All 37 atoms of the complex are included at the positions determined by x-ray crystallography and modified so that the imidazole branches are exactly planar. Interimidazole coupling is modelled by two independent force constants acting along the vectors between atoms denoted by the dashed lines; this was introduced to allow for the effect of steric interaction between the branches. Without this coupling many of the calculated imidazole wag, bend and torsion modes would tend to appear at far too low frequencies with INS intensities much greater than those observed. The graph at the bottom shows the best fitted calculated INS spectrum at low frequency using the final model.

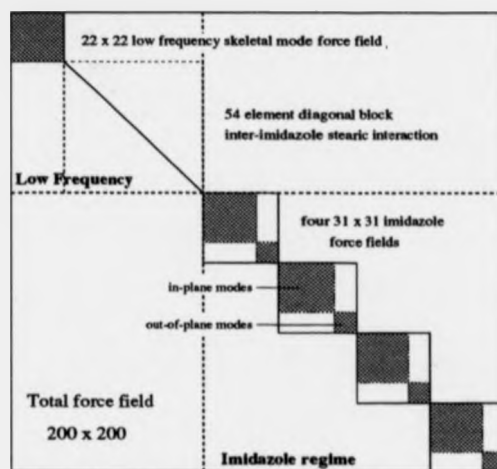


Figure 3.20: Schematic representation of the entire force field associated with the final 37-atom C_2 model for the normal mode analysis of zinc (II) tetraimidazole. The diagram shows that the force field may be regarded as a series of non-interacting blocks each acting on a set of internal coordinates specific to one part of the molecular motion. This effectively partitions the force field into a low frequency regime containing the skeletal mode and inter-imidazole coupling blocks and a high frequency regime containing the internal imidazole blocks.

3.6.4 Low Frequency Regime ($< 500\text{cm}^{-1}$) - Force Field and Eigenvectors

The force field for the model shown in figure 3.19 contains 200×200 elements. It is shown in figure 3.20 sub-divided into six non-interacting blocks that act on six separate sets of internal coordinates. The six sets comprise (i) the set of internal coordinates describing the low frequency skeletal modes (ii) the set of stretch coordinates defining the inter-imidazole coupling used to model the steric interactions between branches and (iii) four sets of internal coordinates describing the internal ring modes of the imidazole branches. It is a fundamental assumption of this model that none of these blocks interact; i.e. low frequency skeletal modes do not couple with the higher frequency internal imidazole modes. Based on this assumption it is possible to inspect each of these blocks as independent force fields relating to specific frequency regimes of the calculated spectrum.

The low frequency fit obtained in figure 3.19 is based on the upper two blocks in figure 3.20; i.e. the skeletal mode force field and the diagonal block containing the inter-imidazole cou-

CHAPTER 3. INELASTIC NEUTRON SCATTERING

internal coordinates, S_i ,
for low frequency
skeletal modes

S_1	=	$R(1, 4)$
S_2	=	$R(1, 13)$
S_3	=	$R(1, 22)$
S_4	=	$R(1, 31)$
S_5	=	$\angle(4, 1, 13)$
S_6	=	$\angle(4, 1, 22)$
S_7	=	$\angle(4, 1, 31)$
S_8	=	$\angle(13, 1, 22)$
S_9	=	$\angle(13, 1, 31)$
S_{10}	=	$\angle(22, 1, 31)$
S_{11}	=	$\tau(\text{about } 1, 4)$
S_{12}	=	$\tau(\text{about } 1, 13)$
S_{13}	=	$\tau(\text{about } 1, 22)$
S_{14}	=	$\tau(\text{about } 1, 31)$
S_{15}	=	$O(1, 4, 3, 5)$
S_{16}	=	$O(1, 13, 12, 14)$
S_{17}	=	$O(1, 22, 21, 23)$
S_{18}	=	$O(1, 31, 30, 32)$
S_{19}	=	$\angle(1, 4, 3)$
S_{20}	=	$\angle(1, 13, 12)$
S_{21}	=	$\angle(1, 22, 21)$
S_{22}	=	$\angle(1, 31, 30)$

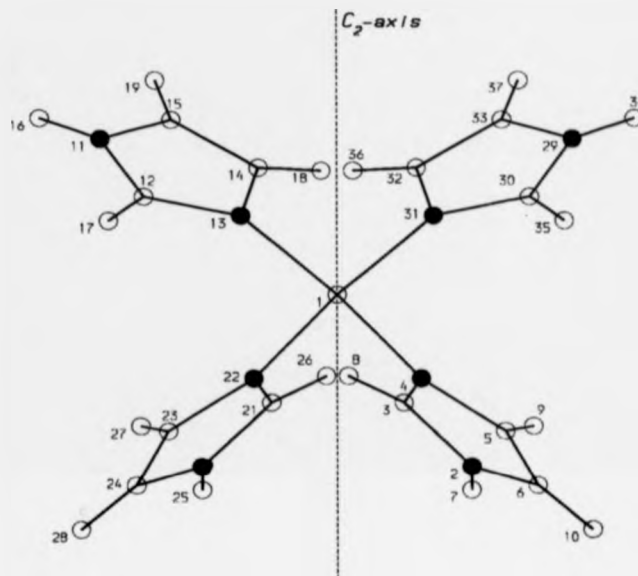


Table 3.11: The internal coordinate set for the 22×22 block of the overall force field (see 3.20) for the sinc (II) tetraimidazole complex. This block is associated with the low frequency skeletal modes of the molecule. $R(a, b)$ denotes a stretching displacement between atoms a and b which may be read from the molecule numbering scheme given on the right hand side. $\angle(a, b, c)$ denotes the angle displacement between atoms a , b and c , $\tau(\text{about } a, b)$ denotes a torsional displacement about the axis described by the vector ab and $O(a, b, c, d)$ denotes an out-of-plane displacement from the plane described by the four atoms a , b , c and d .

pling. The latter is described by just two force constants. The former block is a 22×22 force field referenced to the internal coordinate set given in table 3.11. These internal coordinates describe the skeletal displacements of the molecule if the imidazole rings are considered as rigid entities. The first ten coordinates are the stretch and bend angle displacements describing deformations of the zinc coordination with its four nearest neighbours; this is a non-minimum definition and incurs one redundant coordinate corresponding to all six angle bends, about the zinc position, increasing together.

The elements of the low frequency skeletal mode force field are related by symmetry to reduce the number of free parameters. For C_2 symmetry the reduction is only 2-fold but for

CHAPTER 3. INELASTIC NEUTRON SCATTERING

much of the force field S_4 symmetry was used to further reduce its form since this does not violate the lower C_2 symmetry and was found to be adequate. In fact most of the form of the force field for the final 37-atom C_2 model was inherited from the previous 21-atom S_4 model and only further refined after the introduction of the inter-imidazole coupling block. To minimise the number of independent force constants, as much of the force field as possible was set to zero; in fact all of the non-zero elements are found close to the leading diagonal except from a block coupling the out-of-plane imidazole bends to the tetrahedral deformations. This may be seen in table 3.12 in which the quantitative values of the independent force constants and the qualitative form of the low frequency skeletal force field are presented.

There are 25 independent force constants defining the force field in figure 3.12 and only 21 observed frequencies in the low frequency INS spectrum. However this imbalance is justified since the force field was simultaneously refined with respect to the 21 low frequency modes of the zinc (II) tetraimidazole complex in its two deuterated, forms d_1 - and $3d_{(2,4,5)}$ -. This gave a total of 63 observations which exceeds the 25 free parameters used in the refinement. The force field was also refined with respect to the INS intensities.

The force field generates 22 eigenvectors from which it is possible to interpret the form of the 21 non-zero low frequency skeletal modes. The entire set is depicted in appendix G but six of these modes are presented in figure 3.21 in order to demonstrate the major forms of motion present in the low frequency spectrum.

The modes selected include three tetrahedral modes and one of each of the three forms of imidazole ring libration possible: bend, wag and torsion. It is quite clear from inspection of these diagrams that the tetrahedral modes are vibrations of the core of the molecule (i.e. the greatest displacements are close to the zinc atom) whereas the imidazole librations tend to incur the greatest atom displacements furthest from the zinc atom. This was the assumption made earlier and was instrumental in the assignment of the tetrahedral modes to the INS peaks which are seen to move least upon small changes in the crystal field (due in this case to exchanging the anion from perchlorate to tetrafluoroborate). Furthermore, the tetrahedral modes are seen to be relatively pure and, despite the deviations from exact T_d symmetry, the zinc and its four nearest neighbours appear to exhibit the text-book normal modes of a

CHAPTER 3. INELASTIC NEUTRON SCATTERING

Force Constants (12 diagonal elements) $\text{mdyne}\text{\AA}^{-1}$			Interaction Force Constants (13 off-diagonal elements) $\text{mdyne}\text{\AA}^{-1}$		
A	Zn-N stretch #1	1.111	α	Zn-N/Zn-N interaction	0.27430
B	Zn-N stretch #2	1.084	β	Zn-N/Zn-N interaction	0.03774
C	N-Zn-N deformation #1	0.461	γ	torsion/torsion	0.00086
D	N-Zn-N deformation #2	0.261	δ	bend/bend	-0.01375
E	N-Zn-N deformation #3	0.409	ϵ	bend/bend	-0.02794
F	N-Zn-N deformation #4	0.218	ζ	bend/bend	-0.00998
G	Zn-N torsion #1	0.005	η	bend/bend	-0.01905
H	Zn-N torsion #2	0.008	θ	wag/tetr.deformation	0.00280
I	Imid out-of-plane bend #1	0.090	ι	wag/tetr.deformation	0.00133
J	Imid out-of-plane bend #2	0.073	κ	wag/wag	0.07495
K	Imid in-plane wag #1	0.109	λ	wag/wag	0.01180
L	Imid in-plane wag #2	0.148	μ	wag/wag	0.06801
	Imid-Imid coupling #1	0.064	ν	wag/wag	0.01025
	Imid-Imid coupling #2	0.056			

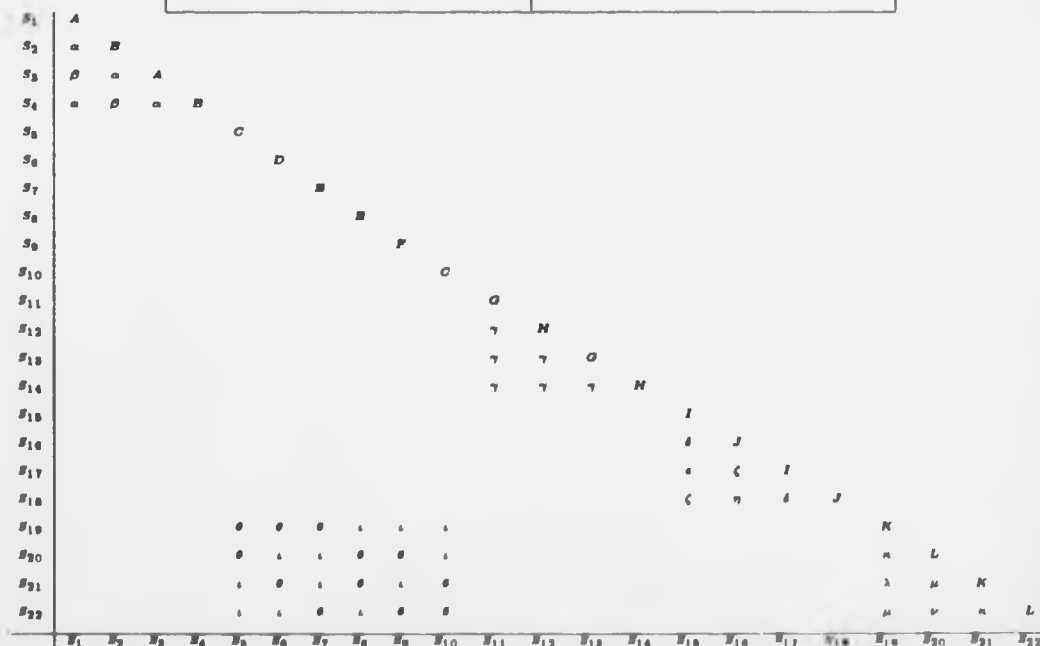


Table 3.12: The 25 independent force constants and the form of the force field used with the final 37-atom C_2 symmetry model to obtain the low frequency skeletal mode vibrational spectrum of sinc (II) tetraimidazole. It is this force field which generates the calculated INS spectrum presented in figure 3.19. The coordinate basis, $S_1 \rightarrow S_{22}$, is the non-minimum set of internal coordinate listed in table 3.11.

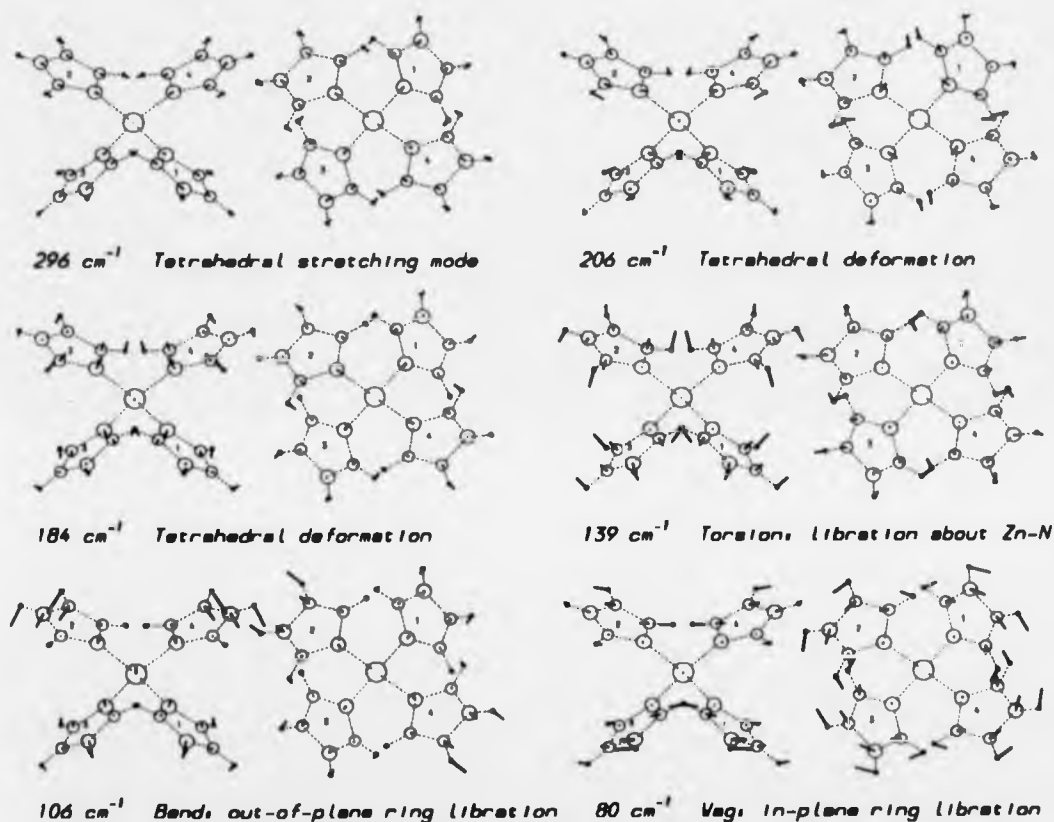


Figure 3.21: Six examples of the low frequency skeletal modes determined from the eigenvectors of the force field given in table 3.12. The form of the modes is shown by the vectors extending from the equilibrium positions of the atoms and the length of the vectors indicates the root-mean-squared displacement of that atom in the ground state of the normal mode. The vectors have been weighted by a factor of 15 for clarity. For each mode the molecule and displacement vectors are shown in two projections: one perpendicular to the C_2 axis and one viewed along the C_2 axis. The normal modes were selected as examples of the significant types of skeletal motion present in the molecule. All 21 low frequency skeletal modes of the sinc (II) tetraimidazole complex are presented in appendix G.

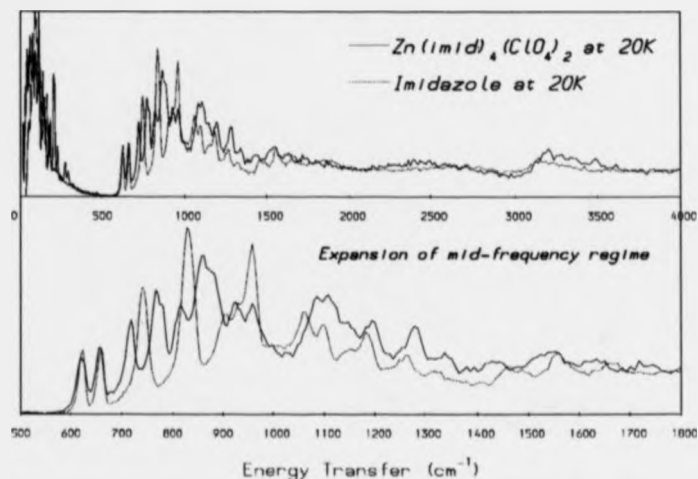


Figure 3.22: Comparison of inelastic neutron scattering spectra of zinc (II) tetraimidazole perchlorate and pure imidazole at 20K. The expansion of the range $500 \rightarrow 1800\text{cm}^{-1}$ is interesting since it shows the changes to the internal mode vibrational spectrum of crystalline imidazole when it is coordinated to a zinc atom.

tetrahedron. Not all of the imidazole librations are as pure and in appendix G it may be seen that several modes are of fairly mixed character.

3.6.5 Imidazole Regime ($> 500\text{cm}^{-1}$) - Mode Assignment

In figure 3.22 the INS spectrum of pure imidazole is compared to that of zinc (II) tetraimidazole perchlorate over the range $500 \rightarrow 1800\text{cm}^{-1}$. This is the range in which most of the fundamental internal modes of imidazole occur. Most of the spectra are similar to one another such that there is a one to one correspondence between peaks, but the spectra are significantly different between 700 and 1000cm^{-1} . This region is attributed to CH and NH out-of-plane wags in the spectrum of pure imidazole and it is probable that the change in the vibrational spectrum is due to different the H-bonding in the zinc complex. The H-bonding in both substances is via the NH bond which has a pure out-of-plane wag mode in imidazole at 961cm^{-1} (i.e. ν_{16} in table 3.8) producing an intense INS peak that is clearly shifted in the zinc complex spectrum. The NH peaks in the zinc complex spectrum (note there are four

CHAPTER 3. INELASTIC NEUTRON SCATTERING

corresponding vibrations since there are four imidazoles per molecule) are identified by comparison with the INS spectrum of the $d_{(1)}$ -deuterated counterpart of zinc (II) tetraimidazole. This was done in figure 3.14 in which the 719 and 820cm^{-1} modes were clearly seen to vanish identifying them unequivocally as NH vibrations. Thus the singlet 961cm^{-1} out-of-plane NH wag in imidazole gives rise to four modes in the zinc complex producing two doublet peaks occurring at 719 and 820cm^{-1} . This splitting is justified by recalling that the H-bonding to the two branches in the asymmetric group is quite dissimilar and the NH wag vibrations are therefore differently affected. Further evidence of the importance of H-bonding on these two peaks may be seen by comparing the INS spectra of zinc (II) tetraimidazole perchlorate and tetrafluoroborate as in figure 3.13. As mentioned earlier the H-bonding in these compounds is different which causes the 719 and 820cm^{-1} peaks in the perchlorate spectrum to shift to 727 and 807cm^{-1} in the tetrafluoroborate case whereas the two spectra superimpose almost exactly at all other frequencies. The other shifted peaks in the $700 \rightarrow 1000\text{cm}^{-1}$ region have very large INS intensities typical of out-of-plane ~~wags~~ CH wags; these would not be expected to split like the NH modes because they do not engage strongly in H-bonding. The out-of-plane CH wags in the zinc (II) tetraimidazole perchlorate spectrum are therefore assigned at 770 , 863 and 882cm^{-1} . Since the two peaks at 623 and 661cm^{-1} in the imidazole spectrum (assigned to ring puckers) do not shift, the assignment of the out-of-plane imidazole modes in the zinc complex is complete.

The in-plane modes in pure imidazole occur above 900cm^{-1} . There is no evidence to suggest any significant change in form of the vibrational spectrum of these modes in the zinc complex although most of the modes appear to shift up in frequency by about 25cm^{-1} . The in-plane NH wag mode is positively identified at 1198cm^{-1} in the perchlorate spectrum by contrasting with the $d_{(1)}$ -deuterated analogue (see figure 3.14). This compares with 1186cm^{-1} in the pure imidazole spectrum; this is a shift of 12cm^{-1} which is consistent with the shifts experienced by all the in-plane modes. Thus, the in-plane NH modes do not appear to be so sensitive to the different H-bonding environment in the zinc complex as the out-of-plane modes. This is probably due to the mixed character of these modes (i.e. they are not pure NH modes).

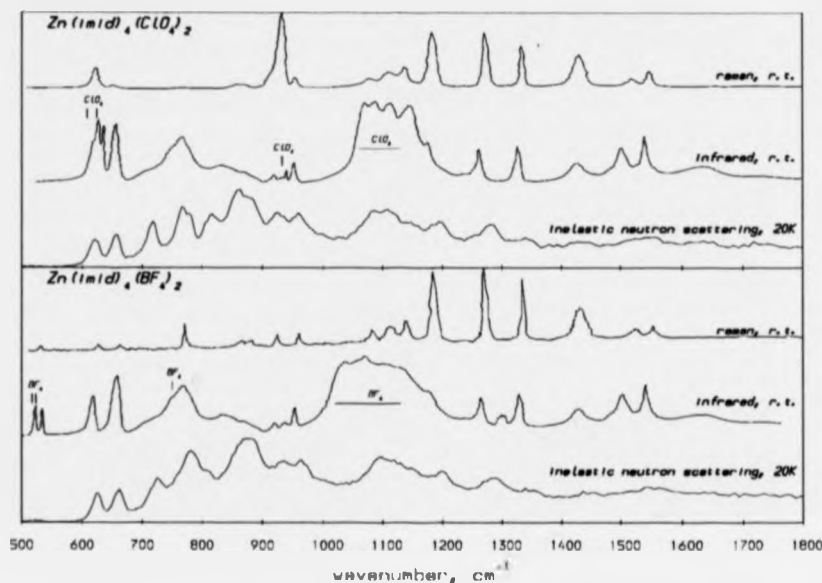


Figure 3.23: Experimental INS, infrared and Raman spectra of zinc (II) tetraimidazole perchlorate and tetrafluoroborate in the range $500 \rightarrow 1800\text{cm}^{-1}$; the spectra correspond to the tabulated data in table 3.13. The infrared spectra were recorded on a Bruker FT-IR ISS Lucke 48 spectrometer. The Raman spectra were measured using an argon ion laser with a 200mW excitation at 20498cm^{-1} , a double monochromator and Spex spectrometer. Both of the optical measurements were made with the assistance of Dr. J.D.Woollins at Imperial College, London. For the infrared spectra the absorptions due to the perchlorate and tetrafluoroborate counter-ions are indicated and are taken from the literature, (115).

More experimental information about the vibrational spectra of the zinc complex in the perchlorate and tetrafluoroborate form is presented in table 3.13. It is compared to the study by Hodgson et al., (60), which is an assignment of the infrared spectrum of zinc (II) tetraimidazole perchlorate. The experimental INS, infrared and Raman spectra are superimposed upon one another in figure 3.23. The optical data do not help much in the determination of the assignments since for C_2 symmetry all modes are active in both infrared and Raman. Even if S_4 symmetry is assumed, which is approximately correct and identifies the A modes which are not active in the infrared, the data does not help the assignment since nearly every band in the spectra is composed of four peaks comprising all symmetries due to the four imidazoles present per molecule. The optical data however do help in pinpointing peaks which

CHAPTER 3. INELASTIC NEUTRON SCATTERING

Experimental Results, (cm^{-1})						Published Results ClO_4 compound Hodgson et al., (60) (cm^{-1})		Refined frequencies 37-atom model (cm^{-1})	
ClO_4			BF_4			ir	assignment	calc.	assignment
INS	ir	Raman	INS	ir	Raman				
						3380	νNH	3380	νNH
						3160	νCH	3160	νCH
						3145	νCH	3145	νCH
						3131	νCH	3131	νCH
	3113			3114					
	2954			2954					
	2849			2849					
	2023								
1640	1634			1632					
1550	1541	1549	1550	1541	1550	1546	νring	1575	νring
	1503	1519		1503	1523	{ 1512 }	νring	1525	$\nu\text{ring}/\delta\text{NH}$
						{ 1508 }	νring		
1433	1429	1429	1449	1430	1430	1431	νring	1433	νring
1342	1329	1333	1348	1329	1334	1331	νring	1336	νring
1284	1264	1270	1292	1264	1271	1267	δCH	1271	δCH
		1231	1201			1230	comb.		
1198	1178	1183	~1151		1183	1183	νring	1194	δNH
1145	1146	1138	~1132		1138	1133	δNH	1111	νring
1111	1114	1109	1100		1109			1099	δCH
1087	1071	1077		1071	1078			1090	δCH
				1037		1050	δCH		
961	953	955	967	953	956	953	δring	971	δring
927	921	931	935	937	922	920	γCH	923	δring
		871	879		877	873	δring	883	γCH
862		860			859	854		862	γCH
863						847			
820	835		807	836		833	γCH	820	$\gamma\text{NH}_{(i)}$
770	767	772	783	768	766	760	γCH	770	γCH
719			727			730	γNH	719	$\gamma\text{NH}_{(ii)}$
658	658	655	663	658	655	652	γring	661	γring
623	626	625	626	618	620	622	$\nu_4\text{ClO}_4$	623	γring
						614	γring		

Table 3.13: Experimental vibrational spectra of zinc (II) tetraimidazole perchlorate and tetrafluoroborate by the methods of inelastic neutron scattering, infrared and Raman in the range $500 \rightarrow 1800\text{cm}^{-1}$. The results are compared to the infrared assignment of the perchlorate spectrum by Hodgson et al., (60). The final two columns present the calculated vibrational frequencies of the zinc complex based on the 37-atom final model (discussed in subsections 3.6.3 and 3.6.4) and the new assignment based on all the work. Note that the hydrogen stretches, νCH and νNH , are assigned to Hodgsons values due to the poor resolution of the INS data at those frequencies; plus the subscripts (i) and (ii) for the γNH mode denote the same mode which vibrates at two frequencies due to the asymmetric H-bonding of the two imidasoles within the asymmetric group.

CHAPTER 3. INELASTIC NEUTRON SCATTERING

are obscured in the INS spectra due to poorer resolution or other nearby peaks and confirm the assignment deduced from the INS spectra alone.

The new assignment is given in the right-hand column of table 3.13. The major disagreements with the assignment of Hodgson et al., (60), are as follows:

1. Hodgson et al. do not identify the splitting of the imidazole out-of-plane NH wag into the two peaks at 719 and 820cm^{-1} (denoted as $\gamma\text{NH}_{(i)}$ and $\gamma\text{NH}_{(ii)}$) and assigns γNH to the lower of the two peaks, (730cm^{-1} in his infrared spectrum) and the 820cm^{-1} band (833cm^{-1} in his infrared spectrum) as a CH wag. The 719 and 820cm^{-1} peaks are both unquestionably NH wags due to their deuteration shifts.
2. The 863 and 882cm^{-1} bands, assigned as CH wags in the present study, are assigned by Hodgson et al. to be due to a single bending ring mode. This can not account for the very large peak intensity seen in the INS spectrum which is typical of large amplitude hydrogen motion.
3. The 961cm^{-1} band, assigned as a bending ring mode in the present study, is assigned by Hodgson et al. to be an out-of-plane CH mode. If this were true it would be expected to produce more intensity in the INS spectrum.
4. The in-plane NH wag at 1198cm^{-1} and the stretching ring deformation at 1145cm^{-1} are assigned the other way around by Hodgson et al.. The NH wag is positively identified at 1198cm^{-1} due to its deuteration shift.
5. The 623cm^{-1} ring pucker is assigned by Hodgson at 614cm^{-1} and the 623cm^{-1} mode as a perchlorate mode. This is not correct since the 623cm^{-1} peak appears in the INS spectrum and perchlorate scarcely generates INS intensity on a hydrogen intensity optimised spectrometer such as TFXA.

3.6.6 Imidazole Regime ($> 500\text{cm}^{-1}$) - Force Field and Eigenvectors

The refinement of the imidazole regime can be treated as an independent problem although the imidazole force field is just part of the whole force field describing the zinc (II) tetraimidazole

CHAPTER 3. INELASTIC NEUTRON SCATTERING

molecule. The imidazole force field is in fact composed of four blocks, one for each of the four imidazole ligands, as depicted in figure 3.20. At the start of the refinement these four blocks were identical and were input as the 31×31 isolated imidazole force field described in section 3.5.4 and presented in appendix F. The internal coordinate basis for each block is the non-minimum basis set, S , given in table 3.4.

The low frequency skeletal modes were refined first. As has been described in section 3.6.4, this required the treatment of steric interaction between the imidazoles to moderate their librations and was effected by a network of stretching force constants connecting imidazoles to imidazoles via their ring atoms. The force constants of these steric interactions were very low but inevitably did cause the calculated frequencies in the imidazole regime to increase in frequency. The in-plane and out-of-plane imidazole modes were then refined separately. As described in the last section, there is no evidence that the form of the in-plane vibrational spectrum is different in the zinc complex than in pure imidazole and so there was no justification for refining the off-diagonal elements of the in-plane block. The in-plane modes were refined with the 15 leading diagonal elements of the force field against the 30 observations of the eigenvalues in both the undeuterated and the $d_{(1)}$ -deuterated case. The refinement of the out-of-plane modes was more complicated. As with isolated imidazole the effect of the H-bonding on the frequency of the NH wags was accommodated for by the NH wag force constant; this was adequate for imidazole since the NH modes are very pure and vibrate independently. For the zinc complex the NH wag had to be determined by two NH wag force constants due to the splitting of this mode, one for each imidazole in the asymmetric group; i.e. giving two sets of two identical imidazole blocks in the force field. Further, the significant change in form of the vibrational spectrum of the in-plane modes meant that it was appropriate to refine the off-diagonal elements as well as the leading diagonals. This involved in total 11 free parameters refined against the 18 observed frequencies in the three isotopic variants. Both the in-plane and out-of-plane blocks of the imidazole force fields were also refined with respect to the INS experimental intensities.

In figure 3.24 the final calculated INS spectrum of zinc (II) tetraimidazole is superimposed on the measured spectrum. (The low frequency calculation has already been presented in

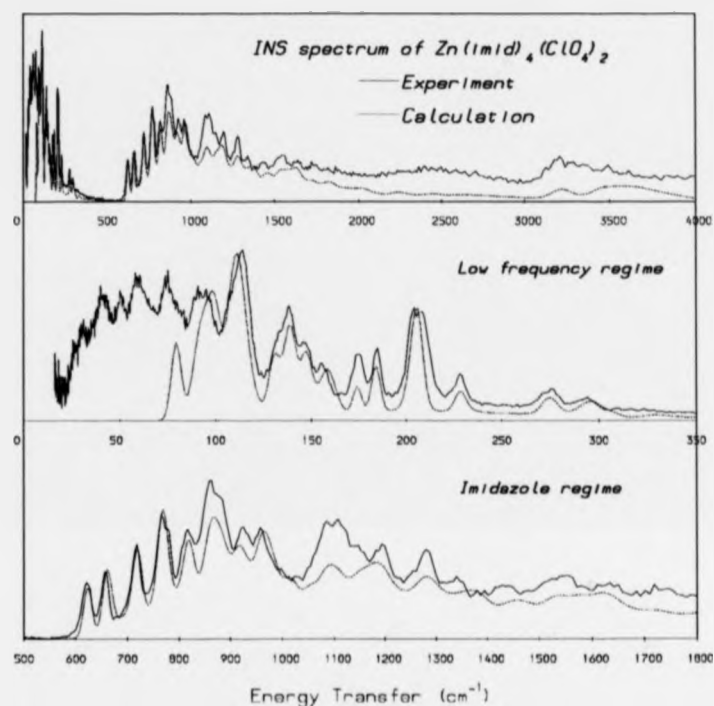


Figure 3.24: Final calculated INS spectrum of the zinc (II) tetraimidazole complex superimposed on the measured INS spectrum of the perchlorate compound. The dynamics were modelled by the full 37-atom model described in the text. The entire range is shown and expanded in the two principal regions of interest. The calculation involves fundamentals, overtones, combination bands and phonon wings based on the experimental spectrum below 500cm^{-1} and an overall refined Debye-Waller factor of 0.025\AA^2 .

figure 3.19 but is shown again here to give the full overview). The calculation determines fundamental, overtone and combination frequencies and intensities and a full numerical powder average was done. Phonon wings are also calculated up to the fourth term based on the experimental spectrum below 500cm^{-1} and using a refined value for the overall Debye-Waller factor of 0.025\AA^2 , i.e. u in Eq. (3.29); a starting estimate of 0.021\AA^2 for the overall Debye-Waller factor was obtained from the isotropic average of the T tensor at 100K from the TLS analysis in chapter 2.

The calculation of the imidazole regime in figure 3.24 is a good fit to experiment up

CHAPTER 3. INELASTIC NEUTRON SCATTERING

to 1000cm^{-1} . This encompasses all of the out-of-plane modes of the imidazoles. However, above 1000cm^{-1} the fit is poorer, especially around 1100cm^{-1} where the calculated peaks lack intensity. This region is principally made up of in-plane CH and NH wags. The implication is that in-plane modes are more greatly restricted in their freedom of vibration than the out-of-plane modes in the dynamic model. This could be a result of the modelling of the steric interaction which may tend to particularly impede the in-plane imidazole modes. However, we can offer no conclusive explanation for the underestimate in this region.

It should be noted, that in the low frequency regime it was necessary to slightly broaden the peak resolution artificially in order to produce this fit. This only applied to peaks lower than 160cm^{-1} in frequency which appear too narrow when calculated with the intrinsic resolution of 1.5% of energy transfer. This implies that the modes below 160cm^{-1} , exclusively bends, wags and torsions of the imidazole branches, are slightly dispersed through the Brillouin zone which indicates some degree of coupling with the acoustic lattice modes. There has been no attempt to reproduce the broad hump underlying all the optical modes at low frequency since this is beyond the scope of the isolated model approach. It should also be noted that it is very difficult to model the broad, featureless region of the spectrum above 1800cm^{-1} ; the calculation typically underestimates the experimental intensity. This is caused by the insufficient number of overtone and combination bands treated (only first harmonics), difficulties in the phonon wing treatment and inadequacies in the intensities predicted using the harmonic approximation.

There are 105 eigenvectors generated by the refined force field that represent the normal modes. The 21 low frequency skeletal modes have already been discussed and are presented pictorially in figure 3.21 and appendix G. This leaves 84 modes (i.e. $42A + 42B$ in C_2 symmetry) belonging to the imidazole regime although these may be sub-divided into 21 groups of four approximately degenerate modes (with the notable exception of the out-of-plane NH wag which further sub-divides into two groups of two). The nature of the 21 groups of modes is very similar to that in the pure imidazole case, depicted in figure 3.12, and consequently the full set is not shown here. However, two of the modes in their ground states are depicted in figure 3.25 with identical scaling as the low frequency modes in figure 3.21

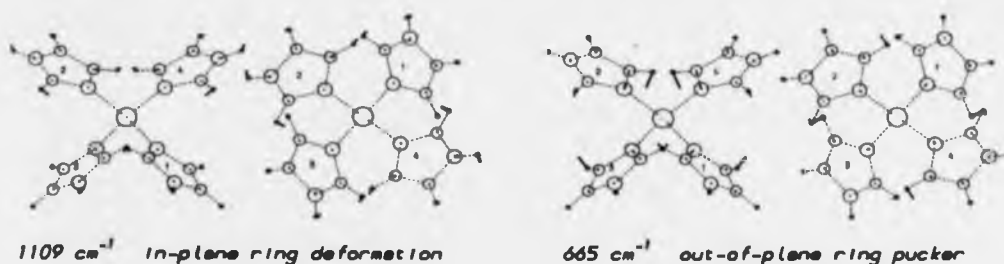


Figure 3.25: Two examples of the calculated ground state normal modes in the imidazole regime of the sinc (II) tetraimidazole complex. The root-mean-squared displacement vectors have been scaled by 15 so that they can be directly compared in magnitude to the low frequency skeletal modes in figure 3.21. It is clear that the high frequency modes contribute far less to the total mean square displacement amplitude than do the skeletal modes. The examples were arbitrarily chosen to show one in-plane mode and one out-of-plane mode. The imidazole modes in the sinc tetraimidazole complex are very similar to the those in pure imidazole as shown in figure 3.12. There are 84 fundamental vibrations in the imidazole regime.

in order to demonstrate the significant reduction in the atomic displacements at the higher frequencies. Although each high frequency mode contributes much less to the mean squared displacements of the atoms than the skeletal modes, there are four times as many to sum over. The exact proportions of the atomic motion in high and low frequency modes are displayed in table 3.14 at three temperatures for zinc, the ring atoms (carbons and nitrogens) and the hydrogens. It is apparent that, even at low temperatures, most of the ring motion is concentrated in the skeletal modes but that a sizeable proportion of the motion is due to imidazole modes and should not be neglected.

3.6.7 Self-Consistency of Force Field - Deuteration

A stringent test of the complete force field for the zinc complex is to establish how well it can reproduce the INS intensity spectra of the $d_{(1)}$ - and $3d_{(2,4,5)}$ -deuterated counterparts of the compound.

The $d_{(1)}$ -deuterated zinc complex is addressed first. This is essentially a test of the NH mode shifts since the residual spectrum remains relatively unaffected upon deuteration. We therefore concern ourselves principally with the modes depicted in figure 3.26. Note that there are three types of NH mode (neglecting the very high frequency NH stretches which are not

CHAPTER 3. INELASTIC NEUTRON SCATTERING

	Percent of total intramolecular rms motion of respective atoms below 500cm^{-1}		
	20K	150K	300K
sinc atom	96%	97%	98%
ring atoms (C and N)	63%	70%	75%
hydrogen atoms	42%	50%	57%

Table 3.14: Proportion of average isotropic root-mean-squared displacements of atoms in the sinc complex owing to skeletal modes vibrating below 500cm^{-1} as a percentage of the total internal motion of the molecule. The figures are deduced from the INS results at each temperature by populating each mode according to the canonical average within the harmonic approximation. The isotropic averages are then found for the above groups of atoms.

easily detectable in the INS spectra) each contributing four bands due to the presence of four imidazoles but that the out-of-plane bands are split in frequency (i.e. NH wag (i) and (ii)) because of the asymmetric H-bonding. The INS intensity spectrum may be calculated using the same force field and the 37-atom model in which the NH hydrogen atoms have been substituted for deuteron mass and scattering cross section. The result is presented in figure 3.27. There is almost no change in the calculated low frequency spectrum as is expected. Below 900cm^{-1} in the imidazole regime significant changes are seen compared to the undeuterated fit. The formerly intense out-of-plane NH wags at 719 and 820cm^{-1} have completely disappeared and reappeared as very weak peaks at ~ 530 and $\sim 660\text{cm}^{-1}$; the $\sim 530\text{cm}^{-1}$ peak is just visible in the measured spectrum. This behaviour corresponds to the assignment made. However in the measured spectrum there are residual peak intensities visible at 719 and as a shoulder at 820cm^{-1} which are not accounted for in the calculation. This probably indicates that the deuteration at the NH positions was not 100% at the time of measurement and that the experimental spectrum is in fact an admixture of the deuterated and undeuterated spectra. This is quite possible since it is known for pure imidazole that the NH position readily re-exchanges at room temperature and therefore some protonation of the ND positions in the sinc complex is also likely to have taken place. If this were so, it would

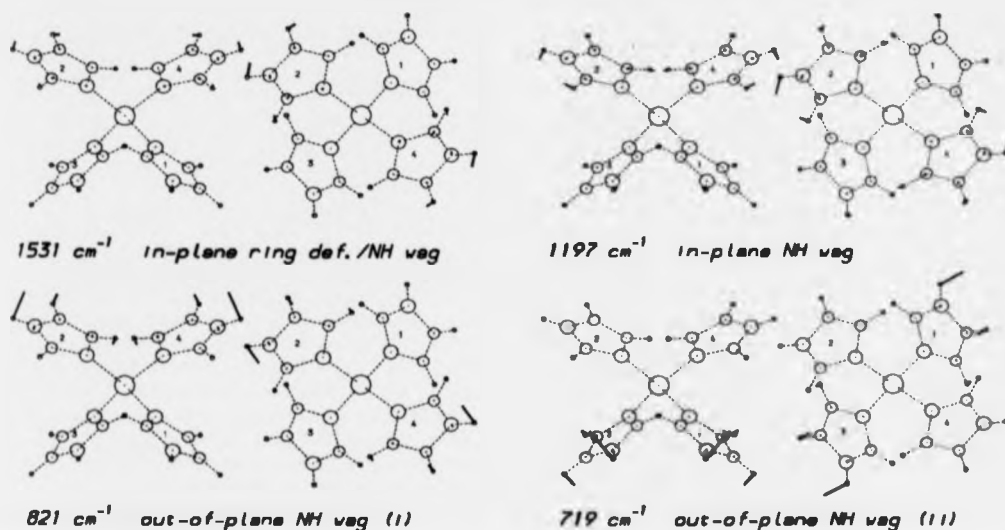


Figure 3.26: The calculated ground state NH modes of sinc (II) tetraimidazole perchlorate. As with figures 3.21 and 3.25 the root-mean-squared atomic displacement vectors are scaled by a factor of 15 for clarity. Note that there are in fact four similar modes for each type of mode displayed, because there are four imidazole ligands, with the notable exception of the out-of-plane NH modes which split into two bands of two modes due to the asymmetric H-bonding. It is these modes that undergo the most pronounced shifts upon deuteration of the NH positions and consequently generate the greatest changes in INS spectral intensity. Note that the nitrogen atoms are depicted by slightly larger circles than the carbon atoms.

be impossible to completely generate the INS intensity of the spectrum via a calculation that assumes 100% NH deuteration since the phonon wing background could not be correctly modelled. This may be seen at the two CH wag peak positions at 780 and 880 cm^{-1} where the lack of intensity in the preceding regions has lowered the background; the individual intensity of these peaks is however correct. One concern in the out-of-plane region below 900 cm^{-1} is the reduction of calculated intensity in the 623 cm^{-1} ring pucker which becomes a shoulder of the 660 cm^{-1} peak; this indicates that too much NH wag character exists in the model of this ring pucker vibration. In general however the out-of-plane modes appear to be satisfactorily modelled.

For the in-plane modes above 900 cm^{-1} , it is more difficult to comment on the quality of the fit since the spectrum only contains broad peaks that are poorly resolved. The peak at

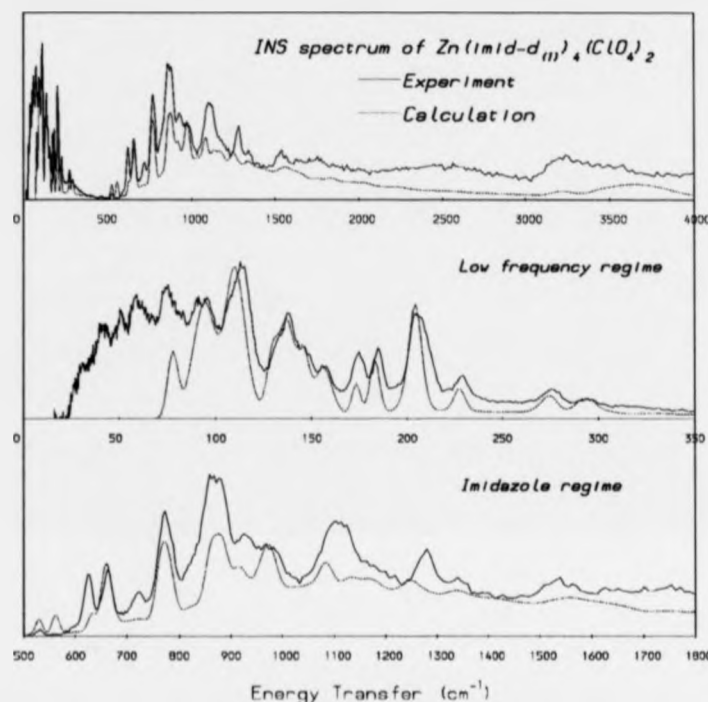


Figure 3.27: Calculated INS spectrum of the zinc (II) tetraimidazole- $d_{(1)}$ complex superimposed on the experimental perchlorate spectrum. The calculation was based on the 200×200 force field generated for the undeuterated zinc complex and the deuterated 37-atom model. All other parameters are the same as those used for the undeuterated calculation in figure 3.24.

970cm^{-1} , an in-plane stretching deformation of the ring, has too much calculated intensity although the situation appears worse than it is because the preceding peaks are underestimated due to the artificially low phonon wing background as explained above. Furthermore, the calculated peak at 1100cm^{-1} is too weak, which was also found in the undeuterated case. It is encouraging, however, to see that the NH mode at 1198cm^{-1} vanishes in the deuterated case.

In summary for the $d_{(1)}$ -zinc complex, the low frequency regime is virtually unchanged as expected, the out-of-plane modes appear to be correctly modelled with the possible exception of one of the ring puckers and the in-plane modes do not show notable inconsistencies if the

CHAPTER 3. INELASTIC NEUTRON SCATTERING

incomplete modelling of the phonon wing background is taken into account. Note that the treatment of the phonon wings is anyway an approximation. The use of the experimental spectrum below 500cm^{-1} to construct the phonon wing background is certainly less appropriate for the zinc complex, which exhibits strong optical peaks in this regime, than it was for the case of pure imidazole.

The situation for the $3d_{(2,4,5)}$ -zinc complex is not so straightforward. As described on page 106, there was concern over the degree of deuteration of the product. Unless the product was 100% pure, which certainly was not the case, the residual protons at the CH positions would have a disproportionate effect on the intensity spectrum due to their very large scattering cross sections and the optimisation of the TFXA spectrometer. The desired product would only contribute weakly to the signal since it is three quarters deuterated. It is also likely that admixtures of all permutations of deuteration are present to some degree. Consequently, it seems unlikely that the modelling of the INS intensity could hope to give a very good fit and only certain points are raised.

The $3d_{(2,4,5)}$ - calculation is presented in figure 3.28. In the imidazole regime the strong peaks at 746, 831 and 1206cm^{-1} are certainly due to NH vibrations; the sample was washed with cold water and there can be little doubt that virtually all the N-positions were protonated. These peaks were consequently used to scale the calculated spectrum since they should be well modelled. The rest of the imidazole regime could not easily be compared.

In the low frequency regime, the tetrahedral modes above 150cm^{-1} remain relatively well modelled although the shifts downwards in frequency upon deuteration are slightly overestimated. Of some concern are the large shifts calculated below 150cm^{-1} which cause the $\sim 140\text{cm}^{-1}$ peaks to merge with the lower frequency intensity. This would appear to indicate that the librational modes of the zinc complex were modelled with too much motion of the C-hydrogens such that the shifts were too large upon deuteration. This is likely to be a shortcoming in the modelling of the steric effect and H-bonding. The imidazoles are only impeded in their motion by the inter-imidazole network of stretches modelling the steric interaction; when the imidazoles are deuterated extensively this is no longer enough to hold them as rigidly in place and they tend to vibrate at lower frequencies than in reality. It is clear

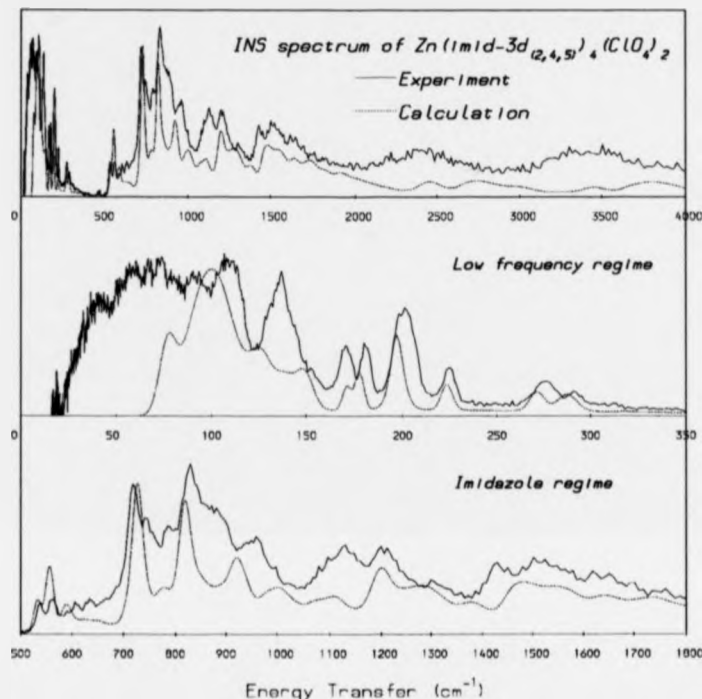


Figure 3.28: Calculated INS spectrum of the zinc (II) tetraimidazole-3d_(2,4,5) complex superimposed on the experimental deuterated perchlorate spectrum. Any comparison is adversely affected by the probable admixtures of protonated residues in the sample which, although small, would contribute strongly to the experimental spectrum because of the large scattering cross section of protons relative to deuterons. It is therefore not possible to model the experimental spectrum very successfully.

that, although the approximation of the steric effect and the treatment of the H-bonding via the NH force constants are sufficient in the undeuterated and d₍₁₎-deuterated case, they are not adequate to cope properly with more extreme changes to the dynamic system.

3.6.8 Summary of INS study of Zinc (II) tetraimidazole

INS data yielded new information on the hydrogen-weighted vibrational density of states of the zinc (II) tetraimidazole complex. Modifying the crystal field, by changing the anion from perchlorate to tetraborofluorate, was seen to only slightly affect the INS spectrum implying

CHAPTER 3. INELASTIC NEUTRON SCATTERING

a well decoupled molecule that would yield to an isolated model dynamic analysis. The vibrational spectrum was considered in two parts: a low frequency part, below 500cm^{-1} , due to skeletal motion and a high frequency part, above 500cm^{-1} , due to internal modes of the imidazole rings. An assignment of the skeletal modes was proposed based on symmetry considerations and the small observed shifts due to substitution of the anion. The peaks which did not shift were assigned to be quasi-tetrahedral vibrations of the core Zn-4N coordination unit; the rest were assigned as librations of the entire imidazole rings. In the high frequency part, the INS intensities, plus additional INS data of the deuterated counterparts of the zinc complex, permitted an improvement over the existing assignment in the literature. In particular, the out-of-plane NH vibrations were seen to be split due to the asymmetric H-bonding, which was not previously reported.

A harmonic force field describing the skeletal modes was constructed by gradually developing a very simple tetrahedral model into the final complex 37-atom model based on the true C_2 symmetry; the evolution of the symmetry of the modes was consistent with the observations. It was found necessary to model the restrictive effect of the steric interaction between imidazole branches by establishing a network of force constants interconnecting the imidazole rings. The high frequency vibrational spectrum was modelled by incorporating the entire force field of pure imidazole, presented in the previous section, as four blocks in the much larger force field for the zinc complex. The imidazole blocks were then subsequently refined to model the changes in the spectrum observed on going from pure imidazole to the complexed form. Out-of-plane vibrations of the imidazole ring required significant changes to the imidazole force field.

The final force field was found to satisfactorily predict the hydrogen-weighted vibrational density of states from comparison with the INS spectrum. The force field also reproduced the density of states in the $d_{(1)}$ -deuterated analogue but was not able to convincingly model that of the $3d_{(2,4,6)}$ -deuterated complex. The latter poor fit was partly the result of an inhomogeneously deuterated sample, however in the low frequency regime, it was clear that the force field was not able to properly emulate the dynamic behaviour of the zinc complex after such substantial changes to its structure.

CHAPTER 3. INELASTIC NEUTRON SCATTERING

The study has demonstrated that the isolated-molecule normal mode analysis approach is able to cope with relatively large structures and accurately reproduce the vibrational spectrum and, more significantly, the hydrogen-weighted vibrational density of states. The principal result of the study is a complete description of the many-body vibrational motion of the zinc (II) tetraimidazole complex.

Chapter 4

Temperature Dependence of EXAFS

4.1 Introduction

In this chapter, a study of the temperature dependence of the *extended x-ray absorption fine structure* (EXAFS) of the zinc (II) tetraimidazole complex is presented and compared with temperature dependent ab initio calculations.

EXAFS spectra contain information about the static and dynamic structure of the environment of the x-ray photon absorbing atom, in this case the zinc atom, due to scattering of excited photoelectrons from neighbouring atoms. The photoelectron scattering affects the observed x-ray absorption since it modifies the final state wave function of the system which determines the transition probability of a core electron from a bound state to a continuum state (i.e. propagating photoelectron state); the x-ray absorption coefficient, μ , is proportional to this transition probability which, within the one-electron approximation, is written by Fermi's Golden Rule as:

$$\mu \propto \sum_f |(\phi_f|\hat{\epsilon} \cdot \mathbf{r}|\phi_i)|^2 \delta(E_f + E_i - \hbar\omega) \quad (4.1)$$

where $|\phi_i\rangle$ and $|\phi_f\rangle$ are the initial and final one-particle eigenstates, with energies E_i and E_f respectively, of the effective one-electron Hamiltonians, $\hbar\omega$ is the x-ray photon energy and $\hat{\epsilon}$ is the x-ray polarisation vector. The normalised EXAFS spectrum, χ , is defined as the oscillatory part of μ with respect to the smooth absorption coefficient, μ_0 , of the isolated atom; i.e.

$$\chi = (\mu - \mu_0)/\mu_0 \quad (4.2)$$

CHAPTER 4. TEMPERATURE DEPENDENCE OF EXAFS

The one-particle theory describing the photoelectron scattering, (1), (76), (93), is generally successful in predicting the shape of the EXAFS spectra but overestimates the calculated amplitudes of the oscillations. Some amplitude reduction is seen when many-body effects are included in the formalism, (12), (74), (e.g. complex energy-dependent exchange-correlation corrections to the atomic potentials and multielectron excitations) but this is not sufficient without some treatment of the disorder of the atomic positions. The disorder introduces an incoherence into the contributions to the EXAFS signal which produces significant damping; the disorder is due to thermal vibrations (and static disorder when present) and consequently the damping of the EXAFS signal has a temperature dependence.

In the case of single scattering of the photoelectron, the effect of disorder may be phenomenologically represented by an amplitude reduction factor, called the Debye-Waller factor, (5). However, the photoelectron also undergoes *multiple scattering* (MS) via closed paths in which the scattering takes place from several atoms. In this case, the correlation in the thermal disorder of the atoms have to be considered since the distribution of instantaneous configurations of the many-segment MS paths determines the damping of the EXAFS. A complete knowledge of the many-body correlation function is required so that a full configurational average of the EXAFS signal can be made; the configurational average determines the resultant EXAFS signal from all the probability weighted instantaneous configurations of the scattering system.

The aim of this study was to calculate an *ab initio* EXAFS spectrum of the zinc (II) tetraimidazole complex, based on the static structure from x-ray crystallography and incorporating the full dynamic structure via a configurational average calculation. A stringent test of the theory is then to predict the *ab initio* temperature dependence of the EXAFS spectrum and compare this to experiment. The vital ingredient was the many-body vibrational correlation function (VCF) which was determined by inelastic neutron scattering and has been discussed in the previous chapter. This study provides a quantitative test of the ability of the current theory to predict observed EXAFS signals when all input parameters are known.

In the following section, several important features of current EXAFS theory are outlined to show how the calculated signal was generated in this study. This includes an outline of

CHAPTER 4. TEMPERATURE DEPENDENCE OF EXAFS

current multiple scattering theory, the one-electron approximation describing the propagation of a photoelectron in an atomic potential, schemes for modelling the corrections to the potentials due to exchange and correlation effects and the muffin-tin approximation for constructing the atomic potentials. Subsequently, the algorithm used to do the configurational average is described; the algorithm assumes a linear behaviour of the phase and amplitude of the partial EXAFS signals about the equilibrium configuration and thus determines the configurational-average as an effective damping applied to the partial signals at equilibrium.

The experimental section describes how the temperature dependent EXAFS data for zinc (II) tetraimidazole were collected and outlines the preliminary analysis of the data in terms of Fourier transforms. The temperature dependent Fourier transforms are used to obtain an estimate of the mean-squared relative displacement of the first scattering shell surrounding the absorbing zinc atom.

The next section describes the details of the configurational averaging calculation. It defines the significant scattering paths to be used in the calculation and makes an important check of the assumption that the phase and amplitude functions are linear in the range of interest.

Finally, the results of the configurational averaging calculation are presented. The effect of the theoretical temperature dependence on the partial signals from individual scattering paths is described including the breakdown of contributions to the damping from the various thermal vibrations of the molecule. The principal result is the comparison of the total theoretical signal with experiment at a range of temperatures. The results are discussed in the final chapter of this thesis.

4.2 Theory

Configurational averaging calculations employed the programme MSXAS, (122), to generate the EXAFS signal. The key elements of the multiple-scattering, curved-wave X-ray absorption theory, (9), (34), (35), (95), (123), implemented in this software are described in the first subsection. In the second subsection, the numerical method, (3), that determines the effect

CHAPTER 4. TEMPERATURE DEPENDENCE OF EXAFS

of the configurational averaging on the partial EXAFS signal from each scattering path is explained. It requires the input of the vibrational correlation function (VCF) obtained in chapter 3 via inelastic neutron scattering; the incorporation of the VCF is explicitly described.

4.2.1 Calculation of EXAFS signal - MSXAS software

4.2.1.1 Multiple scattering theory

The observable that is measured in an EXAFS experiment is the X-ray absorption cross section, σ , as a function of the photon energy $\hbar\omega$; expressed within the framework of partial wave multiple scattering (MS) theory, (9), (34), (35), (95), (123), this quantity is written as

$$\sigma(\hbar\omega) = \sigma_0 \Im m \left[\frac{1}{(2l+1) \sin^2 \delta_l^0} \sum_{LL'} [(\mathbf{I} + \mathbf{T}_a \mathbf{G})^{-1} \mathbf{T}_a]_{LL'}^{00} \right] \quad (4.3)$$

where \mathbf{I} is the unit matrix and σ_0 is a coefficient involving the fine structure constant, α , that determines the strength of the coupling of the X-rays with matter. $\mathbf{G} \equiv G_{LL'}^j$ is the matrix describing the free spherical wave propagation of the photoelectron from site i and angular momentum $L = (l, m)$ to site j and angular momentum $L' = (l', m')$, i.e.

$$\mathbf{G} = \begin{bmatrix} 0 & G^{0,1} & G^{0,2} & \dots & G^{0,N-1} \\ G^{1,0} & 0 & G^{1,2} & \dots & G^{1,N-1} \\ G^{2,0} & G^{2,1} & 0 & \dots & G^{2,N-1} \\ \vdots & \vdots & \vdots & \ddots & \vdots \\ G^{N-1,0} & G^{N-1,1} & G^{N-1,2} & \dots & 0 \end{bmatrix} \quad (4.4)$$

in which

$$G_{LL'}^j = -4\pi \sum_{L''} i^{l''+l'-l'} C_L^{L'} C_{L''}^{L'} h_{l''}^+(kR_{ij}) Y_{L''}(\hat{\mathbf{R}}_{ij}) \quad \text{for } (i \neq j) \quad (4.5)$$

where $C_L^{L'}$ are the Gaunt coefficients¹, h_l^+ are spherical Hankel functions, Y_L are the spherical harmonics and \mathbf{R}_{ij} is the vector connecting the two atoms i and j . $\mathbf{T}_a \equiv [\mathbf{T}_a]_{LL'}^j$ is the matrix containing the scattering information about the atomic scattering centres such

¹ Gaunt coefficients: $C_L^{L'} = \int Y_{L'}^*(\mathbf{k}) Y_L(\mathbf{k}) Y_L(\mathbf{k}) d\mathbf{k}$

that

$$\mathbf{T}_a = \begin{bmatrix} t^0 & 0 & 0 & \dots & 0 \\ 0 & t^1 & 0 & \dots & 0 \\ 0 & 0 & t^2 & \dots & 0 \\ \vdots & \vdots & \vdots & \ddots & \vdots \\ 0 & 0 & 0 & \dots & t^{N-1} \end{bmatrix} \quad (4.6)$$

where $t_l^i = \exp(i\delta_l^i) \sin \delta_l^i$ are the atomic t -matrices (transition factors) in which δ_l^i is the phase shift experienced by the l -component of the photoelectron wave as it scatters from the atom located at site i . The matrix $\tau = (\mathbf{I} + \mathbf{T}_a \mathbf{G})^{-1} \mathbf{T}_a$ contains all the geometrical and scattering information of the atomic system such that an element $\tau_{LL'}^{ij}$ totally describes the photoelectron scattering via all single and multiple scattering paths from an atom i to an atom j . Consequently, the element $\tau_{LL'}^{00}$ in Eq. (4.3) is a complete description of the photoelectron scattering that starts and terminates at the origin atom 0; it is a complex function of the photoelectron wave number, $k = \sqrt{2m\varepsilon}/\hbar$, where ε is the photoelectron energy with respect to the inner potential². For the X-ray scattering at the origin site 0, $\tau_{LL'}^{00}$ acts like an atomic t -matrix which takes into account the perturbing effect of the neighbouring atoms (i.e. the X-ray scattering from the origin atom is inextricably related to the surrounding atoms due to photoelectron MS); the total X-ray absorption cross section in Eq. (4.3) is related to the imaginary part of $\tau_{LL'}^{00}$, and is a statement of the optical theorem³.

The multiple scattering characteristics of the matrix element $\tau_{LL'}^{00}$ become more transparent in the weak scattering limit where $t_l^i(E) G_{LL'}^{ij}(E) \ll 1$ which corresponds to high photoelectron energies; the matrix inverse $[(\mathbf{I} + \mathbf{T}_a \mathbf{G})^{-1} \mathbf{T}_a]_{LL'}^{00}$ may then be written as the

²The photoelectron energy, ε , is defined as $\varepsilon = \hbar\omega + E_i - E_0$ where $\hbar\omega$ is the energy of the X-ray photon, E_i is the eigenvalue of the eigenstate belonging to the effective one-electron Hamiltonian for the initial state and E_0 is the inner potential.

³The optical theorem is a statement of the conservation of flux. It is stated, (121), for a single atom with associated transition matrix t_l as $\sigma_{\text{tot}} = -\frac{4\pi}{k} \text{Im} \sum_l (2l+1) t_l = \frac{4\pi}{k} \text{Im} f(\theta=0)$ where $f(\theta)$ is the atomic scattering factor. The real part of the t -matrix thus determines the strength of scattering whereas the imaginary part describes the flux lost in the forward direction due to scattering.

CHAPTER 4. TEMPERATURE DEPENDENCE OF EXAFS

so-called multiple scattering expansion, (9), (49), i.e.:

$$\tau_{LL'}^{00} = \left[\begin{array}{ccc} \text{single scattering} & \text{double scattering} & \text{triple scattering} \\ t^0 + \sum_{i \neq 0}^{N-1} (t^0 G^{0i} t^i G^{i0} t^0) + \sum_{\substack{i \neq 0 \\ j \neq i \neq 0}}^{N-1} (t^0 G^{0i} t^i G^{ij} t^j G^{j0} t^0) + \sum_{\substack{i \neq 0 \\ j \neq i \\ k \neq j \neq 0}}^{N-1} (t^0 G^{0i} t^i G^{ij} t^j G^{jk} t^k G^{k0} t^0) + \dots \end{array} \right] \quad (4.7)$$

in which each term of the expansion corresponds to the t -matrix for photoelectron scattering of a particular order. For example, the first summation term expresses scattering along all single scattering paths via the atoms at sites i , i.e. $0 \rightarrow i \rightarrow 0$; t^0 therefore symbolises the phase shifts experienced as the photoelectron propagates away from, and back to, the primary absorber at site 0, and t^i describes the phase shifts experienced due to back scattering at site i ; the free propagation of the photoelectron wave between sites $0 \rightarrow i$ and $i \rightarrow 0$ is described by G^{0i} and G^{i0} respectively.

4.2.1.2 One-electron approximation

The success of the MS theory outlined above in predicting X-ray absorption spectra hinges on the calculation of the partial-wave phase shift functions $\delta_l^i(k)$ appearing in the atomic t -matrices and hence on the modelling of the best effective atomic potentials sensed by the photoelectron. To model the atomic potentials properly requires finding the solutions to the many-electron Schrödinger equation in the initial and final states of the system which is impracticable. Instead, the so-called one-electron approximation is used in which the many-particle wave-functions describing the initial and final states are represented as products of single-particle wave-functions, that are eigenfunctions of an effective one-electron Hamiltonian; i.e. for the initial state, Ψ_i^N , of an N -electron system Schrödinger's equation is written as

$$\mathcal{H}_i^N \Psi_i^N = E_i \Psi_i^N \quad (4.8)$$

where, within the one-electron approximation,

$$\Psi_i^N \propto \phi_c(r_N) \Psi_g^{N-1}(r_1, \dots, r_{N-1}) \quad (4.9)$$

CHAPTER 4. TEMPERATURE DEPENDENCE OF EXAFS

in which $\phi_c(\mathbf{r}_N)$ is the core state wave-function and $\Psi_s^{N-1}(\mathbf{r}_1, \dots, \mathbf{r}_{N-1})$ is the product of the $N - 1$ occupied (passive) one-particle ground states of the atom. For the final state, Ψ_f^N , we have

$$\mathcal{H}_f^N \Psi_f^N = E_f \Psi_f^N \quad (4.10)$$

in which

$$\Psi_f^N \propto \phi_k(\mathbf{r}_N) \Psi_a^{N-1}(\mathbf{r}_1, \dots, \mathbf{r}_{N-1}) \quad (4.11)$$

where $\phi_k(\mathbf{r}_N)$ is the wave-function of the excited photoelectron and $\Psi_a^{N-1}(\mathbf{r}_1, \dots, \mathbf{r}_{N-1})$ is the product of the occupied one-particle relaxed ground states in the presence of the core hole. The construction of the occupied ground states both with and without the core hole are based on the so-called $X\alpha$ scattered wave formalism, (65), using Slater determinants. The main result of the one-electron approximation is that the wave-function of the excited photoelectron satisfies a Schrödinger equation of the form

$$\mathcal{H}_k \phi_k(\mathbf{r}_N) = \left[-\frac{1}{2} \nabla^2 + V(\mathbf{r}_N) + V_{sc}(\mathbf{r}_N) \right] \phi_k(\mathbf{r}_N) = E_k \phi_k(\mathbf{r}_N) \quad (4.12)$$

which is valid in the case when the charge density of the system varies slowly over space as compared to the wavelength of the photoelectron (which is a good approximation for EXAFS, (12)). The term $V(\mathbf{r}_N) + V_{sc}(\mathbf{r}_N)$ in Eq. (4.12) represents the so-called *optical potential* of the atom; it consists of two parts, (56), (61): (i) a Coulomb (or Hartree) potential, $V(\mathbf{r}_N)$, in which the repulsive potential of all the bound $N - 1$ electrons is integrated over the extent of the charge density to give an effective Coulomb potential seen by the photoelectron and (ii) a local approximation to the exchange-correlation potential⁴, $V_{sc}(\mathbf{r}_N)$.

⁴The exchange potential is a consequence of the Pauli exclusion principle. The wave-function of the excited electron, ϕ_k , is not orthogonal to the initial one-electron ground states, Ψ_i^N , because they are eigenstates of Hamiltonians with different one-electron potentials, one without and one with a core hole potential. This non-orthogonality causes a violation of Pauli's exclusion principle when ϕ_k is occupied since it implies the one-electron states in Ψ_i^N have an occupancy greater than one. To avoid this a so-called exchange-correction is made to the potential so that the actual one-electron state to which the photoelectron makes its transition is orthogonal to all the initial states, Ψ_i^N . This correction is greatest at threshold and tends to zero at large photoelectron energies.

The correlation correction to the potential is a consequence of the inadequacy of the one-electron approximation to model the electron-electron interaction properly; electrons interact via the Coulomb potential which depends on their instantaneous positions. The averaging inherent in the one-electron model is therefore unable to reproduce this effect completely.

4.2.1.3 Exchange-correlation potential

The exchange-correlation potential (ECP) may be modelled in various schemes within the so-called local density approximation⁵, (73); three commonly used ECP's are discussed in the article by Chou et al., (12): (i) the real $X\alpha$ exchange potential, (134), (135), (ii) the energy-dependent Dirac-Hara potential, (28), (50), and (iii) the complex energy-dependent Hedin-Lundqvist potential, (54), (55), (56), (57), (74). The $X\alpha$ potential is the statistical average of the nonlocal Hartree-Fock potential over all occupied spin states evaluated at the local electron charge density $\rho(r)$, i.e.

$$V_{xc}(r) = -\frac{3\alpha}{2\pi} [3\pi^2 \rho(r)]^{\frac{1}{3}} \quad (4.13)$$

in which α is the adjustable exchange parameter. The $X\alpha$ potential is simple but has no energy dependence and fails at high energies ($E \geq 50\text{eV}$). An energy-dependence is integral to the Dirac-Hara potential and approximates to a $\rho(r)$ dependence instead of $[\rho(r)]^{\frac{1}{3}}$ in the high energy limit (decreasing inversely with energy) and it also reduces to the $X\alpha$ potential in the low energy range. However, this potential is Hermitian (i.e. it produces real eigenvalues in Schrödinger's equation) and so can not account for extrinsic energy losses of the photoelectron; this is done explicitly with the complex energy-dependent Hedin-Lundqvist ECP via the imaginary part of the potential (the real part also reduces to the $X\alpha$ exchange term in the low energy limit).

4.2.1.4 Many-body effects

The one-electron approximation is unable to account for many-body effects; this is partly taken into account in the ECP for electron-electron interactions but the approximation is unable to handle other effects connected with excitation dynamics, such as screening, polarisation, relaxation, decay etc. In particular the relaxation response of the other electrons to the generated core hole, the so-called shake-up and shake-off processes, have been shown to be of great significance, (74). These processes open up additional channels of excitation in

⁵ In the local density approximation, the exchange-correlation correction to the potential is determined from the local charge density and is thus a function of position within the atomic potential.

CHAPTER 4. TEMPERATURE DEPENDENCE OF EXAFS

addition to the primary channel and lead to intrinsic losses that have been modelled phenomenologically through constant reduction factors or by multichannel MS theory, (96).

4.2.1.5 Muffin-tin approximation

A major approximation in the modelling of the atomic potentials is the use of the Muffin-Tin (MT) approximation. For a given system of atoms in which the EXAFS scattering takes place, called the atomic cluster, 3d-space is artificially decomposed into non-overlapping spherical regions centered on the atomic sites; the radii of these spheres are known as the MT radii. Free atom Coulomb potentials are determined within the MT spheres via Poisson's equation using spherically symmetric charge densities, (14); in the interstitial regions the potential is volume averaged to produce a constant interstitial potential. By following this procedure it is generally found that an artificial discontinuity in the potential results at the MT boundaries. The atomic phase shifts, δ_i^l , and hence the atomic t -matrices are determined by matching the radial part of the solution to Schrödinger's equation for the propagating photoelectron at the MT boundaries.

4.2.1.6 MSXAS software

The programme MSXAS, (122), implements the theory outlined in this section. It computes the cluster potential and atomic t -matrices for the set of input atoms; the absorption coefficient is then calculated based on the curved-wave MS approach. The potentials may be calculated according to the $X\alpha$, Dirac-Hara or Hedin-Lunqvist schemes described above and the MT radii may be interactively or automatically⁶ set. MS paths are allowed up to any order. The programme requires the input of an additional parameter, γ , to account for core hole lifetime⁷ and experimental broadening effects.

⁶If the MT-radii are automatically set, the Norman method, (98), is used in which the ratios of nearest neighbour radii are fixed by comparing the ratio of the atomic radii with Z electrons. (Also referred to as the atomic number method). The Norman radii are then foreshortened by a factor of 0.8; this is in order that the Virial theorem, $V = -2T$, is approximately satisfied, T is the total kinetic energy of the electrons in the MT radius and V the potential. (This scale factor was quoted as 0.88 by Chou, (12)).

⁷The core hole lifetime, of the order of 10^{-15} s (K-shell Cu), introduces incoherence in the propagating photoelectron wave which reduces the integrity of the interference and results in an effective damping of the fine structure.

4.2.2 Configurational Averaging Approximation

Atomic disorder is modelled by considering a single atomic cluster centred on an absorbing atom in which the neighbouring atoms are located at their average positions relative to the central atom; each atom has an associated probability density function (pdf) that reproduces the distribution in its displacements with respect to the central atom throughout the sample and over time. Assuming Gaussian displacement pdf's, the damping effect on the partial fine structure from single scattering paths may be approximated by the so-called Debye-Waller factor, (5), (139), of the form $\exp(-2k^2\sigma^2)$ in which σ^2 may be identified as the second moment of the Gaussian displacement pdf along the interatomic vector. In cases where the static disorder may be neglected, this formalism naturally leads to a temperature dependence of the damped single scattering (within the harmonic approximation for thermal disorder) via the canonical average expression for σ^2 given in appendix B; see Eq. (B.11). The Debye-Waller factor is however inadequate in describing the effect of disorder on MS contributions to the fine structure. In this case, knowledge of the many-body displacement correlation function beyond order 2 is required in order to take account of the various instantaneous configurations of the MS paths; this information is redundant in single scattering where the interatomic distance completely describes the path. The true MS contribution is then the weighted average of the signal generated in all configurations of the MS path (i.e. configurational-average).

A method for approximating the damping of MS contributions to EXAFS due to dynamic and static disorder has been proposed, (3), that incorporates the higher-order correlations in the displacement distributions but is far less cumbersome than a brute-force configurational-average. It is based upon the assertion, (4), that any MS signal, χ_n , for an n -segment path of total length R_p , can be expressed in terms of a real amplitude function, $A(k, r)$, and a real phase function, $\phi(k, r)$ via:

$$\chi_n(k) = A(k, r) \sin[kR_p + \phi(k, r)] = A(k, r) \sin \psi(k, r) \quad (4.14)$$

where k is the photoelectron wavevector, r is the basis set of N generalised displacement coordinates describing the geometrical configuration of the MS path and $\psi(k, r)$ is the total phase function. (The functions $A(k, r)$ and $\phi(k, r)$ may be determined for a given configu-

CHAPTER 4. TEMPERATURE DEPENDENCE OF EXAFS

ration from MS theory). The configurational-averaged MS signal is the expectation value of the MS signal in each configuration over the pdf, $\rho(\mathbf{r})$, such that

$$\langle \chi_n(k) \rangle = \int d\mathbf{r} \rho(\mathbf{r}) A(k, \mathbf{r}) \sin \psi(k, \mathbf{r}) \quad (4.15)$$

It is assumed that a multivariate Gaussian distribution in the generalised displacement coordinate basis \mathbf{r} emulates the pdf of the MS path due to dynamic and static disorder; i.e.

$$\rho(\mathbf{r}) = \frac{e^{-(\mathbf{r}^\dagger \mathbf{M} \mathbf{r})/2}}{(2\pi)^{N/2} \det[(\mathbf{M})^\dagger]} \quad (4.16)$$

where \mathbf{r} represents the $(1 \times N)$ column matrix composed of the elements of \mathbf{r} and \dagger the matrix transpose. The $(N \times N)$ matrix \mathbf{M} has been introduced and represents the many-body displacement correlation function of the MS path, with $[\mathbf{M}]_{ij} = \langle r_i r_j \rangle$; within the Gaussian model it constitutes a complete description of the probability of finding the MS path in a given configuration. The principle of the method is to approximately determine the MS signal in displaced configurations by evaluating the behaviour of $A(k, \mathbf{r})$ and $\psi(k, \mathbf{r})$ in the equilibrium configuration only, i.e. at $\mathbf{r} = 0$. This is done by Taylor expanding $A(k, \mathbf{r})$ and $\psi(k, \mathbf{r})$ for small displacements in \mathbf{r} such that

$$\begin{aligned} A(k, \mathbf{r}) &= A(k, \mathbf{r})|_{\mathbf{r}=0} + \nabla A(k, \mathbf{r})|_{\mathbf{r}=0} \cdot \mathbf{r} + \frac{1}{2} (\mathbf{r}^\dagger \mathbf{H} A(k, \mathbf{r})|_{\mathbf{r}=0} \mathbf{r}) + \dots \\ &= A_0 + A_1 \cdot \mathbf{r} + \frac{1}{2} (\mathbf{r}^\dagger A_2 \mathbf{r}) + \dots \end{aligned} \quad (4.17)$$

and

$$\begin{aligned} \psi(k, \mathbf{r}) &= \psi(k, \mathbf{r})|_{\mathbf{r}=0} + \nabla \psi(k, \mathbf{r})|_{\mathbf{r}=0} \cdot \mathbf{r} + \frac{1}{2} (\mathbf{r}^\dagger \mathbf{H} \psi(k, \mathbf{r})|_{\mathbf{r}=0} \mathbf{r}) + \dots \\ &= \psi_0 + \psi_1 \cdot \mathbf{r} + \frac{1}{2} (\mathbf{r}^\dagger \psi_2 \mathbf{r}) + \dots \end{aligned} \quad (4.18)$$

where \mathbf{H} is the Hessian matrix for determining multidimensional second derivatives. (Note that A_0 and ψ_0 are scalars, A_1 and ψ_1 are $(1 \times N)$ column matrices and A_2 and ψ_2 are $(N \times N)$ matrices etc.). Combining these Taylor expansions and the expression for the pdf in Eq. (4.16), the configurational-averaged MS signal given in Eq. (4.15) may be expressed as a series of Gaussian integrals over \mathbf{r} :

$$\langle \chi_n(k) \rangle = \Im \int d\mathbf{r} \frac{e^{-(\mathbf{r}^\dagger \mathbf{M} \mathbf{r})/2}}{(2\pi)^{N/2} \det[(\mathbf{M})^\dagger]} [A_0 + A_1 \cdot \mathbf{r} + \frac{1}{2} (\mathbf{r}^\dagger A_2 \mathbf{r}) + \dots] \exp\{i[\psi_0 + \psi_1 \cdot \mathbf{r} + \frac{1}{2} (\mathbf{r}^\dagger \psi_2 \mathbf{r}) + \dots]\} \quad (4.19)$$

CHAPTER 4. TEMPERATURE DEPENDENCE OF EXAFS

which, considering only first order terms in the Taylor expansions, yields the final result

$$\langle \chi_n(k) \rangle = A_0 \left[1 + \frac{(A_1^\dagger M \psi_1)^2}{A_0^2} \right]^{\frac{1}{2}} e^{-(\psi_1^\dagger M \psi_1)/2} \sin \left[k R_p + \phi_0 + \frac{A_1^\dagger M \psi_1}{A_0} \right] \quad (4.20)$$

The dominant damping term is the factor $e^{-(\psi_1^\dagger M \psi_1)/2}$; its origin⁸ is the Fourier transform into ψ_1 -space of the Gaussian probability distribution which appears in Eq. (4.19) in the integral over r -space. Since ψ_1 is the rate of change of the total phase of the fine structure with respect to r , $\psi_1^\dagger M \psi_1$, is the variance of the total phase over the Gaussian distributions in the path configurations. The damping term reduces to the Debye-Waller factor for single scattering. Note that the configurational-averaging also generates a phase and amplitude correction to the fine structure but these terms are generally very small.

The expression in Eq. (4.20) is a convenient way to determine the configurational-averaged signal from any MS scattering when the displacements of the configurations in r are small and the probability distribution is Gaussian. This is a good approximation for substances with little static disorder at low temperature. The formalism can break down when the equilibrium configuration of a MS path sits at the maximum or minimum of $A(k, r)$ or $\psi(k, r)$ which may arise for scattering between collinear arrangements of atoms; in this case the derivatives A_1 and ψ_1 will be zero and the second order correction terms of the Taylor expansions of $A(k, r)$ and $\psi(k, r)$ cannot be neglected.

The above formalism provides a convenient method of determining the effect of dynamic and static disorder on the MS contributions provided that the matrix of second-moment correlations of the path displacements, M , is known. For the case discussed in this thesis (the zinc (II) tetraimidazole complex) the vibrational correlation function (VCF) for dynamic disorder has been established by inelastic neutron scattering as described in chapter 3. If the assumption is made that static disorder produces negligible atomic displacements with respect to the absorbing zinc atom, then the VCF totally describes M for this molecule. This is an excellent assumption in this case because static disorder does not alter the relative

⁸The specific term in Eq. (4.19) which generates the dominant damping term is the integral: $\int dr \rho(r) e^{i\psi_1 \cdot r}$ which represents the Fourier transform (or characteristic function) of the pdf, $\rho(r)$, into ψ_1 space. If $\rho(r)$ is the Gaussian distribution given in Eq. (4.16) then the integral reduces to its standard form $e^{i\psi_1 \cdot \langle r \rangle - (\psi_1^\dagger M \psi_1)/2}$ in which $\langle r \rangle$ is zero by definition so that $e^{i\psi_1 \cdot \langle r \rangle} = 1$.

CHAPTER 4. TEMPERATURE DEPENDENCE OF EXAFS

positions of atoms within the rigid imidazole rings and is unlikely to significantly displace the imidazole rings from their positions bonded to the zinc atom; it is more likely to manifest itself as displacements of the whole molecule in the crystal lattice which does not affect the EXAFS. The VCF is most conveniently expressed in the normal coordinate basis, \mathbf{Q} , in which Q_i are the mass-weighted generalised coordinates describing the 105 normal modes k of the molecule. In this basis, \mathbf{M} takes the form of a (105×105) diagonal matrix and within the harmonic approximation its elements are given by (see section 3.3.4)

$$[\mathbf{M}]_{ii} = \langle Q_i^2 \rangle = \frac{\hbar}{2\omega_i} \coth \left(\frac{\hbar\omega_i}{k_B T} \right) \quad (4.21)$$

where ω_i is the angular frequency of vibration of the i th normal mode and temperature dependence has been incorporated via the canonical average over energy states at temperature T of a harmonic oscillator. The information about the displacement correlations is contained in the eigenvectors, obtained from solving the secular equation in the normal mode analysis, which transform the normal coordinates into the cartesian basis (see section 3.3.6). The configuration of the molecule in every normal mode may thus be deduced at any point in the vibrational cycle from the second moment of the normal coordinate distribution and the eigenvector transformation. Clearly the MS signals from every scattering path may simultaneously be calculated in the displaced configurations and the phase and amplitude functions compared with those at equilibrium to determine the requisite $A_1(k)$ and $\psi_1(k)$ functions for each path in every normal mode. For reasons of numerical accuracy, the $A_1(k)$ and $\psi_1(k)$ functions were in fact determined for cartesian displacements equivalent to the square-root second-moment displacement of the normal coordinate, $\langle Q_i^2 \rangle^{\frac{1}{2}}$. The phase and amplitude correction term and the dominant damping term exponent are thus determined at any temperature as:

$$\begin{aligned} \frac{A_1(k)^{\dagger} \mathbf{M} \psi_1(k)}{A_0(k)} &\simeq \frac{1}{A_0(k)} \left[A(k, \mathbf{Q})|_{\langle Q_i^2 \rangle^{\frac{1}{2}}} - A(k, 0) \right] \left[\psi(k, \mathbf{Q})|_{\langle Q_i^2 \rangle^{\frac{1}{2}}} - \psi(k, 0) \right] \frac{\hbar}{2\omega_i} \coth \left(\frac{\hbar\omega_i}{2k_B T} \right) \\ \psi_1(k)^{\dagger} \mathbf{M} \psi_1(k) &\simeq \left[\psi(k, \mathbf{Q})|_{\langle Q_i^2 \rangle^{\frac{1}{2}}} - \psi(k, 0) \right]^2 \frac{\hbar}{2\omega_i} \coth \left(\frac{\hbar\omega_i}{2k_B T} \right) \end{aligned} \quad (4.22)$$

Note that the transformation from the generally curvilinear normal coordinate basis to the rectilinear cartesian basis is a first order approximation that only holds if the cartesian displacements remain small. The validity of this approximation is tested in section 4.4.2 over

the range of cartesian displacements used and was found to be sufficient to determine the $A_1(k)$ and $\psi_1(k)$ functions accurately.

4.3 Experimental Procedure

4.3.1 Sample Preparation and Experimental Apparatus

Crystalline zinc (II) tetraimidazole tetraborofluorate was prepared according to the method of Reedijk, (115). The crystals were thoroughly ground in a pestle and mortar and mixed in a 10 : 8 mass ratio with silicon grease (Bayer Silicone high viscosity). The sample/grease mixture was carefully smeared with a razor blade onto $\sim 10\mu\text{m}$ aluminium foil in a 5mm wide gap between two parallel pieces of sticky tape and cut out to form a strip; the sample/grease coating of the aluminium strip was $\sim 0.43\text{mm}$ thick. The silicon grease was chosen because its contraction was found to be approximately the same with decreasing temperature as the aluminium backing so that it was not expected to deform or crack. The sample/silicon ratio was calculated to produce approximately the required step of 1 in the absorption-thickness product⁹, μt , at the edge without exceeding a value of 2. These values ensure that the ionisation chambers operate within their dynamic ranges to avoid non-linearities and to minimise noise. When applying the sample/grease mixture to the aluminium foil care was taken to ensure approximate 2π isotropy in the lie of the monoclinic crystallites by smearing the grease from different directions. The remaining anisotropy about the axis perpendicular to the plane of the sample was subsequently isotropically averaged by positioning the sample at the so-called *magic angle*, (106), with respect to the beam which is known to avoid spurious texturing effects in powder samples.

The EXAFS measurements were performed on the EMBL-EXAFS beamline, (58), in HASYLAB, DESY in Hamburg using x-rays from the DORIS-III storage ring. DORIS-III typically operates at 4.5GeV with currents between 80 and 20mA and lifetimes of 1-4 hours. The monochromator, (110), consists of two separate (111) silicon crystals and is located 20m

⁹The absorption thickness is defined by $\mu t = -\ln(I/I_0)$ where μ is the absorption coefficient, t is the sample thickness and I_0 and I are the x-ray intensities before and after passing through the sample.

CHAPTER 4. TEMPERATURE DEPENDENCE OF EXAFS

from the source and 15m away from the first ionisation chamber. X-rays from the source are restricted in their vertical divergence by slits just before the monochromator. Two pairs of slits after the monochromator define the size of the beam in a tube spectrometer configuration; possible beam shifts therefore manifest themselves only as changes of intensity.

An important piece of apparatus on the beamline is the absolute x-ray energy calibrator, (109). This is composed of a 111-silicon crystal that analyses the residual beam emerging from the second ionisation chamber; for this reason it is important that sufficient flux is left unabsorbed by the ionisation chambers to minimise the effect of the contaminating hard x-rays. When the Bragg condition is satisfied, the 111-crystal back-reflects the beam onto two plastic scintillators attached to photomultiplier tubes. The exact angle of the 111-crystal plane to the incident beam (and hence the absolute energy of the back reflections) is determined by (i) locating degenerate reflections with different Miller indices in one of the scintillator channels and (ii) by establishing the energy splitting of nearly degenerate reflections between the two channels. The back-reflections provide calibrations points at various intervals all through the EXAFS spectrum between which an interpolation can be done that takes account of the oscillatory character of the monochromator winding mechanism. The energy calibration was better than $\pm 0.2\text{eV}$.

4.3.2 Data Collection

The beamline was carefully optimised for high spectral resolution and intensity¹⁰. The mirror usually situated between the post-monochromator slits was removed which improved the resolution¹¹ from 2.5eV to the intrinsic value 1.4eV at the expense of intensity; high resolution was essential for precise absolute energy calibration. The post-monochromator slits were opened to 5mm horizontal and 0.43mm vertical. The ion chambers were filled with a helium/argon gas mixture to a pressure of 200mbar for the front and 300mbar for the back chamber; this corresponds to about one third of the initial flux being absorbed in each of the

¹⁰ The data collection was made with the assistance of Dr. H. F. Nolting, EMBL, Hamburg

¹¹ The resolution is easily measured on this beamline by establishing the full-width at half-maximum, in the photomultiplier-count-rate versus energy spectrum, of a calibration peak from a back-reflection in the vertical plane. Vertical back-reflections are used because they do not suffer the additional broadening effect due to the horizontal divergence of the beam.

CHAPTER 4. TEMPERATURE DEPENDENCE OF EXAFS

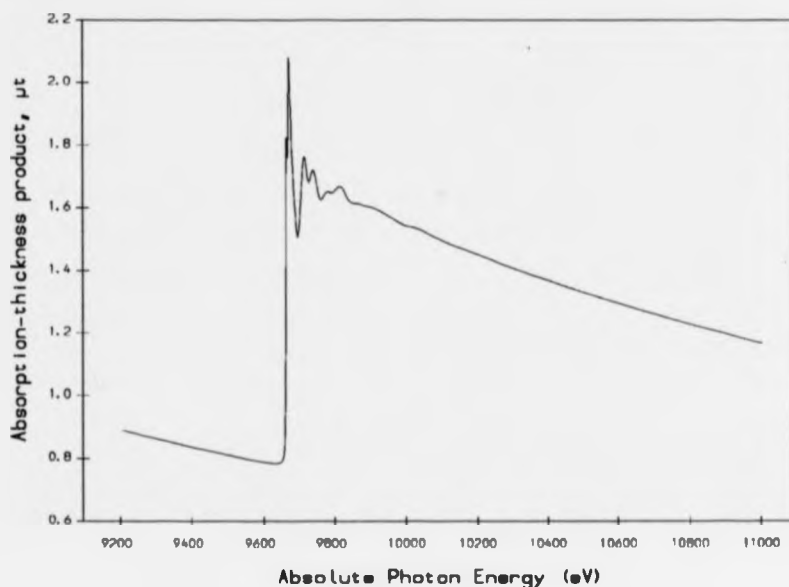


Figure 4.1: Plot showing x-ray absorption at K-edge of zinc (II) tetraimidazole tetrafluoroborate. This spectrum was recorded at 250 K in transmission mode with the sample normal inclined at a magic angle of $\sim 36^\circ$ (defined by $\sin^2 \theta = \frac{1}{3}$) to the incident beam.

chambers leaving a third of the x-ray intensity for absolute energy calibration.

Spectra were measured over the energy range $9200 \rightarrow 11000 \text{ eV}$ giving a $\sim 1300 \text{ eV}$ energy range after the edge; nine calibration back-reflections were found in this range in each channel with three bunched closely around the edge; these regions were fine scanned. A typical absorption plot is shown in figure 4.1 and exhibits virtually the optimum step in the absorption-thickness product of 1.

The fine structure from each absorption spectrum was extracted as the oscillatory function above the edge with respect to a segmented cubic spline curve fit running through the oscillations. The spline curve consisted of five segments, each extending 250 eV , and is assumed to approximate a background function for the oscillations. The amplitudes of the oscillations were determined as the fractions of the step in absorption-thickness, μt , at the edge, between the post-edge spline curve and the extrapolation of a curve fitted to the pre-edge region

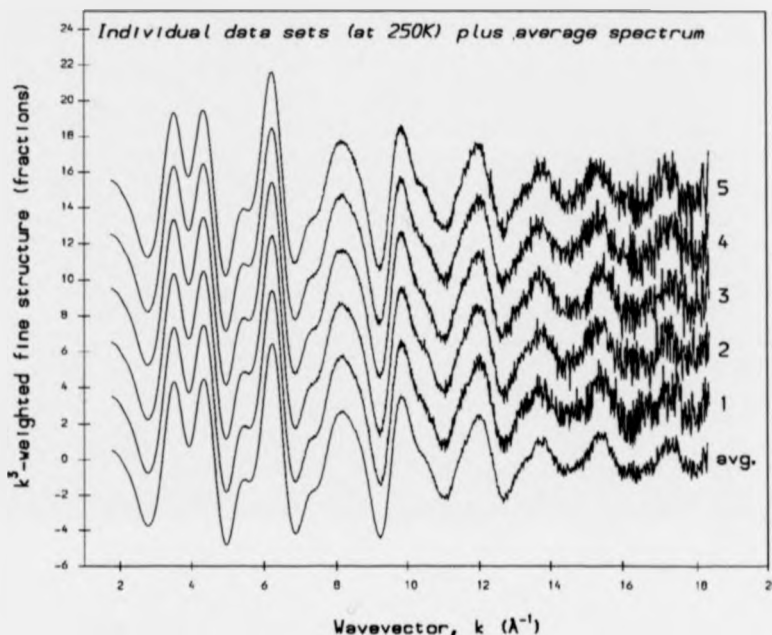


Figure 4.2: Plot showing comparison of five fine-structure spectra of zinc (II) tetraimidazole tetraborofluoride with the average of the five spectra; the data presented in this plot were recorded at 250K but the same averaging procedure was adopted at each temperature. The fine structure are plotted with respect to the photoelectron wavevector, $k = \sqrt{2m(E - E_0)}$, where E_0 is taken to be 9870.5eV. The amplitudes of the fine-structure spectra are in fractions of the step in absorption-thickness at the edge and are weighted by k^3 ; the offset between the spectra is 3 units on the y-scale.

(9200 \rightarrow 9600eV); the pre-edge region was fitted with a polynomial of the form $C\lambda^3 + D\lambda^4$ according to Victoreen's law, (149).

Because of the need for high quality data with low statistical noise, at least five spectra were measured at each temperature and their fine structures averaged; this was only possible because the data was of high resolution and absolute-energy-calibrated. The result of this averaging procedure is depicted in figure 4.2 where the k^3 -weighted fine structures of five spectra are compared to the average of the five spectra.

Data were recorded at seven temperatures: 20K, 50K, 100K, 150K, 200K, 250K,

CHAPTER 4. TEMPERATURE DEPENDENCE OF EXAFS

and 300K starting at high temperature. The spectra were virtually free of glitches¹² at 300K and 250K but at 200K three glitches appeared at about 480eV ($k = 11.2\text{\AA}^{-1}$), 590eV ($k = 12.5\text{\AA}^{-1}$) and 980eV ($k = 16.0\text{\AA}^{-1}$) above the edge; the latter glitch was serious but did not appear again at any other temperature. The other two narrow ($\Delta E \simeq 20\text{eV}$) glitches persisted in all the spectra down to 20K and were possibly due to inhomogeneities that appeared in the sample at low temperature; they vanished again upon raising the temperature above 200K. The glitches were seen to shift significantly in energy by rotating the monochromator 1° about its vertical axis and so a second temperature scan was made with the glitches displaced. In this way real data values were collected throughout the energy range and an average was then made at each temperature of the fine structures with the spurious data points removed (i.e. the gaps in spectra being compensated for by real data points in others for which the monochromator had been rotated).

The complete, averaged data set at the seven temperatures is presented in figure 4.3. The fine structure exhibit the expected increase in damping, especially at high k , with increasing temperature; there are also three well defined shoulders at $k = 5.5\text{\AA}^{-1}$, $k = 7.5\text{\AA}^{-1}$ and $k = 10.5\text{\AA}^{-1}$ which are progressively damped with increasing temperature. However, the spectra do not show large changes in form as a function of temperature.

4.3.3 Preliminary Analysis of Experimental Fine Structures

The conventional method of EXAFS data analysis is to take the Fourier transform of the experimental spectrum, as described in chapter 1, page 2. The moduli of the Fourier transforms of the experimental fine-structure spectra are shown in figure 4.4; they contain information about the modified radial distribution function, with respect to the central atom, that describes the strength of the photoelectron scattering. The features in the Fourier transforms are increasingly damped and less resolved with increasing temperature but remain essentially the same in form (except the 200K spectrum which appears slightly different at a radius of $\sim 3.5\text{\AA}$ which is probably a consequence of the poorer quality fine structure spectrum.)

¹² A glitch is a spurious artifact in the spectrum. The cause of glitches are manifold, but a major cause is due to sharp variations in the transmittance of the monochromator as a function of E .

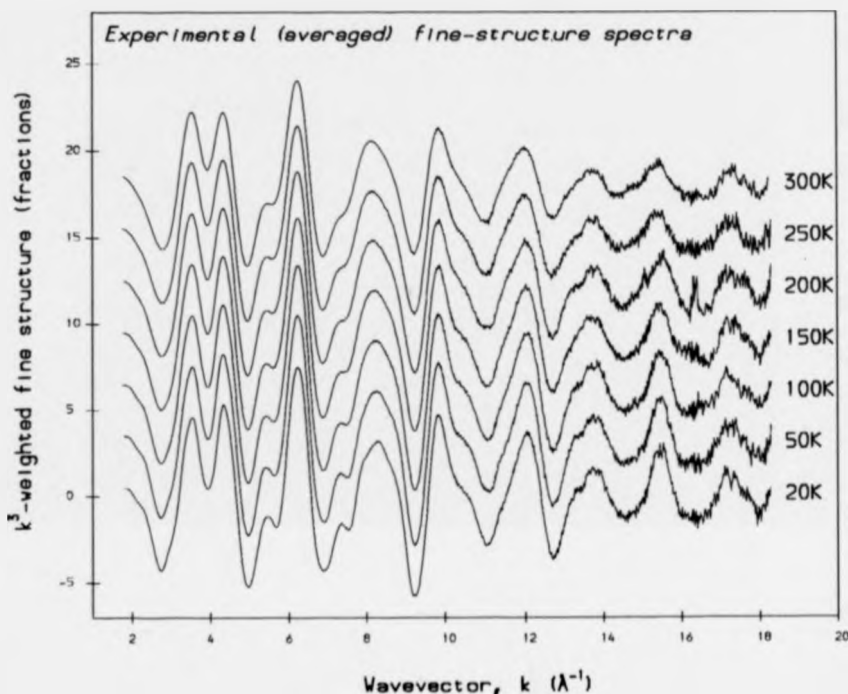


Figure 4.3: Experimentally determined x-ray absorption fine structure of sinc (II) tetraimidazole tetraborofluoride at different temperatures. Each spectrum is k^3 -weighted and constitutes the average of at least five energy-calibrated raw spectra. The k -axis is drawn with respect $E_0 = 9670.5\text{eV}$ and the offset between the spectra is 3.0 units on the y-scale.

The damping is especially apparent for the large peak at $\sim 1.6\text{\AA}$ which may be related to the strength of scattering from the first shell; i.e. back-scattering from the zinc-bonded nitrogens. The Fourier transform spectra beyond 1.6\AA are related to scattering involving atoms beyond the first shell; however it has been shown, (108), for the same compound, that it is impossible to interpret this region without the use of *ab initio* calculations since it is composed of strong MS contributions. (The importance of including MS in interpreting Fourier transform spectra has recently been reiterated for the cases of gas phase SiCl_4 , SiF_4 and SiCH_3 , (27), and for ferrocene and nickelocene, (123)).

The temperature dependent Fourier transform spectra may be used to obtain an estimate

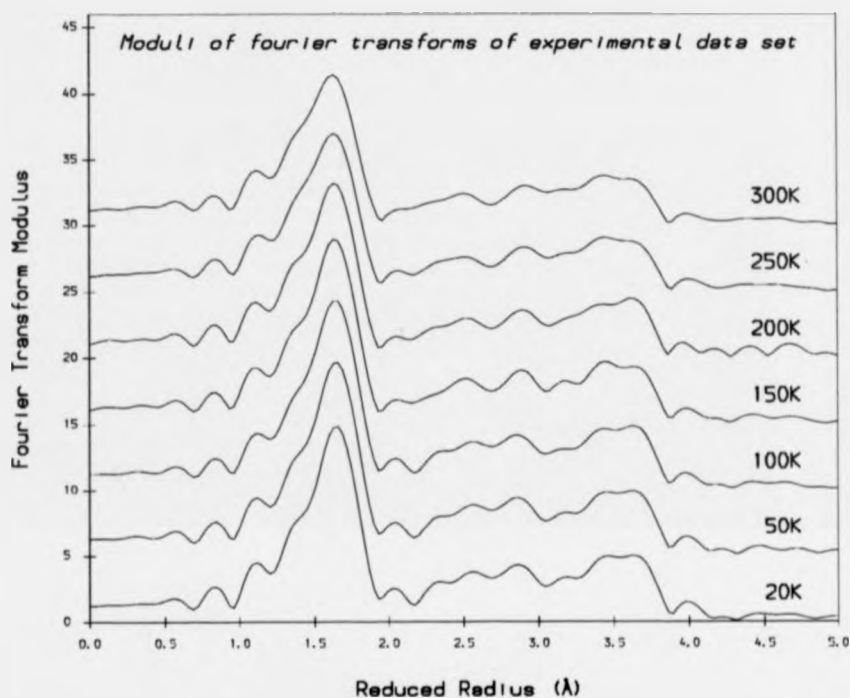


Figure 4.4: Plot of the moduli of the Fourier transforms of the experimental fine-structure spectra shown in figure 4.3 at the various temperatures. The fine-structure spectra were cubic-spline fitted (80 knots) and then transformed over the range 19.5eV ($k = 2.3\text{\AA}$) to 1295.5eV ($k = 18.2\text{\AA}$) with a smoothing function at the window edges. The transform spectra maintain the same form at all temperatures but are increasingly damped at high temperatures; the offset between spectra is 5 units on the y-scale.

of the mean-squared displacements of the Zn-N interatomic distance about its equilibrium value in the following way: The 1.6\AA peaks are isolated (by a window $0.95 \rightarrow 1.95\text{\AA}$) and back-Fourier-transformed to produce approximate fine-structure spectra due to Zn-N back-scattering at each of the experimental temperatures. The back-transformed spectra are presumed to obey single-scattering theory, (127), such that the curvature of the photoelectron wavefront is neglected (i.e. plane-wave approximation) and the asymptotic form of the radial part of the wave function is adopted. Within these approximations, the spectra, $\chi_{(T)}(k)$, are

CHAPTER 4. TEMPERATURE DEPENDENCE OF EXAFS

described by the well known equation

$$\chi_{(T)}(k) = \frac{S(k)}{kR^2} \sin(2kR + \delta'(k)) e^{-2R/\lambda} e^{-2\sigma^2 k^2} \quad (4.23)$$

where T is the experimental temperature, $S(k)$ is an amplitude function for back-scattering from the N-atom, R is the average Zn-N interatomic distance, $\delta'(k)$ is the total phase shift experienced by the back-scattered wave for the Zn-N path, λ is the mean free path of the photoelectron and $e^{-2\sigma^2 k^2}$ is the Debye-Waller factor. The ratio of the back-scattered fine structure at two temperatures, T_1 and T_2 , is thus given by

$$\frac{\chi_{(T_1)}(k)}{\chi_{(T_2)}(k)} = \frac{\exp[-2\sigma_{(T_1)}^2 k^2]}{\exp[-2\sigma_{(T_2)}^2 k^2]} = \exp[-2\Delta\sigma_{(\Delta T_{12})}^2 k^2] \quad (4.24)$$

where $\Delta\sigma_{(\Delta T_{12})}^2$ is the change in σ^2 over the temperature jump ΔT_{12} . A plot of $\ln(\chi_{(T_1)}/\chi_{(T_2)})$ versus k^2 should therefore yield a straight line passing through the origin with gradient $-2\Delta\sigma_{(\Delta T_{12})}^2$ and, since there are a range of experimental temperatures, it is possible to plot $\Delta\sigma^2$ as a function of ΔT . If σ^2 is identified as the mean-squared displacement of the Zn-N interatomic distance about its equilibrium value then σ_0^2 is the value of σ^2 at $T = 0K$. Based on the assumption that σ^2 obeys the Einstein model for lattice vibrations, $\Delta\sigma^2$ may thus be written as

$$\Delta\sigma^2 = \sigma_0^2 \left[\coth \left(\frac{E_i}{2k(\Delta T_{12} - T_1)} \right) - 1 \right] \quad (4.25)$$

where E_i is an associated Einstein energy for the Zn-N vibrations and T_1 is a low experimental temperature at which only ground state Zn-N vibrational energy levels are assumed to be filled (i.e. for the data set here we may take T_1 to be 20K). Within this approximation, the value of σ_0^2 may be determined from the plot of $\Delta\sigma^2$ against ΔT either by best-fitting the coth expression in Eq. (4.25) with the free parameters σ_0^2 and E_i or by extrapolating the linear part of the plot at large ΔT_{12} , the intercept on the axis $\Delta T_{12} = -T_1$ being equal to σ_0^2 .

The above procedure was followed by comparing the back-transformed spectra at all temperatures to the one at 20K. An example of the plot of $\ln(\chi_{(T_1)}/\chi_{(T_2)})$ versus k^2 is shown in figure 4.5 for $T_2 = 250K$; it is typical of all temperatures. The plotted curve is shown with the broad error bars generated from the errors of the back-transformed fine-structures. It is clearly non-linear and so a line had to be best fitted from which the gradient $-2\Delta\sigma_{(\Delta T_{12})}^2$

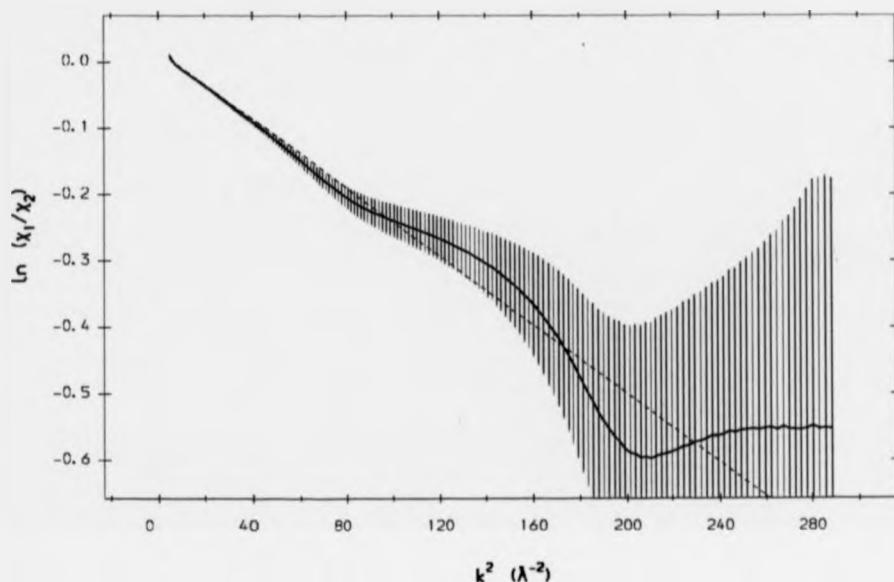


Figure 4.5: Example plot of $\ln(\chi_{(T_1)}/\chi_{(T_2)})$ versus k^2 where T_2 is 250 K and $T_1 = 20$ K. $\chi_{(T_1)}$ and $\chi_{(T_2)}$ are the amplitudes of the back-transformed fine structures of the first shell peaks (1.6 Å) in the Fourier transform spectra shown in figure 4.4. The dashed line depicts the line of best fit running through the plotted curve (bold line); the error bars are shown for the plotted curve and are determined from the experimental fine structure error. The gradient of the best-fitted line is equivalent to $-2\Delta\sigma_{(\Delta T_{12})}^2$ and constitutes one of the points in figure 4.6.

was established with an associated error determined from the gradients of other possible lines passing through the plotted curve. From the Fourier transform spectra at seven temperatures, six values of $\Delta\sigma_{(\Delta T_{12})}^2$ were established with error bars and are plotted against ΔT_{12} in figure 4.6. The ΔT_{12} range was not sufficient to reach the linear regime of the coth term in Eq. (4.25) (in this case the linear regime starts > 500 K) and so σ_0^2 and E_i had to be determined by a least squares fit of the coth expression to the data points shown. The result was $\sigma_0^2 = (2.5 \pm 0.5) \times 10^{-3} \text{ Å}^2$ for the mean-squared deviation of the Zn-N interatomic distance and $E_i = (36 \pm 5) \text{ meV}$ for the Einstein energy. The large error margins on these values are a consequence of the low sensitivity of the fitted coth function to changes in σ_0^2 or E_i ; they were determined from the values at which the fitted function lay at the extremes of the error

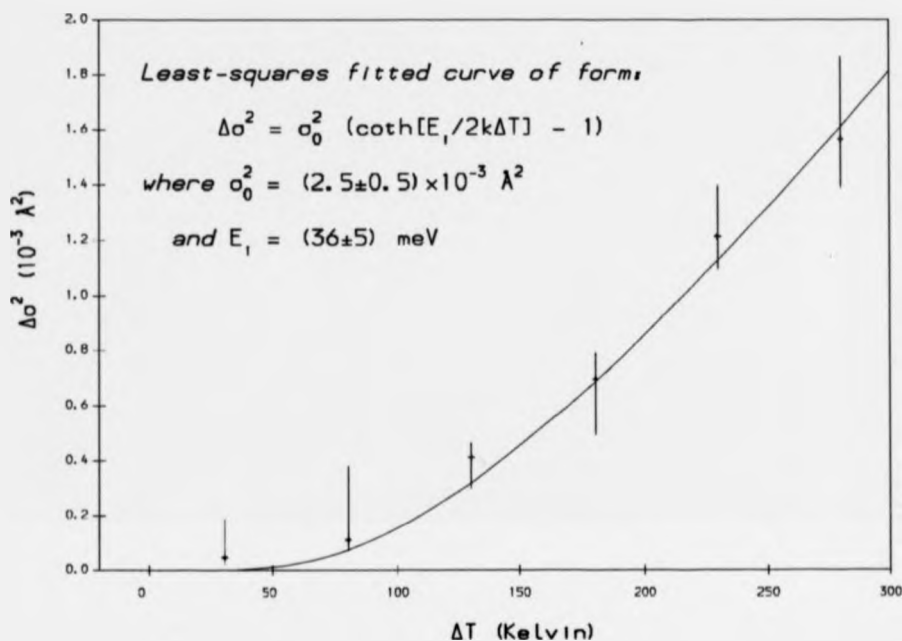


Figure 4.6: Plot of $\Delta\sigma^2$ versus ΔT_{12} where $\Delta T_{12} = T_2 - T_1$ and T_1 and T_2 are temperatures at which x-ray absorption data was collected; $\Delta\sigma^2$ is the corresponding change in the mean-squared deviation of the Zn-N interatomic distance. The experimental points may be best-fitted by a function of the form shown (within the Einstein model of lattice vibrations) where E_1 is an Einstein energy associated with the Zn-N vibrations and σ_0^2 is the mean-squared deviation of the interatomic distance when all vibrations are in their ground state. This method is a direct way to obtain a value for the mean-squared displacement of the first shell distance from the x-ray absorption data alone.

bars shown in figure 4.6.

4.4 Configurational-Averaging Computation

4.4.1 EXAFS Signal without Damping

The EXAFS signal was calculated by MSXAS, (122), using energy-dependent complex Hedin-Lundqvist potentials. 21 atoms were included in the zinc (II) tetraimidazole cluster which was defined as a central zinc atom and two pairs of symmetry equivalent imidazole rings. The atom coordinates were obtained from x-ray crystallography of zinc (II) tetraimidazole borofluorate

CHAPTER 4. TEMPERATURE DEPENDENCE OF EXAFS

at 100K and modified so that the imidazole rings were exactly planar; they were the same coordinates as those used in the normal mode analysis in chapter 3 and are listed for the asymmetric unit in table 3.9. Muffin-tin radii were generated by the Norman criterion, (98), and foreshortened by a factor of 0.8; the zinc MT radius was 1.128Å and those of the carbon and nitrogen atoms in the range 0.81 → 0.86Å. Consequently there was no overlap of the MT spheres along the Zn-N vectors but an overlap of 0.25 → 0.30Å between MT spheres within the imidazole rings. The whole cluster was contained within an outer sphere of 5.04Å. Phase shifts were calculated for each potential up to $l = 20$. Other parameters entered to the programme included the core ionisation potential of 710.08 Rydbergs (9660.7eV) and an additional parameter, $\gamma = 0.07$ Rydbergs (0.95eV) to account for core hole lifetime and experimental broadening effects. The total Debye-Waller factor and the damping factors for each path were all set to zero so that the signal does not take any account of disorder effects.

The calculated signal including all 160 possible single, double and triple scattering paths in the asymmetric unit is shown in figure 4.7 superimposed on the experimental spectrum at 20K. The theory mostly reproduces the correct form of the curve, although there is a notable discrepancy at $k = 8.3\text{\AA}^{-1}$; the phase of the oscillations are also well predicted. However a major cause for concern are the amplitudes of the theoretical curve which appear too small and thus allow no scope for treatment of the damping of the signal due to disorder. For example, the amplitudes of the fine-structure maxima in the range $k = 9 \rightarrow 13\text{\AA}^{-1}$ are so similar in the two plots that any treatment of damping would cause the theoretical signal to be underestimated. Thus it may be anticipated that configurational-averaging calculations based on this EXAFS signal do not produce a good agreement with experiment.

The theoretical calculation references the photoelectron energy (and hence the wavevector zero, i.e. $k = 0$) with respect to an energy, E_0 . This is the *vacuum level* and represents the absolute photon energy required to ionise a core electron in the zinc atom and excite it to a continuum state with exactly zero kinetic energy; in other words the zero of the theoretical scale is the level of the effective potential for the photoelectron at infinite distance, measured on the photon energy scale. Due to the good agreement in the oscillatory phase of the theory and experiment it is possible to superimpose the two fine-structure spectra and hence

CHAPTER 4. TEMPERATURE DEPENDENCE OF EXAFS

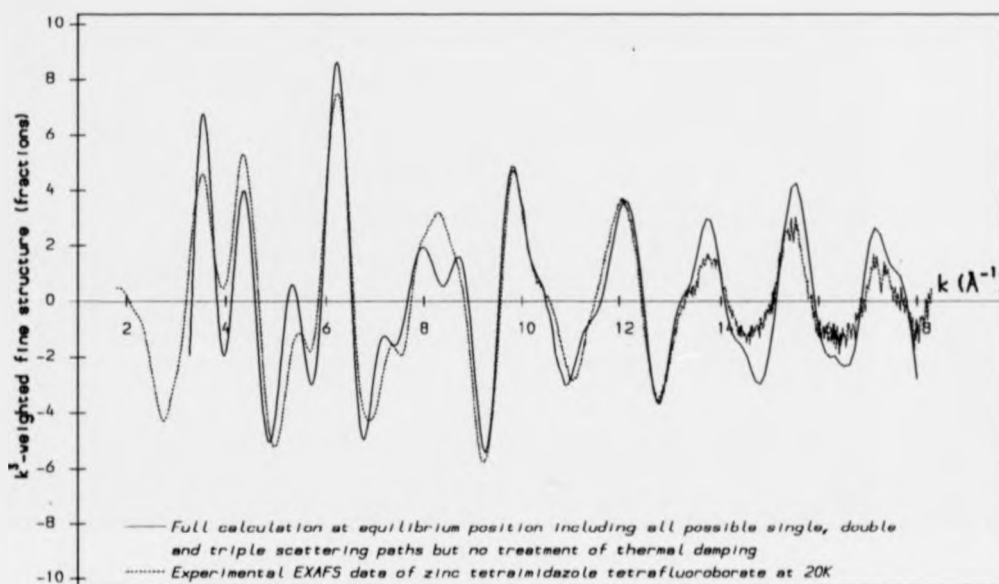


Figure 4.7: Superposition of experimental and theoretical EXAFS curves for the zinc (II) tetraimidazole complex. The theoretical curve was calculated without any modelling of the damping due to disorder. The k -axis (wavevector) for the experimental spectrum is referenced with respect to $E_0 = 9670.5\text{eV}$. Of concern in this plot is the lack of theoretical amplitude, which is particularly evident in the region $k = 9 \rightarrow 13\text{\AA}^{-1}$, since there is no scope for modelling of the damping due to disorder, e.g. thermal damping.

establish E_0 from the zero point of the theoretical curve. The vacuum level was thus evaluated at $(9670.5 \pm 2.0)\text{eV}$ on the calibrated energy scale; (the error margin was determined from the maximum observed offset of the theoretical from the experimental curve when the two were superimposed). The absolute photon energy at which a core electron is ionised and excited to the Fermi level may also be estimated as the energy of the point of inflexion of the absorption edge; it was found to occur at $(9664 \pm 0.5)\text{eV}$. The gap between the Fermi level and the vacuum level constitutes the work function, Φ , of the zinc atom for photoelectric emission; the value of Φ is thus $(6.5 \pm 2.1)\text{eV}$. The positions of the vacuum level and the Fermi level with respect to the absorption edge are depicted in figure 4.8.

Not all of the 160 single, double and triple scattering paths in the asymmetric unit produce significant contributions to the total theoretical EXAFS signal. The MS paths were ordered in

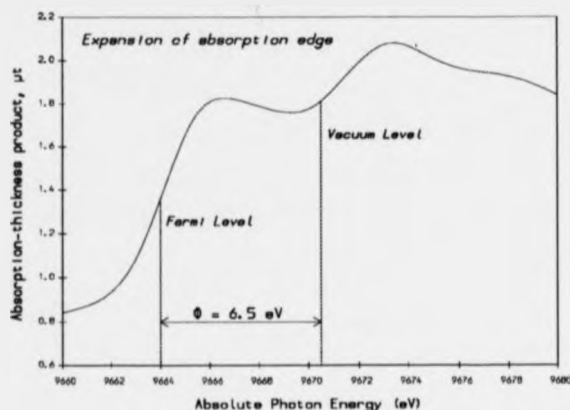
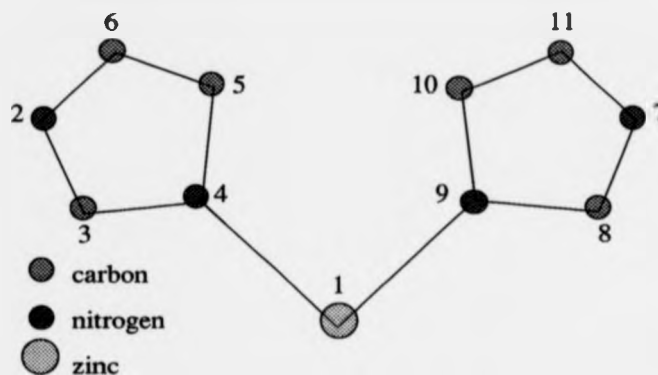


Figure 4.8: Expansion of the x-ray absorption K-edge of zinc (II) tetraimidazole tetrafluoroborate. Indicated on the diagram is the vacuum level, E_0 , determined from the superposition of the theoretical EXAFS spectrum with the experiment, and the Fermi level, defined as the point of inflexion of the absorption edge. The energy difference between the two is equivalent to the work function, Φ . The core ionisation energy (not shown) was defined as 9660.7 eV.

importance according to the maximum calculated amplitudes in the k^3 -weighted fine structure spectra and it was found that only the sixty most significant paths were needed to generate a signal that was not perceptibly different from the full calculation shown in figure 4.7. The sixty MS paths are listed in table 4.1 for the asymmetric unit of the molecule and represent the paths used in the configurational-averaging calculations in this thesis. The k^3 -weighted fine-structure contributions of the top forty paths given in table 4.1 are displayed in figure 4.9 with the same amplitude scales for comparison. As expected, the two most important paths in the asymmetric unit are the Zn-N-Zn back-scattering paths. In fact, of the 20 most significant paths, 16 incorporate the Zn - N vector; mean-squared-displacements in this vector are therefore expected to strongly influence the damping of the total spectrum due to disorder; this may be recalled when examining the results of the configurational averaging calculations. The last few of the forty paths appear negligible (their maximum amplitudes being of the order of only 6% of the Zn-N back-scattering amplitude) but the sum effect of many such contributions should not be ignored. The importance of double and triple scattering contributions in this system (evident in figure 4.9) further underlines the necessity

asymmetric unit of zinc (II) tetraimidazole complex



1. 1 9 1	21. 1 5 6 1	41. 1 7 11 9 1
2. 1 4 1	22. 1 2 3 4 1	42. 1 4 2 6 1
3. 1 9 11 1	23. 1 7 8 9 1	43. 1 2 6 5 1
4. 1 8 7 9 1	24. 1 10 11 1	44. 1 7 11 10 1
5. 1 3 2 4 1	25. 1 6 1	45. 1 9 7 11 1
6. 1 4 6 1	26. 1 11 1	46. 1 3 2 3 1
7. 1 8 1	27. 1 2 4 1	47. 1 4 5 4 1
8. 1 3 1	28. 1 7 9 1	48. 1 2 6 4 1
9. 1 10 1	29. 1 9 10 11 1	49. 1 5 6 5 1
10. 1 4 2 4 1	30. 1 4 5 6 1	50. 1 3 6 5 1
11. 1 5 1	31. 1 3 4 1	51. 1 8 11 10 1
12. 1 4 6 5 1	32. 1 4 3 4 1	52. 1 7 11 1
13. 1 9 11 10 1	33. 1 9 8 9 1	53. 1 2 6 1
14. 1 9 10 1	34. 1 8 7 8 1	54. 1 3 5 1
15. 1 9 11 9 1	35. 1 8 9 1	55. 1 8 10 1
16. 1 9 7 9 1	36. 1 8 7 11 1	56. 1 7 8 1
17. 1 4 5 1	37. 1 8 7 10 1	57. 1 4 2 5 1
18. 1 4 6 4 1	38. 1 3 2 6 1	58. 1 10 11 10 1
19. 1 7 1	39. 1 9 10 9 1	59. 1 9 1 9 1
20. 1 2 1	40. 1 3 2 5 1	60. 1 4 1 4 1

Table 4.1: The sixty most significant photoelectron scattering paths in the asymmetric unit of the zinc (II) tetraimidazole molecule including single, double and triple scattering. The paths were ordered according to the maximum amplitude appearing in the k^3 -weighted fine structure spectra for each path; the fine structure contributions of the top forty MS paths in this list are shown in figure 4.9.

CHAPTER 4. TEMPERATURE DEPENDENCE OF EXAFS

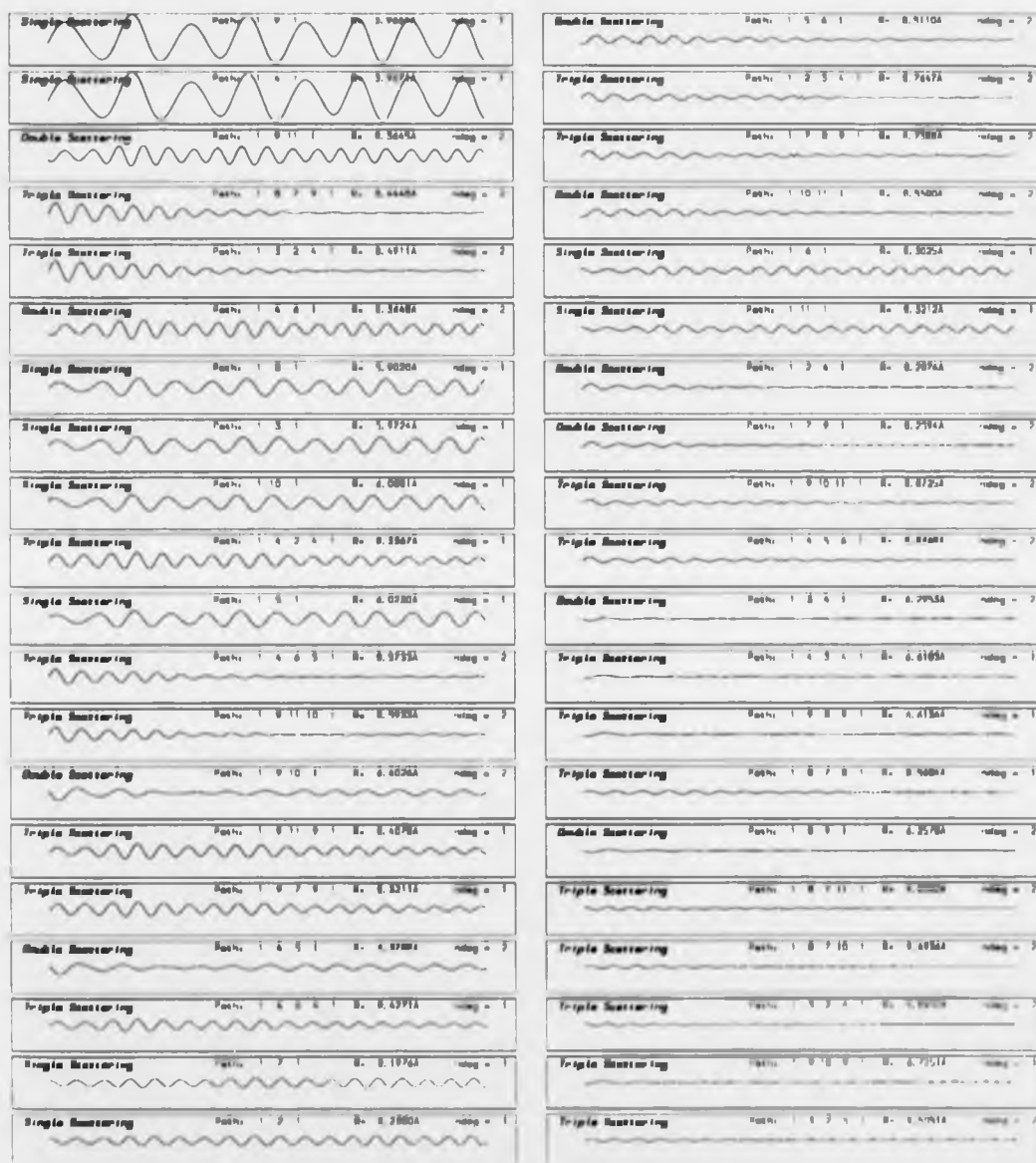


Figure 4.9: The k^3 -weighted fine structure contributions of the forty most important multiple-scattering paths in the sinc (II) tetraimidazole cluster taken from the list in table 4.1. The axes of the spectra are not annotated for clarity; the y-axis is the k^3 -weighted amplitude and ranges from -1.9 to 1.9 and the x-axis is the photoelectron wave vector from $k = 2.0 \text{ \AA}^{-1}$ to $k = 19 \text{ \AA}^{-1}$.

to go beyond the single scattering approximation when analysing EXAFS data.

4.4.2 Test of Configurational-Averaging Algorithm

The first order configurational-averaging approximation outlined in section 4.2.2 is valid when the phase and amplitude functions, ($\psi(k, r)$ and $A(k, r)$ for each path) vary linearly over the range of molecular configurations. In the case of displacements due to thermal vibrations, this implies that the phase and amplitude derivative functions, $\psi_1(k)$ and $A_1(k)$, must be the same when evaluated at all points in the displacement cycle of a given vibrational normal mode. This requirement is complicated by two factors:

1. The mean-squared displacements due to the various normal modes are summed for each atom to produce the total mean-squared displacement undergone by the atom. $\psi_1(k)$ and $A_1(k)$ must therefore be the same for the normal mode vibration about any point in the probability distribution function due to all the other normal modes.
2. The normal vibrations are properly expressed in the normal coordinate basis which in general is curvilinear. The individual atomic displacements however are most conveniently expressed in the rectilinear cartesian coordinate basis as infinitesimal displacements. This approximation only holds for linear or for very small curved atomic trajectories; it may break down for large curved trajectories which deviate significantly from the approximated linear paths leading to false evaluations of $\psi_1(k)$ and $A_1(k)$.

The above concerns were investigated by examining scattering from three nearly collinear atoms in the zinc (II) tetraimidazole complex: the absorbing zinc, and the two nitrogen atoms in one imidazole ring. A diagram is given in figure 4.10 showing the relative positions of the atoms. These atoms were chosen because the phase and amplitude functions were expected to change rapidly (for double and triple scattering) when the outer nitrogen displaces. This is because the nearly collinear arrangement means that each atom sits in or near the direction of strong forward- or back-scattering of the other atoms; these scattering lobes become narrow at high photoelectron energies (see reference (108)) and consequently the scattering from the other atoms seen by the outer nitrogen changes rapidly when it displaces through the lobe.

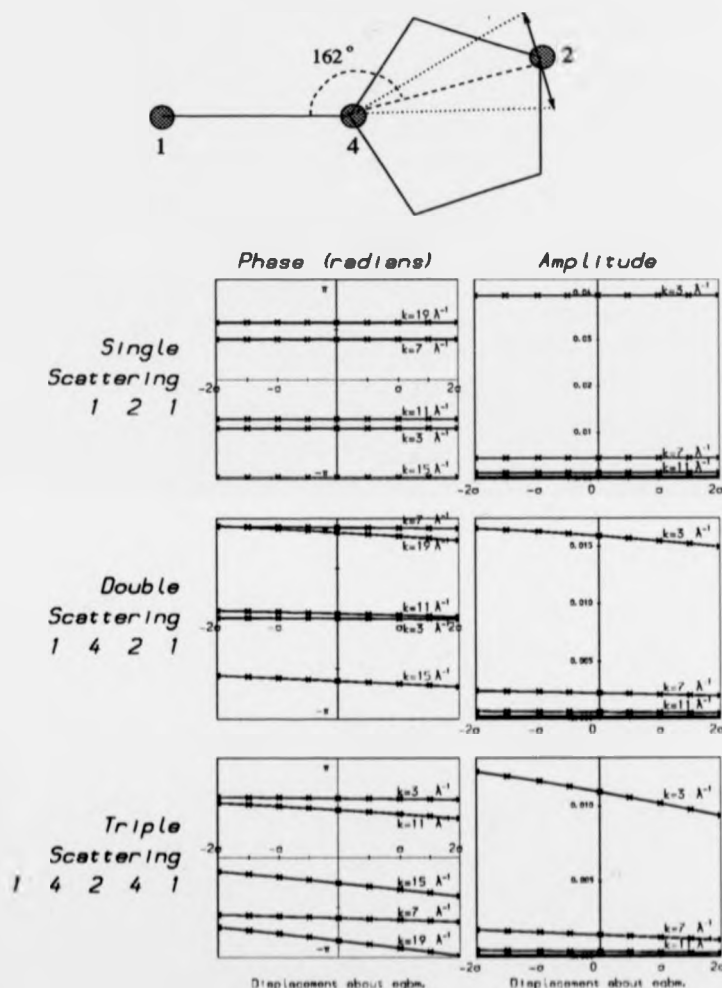


Figure 4.10: Test of the validity of the first order configurational averaging approximation. The scattering in the three paths shown was calculated for nine displacements of the outer nitrogen (labelled 2) along the linear trajectory indicated. The maximum displacement was $\pm 0.22 \text{ \AA}$ from equilibrium which is equal to twice the standard deviation displacement of the atom in this direction due to all normal modes at 300 K as determined from inelastic neutron scattering. The atomic arrangement chosen and the linearity and magnitude of the displacements provided a stringent test of constant variation of the phase and amplitude functions. All plots are linear, (i.e. the first derivative is constant) and so the first order approximation is considered sufficient for this molecule.

CHAPTER 4. TEMPERATURE DEPENDENCE OF EXAFS

In other words this arrangement constitutes a severe test of the constancy of the $\psi_1(k)$ and $A_1(k)$ functions when the outer nitrogen is displaced. Only the outer nitrogen was displaced in this test, along a linear trajectory perpendicular to the N-N vector and in the imidazole plane. The phase and amplitude functions were established at nine points on this trajectory and were plotted for five values of photoelectron wavevector, k . The greatest magnitude of the nitrogen displacement was $\pm 0.22 \text{ \AA}$ from equilibrium, which constitutes twice the maximum standard deviation (2σ) of the displacement in this direction at 300 K due to all 105 normal modes of the molecule as established from inelastic neutron scattering. The results of the test are shown in figure 4.10 and demonstrate that the phase and amplitude functions are linearly varying for this trajectory even as far out as 2σ at 300 K . The $\psi_1(k)$ and $A_1(k)$ functions are actually determined at displacements of 1σ for each normal mode; consequently this test indicates that the first order approximation used in the configurational averaging algorithm is sufficient.

The graphs in figure 4.10 demonstrate that the phase function varies most rapidly at high photoelectron energies whereas the amplitude function tends to have the greatest gradient at low k . Thus the dominant damping term $\exp[-(\psi_1^\dagger M \psi_1)/2]$ in Eq. (4.20) tends to produce the most damping at high k whereas the phase and amplitude corrections, given by $(A_1^\dagger M \psi_1)/A_0$, are greatest at low k .

4.5 Results

4.5.1 Individual Multiple Scattering Paths

The effect of the configurational averaging calculation on the partial EXAFS signal from each of the 60 most significant MS paths was determined. An example is given in figure 4.11 for the Zn-N back-scattering path (1 9 1); this path generates the largest contribution to the undamped total EXAFS signal. The damping effect of the thermal motion is pronounced and is seen to increase with temperature as expected; at 20 K and $k = 17 \text{ \AA}^{-1}$ it causes 80% reduction in the peak amplitude which is effectively the damping due only to zero point motion of the molecule. At 300 K , at the same point in the spectrum, the damping attenuates

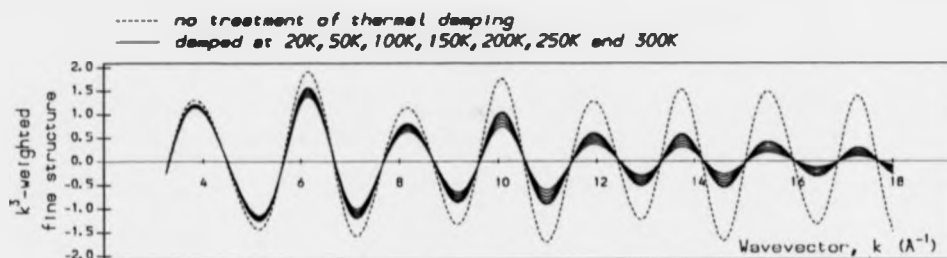


Figure 4.11: Partial EXAFS signal from the Zn-N single scattering path. The dashed line indicates the signal generated in the equilibrium configuration with no treatment of thermal damping. The solid lines represent the same signal after correction for thermal motion of the Zn-N interatomic distance in the 105 normal modes of the molecule at seven different temperatures.

the signal by more than 90%. There is no significant phase shift of the signal for this path, even at low k which is where the phase correction term is greatest. Similar plots showing the temperature dependence of the partial EXAFS signals are presented in appendix H for the ten most important paths of one of the imidazoles in the asymmetric unit. The damping of the signals is of the same order of magnitude for the various paths and none show significant phase shifts except the 1 4 5 1 double scattering path which does exhibit visible shifts at low k .

The configurational averaging calculation also yields a detailed breakdown of the contribution of each of the 105 normal modes of the molecule to the damping of the partial EXAFS signal. An example of this is given in figure 4.12 for the same Zn-N back-scattering path discussed above. The effect of each normal mode is split into its contributions to the two distinct correction terms in the first order configurational averaging formula in Eq. (4.20). The first bar chart in figure 4.12 shows how much each normal mode contributes to the exponent of the dominant damping, i.e. $-(\psi_1^\dagger \mathbf{M} \psi_1)/2$, for $k = 12 \text{ \AA}^{-1}$ which represents the mid-range of the spectrum. It shows the contributions both at 20K (white bars) and at 300K (black bars). The exponential of the sum of the $-(\psi_1^\dagger \mathbf{M} \psi_1)/2$ terms from each normal mode determines the damping effect on the spectrum. The second bar chart in figure 4.12 similarly depicts the contributions of each normal mode to the correction term $(A_1^\dagger \mathbf{M} \psi_1)/A_0$ at 20K and 300K

CHAPTER 4. TEMPERATURE DEPENDENCE OF EXAFS

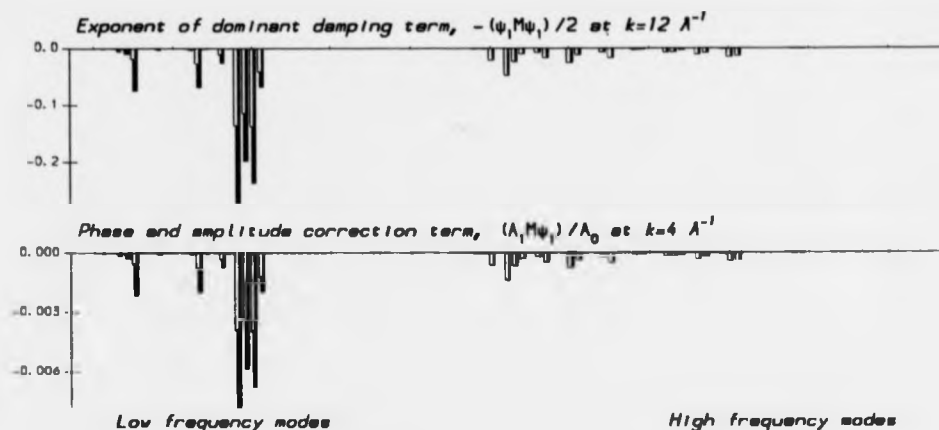


Figure 4.12: Partial contributions of the 105 normal modes to the correction terms in the first order configurational averaging approximation (see Eq. (4.20)) for the same Zn-N back-scattering path shown in figure 4.11. The white bars represent the contribution from each normal mode at 20K and the black bars at 300K. The bars are positioned in order of increasing frequency from left to right.

which are seen to be very small.

The two bar charts show very similar distributions for this path. The low frequency vibrations generate the greatest damping since they produce the largest mean-squared displacements of the atoms. The contributions from the low frequency modes increases faster with increasing temperature than the high frequency modes because the mean-squared displacements of the low frequency modes increase faster with temperature. For this path the greatest damping is generated by the four large contributions at low frequency; these correspond to the four tetrahedral stretch modes of the molecular skeleton (including the tetrahedral breathing mode). These four modes produce the largest displacements in the Zn-N interatomic distance and hence introduce the greatest degree of incoherence in the back-scattering from the nitrogen atom.

In appendix H similar bar charts are presented for the ten most important scattering paths from one of the imidazole branches. In general, the greatest contributions to the damping come from the low frequency modes. A notable exception is the triple scattering path 1 4 6 5 1 which exhibits large contributions to the dominant damping term from high

CHAPTER 4. TEMPERATURE DEPENDENCE OF EXAFS

frequency imidazole ring in-plane stretching modes in the range $900 \rightarrow 1600\text{cm}^{-1}$. However the imidazole ring out-of-plane normal modes only contribute negligibly to the damping of all paths; this corresponds to a range $300 \rightarrow 900\text{cm}^{-1}$ in the vibrational spectrum of the molecule which does not generate any significant damping of the total EXAFS spectrum. Unlike the Zn-N back-scattering paths (1 4 1 and 1 9 1), for most paths the two bar charts are not similar; in fact for many paths the phase and amplitude correction contributions are often positive as well as negative. Very little damping is due to torsional librations of the imidazole branches since this does not greatly affect the shape of the scattering paths.

By inspecting the bar charts in appendix H, it is evident that the same four low frequency Zn-N tetrahedral stretch modes of the molecule (discussed above) produce very large damping contributions for all the paths. In fact, for the ten paths considered, they are the dominant contributors to the damping for all but the triple scattering path 1 4 6 5 1. This path is by far the most damped path (virtually 100% above $k = 12\text{\AA}^{-1}$) and much of the damping is due to rigid-imidazole wags and bends.

4.5.2 Temperature Dependence of Total EXAFS Spectrum

The configurationally averaged total EXAFS spectra at various temperatures are presented in figure 4.13 superimposed on the experimental EXAFS data. The comparison of the theoretical and experimental amplitudes of the signal show large discrepancies; the calculated signal underestimates the true amplitudes at many points in the spectrum. The temperature dependence is however well modelled for the peaks around $k = 6$, $k = 14$ and $k = 17\text{\AA}^{-1}$. The behaviour of the theoretical and experimental spectra with temperature becomes more transparent when the information in figure 4.13 is redisplayed separately as in figure 4.14. From this plot it may be seen that the changes in the two sets of spectra, as a function of temperature, are similar even though the signal is not correctly modelled.

Finally the Fourier transforms of the theoretical spectra are shown as a function of temperature in figure 4.15 and may be compared with those of the experimental spectra in figure 4.4. (Note that the transform window for the theoretical spectra was slightly smaller than that used for the experimental spectra due to the smaller calculated signal range; the Fourier trans-

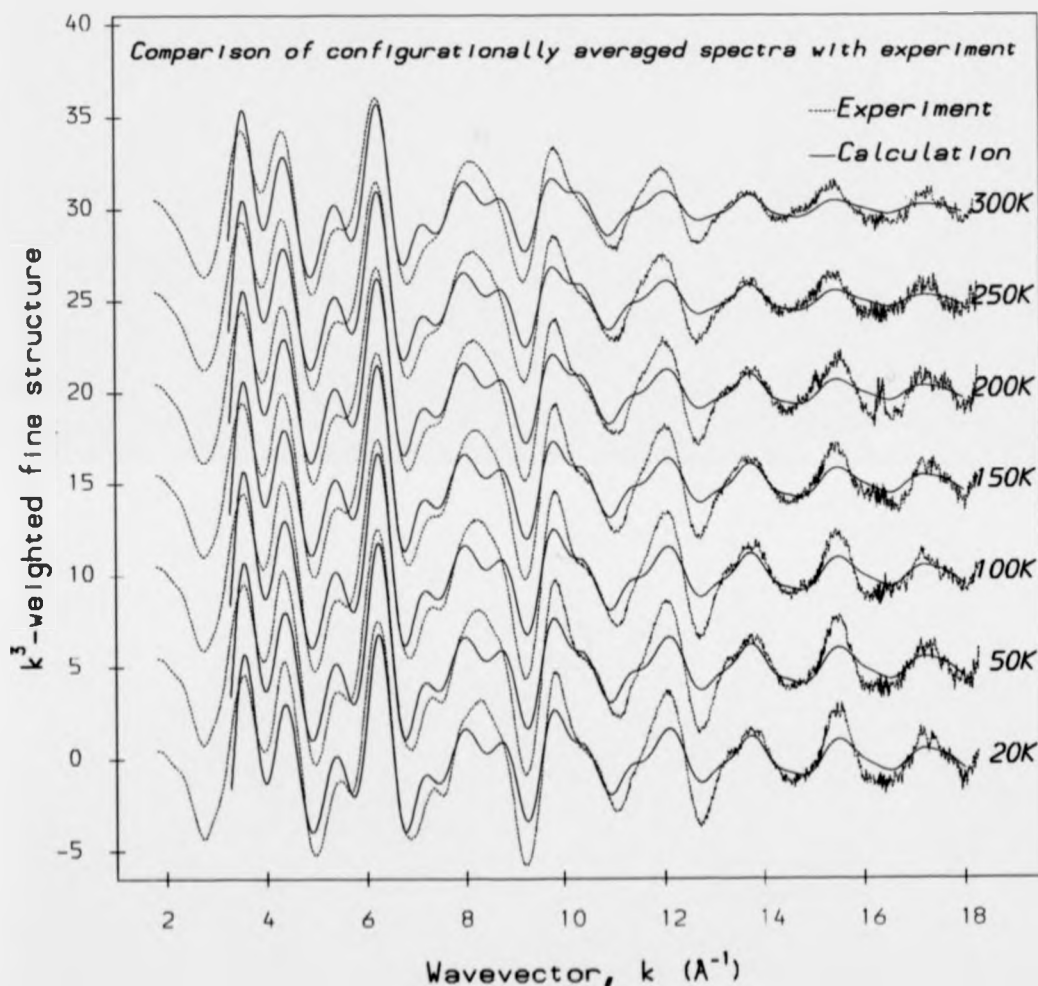


Figure 4.13: Theoretical and experimental temperature dependence of the EXAFS spectrum of the zinc (II) tetraimidazole complex. The theoretical spectra include a full configurational-average treatment of the damping effect due to the thermal motion of the molecule but appear to underestimate the true amplitude of the signal at many points in the spectrum.

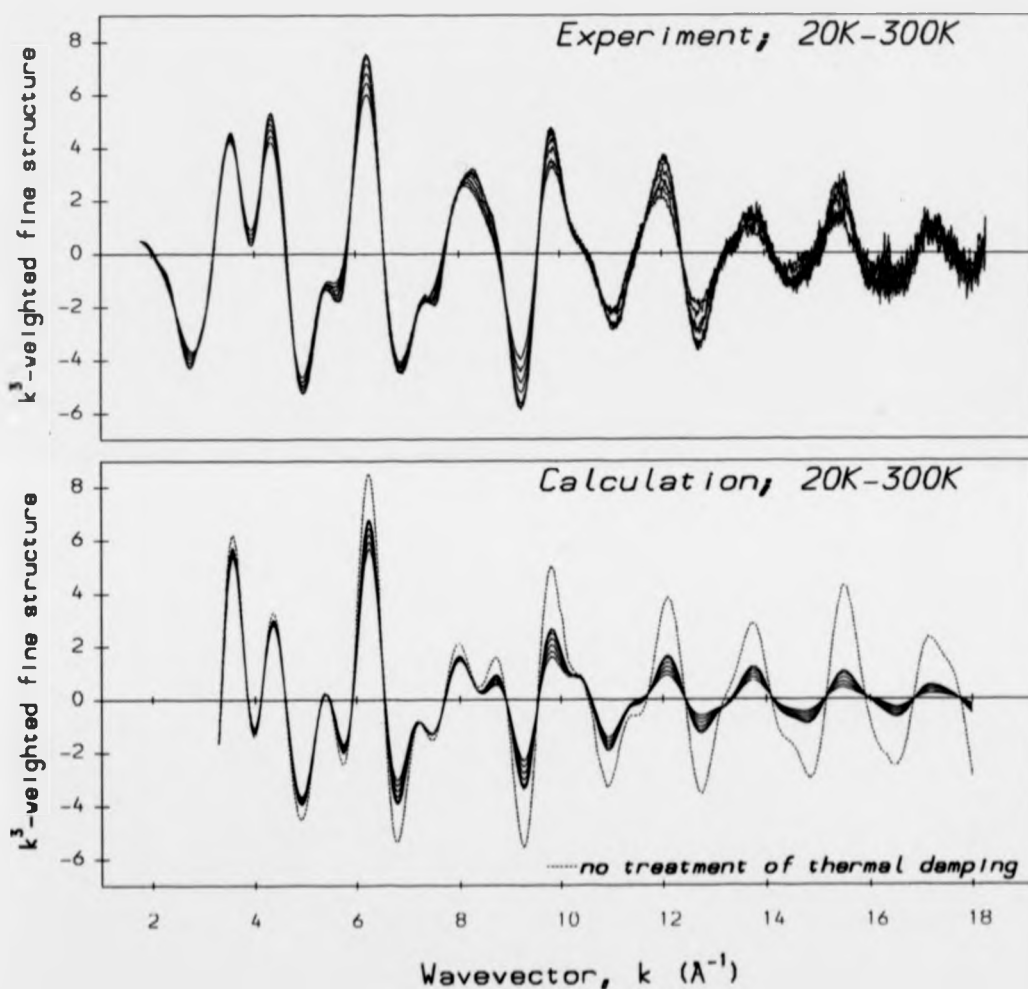


Figure 4.14: Theoretical and experimental temperature dependence of the EXAFS spectrum of the zinc (II) tetraimidazole complex. This plot redisplayes the information shown in figure 4.13 so that the theoretical and experimental signals are presented separately. The dashed line in the lower plot shows the theoretical signal generated with no treatment of the damping due to thermal motion.

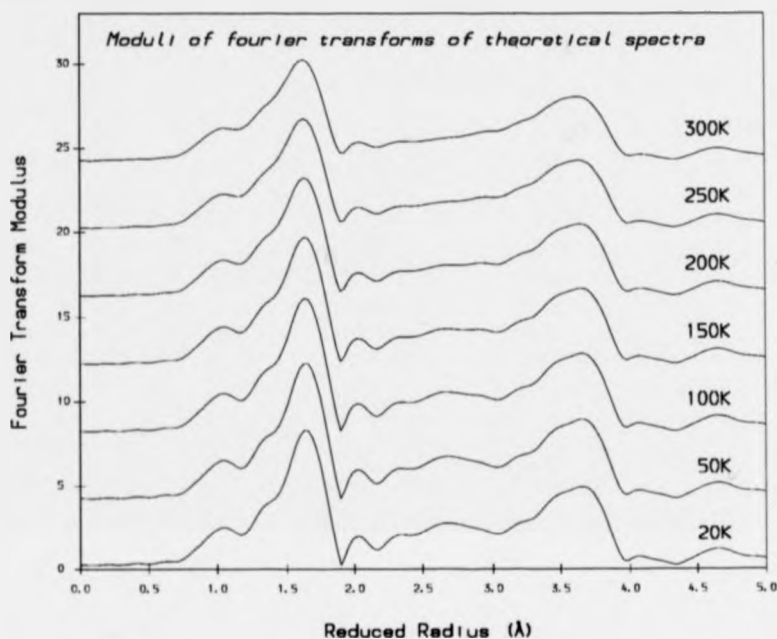


Figure 4.15: Plot of the moduli of the Fourier transforms of the theoretical fine-structure spectra shown in figures 4.13 and 4.14. The fine-structure spectra were cubic-spline fitted (80 knots) and then transformed over the range 41eV ($k = 3.3\text{\AA}$) to 1200eV ($k = 17.7\text{\AA}$). The offset between spectra is 4 units on the y-scale.

forms of the experimental spectra are however virtually unchanged when determined over the smaller window and figures 4.4 and 4.15 may therefore be directly compared.) The Fourier transforms of the theoretical and experimental spectra have approximately the same form although the mid-range ($2.0 \rightarrow 3.2\text{\AA}$) in the theoretical case is not as resolved such that nearly all features are washed out at high temperature. The magnitude of the Fourier transform modulus is much smaller in the theoretical case than in the experimental case which is a consequence of the underestimate of the EXAFS amplitudes in the configurationally averaged spectra.

The implications of these results are discussed in the following and final chapter of this thesis.

Chapter 5

Discussion

The key ingredient to the configurational average calculation, presented in the last chapter, is the many-body vibrational correlation function (VCF) of the molecule obtained via inelastic neutron scattering (INS), described in chapter 3; therefore, in the next section, the confidence that may be placed in the VCF is assessed. This is done by comparing the atomic displacements implied by the VCF from INS studies with the same quantities determined via the TLS analysis of the crystallography data (described in chapter 2). In addition, the Zn-N interatomic displacements, which were shown in the last chapter to be the main contributors to thermal damping, are compared with values from TLS and EXAFS experiment. Finally, the assumption of harmonicity, implicit in the determination and implementation of the VCF, is discussed.

The causes of the underestimate in the theoretical amplitude are discussed in the subsequent section. It is described how the artificial energy discontinuity in the modelling of the optical potentials at the Muffin-Tin boundary significantly perturbs the amplitude function throughout the EXAFS spectrum. It is argued that the incorrect modelling of the amplitude function impairs a proper data analysis.

In the following section some current approaches to EXAFS data analysis are briefly overviewed with an emphasis on their treatment of the damping due to thermal and static disorder. The implications of the configurational averaging results presented in this thesis to these approaches are discussed.

Finally, the conclusions of this study are summarised.

5.1 Confidence in the Vibrational Correlation Function (VCF)

The VCF is constructed from the eigenvectors of a harmonic force field which models the vibrations of the zinc (II) tetraimidazole complex as an isolated molecule. Clearly this is only an approximation of the real vibrating system, which is coupled to some degree to the rest of the lattice, but the model does successfully reproduce the hydrogen-weighted INS vibrational density of states of the molecule at 20K. This is a sensitive test of the atomic displacements described by the VCF since the intensities of the peaks in the INS spectrum are directly related to the mean-squared displacement amplitudes of the hydrogen atoms in the molecule in each vibrational normal mode. It is, however, extremely difficult to assign error margins to the atomic displacements defined by the VCF since these depend on many factors; for example, the discrepancies between the calculated and experimental INS peak intensities and energies are difficult to translate into error margins in individual atomic displacements since the peak is generally a sum of contributions from many atoms. Furthermore, the accurate modelling of the peak intensities depends on the correct description of broad background features in the INS spectrum such as phonon wings or on the correct modelling of nearby peaks. It is also possible that undetected mistakes in the energy assignment of normal modes will lead to incorrect atomic displacements.

Thus, due to the difficulty in assigning error margins, it is important that the VCF is checked for consistency with other techniques. This has already been done to some extent in chapter 3 since the frequencies of the normal modes of vibration were extensively checked against infrared and Raman values and values from *ab initio* force field calculations, but this provides no check of the atomic displacements in each normal mode. The calculated INS intensities (and hence indirectly the mean-squared atomic displacements of the VCF) were checked for self-consistency against INS spectra of deuterated states of the molecule; a more independent check, however, is to directly compare the atomic displacements with those obtained from another method; i.e. TLS analysis. This is therefore done in the following subsection.

5.1.1 Consistency of Atomic Displacements from INS and TLS Studies

The TLS analysis of x-ray crystallography data gives estimates of the total mean-squared atomic displacements with respect to the molecular centre of mass at two temperatures, 100K and 150K. It thus provides a means of directly checking the atomic displacements described by the VCF via a method which is fundamentally different from INS. The VCF's at 100K and 150K are generated from the VCF at very low temperature assuming perfectly harmonic normal vibrations; the comparison with the TLS therefore may indicate the validity of the harmonic approximation since any anharmonic components will contribute to the TLS mean-squared displacements. A significant underestimate of the TLS displacements at these temperatures may be evidence of anharmonicity.

Both the TLS and INS analyses hinge on the validity of the assumption that the zinc (II) tetraimidazole molecule may be treated as effectively isolated; in other words that the internal vibrational modes are distinct from the lattice vibrations. This is supported by the insensitivity of the INS spectrum of the zinc (II) tetraimidazole complex to modifications in the crystal field incurred by changing the counterion in the crystal from perchlorate to tetrafluoroborate, see figure 3.13. Further evidence was the lack of peak broadening in the INS spectrum in all modes, except those below 160cm^{-1} which were only slightly broadened beyond the intrinsic resolution. This indicates that most of the internal modes are non-dispersive which supports the notion that they are decoupled from lattice modes.

In order to make the comparison, the mean-squared atomic displacements described by the VCF from the INS study had to be summed for each atom over all normal modes; this is because the TLS analysis does not separate the total displacements into contributions from various modes. The comparison is depicted in bar chart form in figure 5.1 for root-mean-squared displacements of the imidazole ring atoms along two projections. The *stretch* rms displacements correspond to the projection in the plane of the imidazole ring and parallel to the Zn-N bond. The *wag* rms displacements correspond to the projection in the plane of the imidazole ring and perpendicular to the Zn-N bond.

In the stretch projection, the agreement between the two techniques is satisfactory; the average discrepancy in the rms displacements is 25%. The TLS rms displacements are con-

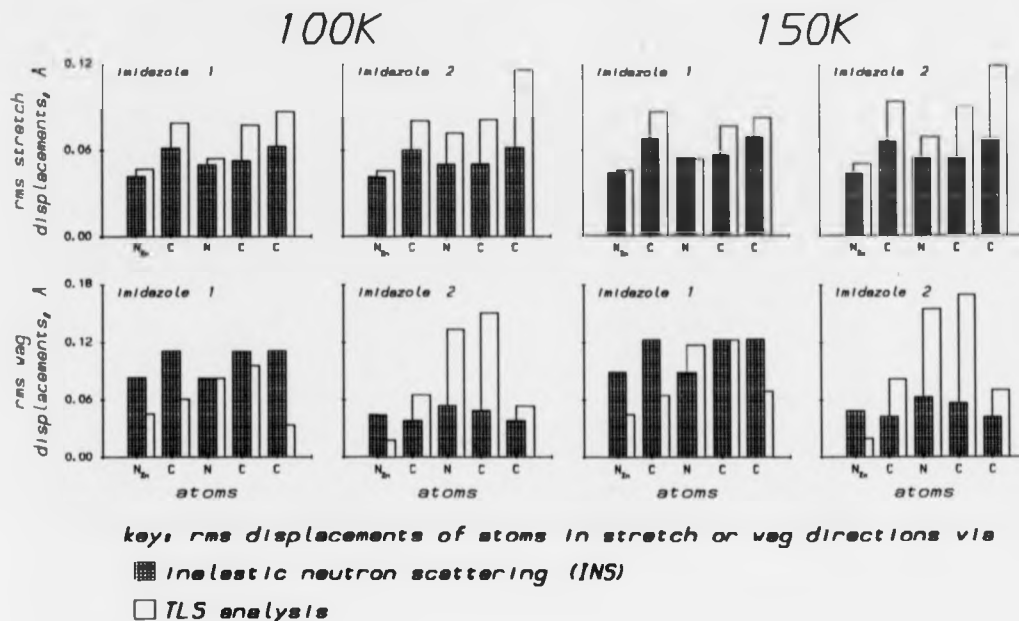


Figure 5.1: Comparison of results from the TLS analysis and INS study. The bar charts depict the root-mean-squared displacement amplitudes of each of the five ring atoms in the two asymmetric imidazole branches of the zinc (II) tetraimidazole complex. The rms displacements (in Å) are in the frame of the molecule centre of mass and are projections in the stretch direction (top row) and the wag direction and are shown at the two temperatures at which the TLS analysis was done.

sistently greater than those generated by the VCF from the INS study which would suggest the presence of anharmonicity; however most of the INS values lie within the calculated maximum error margin of the TLS rms displacements ($\pm 0.03\text{Å}$) so it cannot be stated that the harmonic assumption breaks down at these temperatures. In both methods, the outer nitrogens of the imidazole rings are seen to undergo less motion in the stretch direction than the carbon atoms. This may be due to the restricting effect of the H-bonding on this nitrogen; it is encouraging to see that it has also been reproduced in the INS case where the H-bonding is approximated by stiffening the N-H bond. It should be noted how well the rms displacements of the zinc-bonded nitrogen (denoted N_{zn} in figure 5.1) agree between the two methods; the values in the bar chart for this displacement are therefore tabulated in table 5.1. These values

rms displacements of Zn-bonded N-atom in stretch direction, Å								
	20K		100K		150K		300K	
	TLS	INS	TLS	INS	TLS	INS	TLS	INS
imidazole 1	-	0.040	0.047	0.042	0.046	0.044	-	0.052
imidazole 2	-	0.040	0.047	0.041	0.050	0.043	-	0.051

Table 5.1: Comparison of the root-mean-squared displacements of zinc-bonded nitrogen projected along the Zn-N vector and in the frame of the molecule centre of mass via the methods of TLS and INS. Note that these values are not the same as the rms displacements of the Zn-N interatomic distance (i.e. not the Zn-N pair correlation function). The calculated error of the TLS values in this case is $\pm 0.011\text{\AA}$.

alone however do not represent the Zn-N pair correlation function (the quantity determining EXAFS damping along the Zn-N path) since they are only the displacements of the nitrogen and take no account of the relative motion of the zinc atom.

In the wag projection, the agreement is not so good; this was anticipated since the TLS analysis typically models translational motion better than librational. The real maximum error margin for the TLS rms displacements in this direction is likely to be greater than the calculated one of $\pm 0.03\text{\AA}$ since the crude model for the separation of internal and overall motion is not so appropriate for these kinds of librational displacements. Nevertheless the values are of the same order of magnitude; the average agreement between the values from TLS and INS for this projection is $\pm 70\%$. It is interesting to observe in table 5.1 that the overall wag displacements of imidazole 2 are approximately 50% smaller than those of imidazole 1. This pattern may be explained by the asymmetry in the hydrogen bonding to the two unique imidazoles in the asymmetric group whereby the H-bonds from imidazole 2 are shorter and more linear and therefore stronger. For example, in the tetrafluoroborate complex, the H-bond $\text{NH}\cdots\text{F}$ from imidazole 2 is $2.747(2)\text{\AA}$ long compared to $2.949(2)\text{\AA}$ from imidazole 1 and the angles formed by the bonds are 155° and 124° respectively.

Values from the TLS analysis in the out-of-plane projection relative to the imidazole rings

(bend) could not be established, as described in chapter 2. This was due to an overestimate of the L tensor about one principal axes which resulted in negative values for the internal displacements in this projection. In this case, the Zn-4N rigid-body model used to identify the overall translational and librational displacements of the molecule clearly failed. This is because the zinc-bonded nitrogens strongly participate in out-of-plane internal motion as may be observed in figure 3.21 and appendix G. However, it may also be seen that the zinc-bonded nitrogen participates far less in the low frequency in-plane wag modes of the molecule; in other words, the INS study demonstrates what was suspected in the TLS study, that the wag librational axis passes close to the zinc-bonded nitrogen whereas the bend librational axis is displaced towards the centre of the ring.

The TLS analysis can only be considered as an indication of the magnitudes of the displacements. As was discussed in chapter 2, the process of subtracting large molecular mean-squared displacements from the overall observed mean-squared displacements, which are only slightly larger, to leave estimates of the internal motion, incurs large error margins. The TLS analysis is also based on very broad assumptions about the nature of the internal motion in the molecule and takes no account of correlations in the atomic motion. In this case, the TLS analysis should be most reliable in predicting the mean-squared displacements projected in the stretch direction; these values are seen to agree well with those predicted by the VCF. It is precisely this motion which dominates the damping effect on the EXAFS spectrum and so it is essential that it is well modelled by the VCF. This is discussed further in the next subsection.

5.1.2 Check of Zn-N Pair Correlation Function

It was noted in chapter 4 that the tetrahedral stretching modes of the molecule dominate the damping effect of the EXAFS for the zinc (II) tetraimidazole molecule. In particular, the mean-squared displacements of the Zn-N interatomic distance, i.e. the Zn-N pair correlation function, are instrumental in determining the overall damping effect on the EXAFS spectrum.

The pair correlation function deduced from the VCF, via the INS study, may be directly checked against the experimental value determined directly from the temperature de-

pendent EXAFS data as described in section 4.3.3. The EXAFS data yielded a value of $\sigma_0^2 = (2.5 \pm 0.5) \times 10^{-3} \text{\AA}^2$, with all motion quenched in the ground state, which compares favourably with the value described by the VCF of $2.6 \times 10^{-3} \text{\AA}^2$.

The experimental value of $\sigma_0^2 = (2.5 \pm 0.5) \times 10^{-3} \text{\AA}^2$ for the Zn-N pair correlation function, and the associated error margin, permit a rapid check of the magnitude of the damping calculated for the EXAFS spectrum at 20K via configurational averaging. In the high k region, single scattering along the Zn-N-Zn paths dominates the EXAFS and may effectively be modelled via the plane wave approximation, see Eq. (4.23), and so the damping may be easily estimated by inserting the pair correlation function into the Debye-Waller factor, $e^{-2k^2\sigma^2}$. For example, at $k = 17 \text{\AA}^{-1}$ the peak in the EXAFS spectrum is nearly completely described by Zn-N single scattering; if σ^2 is taken as $2.6 \times 10^{-3} \text{\AA}^2$ (as it was in the configurational averaging calculation using the VCF) the signal is damped by $\sim 80\%$. Alternatively, if σ^2 is taken as $2.0 \times 10^{-3} \text{\AA}^2$, which is the lower extreme of the error range for the experimental value, the damping of the EXAFS signal at $k = 17 \text{\AA}^{-1}$ is $\sim 70\%$; this would still result in a distinct underestimate of the true EXAFS signal in this k -range.

5.1.3 Anharmonicity

The determination of the VCF hinges on the assumption that the probability distribution functions (pdf's) of atomic disorder are described by trivariate Gaussians in the generalised coordinate basis. In reality, this assumption is only an approximation since the true interatomic potentials are certainly anharmonic in form. The essential question, therefore, is whether the harmonic approximation is adequate in this case to model the VCF with respect to its damping effect on the EXAFS spectra.

Anharmonicities in molecular vibrations manifest themselves as broadening and splitting of peaks in the INS spectrum. This phenomenon was not found in the INS spectra of imidazole and the zinc (II) tetraimidazole complex at 20K except at the lowest frequencies in the latter spectrum, i.e. below 160cm^{-1} , where slight broadening was observed; this corresponds to the librations of the imidazole rings, i.e. wags, bends and torsions. This kind of motion produces small contributions to the overall damping of the EXAFS, which is dominated by the skeletal

tetrahedral modes, and so the magnitude of the total damping is not expected to be sensitive to errors in the modelling of the librational mode potentials. The peaks in the INS spectrum due to skeletal tetrahedral modes do not exhibit peak broadening at 20K which suggests that a quasi-harmonic model is appropriate for these modes, according to White et al., (119).

The thermal damping is dominated by the effect of the Zn-N pair correlation function. This may be checked for the presence of anharmonic effects directly from the temperature dependent experimental EXAFS spectra since the first coordination shell peak in the Fourier transform at each temperature may be interpreted to determine the extent of elongation in the Zn-N mean interatomic distance. It was found that that there was no change in the mean interatomic distance between the data at 20K and 50K but that successive data sets indicated a consistent elongation. The 300K data set indicates an elongation in the $\sim 2\text{\AA}$ Zn-N bond of $(5 \pm 1) \times 10^{-3}\text{\AA}$, or 0.25%. This corresponds to a thermal expansion coefficient of $(8 \pm 2) \times 10^{-6}$ which is intermediate between typical values for ionic solids (e.g. KCl = 37×10^{-6}) and covalent solids (e.g. silicon = 2.6×10^{-6}) at 300K. In an article by Eisenberger and Brown, (36), the effect of the anharmonicity of the pair correlation function on EXAFS spectra from metallic zinc was considered; the linear expansion coefficient of metallic zinc is 61×10^{-6} which is an order of magnitude larger than that estimated for the Zn-N pair correlation function. Clearly, anharmonicity is present in the Zn-N pair correlation potential but it does not appear to be a large effect and it is not expected that it will significantly alter the EXAFS damping which it dominates. In addition, the lack of broadening of the INS peaks attributed to motion that largely determines the Zn-N pair correlation function, i.e. the tetrahedral stretching motion, indicates that at low temperatures the pair correlation function may be considered quasi-harmonic.

It has thus been established that the Zn-N pair correlation function, at least at 20K, is well modelled by a Gaussian pdf and, from the last subsection, that its magnitude has been correctly entered into the EXAFS configurational averaging calculations. Consequently, we may be confident in the assertion that the theory produces an underestimate of the true EXAFS signal at high k and that this is not just an artifact of the calculation. It is therefore logical to conclude that the underestimate of the theoretical amplitude, observed in the lower

k regime of the spectrum, is also genuine.

As a final note, it could be the subject of a future analysis to try to extract the anharmonic form of the Zn-N pair potential from the temperature dependent EXAFS data by evaluating the coefficient of a cubic term in the expression for the potential in Hamiltonian. It may then be possible to add an anharmonic term to the harmonic description of the VCF, as determined from INS at 20K, and thus model the effect of the Zn-N anharmonicity directly on the damping of the EXAFS.

5.2 Discussion of Configurational Averaging Results

The underestimate of the configurational averaged spectral amplitudes compared with experiment stems from a corresponding underestimate of the theoretical amplitude in the undamped signal. This was suggested in figure 4.7, in which the theoretical signal appears to leave no scope for damping, and was confirmed by the *ab initio* temperature dependence calculation depicted in figures 4.13 and 4.14. One explanation is that the damping due to the extrinsic and intrinsic energy losses of the photoelectron are overestimated; in other words the imaginary component of the phase shifts (t -matrices), generated by using the complex, energy-dependent Hedin-Lundqvist potentials, are too large. Another reason could be an underestimate in the theoretical backscattering amplitudes predicted by the potentials. However, the situation is complicated because there is clear evidence that the discontinuity in the potentials at the muffin-tin (MT) boundary strongly perturbs the theoretical amplitude. This is illustrated in figure 5.2 in which the theoretical amplitude functions in the equilibrium configuration, $A_0(k)$, of the ten most significant scattering paths, are plotted with k^3 -weighting. All the functions clearly exhibit an oscillatory modulation with the same period which is characteristic of internal photoelectron scattering at the MT boundary within the emitter (zinc) potential; notice that the perturbation caused by the MT discontinuity extends into the high k region and is not just confined to the near-edge (XANES) region of the spectrum as it is frequently believed to do. The variation in the k^3 -weighted amplitude functions due to the oscillatory modulation is as much as $\pm 25\%$, which is significant.

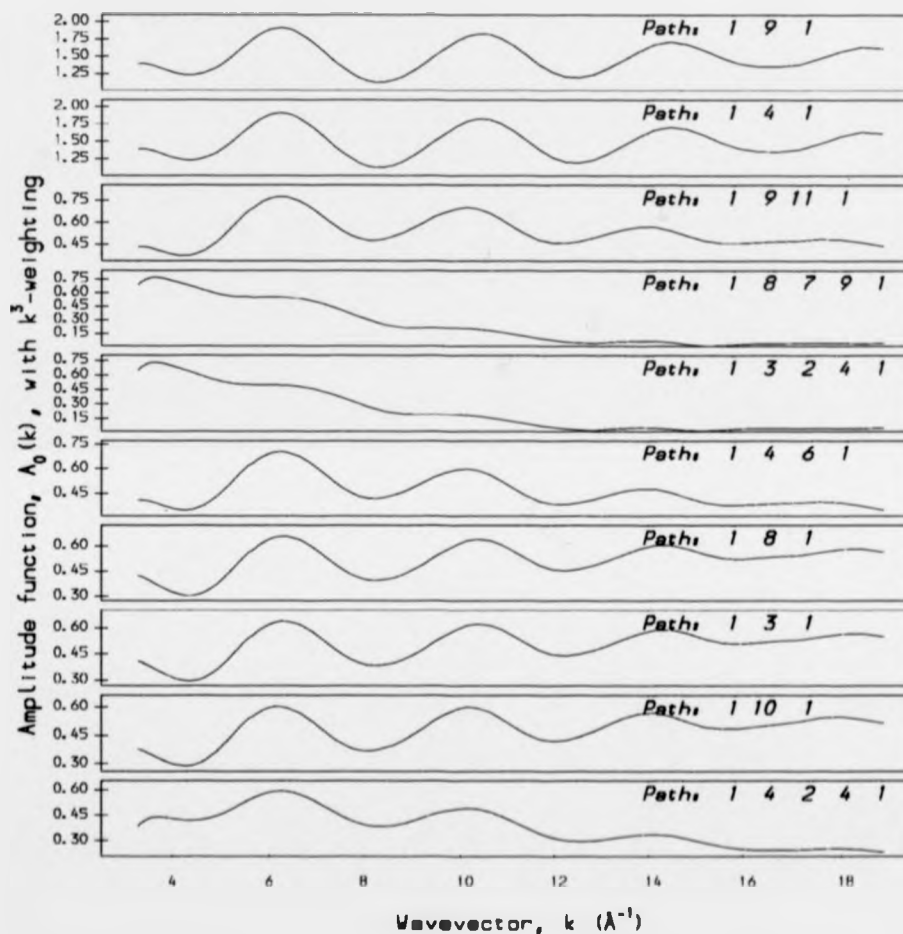


Figure 5.2: Plots of the theoretical amplitude function, $A_0(k)$, of the ten most significant scattering paths of the sinc (II) tetraimidazole complex. The functions clearly exhibit the same oscillatory modulation which is evidence of the perturbation in the theoretical photoelectron scattering caused by the energy discontinuity in the optical potential of the sinc atom at the Muffin-Tin boundary.

The effect the MT perturbation has on the amplitude of the total spectrum may be seen by referring back to figure 4.13 in which it was seen that not all of the peaks were underestimated after the configurational average. The well modelled peaks, for example the one at $k = 14\text{\AA}^{-1}$, correspond to the peaks in the oscillatory amplitude envelope of the amplitude function. Consequently, it is difficult to state exactly the origin of the underestimate in the total EXAFS theoretical amplitude; on inspection it appears that it is a combination of an overestimate in the damping due to intrinsic/extrinsic losses plus the perturbation of the amplitude function caused by internal scattering of the propagating photoelectron from the MT boundary discontinuity.

The incorrect modelling of the theoretical amplitude clearly affects the Fourier transforms of the calculated temperature-dependent spectra both in amplitude and form, as is seen by comparing figures 4.4 and 4.15. The MT perturbation generates an artificial peak in the Fourier transform of the calculated EXAFS, at the reduced radius of 1.1\AA . The transform spectra are also underestimated in amplitude in all but the the high frequency components of the EXAFS spectrum, which appear at a reduced radius of 3.6\AA in the Fourier transform. In other words, the theoretical amplitude does not produce a uniform underestimate of the EXAFS amplitude; i.e. the theoretical Fourier transform is not simply a scaled down version of the experimentally generated one. Therefore, unless the amplitude underestimate is properly treated, the structural and dynamic information of the EXAFS beyond the first shell cannot be reliably extracted.

The configurational averaging calculation yields important information as to the breakdown in the contributions to the thermal damping from the 105 normal modes of the molecule. It shows that the contributions to the damping from individual high frequency normal modes, the internal vibrations of the imidazole rings, are small. However, they are not negligible due to the multiplicity of the high frequency modes. For example, in the case of displacements in the Zn-N interatomic distance, which is the most significant type of motion as far as thermal damping is concerned, 23% of the mean-squared displacement is due to internal modes of the imidazole rings. For some multiple scattering paths, the proportion is much higher although few important paths are actually dominated by damping due to imidazole ring modes. In

other words, the thermal damping can not be properly modelled by considering only the low frequency skeletal modes of the molecule.

5.3 Implications for EXAFS Analysis

In this section, a brief overview is given of some of the common approaches to EXAFS data analysis in terms of treatment of thermal parameters. This is followed by a discussion of the implications to these approaches of the results presented in this thesis.

5.3.1 Various Approaches to EXAFS Data Evaluation

EXAFS data analysis is currently embodied by three software packages: EXCURVE, (48), (140), FEFF, (94), and GNXAS, (40) which has the same parentage as MSXAS, (122), which was employed in this thesis.

The analysis system EXCURVE, (48), (51), (140), developed at Daresbury Laboratory, is based on a fast, exact formulation for single and multiple scattering (MS) up to order 3 incorporating a spherical wave treatment. The multiple-scattering calculation has been made faster by the inclusion of a small-atom approximation, (47). The Muffin-Tin optical potentials are determined according to the prescription of Mattheiss, (90), and an $X\alpha$ model is used for the exchange-correlation correction with an adjustable parameter to compensate for the lack of energy dependence. FEFF, (94), is based on essentially the same theory as EXCURVE; it incorporates the additional concept of an effective scattering amplitude, analogous to the plane-wave scattering amplitude, which is applied to multiple scattering, (107), (117). GNXAS constructs the optical potentials using the Hedin-Lundqvist plasmon pole approximation, (54), (55), (56), (57), (74), which incorporates a complex, energy-dependent term to model the intrinsic photoelectron losses.

All these packages obtain structural information in the same way via a multiparameter fit of an *ab initio* EXAFS curve to an experimental EXAFS spectrum. Included in the fit is a parameterised model for the static and dynamic structure of the subject system and it is optimising this model that yields values for coordination numbers, bond lengths, and

possibly bond angles and disorder information. Other parameters are included in the fit and these are basically the same for each package although EXCURVE does permit the potentials to be varied. Recently, EXCURVE has been adapted in an effort to reduce the number of free parameters typically refined in the cases of biological systems; it is described as constrained and restrained refinement, (6). The structural parameters are constrained to certain idealised values taken from comparison with known systems and restrained such that any deviations from these idealised values are incorporated in the object function that is minimised. The principal difference between FEFF and EXCURVE is that, in FEFF, the various multiple scattering contributions are separated out; the phase and amplitude functions are thus deduced for each MS path. Then, within the approximation that the phase and amplitude functions vary linearly over small displacements of the free parameters, the EXAFS spectrum may be determined, via their first derivatives, at any point in parameter space without having to recalculate the spectrum. This enhances the computation speed by an order of magnitude compared to EXCURVE. The approach is described for the case of copper, (94), in which a good fit to experimental data was obtained with six free parameters including the mean free path, the zero of the energy scale, E_0 , a structural parameter and three parameters reproducing the thermal damping for the first three shells via the Debye-Waller scheme. The thermal parameters were underestimates of the experimental values for the first two shells (quoted in the same article) by 30% and 70%.

In FEFF and EXCURVE, disorder is treated via phenomenological amplitude reduction factors (Debye-Waller) associated with each coordination shell; recent studies using these packages to analyse metal-coordinated imidazole systems may be found in the literature, (6), (7), (71). This treatment is in contrast to GNXAS where the damping due to thermal and static disorder is treated fully via the configurational average scheme employed in this thesis, (3). This is possible because the multiple-scattering contributions are separated out such that a phase and amplitude function for each path may be deduced to describe the partial signal. For a single-scattering path, one quantity, analogous to the Debye-Waller-like value σ^2 , is required to define the thermal damping in the same manner as for the above methods. However, for scattering in a three segment path, six parameters are required to com-

pletely define a symmetric covariance matrix that represents the 3-body correlation function. Thus, potentially, GNXAS can reveal information about distribution functions of higher order than the pair correlation function as is demonstrated in a recent study of simple brominated hydrocarbons, (10).

5.3.2 Significance of Results for Structure Determination

The approaches to EXAFS data evaluation described above share a common feature in that they are all multiparameter fits of a calculation to an observation; this raises the question as to how many refinable parameters are justifiable for a particular case and how the parameters may be interpreted. Mustre et al., (94), clarify the former point by defining a number of independent experimental observations, from the energy range and Fourier transform range used, which must not be exceeded by the number of refined parameters. However, in order to be able to interpret the refined parameters in a physical sense it is essential that they are relatively uncorrelated and that they correspond to an adequate physical model for the system.

It has been shown, (107), that some of the parameters typically refined in an EXAFS data analysis are highly correlated. For example, over the energy band $61 \rightarrow 548\text{eV}$ ($k = 4 \rightarrow 12\text{\AA}^{-1}$) the wavevector zero, E_0 , and the first shell distance, R_1 , are correlated by 0.96; the first shell coordination number, N_1 , and disorder parameter, σ_1^2 , for the first shell are correlated by 0.93. The correlations are greater over narrower energy bands. Parameters treating the disorder are relatively uncorrelated with one another, and therefore should be well determined via refinement, provided that they damp partial EXAFS signal of distinct periodicities. This is certainly the case for σ^2 for the first coordination shell but parameters for more distant shells may be more correlated with one another since multiple-scattering causes more than one periodicity to be associated with scattering from these shells. It is therefore essential to analyse EXAFS data over a wide energy range and to choose the free parameters associated with disorder damping carefully.

Even if the free parameters are refined with relative certainty, the interpretation of the refined quantities hinges on the physical model used. The simple Debye-Waller-like treatment

of damping due to disorder in the approaches of EXCURVE and FEFF is inappropriate in dealing with the damping of multiple scattering paths. It has been shown, (3), that there are significant deviations from the $\exp(-2\sigma^2 k^2)$ nature of the damping for multiple scattering paths, especially for large disorder. In fact, as argued by Filipponi et al., (40), even if the damping were approximated by a function of the form $\exp(\alpha k^2)$, the meaning of the refined quantity could not be thought of as describing the disorder of a given shell. In other words, the refined quantities treating the disorder beyond the first shell will be, in many cases, meaningless. The GNXAS approach treats the damping due to disorder via a configurational average which does permit a physical interpretation of the refined quantities beyond the first shell in terms of disorder. However the method necessitates additional parameters and it is not apparent how correlated the various parameters are.

In summary, it is essential that the damping due to thermal and static disorder be treated via a configurational average (as incorporated in GNXAS) if the multiple scattering is to be modelled correctly and the refined parameters are to yield any information about the disorder of the scattering system. Unfortunately, this implies extra parameters to be refined which may be correlated and therefore difficult to determine.

Finally, the multiparameter fit is only as good as the theory which generates the signal. It has been shown in this thesis that the theory produces an underestimate of the EXAFS amplitude and that the amplitude is significantly perturbed by the presence of the Muffin-Tin discontinuity. The implication is that the quantities refined to model the damping due to disorder will themselves be significantly underestimated. This is born out by the quantities determined in the articles by Mustre et al. and Filipponi et al., discussed above, which both produced underestimates of the disorder parameters as compared with the cited experimental values. The incorrect modelling of the theoretical amplitude will undoubtedly also lead to systematic errors in the evaluation of structure and dynamic parameters beyond the first scattering shell.

A possible future check would be to apply each of the packages to the zinc (II) tetraimidazole molecule and refine parameters for the structure and disorder at the various temperatures. The refined quantities could be compared with the known values from the inelastic neutron

scattering study. This would provide a quantitative check of the ability of each package to yield meaningful values for the thermal disorder beyond the pair correlation function. It is anticipated that the refined values would represent a significant underestimate of the INS determined values for disorder.

5.4 Conclusions

In this thesis, a comprehensive temperature dependent study of the EXAFS spectra of the zinc (II) tetraimidazole molecule has been presented. The EXAFS temperature dependence was predicted by effecting a full configurational analysis and was seen to produce a significant underestimate of the theoretical amplitude compared to the experimental spectrum; the phase of the EXAFS signal was modelled well.

The configurational averaging calculation permits a breakdown of the partial contribution of each mode to the damping of each multiple scattering signal. It is seen that the low frequency skeletal modes of the molecule are dominant in the damping and become increasingly so as the temperature is increased. Of these low frequency modes, the four modes involving tetrahedral stretching of the Zn-N bonds are the most significant in generating damping in most of the principal multiple scattering signals. Low frequency torsional modes scarcely contribute to the damping. We note that, although the damping is dominated by the low frequency modes, the high frequency internal modes of the imidazole rings cannot be neglected. The out-of-plane imidazole modes do not contribute to the damping but the in-plane modes can contribute up to 25% of the exponent of the damping term (i.e. 15% of the damping for Zn-N backscattering).

The essential ingredient to the configurational average was the full many-body vibrational correlation function (VCF) of the molecule which was determined via a full normal mode analysis based on inelastic neutron scattering data. We note, from the normal mode analysis, that it is not possible to assess the quality of a vibrational force field from vibrational frequencies alone but that extra information is required about the atomic displacements (e.g. via inelastic neutron scattering data). This observation pertains to many published *ab initio*

vibrational force fields for small molecules where the elements are scaled to yield a good fit of the calculated to the experimental vibrational frequencies; these force fields produce widely differing results concerning the atomic displacements.

The atomic displacements predicted by the VCF were checked for consistency with those obtained from TLS analysis and yielded a satisfactory agreement (i.e. $\pm 50\%$ mean discrepancy in all projections considered). We note that TLS is a useful method for determining quantities that are very difficult to obtain from other methods but that it incurs large errors in the results produced. The errors are two-fold: Firstly, the calculated errors are large since the desired quantity is the small difference between two displacements and the experimental errors are proportionally larger with respect to this difference. Secondly, the determination of intramolecular displacements is based on some broad assumptions about the nature of both the intra- and intermolecular motion. The method is also incapable of determining correlations in the atomic motion.

The Zn-N pair correlation function predicted by the INS study was $2.6 \times 10^{-3} \text{\AA}^2$ and was compared to the same quantity determined directly from the experimental temperature dependent EXAFS study, $(2.5 \pm 0.5) \times 10^{-3} \text{\AA}^2$. The error bars on the experimental value permitted a check of the assertion that the EXAFS theoretical amplitude was underestimated by comparing the damping in the high k region, where the Zn-N pair correlation function dominates, when the pair correlation function is $2.0 \times 10^{-3} \text{\AA}^2$. The result showed that the theoretical amplitude was significantly underestimated even for values of the Zn-N pair correlation function at the extremes of the broad error bars. Anharmonicity of the Zn-N pair correlation potential was found to be small.

The incorrect theoretical modelling of the EXAFS signal is partly attributable to a modulation of the theoretical amplitude function caused by internal scattering of the photoelectron within the emitter potential by the artificial energy discontinuity at the Muffin-Tin boundary. The perturbation is severe, as much as $\pm 25\%$ about the mean k^3 -weighted amplitude, and persists strongly in the high k region. This effect impairs a correct interpretation of the experimental amplitude. The modulation of the amplitude could be removed by artificially eliminating the Muffin-tin discontinuity or by overlapping Muffin-tin spheres; the latter is

strictly forbidden by formal scattering theory but can improve the modelling. However, taking such measures can result in a serious deterioration in the phase of the EXAFS signal, which is presently seen to be well-modelled. An alternative method would be to employ full potentials that are not based on the Muffin-tin approximation and work is progressing in this field, (42), (97).

As well as the Muffin-tin perturbation, the theoretical amplitude is also significantly underestimated. This could be due to an overestimate in the damping of the intrinsic losses of the photoelectron which would require some modifications to the imaginary component of the Hedin-Lundqvist potential.

The consequence of the amplitude underestimate for the current methods of EXAFS data evaluation is that the refined parameters modelling the atomic disorder will, in general, be significantly underestimated. The values for shell distances beyond the first shell may also be affected by the incorrect form of the theoretical amplitude function. We note that it is important to analyse EXAFS data using a configurational average of multiple scattering paths but that caution should be used in dealing with the extra refinable parameters since they may be strongly correlated with one another.

In conclusion, this study is a benchmark test of multiple-scattering theory and has shown that problems exist particularly in the determination of the *ab initio* amplitude of the signal. This may lead to systematic errors when the theory is applied to actual structure determination problems.

Appendix A

Extension to Standard TLS Theory

In this appendix, an extension to the standard TLS theory (section 2.2) is described. It is not implemented in this study, for the reasons described in section 2.6, but is included for completeness.

The standard TLS analysis determines the translational and librational displacement distributions of a designated rigid-body but it does not take account of correlations between rigid-bodies nor does it distinguish between different contributions to the ADP's from internal motion, lattice vibrations or static disorder. An extension to the model was initiated by Johnson, (64), and formalised by Dunitz and White, (33), in order to allow for large scale internal librations between defined rigid-bodies. This approach, known as the *segmented rigid-body model*, assigns an additional parameter, $\langle \varphi^2 \rangle$, as the mean-squared torsional amplitude of groups suspected of undergoing significant torsional motion about a predefined axis. The method results in a **T**, **L** and **S** tensor for the bulk of the molecule and an additional torsional amplitude for the so-called *attached rigid-groups* (ARG's). The ARG is considered to experience a *riding motion* with the torsional motion superimposed on top.

However, in this basic form, the segmented rigid-body model has major limitations. The most important problem is that the model totally neglects correlations in displacements between the main rigid-body and the ARG. This requires analogous terms to those expressed in the **S** tensor which couple the internal torsional second moments to those of the overall translational and librational pdf's. Thus, the ADP's of an individual atom in the ARG should

APPENDIX A. EXTENSION TO STANDARD TLS THEORY

be determined from a modified form of Eq. (2.7) such as, (11):

$$U = \left[\begin{array}{c|c|c} \mathbf{I} & \mathbf{A} & \mathbf{I} \end{array} \right] \left[\begin{array}{c|c|c} \mathbf{T} & \mathbf{S}^\dagger & \mathbf{M}_t \\ \hline \mathbf{S} & \mathbf{L} & \mathbf{M}_t \\ \hline \mathbf{M}_t^\dagger & \mathbf{M}_t^\dagger & \mathbf{M} \end{array} \right] \left[\begin{array}{c} \mathbf{I} \\ \hline \mathbf{A}^\dagger \\ \hline \mathbf{I} \end{array} \right] \quad (\text{A.1})$$

The three additional coupling tensors become transparent in an orthogonal coordinate system in which one axis is parallel to the internal torsional axis; i.e.

$$\begin{aligned} \mathbf{M}_t(\varphi) &= \begin{bmatrix} 0 & 0 & \langle \lambda_1^\perp \varphi \rangle \\ 0 & 0 & \langle \lambda_2^\perp \varphi \rangle \\ 0 & 0 & \langle \lambda_3^\parallel \varphi \rangle \end{bmatrix} \\ \mathbf{M}_t(\varphi) &= \begin{bmatrix} 0 & 0 & \langle t_1^\perp \varphi \rangle \\ 0 & 0 & \langle t_2^\perp \varphi \rangle \\ 0 & 0 & \langle t_3^\parallel \varphi \rangle \end{bmatrix} \\ \mathbf{M}(\varphi) &= \begin{bmatrix} 0 & 0 & 0 \\ 0 & 0 & 0 \\ 0 & 0 & \langle \varphi^2 \rangle \end{bmatrix} \end{aligned} \quad (\text{A.2})$$

(This formalism is analogously applicable to an internal translational degree of freedom, (11)). By introducing these coupling terms a new indeterminacy arises in the value of the internal torsional displacements and the parallel component of the overall librational displacements, λ^\parallel . From the observed ADP's it is only possible to deduce the quadratic average of $(\lambda^\parallel + \varphi)$ which is $\langle (\lambda^\parallel)^2 \rangle + \langle \varphi^2 \rangle + 2\langle \lambda^\parallel \varphi \rangle$ in which the terms $(\langle \varphi^2 \rangle + 2\langle \lambda^\parallel \varphi \rangle)$ can not be separated. This is analogous to the indeterminacy in the diagonal elements of \mathbf{S} . Consequently the value obtained for the mean-squared torsional motion of the ARG is only meaningful when it is large compared to the parallel component of the overall librational displacements in \mathbf{L} , (32). The introduction of an ARG to model one extra internal degree of freedom generally implies the addition of six extra independent parameters to be deduced from the atomic ADP's.

Appendix B

Mean-Squared-Deviation of Harmonic Oscillator

The following arguments may be found in most standard texts on Quantum Mechanics. The following derivation has been composed from reference to (91), (92) and (100).

We consider a one dimensional simple harmonic oscillator (SHO) in which the deviation of the system about equilibrium is denoted by the dimensionless coordinate, ξ . The normalised Hamiltonian wave function of the n^{th} stationary state is of the form

$$\psi_n(\xi) = A_n H_n(\xi) e^{-\frac{\xi^2}{2}} \quad (\text{B.1})$$

The special functions $H_n(\xi)$ are the Hermite polynomials and A_n are the normalisation constants given by

$$A_n = \left(\frac{\mu\omega_0}{\hbar\pi^{1/2}} \right)^{1/4} \frac{1}{\sqrt{2^n n!}} \quad (\text{B.2})$$

in which μ is the reduced mass and ω_0 is the frequency of oscillation. The energy of the n^{th} stationary state is

$$E_n = \hbar\omega_0 \left(n + \frac{1}{2} \right) \quad (\text{B.3})$$

We wish to determine the quantum mechanical *expectation value*¹ of the squared deviation, ξ^2 , in a given state n . This is given by substitution of Eq. (B.1) into the expression

$$\langle \xi^2 \rangle_n = \langle n | \xi^2 | n \rangle \equiv \int_{-\infty}^{\infty} \psi_n^*(\xi) \xi^2 \psi_n(\xi) d\xi \quad (\text{B.4})$$

Evaluation of the integral may be shown (see (92) chapter 9) to yield the analytical form

$$\langle \xi^2 \rangle_n = n + \frac{1}{2} \quad (\text{B.5})$$

¹ Also known as the mean value or average value

APPENDIX B. MEAN-SQUARED-DEVIATION OF HARMONIC OSCILLATOR

The expectation value of ξ^2 of an ensemble of identical SHO's at a particular temperature, T , may be expressed as the following summation over all the stationary states

$$\langle \xi^2 \rangle = \frac{\sum_n \langle \xi^2 \rangle_n P_n(\omega_0, T)}{Z} \quad (\text{B.6})$$

in which $P_n(\omega_0, T)$ describes the probability of occupation of the n^{th} state and Z is the partition function. The SHO obeys Maxwell-Boltzmann statistics since it is non-interacting with other SHO's in the ensemble and the probability of occupation of an energy state is thus independent for each oscillator. Eq. (B.6) may consequently be rewritten as the following canonical average

$$\langle \xi^2 \rangle = \frac{\sum_n \langle \xi^2 \rangle_n e^{-\frac{E_n}{k_B T}}}{\sum_n e^{-\frac{E_n}{k_B T}}} \quad (\text{B.7})$$

in which $e^{-\frac{E_n}{k_B T}}$ is the thermodynamic factor. Substitution of Eq. (B.3) and Eq. (B.5) into the above yields

$$\langle \xi^2 \rangle = \frac{\sum_n (n + \frac{1}{2}) e^{-\frac{\hbar \omega_0}{k_B T}}}{\sum_n e^{-\frac{\hbar \omega_0}{k_B T}}} \quad (\text{B.8})$$

which may easily be evaluated using standard summation formulae² to give

$$\langle \xi^2 \rangle = \frac{1}{2} (1 + e^{-\frac{\hbar \omega_0}{k_B T}}) (1 - e^{-\frac{\hbar \omega_0}{k_B T}})^{-1} \equiv \frac{1}{2} \coth \left(\frac{\hbar \omega_0}{2k_B T} \right) \quad (\text{B.9})$$

The result may also be expressed in terms of linear displacement from equilibrium, x , by using the relationship

$$x = \sqrt{\frac{\hbar}{\mu \omega_0}} \xi \quad (\text{B.10})$$

in which μ is the reduced mass of the oscillatory system. If it is noted that the mean value of x is by definition zero (i.e. $\langle x \rangle = 0$) the required result may be denoted as the *variance* or *dispersion*, σ^2 , of the linear displacement of a SHO and expressed as

$$\sigma^2 = \langle (x - \langle x \rangle)^2 \rangle = \langle x^2 \rangle = \frac{\hbar}{2\mu \omega_0} \coth \left(\frac{\hbar \omega_0}{2k_B T} \right) \quad (\text{B.11})$$

² $\sum_n e^{-n\alpha} = (1 - e^{-\alpha})^{-1}$ and $\sum_n n e^{-n\alpha} = e^{-\alpha} (1 - e^{-\alpha})^{-2}$

Appendix C

Symmetry Species of Normal Modes

This appendix presents a standard group theoretical technique which may be found in most standard texts on Group Theory ¹.

A given molecule possesses symmetry denoted by the point group, \mathcal{G} , which contains the n operations A . Depending on the displacement coordinate set selected, the group operations may be represented by n transformation matrices, $\mathbf{R}(A)$. For each operation, A , a quantity, $\chi(A)$, known as the *character* may be defined as the trace of the transformation matrix, $\mathbf{R}(A)$, i.e.

$$\chi(A) = \text{Tr} \mathbf{R}(A) \quad (\text{C.1})$$

Clearly there is an infinite number of sets of transformation matrices, $\mathbf{R}(A)$, since there is an infinite choice for the displacement coordinate set, but the characters, $\chi(A)$, will always be the same. A given coordinate basis set constitutes one *representation* of the group, \mathcal{G} . Frequently, a representation may be transformed such that the transformed set forms sub-sets of coordinates that are non-mixing under operations of \mathcal{G} . The original representation is then described as *reducible*. A transformation can always be found that produces new reduced representations which, despite any further coordinate transformations, cannot be made to reduce further; these sub-sets are known as *irreducible representations* of the group \mathcal{G} . Group representation theory states that *for each point group there are only a definite small number of non-equivalent irreducible representations possible*. An arbitrary representation, $\mathbf{R}(A)$, of

¹The text referred to in compiling this appendix was Leach and Newman, (77).

APPENDIX C. SYMMETRY SPECIES OF NORMAL MODES

\mathcal{G} may therefore be decomposed as follows

$$\mathbf{R}(A) = \begin{bmatrix} \mathbf{R}^{(\mu_1)}(A) & 0 & 0 & 0 \\ 0 & \mathbf{R}^{(\mu_2)}(A) & 0 & 0 \\ 0 & 0 & \mathbf{R}^{(\mu_3)}(A) & 0 \\ 0 & 0 & 0 & \text{etc.} \end{bmatrix} \quad (\text{C.2})$$

in which $\mathbf{R}^{(\mu)}(A)$ represent the irreducible representations of the operation A . Reducing an arbitrary representation is effectively the same as block-diagonalising the transformation matrices; the non-mixing property of the reduced representations is evident from the off-diagonal zero blocks in Eq. (C.2). This decomposition may be written in terms of a symbolic sum, i.e.

$$\begin{aligned} \mathbf{R}(A) &= \mathbf{R}^{(\mu_1)}(A) \oplus \mathbf{R}^{(\mu_2)}(A) \oplus \mathbf{R}^{(\mu_3)}(A) \oplus \dots \\ &= \sum_{\mu} m_{\mu} \mathbf{R}^{(\mu)}(A) \end{aligned} \quad (\text{C.3})$$

where the m_{μ} denote the number of equivalent irreducible representations $\mathbf{R}^{(\mu)}$ in \mathbf{R} ; m_{μ} is known as the *multiplicity* of $\mathbf{R}^{(\mu)}$ in \mathbf{R} . Taking the trace of both sides of Eq. (C.3), and by comparison with Eq. (C.1), the relationship between the characters of the arbitrary and irreducible representations is obtained

$$\chi(A) = \sum_{\mu} m_{\mu} \chi^{(\mu)}(A) \quad (\text{C.4})$$

Clearly, for every point group there is an associated set of characters, one for each irreducible representation in each operation class; the number of irreducible representations is equal to the number, k , of classes in a group. It is customary to represent these sets of characters in $k \times k$ *character tables*, one for each point group; they are tedious to derive but are given as standards in most texts on group theory².

Irreducible representations are classified into *symmetry species* by the following conventions;

- A denotes one dimension. Principal rotation operation has character +1.
- B denotes one dimension. Principal rotation operation has character -1

²For examples of character tables (those that are required in this thesis) see appendix E.

APPENDIX C. SYMMETRY SPECIES OF NORMAL MODES

- E denotes two dimensions or complex conjugates of one dimensional pairs.
- T (often read as F in the literature) denotes three dimensions.

All vibrational normal modes are identified as belonging to one of these symmetry species; the dimensions in this case indicate the degeneracy of the modes.

The characters of the irreducible representations satisfy the following orthogonality relations

$$\sum_A \chi^{(\mu)}(A) \chi^{(\nu)*}(A) = 0 \quad (\text{C.5})$$

$$\sum_A \chi^{(\mu)}(A) \chi^{(\mu)*}(A) = g \quad (\text{C.6})$$

where g is the order of G and $*$ denotes the complex conjugate. If Eq. (C.4) is multiplied by $\chi^{(\nu)*}$, then, using the above orthogonality relations, we get

$$\begin{aligned} \sum_A \chi(A) \chi^{(\nu)*}(A) &= \sum_A \left[\sum_{\mu} m_{\mu} \chi^{(\mu)}(A) \right] \chi^{(\nu)*}(A) \\ &= \sum_{\mu} m_{\mu} \left[\sum_A \chi^{(\mu)}(A) \chi^{(\nu)*}(A) \right] \\ &= m_{\nu} g \end{aligned}$$

Which yields the desired result

$$m_{\nu} = \frac{1}{g} \sum_A \chi(A) \chi^{(\nu)*}(A) \quad (\text{C.7})$$

The multiplicity determines which irreducible representations are present and allows the reduction, Γ , to be written as a linear combination of the symmetry species, ν (i.e. $\nu = \{A, B, E, T\}$).

$$\Gamma = \sum_{\nu} m_{\nu} \nu \quad (\text{C.8})$$

This appendix has demonstrated that, if the character table (i.e. $\chi^{(\nu)}(A)$) is known, and the total character, $\chi(A)$, of the system has been established from the arbitrary representation, $R(A)$, it is straightforward to obtain the symmetry species of the normal modes from Eq. (C.7) and Eq. (C.8).

Note that this appendix has only dealt with the qualitative reduction of arbitrary representations. The derivation of the transformations yielding the irreducible representations is discussed in appendix D.

Appendix D

Projection of Symmetry Coordinates

In this appendix, the group theoretical technique for determining the explicit transform from internal coordinates, S_i , to internal *symmetry* coordinates, S'_k , is explained; essentially it involves the derivation of so-called *projection operators* in order to project the S_i basis into a linear combination, which may then be accepted as a valid basis for the S'_k irreducible representation. This is equivalent to finding the **W** transform discussed in section 3.3.8.

Firstly, we consider the action of the operations, A , of the point group \mathcal{G} on the irreducible representations, ν , of the internal symmetry coordinates, $S'_k{}^{(\nu)}$. By definition

$$AS'_k{}^{(\nu)} = \sum_{l=1}^{n_\nu} R'_{lk}{}^{(\nu)}(A) S'_l{}^{(\nu)} \quad (\text{D.1})$$

in which the $R'_{lk}{}^{(\nu)}(A)$ are elements of the $\mathbf{R}^{(\nu)}(A)$ transformation matrices introduced in appendix C; the $\mathbf{R}^{(\nu)}(A)$ are the inequivalent, irreducible unitary representations of the group, \mathcal{G} . It can be shown¹ from *Schur's Lemma*² that the following orthogonality theorem holds:

$$\sum_A R'_{ij}{}^{(\alpha)*}(A) R'_{lk}{}^{(\beta)}(A) = \frac{g}{n_\alpha} \delta_{\alpha\beta} \delta_{il} \delta_{jk} \quad (\text{D.2})$$

where g is the order of \mathcal{G} and n_α is the dimension of \mathbf{R}^α ; the δ_{xy} are the Kronecker delta symbols (i.e., $\delta_{xy} = 1$ if $x = y$ and $\delta_{xy} = 0$ if $x \neq y$). Thus, multiplying Eq. (D.1) by $R'_{ij}{}^{(\mu)*}(A)$, summing over A , and applying Eq. (D.2), we get

$$\sum_A R'_{ij}{}^{(\mu)*}(A) AS'_k{}^{(\nu)} = \sum_{l=1}^{n_\nu} \sum_A R'_{ij}{}^{(\mu)*}(A) R'_{lk}{}^{(\nu)}(A) S'_l{}^{(\nu)}$$

¹ See (77), appendix III.

² Schur's Lemma states: Any matrix which commutes with all the matrices of an irreducible representation must be a multiple of the unit matrix.

APPENDIX D. PROJECTION OF SYMMETRY COORDINATES

$$\begin{aligned}
 &= \sum_{l=1}^{n_\nu} \left[\frac{g}{n_\nu} \delta_{\mu\nu} \delta_{il} \delta_{jk} \right] S_l^{(\nu)} \\
 &= \frac{g}{n_\nu} \delta_{\mu\nu} \delta_{jk} S_i^{(\nu)}
 \end{aligned} \tag{D.3}$$

Setting $i = j$ to find the trace of $R_{ij}^{(\mu)*}(A)$, Eq. (D.3) may be re-expressed in terms of the characters of the irreducible representations, $\chi^{(\mu)*}(A)$, (refer to Eq. (C.1)), i.e.,

$$\sum_A \chi^{(\mu)*}(A) A S_k^{(\nu)} = \frac{g}{n_\nu} \delta_{\mu\nu} S_k^{(\nu)} \tag{D.4}$$

At this point in the derivation, the *projection operators* may be identified as

$$P^{(\nu)} = \frac{n_\nu}{g} \sum_A \chi^{(\nu)*}(A) A \tag{D.5}$$

such that Eq. (D.4) may be rewritten, to give the important result

$$P^{(\nu)} S_k^{(\nu)} = S_k^{(\nu)} \tag{D.6}$$

An element S_t of the internal coordinate basis may always be written as a linear combination of the internal symmetry coordinates, such that

$$S_t = \sum_k \sum_\nu a_{kt}^{(\nu)} S_k^{(\nu)} \tag{D.7}$$

in which the $a_{kt}^{(\nu)}$ are constants. If both sides of Eq. (D.7) are operated upon by the projection operator, $P^{(\nu)}$, the desired transformation from S_t to $S_k^{(\nu)}$ may be obtained:

$$P^{(\mu)} S_t = \sum_k a_{kt}^{(\mu)} S_k^{(\mu)} \tag{D.8}$$

The $a_{kt}^{(\mu)}$ therefore constitute the elements of the transform \mathbf{W} .

In order to be able to apply the projection operators, $P^{(\mu)}$, it is necessary to know (i) the character table of the group, (i.e., $\chi^{(\mu)}(A)$) and (ii) the effect of group operations on the internal coordinate basis, S_t .

Appendix E

Character Tables

This appendix presents those character tables of group theory that are referred to in the main body of text. In each case the rows correspond to the symmetry species and the columns to classes of symmetry operations.

T_d	E	$8C_3$	$3C_2$	$6\sigma_d$	$6S_4$
A_1	1	1	1	1	1
A_2	1	1	1	-1	-1
E	2	-1	2	0	0
T_1	3	0	-1	-1	1
T_2	3	0	-1	1	-1

Table E.1: Character table of the tetrahedral point group, T_d .

S_4	E	C_2	S_4	S_4^3
A	1	1	1	1
B	1	1	-1	-1
E	$\begin{cases} 1 & -1 & i & -i \\ 1 & -1 & -i & i \end{cases}$			

Table E.2: Character table of the point group S_4 .

C_s	E	σ_h	C_2	E	C_2
A'	1	1	A	1	1
A''	1	-1	B	1	-1

Table E.3: Character tables of the point groups C_s and C_2 .

Imidazole Force Field: Non Minimum Basis

ZEROS

202

Appendix G

Low Frequency Skeletal Modes of Zinc Tetraimidazole Complex



296 cm^{-1} A_1 Tetrahedral stretch



277 cm^{-1} B_1 Tetrahedral stretch



274 cm^{-1} B_1 Tetrahedral stretch



228 cm^{-1} A_1 Tetrahedral stretch



206 cm^{-1} A_1 Tetrahedral deformation

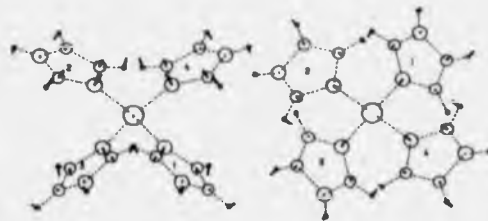


205 cm^{-1} B_1 Tetrahedral deformation

APPENDIX G. LOW FREQUENCY SKELETAL MODES OF ZINC
TETRAIMIDAZOLE COMPLEX



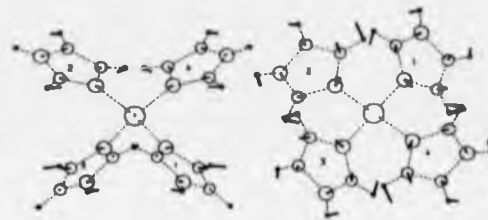
204 cm^{-1} B_1 Tetrahedral deformation



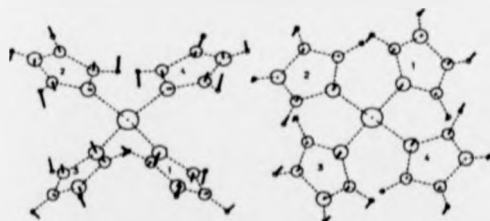
184 cm^{-1} A_1 Tetrahedral deformation



174 cm^{-1} A_1 Tetrahedral deformation



158 cm^{-1} A_1 Imidazole wag



147 cm^{-1} B_1 Imidazole bend



139 cm^{-1} A_1 Imidazole torsion



131 cm^{-1} B_1 Imidazole bend



117 cm^{-1} A_1 Imidazole bend

APPENDIX G. LOW FREQUENCY SKELETAL MODES OF ZINC
TETRAIMIDAZOLE COMPLEX



113 cm^{-1} B_1 Imidazole torsion



110 cm^{-1} B_1 Imidazole torsion



106 cm^{-1} A_1 Imidazole bend



100 cm^{-1} B_1 Imidazole wag



97 cm^{-1} B_1 Imidazole wag



92 cm^{-1} A_1 Imidazole torsion



80 cm^{-1} A_1 Imidazole wag

Appendix H

Temperature Dependence of Individual Multiple Scattering Paths

The next few pages illustrate the calculated temperature dependence of individual MS paths in the zinc (II) tetraimidazole complex. The paths illustrated are the ten most important scattering paths through one of the imidazole branches; the results for the other branch in the asymmetric group are similar. The paths are:

- | | |
|--------------|--------------|
| 1. 1 4 1 | 6. 1 5 1 |
| 2. 1 3 2 4 1 | 7. 1 4 6 5 1 |
| 3. 1 4 6 1 | 8. 1 4 5 1 |
| 4. 1 3 1 | 9. 1 4 6 4 1 |
| 5. 1 4 2 4 1 | 10. 1 2 1 |

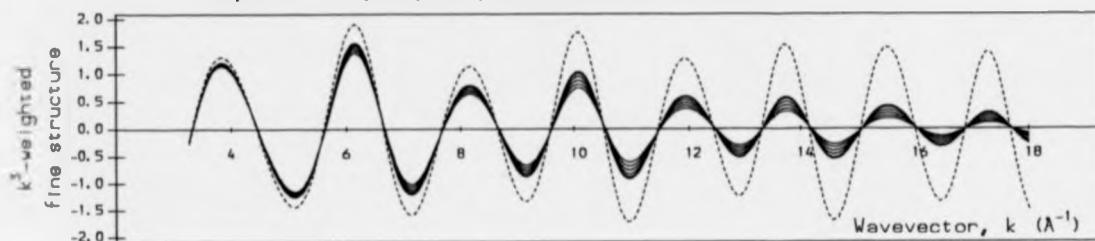
where the atomic labelling is given in table 4.1 in the main text.

Each diagram shows the partial EXAFS signal due to the path with and without the configurational averaging treatment. The bar charts show the partial contributions of the 105 normal modes to the dominant damping term and correction term of the configurational averaging formula given in Eq. (4.20). They therefore indicate the significance of each mode to the damping of the MS path; note that each bar chart is composed of white bars, showing the partial contributions at 20K, and black bars, showing the partial contributions at 300K.

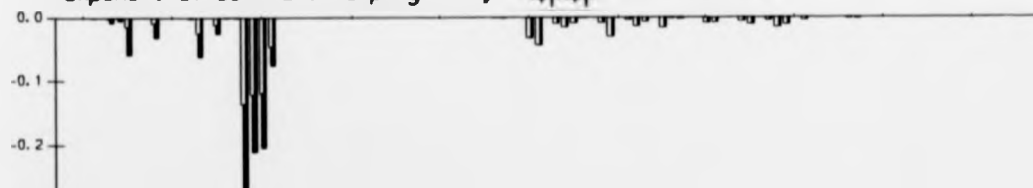
APPENDIX H. TEMPERATURE DEPENDENCE OF INDIVIDUAL MULTIPLE SCATTERING PATHS

Single Scattering Path 1 4 1 , $R = 3.9671 \text{ \AA}$, degeneracy 1

----- no treatment of thermal damping
— damped at 20K, 50K, 100K, 150K, 200K, 250K and 300K



Contributions to damping terms from the 105 normal modes at: 20K (white) 300K (black)
Exponent of dominant damping term, $-(\psi_i M \psi_i)/2$ at $k=12 \text{ \AA}^{-1}$



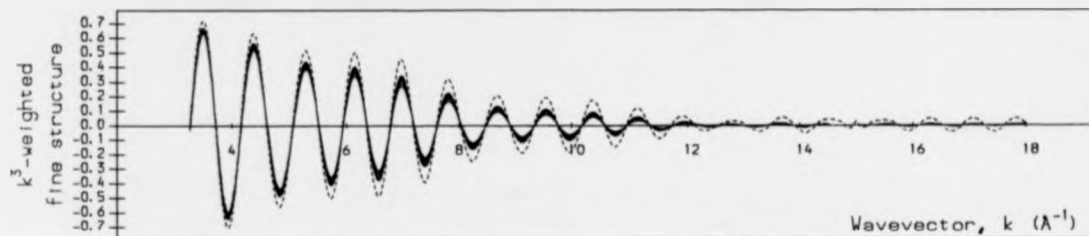
Phase and amplitude correction term, $(\lambda_i M \psi_i)/\lambda_0$ at $k=4 \text{ \AA}^{-1}$



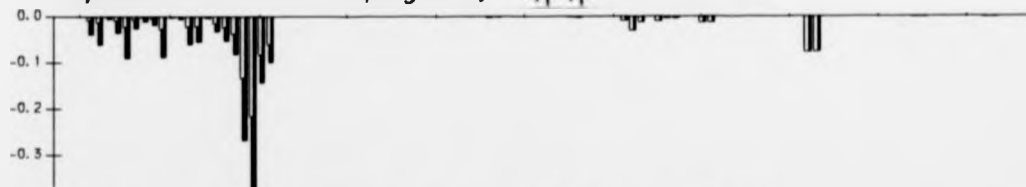
APPENDIX H. TEMPERATURE DEPENDENCE OF INDIVIDUAL MULTIPLE SCATTERING PATHS

Triple Scattering Path 1 3 2 4 1, $R = 8.4911 \text{ \AA}$, degeneracy 2

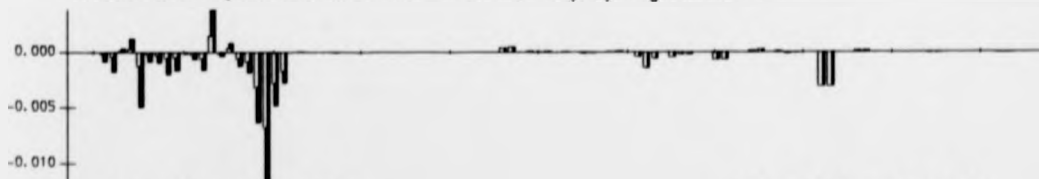
----- no treatment of thermal damping
— damped at 20K, 50K, 100K, 150K, 200K, 250K and 300K



Contributions to damping terms from the 105 normal modes at: 20K (white) 300K (black)
Exponent of dominant damping term, $-(\psi_1 M \psi_1) / 2$ at $k = 12 \text{ \AA}^{-1}$



Phase and amplitude correction term, $(\lambda_1 M \psi_1) / \lambda_0$ at $k = 4 \text{ \AA}^{-1}$



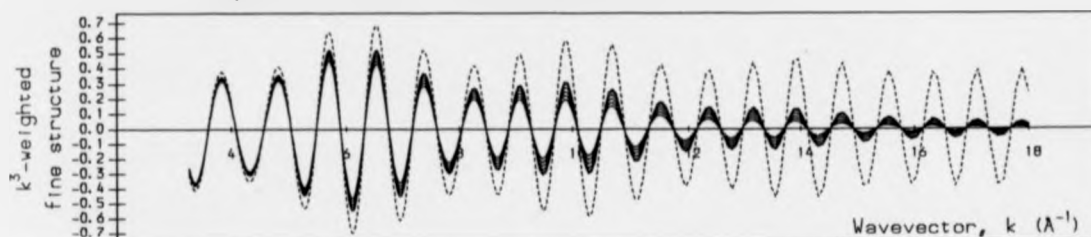
Low frequency modes

High frequency modes

APPENDIX H. TEMPERATURE DEPENDENCE OF INDIVIDUAL MULTIPLE SCATTERING PATHS

Double Scattering Path 1 4 6 1 , $R = 8.3648 \text{ \AA}$, degeneracy 2

----- no treatment of thermal damping
— damped at 20K, 50K, 100K, 150K, 200K, 250K and 300K

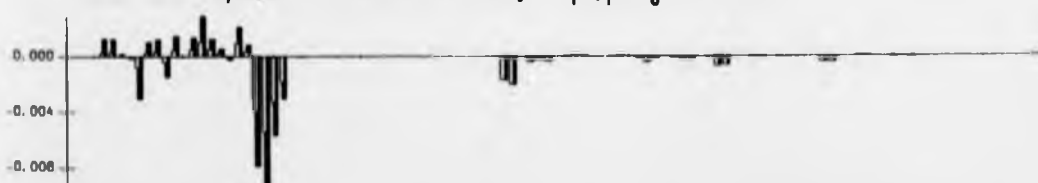


Contributions to damping terms from the 105 normal modes at: 20K (white)
300K (black)

Exponent of dominant damping term, $-(\psi_1 M \psi_1) / 2$ at $k = 12 \text{ \AA}^{-1}$



Phase and amplitude correction term, $(\Lambda_1 M \psi_1) / \Lambda_0$ at $k = 4 \text{ \AA}^{-1}$



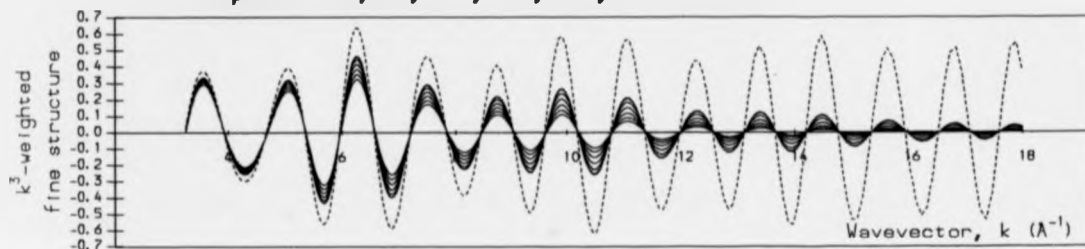
Low frequency modes

High frequency modes

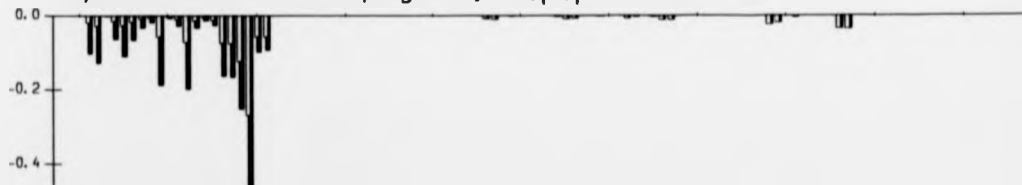
APPENDIX H. TEMPERATURE DEPENDENCE OF INDIVIDUAL MULTIPLE SCATTERING PATHS

Single Scattering Path 1 3 1 , $R = 5.9724 \text{ \AA}$, degeneracy 1

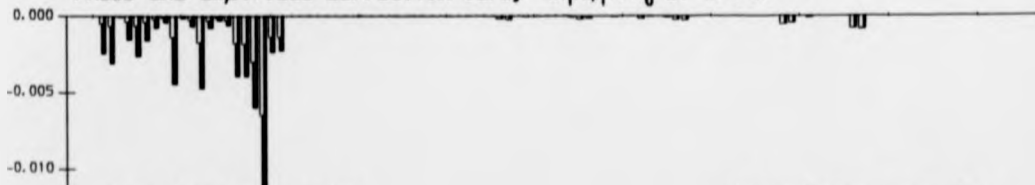
----- no treatment of thermal damping
— damped at 20K, 50K, 100K, 150K, 200K, 250K and 300K



Contributions to damping terms from the 105 normal modes at: 20K (white)
300K (black)
Exponent of dominant damping term, $-(\psi_1 M \psi_1)/2$ at $k = 12 \text{ \AA}^{-1}$



Phase and amplitude correction term, $(\Lambda_1 M \psi_1)/\Lambda_0$ at $k = 4 \text{ \AA}^{-1}$



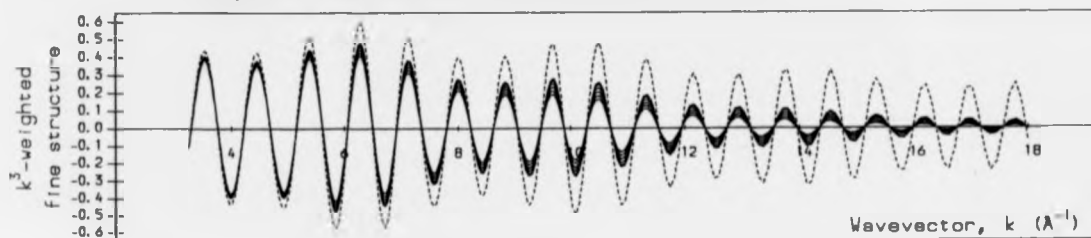
Low frequency modes

High frequency modes

APPENDIX H. TEMPERATURE DEPENDENCE OF INDIVIDUAL MULTIPLE SCATTERING PATHS

Triple Scattering Path 1 4 2 4 1, $R = 8.3367 \lambda$, degeneracy 1

----- no treatment of thermal damping
— damped at 20K, 50K, 100K, 150K, 200K, 250K and 300K

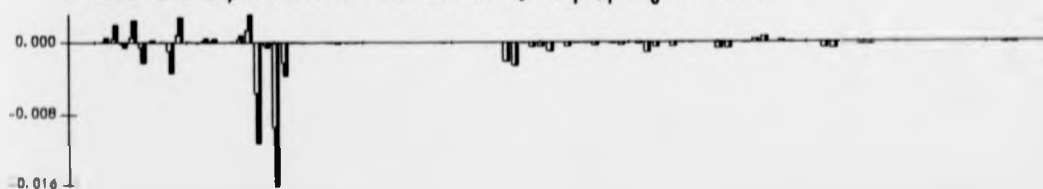


Contributions to damping terms from the 105 normal modes at: 20K (white)
300K (black)

Exponent of dominant damping term, $-(\psi_1 M \psi_1)/2$ at $k=12 \text{ Å}^{-1}$



Phase and amplitude correction term, $(\lambda_1 M \psi_1)/\lambda_0$ at $k=4 \text{ Å}^{-1}$



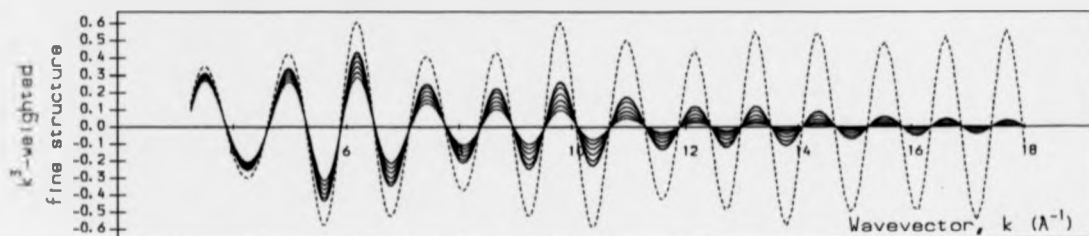
Low frequency modes

High frequency modes

APPENDIX H. TEMPERATURE DEPENDENCE OF INDIVIDUAL MULTIPLE SCATTERING PATHS

Single Scattering Path 1 5 1 , $R = 6.0230 \text{ \AA}$, degeneracy 1

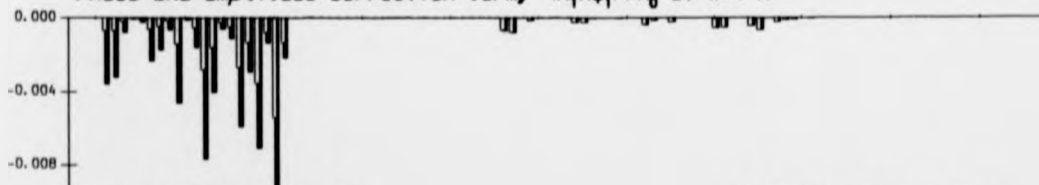
----- no treatment of thermal damping
— damped at 20K, 50K, 100K, 150K, 200K, 250K and 300K



Contributions to damping terms from the 105 normal modes at: 20K (white)
Exponent of dominant damping term, $-(\psi_1 M \psi_1)/2$ at $k = 12 \text{ \AA}^{-1}$ 300K (black)



Phase and amplitude correction term, $(\Lambda_1 M \psi_1)/\Lambda_0$ at $k = 4 \text{ \AA}^{-1}$



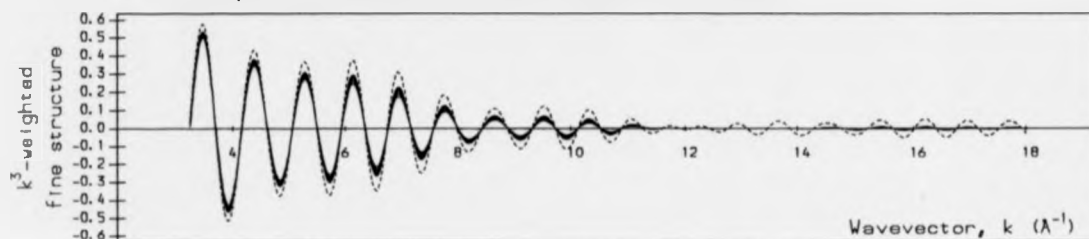
Low frequency modes

High frequency modes

APPENDIX H. TEMPERATURE DEPENDENCE OF INDIVIDUAL MULTIPLE SCATTERING PATHS

Triple Scattering Path 1 4 6 5 1, $R = 8.5733 \text{ \AA}$, degeneracy 2

----- no treatment of thermal damping
— damped at 20K, 50K, 100K, 150K, 200K, 250K and 300K



Contributions to damping terms from the 105 normal modes at: 20K (white) 300K (black)
Exponent of dominant damping term, $-(\psi, M\psi_1)/2$ at $k=12 \text{ \AA}^{-1}$



Phase and amplitude correction term, $(A_1 M \psi_1)/A_0$ at $k=4 \text{ \AA}^{-1}$

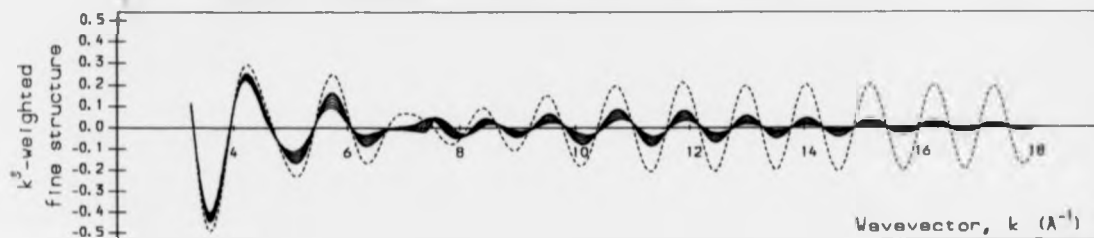


APPENDIX H. TEMPERATURE DEPENDENCE OF INDIVIDUAL MULTIPLE SCATTERING PATHS

Double Scattering Path 1 4 5 1 , $R = 6.3788 \text{ \AA}$, degeneracy 2

----- no treatment of thermal damping

— damped at 20K, 50K, 100K, 150K, 200K, 250K and 300K



Contributions to damping terms from the 105 normal modes at: 20K (white) 300K (black)

Exponent of dominant damping term, $-(\psi_1 M \psi_1)/2$ at $k = 12 \text{ \AA}^{-1}$



Phase and amplitude correction term, $(A_1 M \psi_1)/A_0$ at $k = 4 \text{ \AA}^{-1}$

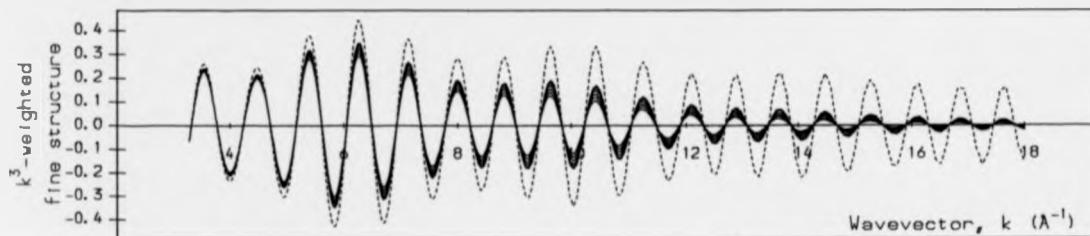


APPENDIX H. TEMPERATURE DEPENDENCE OF INDIVIDUAL MULTIPLE SCATTERING PATHS

Triple Scattering Path 1 4 6 4 1, $R = 8.4271 \text{ \AA}$, degeneracy 1

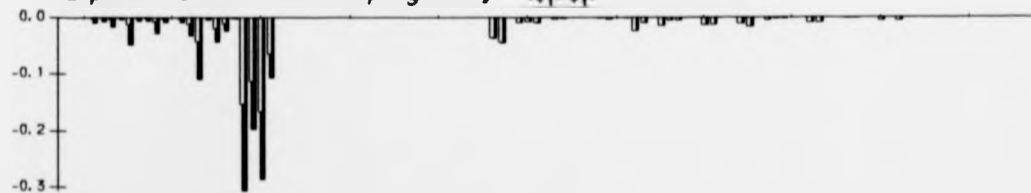
----- no treatment of thermal damping

— damped at 20K, 50K, 100K, 150K, 200K, 250K and 300K

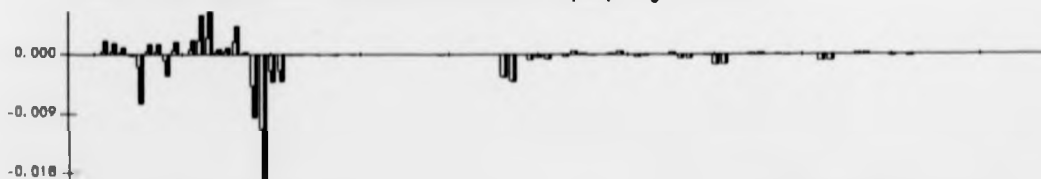


Contributions to damping terms from the 105 normal modes at: 20K (white) 300K (black)

Exponent of dominant damping term, $-(\psi_1 M \psi_1) / 2$ at $k = 12 \text{ \AA}^{-1}$



Phase and amplitude correction term, $(A_1 M \psi_1) / A_0$ at $k = 4 \text{ \AA}^{-1}$



Low frequency modes

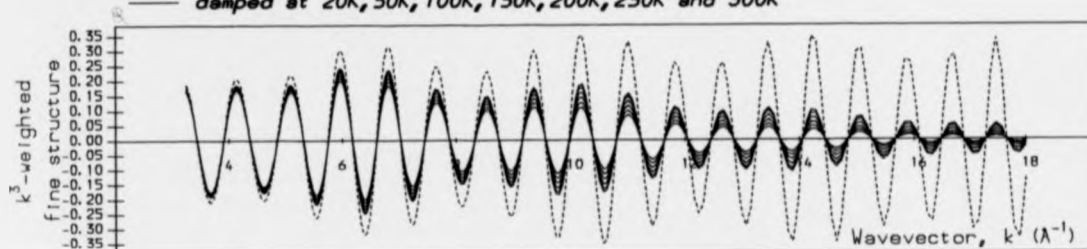
High frequency modes

APPENDIX H. TEMPERATURE DEPENDENCE OF INDIVIDUAL MULTIPLE SCATTERING PATHS

Single Scattering Path 1 2 1 , $R = 8.2380 \text{ \AA}$, degeneracy 1

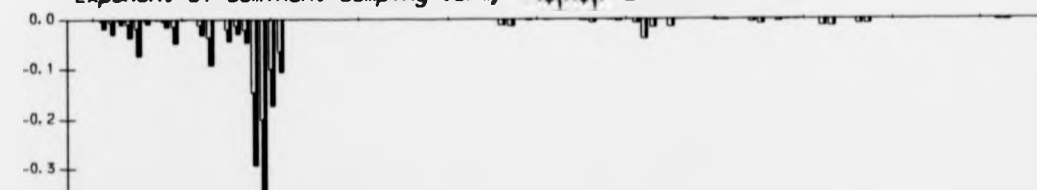
..... no treatment of thermal damping

— damped at 20K, 50K, 100K, 150K, 200K, 250K and 300K

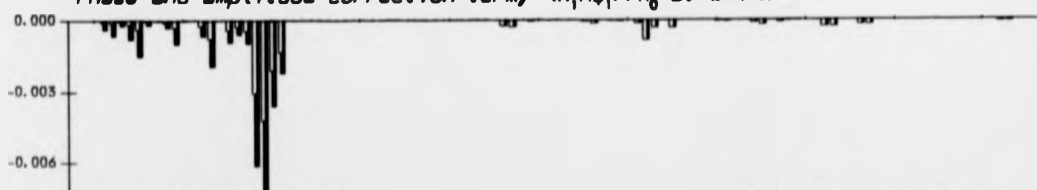


Contributions to damping terms from the 105 normal modes at: 20K (white)
300K (black)

Exponent of dominant damping term, $-(\psi_1 M \psi_1) / 2$ at $k = 12 \text{ \AA}^{-1}$



Phase and amplitude correction term, $(\lambda_1 M \psi_1) / \lambda_0$ at $k = 4 \text{ \AA}^{-1}$



Low frequency modes

High frequency modes

References

- [1] C. A. Ashley and S. Doniach. Theory of extended x-ray absorption edge fine structure (EXAFS) in crystalline solids. *Phys.Rev.B*, 11:1279, 1975.
- [2] C. A. Bear, K. A. Duggan, and H. C. Freeman. Tetraimidazolezinc(II) perchlorate. *Acta Cryst.*, B31:2713, 1975.
- [3] M. Benfatto, C. R. Natoli, and A. Filipponi. Thermal and structural damping of the multiple scattering contributions to the x-ray absorption fine structure. *Phys.Rev.B*, 40(14):9626, 1989.
- [4] M. Benfatto, C. R. Natoli, A. Bianconi, J. Garcia, A. Marcelli, M. Fanfoni, and I. Davoli. Multiple scattering regime and higher order correlations in x-ray absorption spectra of liquid solutions. *Phys.Rev.B*, 34(8):5774, 1986.
- [5] G. Beni and P. M. Platzman. Temperature and polarization dependence of extended x-ray absorption fine structure spectra. *Phys.Rev.B*, 14:1514, 1976.
- [6] N. Binstead, R. W. Strange, and S. S. Hasnain. Constrained and restrained refinement in EXAFS data analysis with curved wave theory. *Biochemistry*, 31:12117-12125, 1992.
- [7] N. J. Blackburn, R. W. Strange, L. M. McFadden, and S. S. Hasnain. Anion binding to bovine erythrocyte superoxide dismutase studied by x-ray absorption spectroscopy. A detailed structural analysis of the native enzyme and the azido and cyano derivatives using a multiple scattering approach. *J. Am. Chem. Soc.*, 109:7162-7170, 1987.
- [8] C. P. Brock, W. B. Schweizer, and J. D. Dunitz. *J. Am. Chem. Soc.*, 107:6964-6970, 1985.
- [9] C. Brouder, M. F. Ruiz-López, R. F. Pettifer, M. Benfatto, and C. R. Natoli. Systematic approach to the calculation of the polarization-dependent (and polarization-averaged) general term of the curved-wave multiple scattering series in the X-ray absorption cross section. *Phys.Rev.B*, 39(3):1488, 1989.
- [10] E. Burattini, P. D'Angelo, A. D. Cicco, A. Filipponi, and N. V. Pavel. Multiple scattering x-ray absorption analysis of simple brominated hydrocarbon molecules. *J. Phys. Chem.*, 97:5486-5494, 1993.
- [11] H. B. Bürgi. Interpretation of atomic displacement parameters: intramolecular translational oscillation and rigid-body motion. *Acta Cryst.*, B45:383-390, 1989.
- [12] S. H. Chou, J. J. Rehr, E. A. Stern, and E. R. Davidson. Ab initio calculation of extended x-ray absorption fine structure in Br₂. *Phys.Rev.B*, 35(6):2604, 1987.
- [13] D. Christen, J. H. Griffiths, and J. Sheridan. *Z. Naturforsch.*, 36A:1378, 1981.
- [14] E. Clementi and C. Roetti. *Atomic and Nuclear Data Tables*, 14:177, 1974.
- [15] G. Coddens, F. Fillaux, G. J. Kearley, J. Tomkinson, and W. Wegner. The effects of NH₃ free rotations on the inelastic neutron scattering spectrum of Ni(NH₃)₂Ni(CN)₂.C₆D₆ at 20k. to be published, 1993.

REFERENCES

- [16] L. Colombo, P. Bleckmann, B. Schrader, R. Schneider, and T. Plesser. Calculation of normal vibrations and intra- and intermolecular force constants in crystalline imidazole. *J.Chem.Phys.*, 61(8):3270, 1974.
- [17] H. J. Conroy. *J.Chem.Phys.*, 47:5307, 1967.
- [18] M. Cordes and J. Walter. *Spectrochim. Acta*, 24A:237, 1968.
- [19] C. Coulombeau, Z. Dhaouadi, M. Ghomi, H. Jobic, and J. Tomkinson. Vibrational mode analysis of guanine by neutron inelastic scattering. *Eur.Biophys.J.*, 19:323-326, 1991.
- [20] S. P. Cramer. *Adv.Inorg.Bioinorg.Mech.*, 2:259, 1983.
- [21] S. P. Cramer. Biochemical application of x-ray absorption spectroscopy. In D. C. Koningsberger and R. Prins, editors, *X-ray absorption spectroscopy*, page 257, New York, 1988. Wiley.
- [22] S. P. Cramer and K. O. Hodgson. *Prog.Inorg.Chem.*, 25:1, 1979.
- [23] D. W. J. Cruickshank. *Acta Cryst.*, 9:756-758, 1956.
- [24] D. W. J. Cruickshank. *Acta Cryst.*, 9:754-756, 1956.
- [25] D. W. J. Cruickshank. *Acta Cryst.*, 14:896-897, 1961.
- [26] S. J. Cyvin. *Molecular Vibrations and Mean Square Amplitudes*. Elsevier Publishing Company, Amsterdam, 1968.
- [27] A. Di Cicco, S. Stizza, A. Filipponi, F. Boscherini, and S. Mobilio. X-ray absorption investigation of SiX_4 ($X = Cl, F, CH_3$). *J.Phys.B*, 25:2309, 1992.
- [28] P. A. M. Dirac. *Proc.Cambridge Philos.Soc.*, 26:376, 1930.
- [29] R. Ditchfield, W. Hehre, and J. Pople. *J.Chem.Phys.*, 54:724, 1971.
- [30] J. D. Dunitz. *Trans.Am.Crystallogr.Assoc.*, 20:1-14, 1984.
- [31] J. D. Dunitz, E. F. Maverick, and K. N. Trueblood. Atomic measurements in atomic crystals from diffraction measurements. *Angew.Chem.Int.Ed.Engl.*, 27:880-895, 1988.
- [32] J. D. Dunitz, V. Schomaker, and K. N. Trueblood. Interpretation of atomic displacement parameters from diffraction studies of crystals. *J.Phys.Chem.*, 92:856-867, 1988.
- [33] J. D. Dunitz and D. N. J. White. *Acta Cryst.*, 29:93-94, 1973.
- [34] P. J. Durham. Theory of XANES. In D. C. Koningsberger and R. Prins, editors, *X-ray absorption - Principles, applications, techniques of EXAFS, SEXAFS and XANES*, volume 92 of *Chemical Analysis: A series of Monographs on Analytical Chemistry*, page 53, New York, 1988. John Wiley & Sons.
- [35] P. J. Durham, J. B. Pendry, and C. H. Hodges. *Comput.Phys.Commun.*, 25:193, 1982.

REFERENCES

- [36] P. M. Eisenberger and G. S. Brown. The study of disordered systems by EXAFS: limitations. *Solid State Communications*, 29:481-484, 1979.
- [37] P. M. Eisenberger and B. M. Kincaid. *Science*, 200:1441, 1978.
- [38] K. Fan, Y. Xie, and J. Boggs. A study of the vibrational behaviour of imidazole by the ab initio gradient method. *Theochem*, 29(3-4):339-50, 1986.
- [39] G. Filippini and C. M. Gramaccioli. Thermal motion analysis in tetraphenylmethane: a lattice-dynamical approach. *Acta Cryst.*, B42:605-609, 1986.
- [40] A. Filipponi, A. D. Cicco, T. A. Tyson, and C. R. Natoli. Ab-initio modelling of x-ray absorption spectra. *Solid State Comm.*, 78(4):265-268, 1991.
- [41] F. Fillaux, J. Tomkinson, and J. Penfold. Proton dynamics in the hydrogen bond. the inelastic neutron scattering spectrum of potassium hydrogen carbonate at 5K. *Chem.Phys.*, 124:425-437, 1988.
- [42] D. L. Foulis, R. F. Pettifer, C. R. Natoli, and M. Benfatto. Full-potential scattered wave calculations for molecules and clusters: fundamental tests of the method. *Phys.Rev.A*, 41:6922, 1990.
- [43] L. M. Goldsmith and C. E. Strouse. *J.Am.Chem.Soc.*, 99:7580-7589, 1977.
- [44] H. Goldstein. *Classical Mechanics*. Addison-Wesley Publishing Company, Reading, Massachusetts, 2nd edition, 1980.
- [45] D. Graham, J. Howard, T. C. Waddington, and J. Tomkinson. *J.Chem.Soc.Faraday Trans.II*, 79:1713, 1983.
- [46] E. Grech, Z. Malarski, and L. Sobczyk. Coupling of $\nu(\text{nh}\cdots\text{n})$ vibrations with the $\gamma(\text{nh}\cdots\text{n})$ overtone in solid imidazole derivatives. *Spectrochimica Acta*, 48A:519, 1992.
- [47] S. J. Gurman. The small-atom approximation in EXAFS and surface EXAFS. *J.Phys.C*, 21:3699-3717, 1988.
- [48] S. J. Gurman, N. Binstead, and I. Ross. *J.Phys.C*, 17:143, 1984.
- [49] S. J. Gurman, N. Binstead, and I. Ross. *J.Phys.C*, 19:1845, 1986.
- [50] S. Hara. *J.Phys.Soc.*, 26:376, 1967.
- [51] J. E. Harris, D. W. L. Hukins, and S. S. Hasnain. *J. Phys. C*, 19:6859, 1986.
- [52] S. S. Hasnain. *Life Chem.Rep.*, 4:273, 1987.
- [53] S. S. Hasnain and C. D. Garner. *Prog.Biophys.Mol.Biol.*, 50:47, 1987.
- [54] L. Hedin and B. I. Lundqvist. *J.Phys.C*, 4:2064, 1971.
- [55] L. Hedin and B. I. Lundqvist. *J.Phys.C*, 4:2347, 1971.
- [56] L. Hedin and S. Lundqvist. *Solid State Physics*, 23:1, 1969.

REFERENCES

- [57] L. Hedin and S. Lundqvist. *J. Phys. C*, 3:73, 1972.
- [58] C. Hermes, E. Gilberg, and M. H. J. Koch. *Nucl. Instr. Meth.*, 22:207, 1984.
- [59] F. L. Hirschfeld. *Acta Cryst. A*, 32:239-244, 1978.
- [60] J. B. Hodgson, G. C. Percy, and D. A. Thornton. The infrared spectra of imidazole complexes of first transition series metal(II) nitrates and perchlorates. *J. Mol. Struct.*, 66:81-92, 1980.
- [61] C. J. Joachain. *Quantum Collision Theory*. North-Holland, Amsterdam, 1975.
- [62] C. K. Johnson. ORTEP: A FORTRAN thermal ellipsoid plot program for crystal structure illustrations; Report ornl-3794. Technical report, Oak Ridge National Laboratory, Oak Ridge, TN, 1965.
- [63] C. K. Johnson. An introduction to thermal motion analysis. In F. R. Ahmed, editor, *Crystallographic Computing - Proceedings of the 1969 international summer school on crystallographic computing*. Munksgaard, 1970.
- [64] C. K. Johnson. *Thermal Neutron Diffraction*, pages 132-160. Oxford University Press, London, 1970.
- [65] K. H. Johnson. *Adv. Quantum Chem.*, 7:143, 1973.
- [66] N. Joop and N. Zimmermann. *Z. Phys. Chem.*, 42:61, 1964.
- [67] G. J. Kearley. A profile-refinement approach for normal-coordinate analyses of inelastic neutron-scattering spectra. *J. Chem. Soc. Faraday Trans. 2*, 82:41, 1986.
- [68] G. J. Kearley and J. Tomkinson. CLIMAX: a program for force constant refinement from inelastic neutron spectra. In *Inst. Phys. Conf. Ser. No. 107*, volume 6, page 245, Rutherford Appleton, 1990. Neutron Scatt. Data Anal. Workshop.
- [69] G. J. Kearley, J. Tomkinson, and J. Penfold. New constraints for normal mode analysis of inelastic neutron scattering spectra: application to the HF_2^- ion. *Z. Phys. B - condensed matter*, 69:63-67, 1987.
- [70] S. King. *J. Phys. Chem.*, 74:2133, 1970.
- [71] P. F. Knowles, R. W. Strange, N. J. Blackburn, and S. S. Hasnain. EXAFS studies on pig plasma amine oxidase. A detailed structural analysis using the curved wave multiple scattering approach. *J. Am. Chem. Soc.*, 111:102-107, 1989.
- [72] L. Koester and W. Yelon. *Summary of low energy neutron scattering lengths and cross sections*. Netherlands Energy Research Foundation, 1982.
- [73] W. Kohn and L. J. Sham. *Phys. Rev. A*, 140:133, 1965.
- [74] P. A. Lee and G. Beni. New method for the calculation of atomic phase shifts: application to extended x-ray absorption fine structure (EXAFS) in molecules and crystals. *Phys. Rev. B*, 15:2862, 1977.

REFERENCES

- [75] P. A. Lee, P. H. Citrin, P. Eisenberger, and B. M. Kincaid. *Rev. Mod. Phys.*, 53:769, 1981.
- [76] P. A. Lee and J. B. Pendry. Theory of extended x-ray absorption fine structure. *Phys. Rev. B*, 11:2795, 1975.
- [77] J. W. Leech and D. J. Newman. *How to use Groups*. Methuen and Co. Ltd., London, 1969.
- [78] K. Link, H. Grimm, B. Dorner, H. Zimmermann, H. Stiller, and P. Bleckmann. Determination of the lattice vibrations of imidazole by neutron scattering. *J. Phys. Chem. Solids*, 46:135-142, 1985.
- [79] P. W. Loeffen, R. F. Pettifer, and N. Alcock. Crystal structure and TLS-analysis of zinc (II) tetraimidazole borofluorate. *to be published*, 1994.
- [80] P. W. Loeffen, R. F. Pettifer, and F. Fillaux. Vibrational spectrum of imidazole from inelastic neutron scattering: force field based on single crystal and deuteration studies. *to be published*, 1994.
- [81] G. F. Longster and J. W. White. Vibrational assignments in polymer neutron-scattering by atomic substitution. *J. Chem. Phys.*, 48(11):5271, 1968.
- [82] S. W. Lovesey. *Theory of Neutron Scattering from Condensed Matter*. Oxford University Press, Oxford, 1984.
- [83] S. W. Lovesey. Condensed matter physics, dynamic correlations. In *Frontiers in Physics*, volume 61, Palo Alto, 1986. Benjamin/Cummings.
- [84] M. Majoube. In *6th. Intern. Conf. Raman Spectroscopy*, vol. 2, London, 1978. Heydon.
- [85] M. Majoube, September 1991. Private Communication.
- [86] M. Majoube, M. Henry, L. Chinsky, and P. Turpin. Preresonance raman spectra for imidazole and imidazolium ion: interpretation of the intensity enhancement from a precise assignment of normal modes. *Chem. Phys.*, 169:231-241, 1993.
- [87] M. Majoube and G. Vergoten. Lattice vibrations of crystalline imidazole and ^{15}N and D substituted analogs. *J. Chem. Phys.*, 76(6):2838, 1982.
- [88] M. Majoube and G. Vergoten. Assignment of normal modes for imidazole on the basis of 3-21G and 4-21G ab initio force fields. *J. Mol. Struct.*, 266:345-352, 1992.
- [89] J. Mathews and J. L. Walker. *Mathematical Methods of Physics*. Addison-Wesley Publishing Company, New York, 2nd edition, 1970.
- [90] L. F. Mattheiss, J. H. Wood, and A. C. Switendick. *Methods in Computational Physics*, volume 8, page 63. Academic Press, New York, 1968.
- [91] A. Messiah. *Quantum Mechanics - Volume I*. North Holland Publishing Company, Amsterdam, 1965.

REFERENCES

- [92] M. A. Morrison. *Understanding Quantum Physics*. Prentice Hall, Englewood Cliffs, New Jersey, 1990.
- [93] J. E. Müller and W. L. Schaich. Single-scattering theory of x-ray absorption. *Phys.Rev.B*, 27(10):6489, 1983.
- [94] J. Mustre, Y. Yacoby, E. A. Stern, and J. J. Rehr. Analysis of experimental extended x-ray absorption fine-structure EXAFS data using calculated curved-wave, multiple-scattering EXAFS spectra. *Phys.Rev.B*, 42(17):10843, 1990.
- [95] C. R. Natoli and M. Benfatto. In P. Lagarde, D. Raoux, and J. Petiau, editors, *EXAFS and near-edge structure IV*, Paris, 1986.
- [96] C. R. Natoli, M. Benfatto, C. Brouder, M. F. R. López, and D. L. Foulis. Multichannel multiple scattering theory with general potentials. *Phys.Rev.B*, 42(4), 1990.
- [97] C. R. Natoli, M. Benfatto, and S. Doniach. Use of general potentials in multiple-scattering theory. *Phys.Rev.A*, 34(6):4682, 1986.
- [98] G. J. Norman. Non-empirical versus empirical choices for overlapping-sphere radii ratios in SCF-X α -SW calculations on ClO $_4^-$ and SO $_2$. *Molec.Phys.*, 31:1191, 1975.
- [99] A. Novak, P. Saumagne, and L. Bok. *J.Chim.Phys.*, 60:1385, 1963.
- [100] L. Pauling and E. B. Wilson, Jr. *Introduction to Quantum Mechanics*. McGraw-Hill, New York, 1935.
- [101] G. S. Pawley, P. A. Reynolds, J. K. Kjems, and J. W. White. A model calculation of the inelastic neutron scattering spectra from polycrystalline naphthalene. *Solid State Comm.*, 9:1353-1357, 1971.
- [102] J. B. Pendry. EXAFS - a critical review. In S. S. Hasnain, editor, *X-ray absorption fine structure*, XAFS IV, Chichester, 1991. Ellis-Horwood.
- [103] J. Penfold and J. Tomkinson. *Rutherford Appleton Laboratory Internal Report*, RAL-86-019, 1986.
- [104] C. Perchard, A.-M. Bellocq, and A. Novak. Spectres de vibration de l'imidazole, de l'imidazole (D)-1, de l'imidazole (D $_3$)-2,4,5 et de l'imidazole (D $_4$). *J.Chim.Phys.*, 62:1344-58, 1965.
- [105] C. Perchard and A. Novak. far-infra red spectra and hydrogen-bond frequencies of imidazole. *J.Chem.Phys.*, 48(7):3079, 1967.
- [106] R. F. Pettifer, C. Brouder, M. Benfatto, C. R. Natoli, C. Hermes, and M. F. López. Magic angle theorem in powder x-ray absorption spectroscopy. *Phys.Rev.B*, 42(1), 1990.
- [107] R. F. Pettifer and A. D. Cox. The reliability of ab initio calculations in extracting structural information from EXAFS. In *EXAFS and Near-Edge Structure*, page 66. Springer Verlag, 1983.
- [108] R. F. Pettifer, D. L. Foulis, and C. Hermes. Multiple scattering calculations for biological catalysts. *Journal de Physique*, 47(12):545, 1986.

REFERENCES

- [109] R. F. Pettifer and C. Hermes. Absolute energy calibration of x-ray radiation from synchrotron sources. *J. Appl. Cryst.*, 18:404-412, 1985.
- [110] R. F. Pettifer and C. Hermes. An x-ray monochromator suitable for studying biological systems. *Journal de Physique*, 47(12):127, 1986.
- [111] L. Powers. *Biochim. Biophys. Acta*, 683:1, 1982.
- [112] R. Prins and D. C. Koningsberger. Catalysis. In D. C. Koningsberger and R. Prins, editors, *X-ray absorption spectroscopy*, page 321, New York, 1988. Wiley.
- [113] P. Pulay. *Theor. Chim. Acta*, 50:299, 1979.
- [114] P. Pulay, G. Fogarasi, F. Pang, and J. Boggs. *J. Am. Chem. Soc.*, 101:2550, 1979.
- [115] J. Reedijk. Pyrazoles and Imidazoles as ligands. Part I. some simple metal(II) perchlorates and tetrafluoroborates solvated by neutral pyrazole and imidazole. *RECUEIL*, 88:1451, 1969.
- [116] J. J. Rehr, R. C. Albers, and J. M. de Leon. *Physica*, B158:417, 1989.
- [117] J. J. Rehr, R. C. Albers, C. R. Natoli, and E. A. Stern. New high-energy approximation for x-ray absorption near-edge structure. *Phys. Rev. B*, 34:4350, 1986.
- [118] P. A. Reynolds, J. K. Kjems, and J. W. White. Experimental lattice vibrational dispersion curves for β -phase $p\text{-C}_6\text{H}_4\text{Cl}_2$ at 295K and 90K, and acoustic velocities for β -phase $p\text{-C}_6\text{H}_4\text{Cl}_2$ at 295K compared with a general crystal potential for the chlorobenzenes. In *Neutron Inelastic Scattering*, volume 301, pages 195-206, Vienna, 1972. I.A.E.A.
- [119] P. A. Reynolds, J. K. Kjems, and J. W. White. High-resolution inelastic neutron scattering from some aromatic molecular polycrystals for study of crystal excitations and anharmonic effects. *J. Chem. Phys.*, 56(6):2928, 1972.
- [120] P. A. Reynolds and J. W. White. Inelastic neutron scattering from molecular and crystal excitations in aromatic molecular crystals. *Farad. Soc.*, 48:131, 1969.
- [121] L. S. Rodberg and R. M. Thaler. *Introduction to the quantum theory of scattering*, volume 26 of *Pure and Applied Physics*. Academic Press, New York, 1967.
- [122] M. F. Ruiz-Lopez, F. Bohr, A. Filipponi, A. D. Cicco, T. A. Tyson, M. Benfatto, and C. R. Natoli. MSXAS package (V92.1). In S. S. Hasnain, editor, *X-Ray Absorption Fine Structure*, pages 75-77, New York, 1991. Ellis-Horwood.
- [123] M. F. Ruiz-Lopez, M. Loos, J. Goulon, M. Benfatto, and C. R. Natoli. Reinvestigation of the EXAFS and XANES spectra of ferrocene and nickelocene in the framework of multiple scattering theory. *Chem. Phys.*, 121:419, 1988.
- [124] J. Sadlej and W. Edwards. Correlated ab initio geometry and vibrational spectra of imidazole and its different forms. *Int. J. Quant. Chem.*, 26:409-420, 1992.
- [125] J. Sadlej, A. Jaworski, and K. Miaskiewicz. A theoretical study of the vibrational spectra of imidazole and its different forms. *J. Mol. Struct.*, 274:247-257, 1992.

REFERENCES

- [126] D. R. Sandstrom and F. W. Lytle. *Ann.Rev.Phys.Chem.*, 30:215, 1979.
- [127] D. E. Sayers, E. A. Stern, and F. Lytle. *Phys.Rev.Lett.*, 27:1204, 1971.
- [128] W. L. Schaich. Comment on the theory of extended x-ray absorption fine structure. *Phys.Rev.B*, 8:4028, 1973.
- [129] N. E. Schlotter and B. Hudson. Tetraphenyl-group IV B compounds: flexible molecules with high symmetry crystals. I. Assignment of low frequency infrared and raman bands. *J.Chem.Phys.*, 76(10):4844, 1982.
- [130] N. E. Schlotter and B. Hudson. A test of the validity of non-bonded potential energy functions: the ability of an empirical energy function the reproduce the structure and low-frequency vibrations of a flexible molecule in a van der Waals crystal. *J.Phys.Chem.*, 90:719-721, 1986.
- [131] V. Schomaker and K. N. Trueblood. *Acta Cryst.*, B24:63-76, 1968.
- [132] R. A. Scott. In C. H. W. Hirs and S. N. Timasheff, editors, *Methods in Enzymology*, volume 117, page 414, Orlando, Florida, 1985. Academic Press.
- [133] G. M. Sheldrick. *SHELXTL PLUS*. Nicolet XRD Corporation, 1986.
- [134] J. C. Slater. *Phys.Rev.*, 81:385, 1951.
- [135] J. C. Slater. *The self-consistent field for molecules and solid, Quantum theory of molecules and solids*, volume 4. McGraw-Hill, New York, 1974.
- [136] A. L. Smith. Low frequency vibrational spectra of group IV-A phenyl compounds. *Spectrochimica Acta*, 24A:695-706, 1968.
- [137] E. A. Stern. *Contemp.Phys.*, 19:289, 1978.
- [138] E. A. Stern and S. M. Heald. In E. E. Koch, editor, *Handbook on Synchrotron Radiation*, volume 1, New York, 1983. North Holland.
- [139] E. A. Stern, D. E. Sayers, and F. W. Lytle. Extended x-ray absorption fine structure technique; III Determination of physical parameters. *Phys.Rev.B*, 11:4836, 1975.
- [140] R. W. Strange, N. J. Blackburn, P. F. Knowles, and S. S. Hasnain. *J.Am.Chem.Soc.*, 109:7157-7162, 1987.
- [141] R. W. Strange, S. S. Hasnain, N. J. Blackburn, and P. F. Knowles. *J.Phys.(Paris)*, 47:593-596, 1986.
- [142] M. W. Thomas and R. E. Ghosh. Incoherent inelastic neutron scattering from hexamethylene-tetramine and adamantane. *Molec.Phys.*, 5:1489-1506, 1975.
- [143] J. Tomkinson, C. J. Carlile, S. W. Lovesey, R. Osborn, and A. D. Taylor. Pulsed neutron studies of materials. In R. J. H. Clark and R. E. Hester, editors, *Spectroscopy of Advanced Materials*, chapter 3, pages 135-213. John Wiley and Sons Ltd, 1991.
- [144] J. Tomkinson and G. J. Kearley. Phonon wings in inelastic neutron scattering spectroscopy: the harmonic approximation. *J.Chem.Phys*, 91(9):5164, 1989.

REFERENCES

- [145] J. Tomkinson, M. Warner, and A. D. Taylor. Powder averages for neutron spectroscopy of anisotropic molecular oscillators. *Mol.Phys.*, 51(2):381-392, 1984.
- [146] K. N. Trueblood and J. D. Dunitz. *Acta Cryst. B*, 39:120-133, 1983.
- [147] J. F. Twisleton and J. W. White. Interchain force field of polyethylene by neutron scattering. In *Neutron Inelastic Scattering*, page 301, Vienna, 1972. I.A.E.A.
- [148] L. Van Hove. *Phys.Rev.*, 95:249, 1954.
- [149] J. A. Victoreen. *J. Appl. Phys.*, 19:855, 1948.
- [150] T. C. Waddington, J. Howard, K. P. Brierley, and J. Tomkinson. Inelastic neutron scattering spectra of alkali metal (Na,K) bifuorides: the harmonic overtone of ν_3 . *Chem.Phys*, 64:193-201, 1982.
- [151] K. D. Watenpaugh, L. C. Sieker, and L. H. Jensen. *J.Mol.Biol.*, 138:615-633, 1980.
- [152] D. Watkin. *CRYSTALS - Issues 9 for DEC-VAX*. Chemical Crystallography Laboratory, Oxford, December 1989.
- [153] J. W. White. *Spectral Assignment in inelastic neutron scattering by atomic substitution techniques*. N.B.S. Special Publication, 1969.
- [154] G. Will. *Nature*, 198:575, 1963.
- [155] E. B. Wilson, Jr. *J.Chem.Phys.*, 7:1047, 1939.
- [156] E. B. Wilson, Jr., J. C. Decius, and P. C. Cross. *Molecular Vibrations - The Theory of Infrared and Raman Vibrational Spectra*. Dover Publications, Inc., New York, 1955.
- [157] V. Yachandra, L. Powers, and T. G. Spiro. X-ray absorption spectra and the coordination number of Zn and Co carbonic anhydrase as a function of pH and inhibitor binding. *J.Am.Chem.Soc.*, 105:6596-6604, 1983.
- [158] Q. C. Yang, M. F. Richardson, and J. D. Dunitz. *J.Am.Chem.Soc.*, 107:5535-5537, 1985.
- [159] B. Zelei. Vibrational spectra and infrared dichroism of tetraphenylmethane, PH_4C . *Spectrochimica Acta*, 42A(10):1119-1125, 1986.
- [160] H. Zelsmann, P. Excoffon, and Y. Marechal. Far-infrared spectra of imidazole monocrystals. *Chem.Phys.Lett.*, 110(3):285, 1984.